UNIVERSITÀ DEGLI STUDI DI TORINO

PHD PROGRAM

DEPARTMENT OF PHYSICS

PhD Program in Physics – XXXVI cycle

Fabrication and characterization of solid-state quantum emitters in large energy gap semiconductors

Candidate:

Elena Nieto Hernández

Supervisor:

Prof. Jacopo Forneris

Co-supervisor:

Dr. Sviatoslav Ditalia Tchernij

PhD Program Coordinator:

Prof. Paolo Olivero

Academic years 2021 – 2024

To my parents and my siblings

To Amalia, Jose and Carmen

"Caminante, son tus huellas
el camino y nada más;
Caminante, no hay camino,
se hace camino al andar.
Al andar se hace el camino,
y al volver la vista atrás
se ve la senda que nunca
se ha de volver a pisar.
Caminante no hay camino
sino estelas en la mar."-

Antonio Machado

Acknowledgments

The three years spent in the Solid-State Group at the University of Turin doing experimental work have brought me immense happiness and knowledge. These years wouldn't have been the same without the support of those around.

For this reason, I would like to express my gratitude to both my supervisor Prof. Jacopo Forneris, and co-supervisor Dr. Sviatoslav Ditalia Tchernij, for following me with enormous patience and availability, guiding me since my very first day in a new group and a new country. I want to thank both for all the support during the experimental work and all the fruitful scientific discussions that have helped me to start building my career as a scientist and develop all the work presented in this thesis.

I would like to thank Prof. Paolo Olivero as the head of the *Diamond* group for all the scientific support and for welcoming me into his group 3 years ago. To Prof. Ettore Vittone I express my biggest gratitude for allowing me to participate in the building up of the ion implanter and for leading the Solid-State Group towards interesting scientific advancements. I thank Prof. Federico Picollo for all the experimental help and scientific discussions.

As part of a Marie Skłodowska-Curie Innovative Training Networks' program, LasIonDef, I would like to acknowledge the whole project. I would like to thank Dr. Shane Eaton for all the work carried out as the head of the project, allowing me to acquire deep scientific knowledge not only in my specific field but also in what my colleagues were working on. This project gave me the opportunity to see the importance of networking inside the scientific community and listening to the advices and ideas of other colleagues but also to travel and visit other labs, to see and perform experiments outside of my comfort zone. In particular, I would like to thank Prof. J.P. Hadden and Prof. Anthony Bennett for welcoming me into their group to perform some experiments at Cardiff University and to Prof. Alexander Kubanek, for allowing me to visit his group and participate in some interesting experiments at Ulm University, both these experiences were very gainful from a personal and scientific perspective. For these experiences and for all the other ones lived together, I would like to thank Bilge and Selene, who helped me in Cardiff and Ulm, to feel like home. To Giulio, Juan and Alex thank you for making these three years of project much funnier, I am grateful to have met the three of you and happy to call you both colleagues and friends.

I would like to thank my Diamond colleagues in Turin, especially Pietro, Adam, Greta, Veronica, Sofia, Matija and Nour Hanne, thanks for all the wonderful lab experiences and help.

To my colleagues and friends, Emilio, Vanna, Elisa and Gabriele, none of my outcomes from these three years would have been possible without your help. Thank you for the scientific discussions, personal advice and great time spent together. I will always be grateful for the quantum family we have built.

Outside of the lab it is time to thank my Spanish friends from Turin, specifically, Alberto, Arturo, Cristian, Alba and Dani, who throughout the years became more family than friends, making Torino feel like home. To my friends in Spain, Aida and Clara, thanks for always supporting me on my life decisions and cheering my life up. Thanks also to my master's thesis friends, I am really grateful for you and your friendship.

Finally, I would like to thank my family. I could have not arrived where I am today if it was not for their unconditional support in every decision I have made. I would like to especially thank my mother, for the everyday morning hour of talking during these three years, that made my journey much easier and pushed me to continue doing what I like in the best way possible. Thanks to my father and siblings for always holding my hand through every step in life. Thanks to my grandparents, I am well aware I couldn't have arrived here if it weren't for their help and support through my physics degree years, back in Salamanca. Lastly, thanks to Carmen, my niece, for making my face and life much more cheerful.

Technical acknowledgements

This work was supported by the following projects: ‘Training on LASer fabrication and ION implantation of DEFects as quantum emitters’ (LasIonDef) project funded by the European Research Council under the ‘Marie Skłodowska-Curie Innovative Training Networks’ program, ‘Intelligent fabrication of QUANTum devices in DIAmond by Laser and Ion Irradiation’ (QuantDia) project funded by the Italian Ministry for Instruction, University and Research within the ‘FISR 2019’ program; experiments ROUGE and PICS4ME, funded by the 5th National Commission of the Italian National Institute for Nuclear Physics (INFN); Project “Piemonte Quantum Enabling Technologies” (PiQuET), funded by the Piemonte Region within the “Infra-P” scheme (POR-FESR 2014-2020 program of the European Union); “Departments of Excellence” (L. 232/2016), funded by the Italian Ministry of Education, University and Research (MIUR); “Ex post funding of research - 2021” of the University of Torino funded by the “Compagnia di San Paolo”.

List of contents

List of figures

List of tables

List of Acronyms

AFM	Atomic Force Microscopy
AlN	Aluminum Nitride
APDs	Avalanche PhotoDiodes
CVD	Chemical Vapor Deposition
CW	Continuous wave
DFT	Density Functional Theory
EPR	Einstein-Podolsky-Rosen
ERDA	Elastic Recoil Detection Analysis
ES	Excited state
FC	Faraday Cup
FCC	Face Centered Cubic
FIB	Focused Ion Beam
FWHM	Full Width Half Maximum
G4V	Group IV
GaN	Gallium Nitride
GeV	Germanium Vacancy
GS	Ground state
HBT	Hanbury Brown and Twiss
HPHT	High pressure High temperature
HVPE	Hydride Vapor phase Epitaxy
IBIC	Ion Beam Induced Charge
LINAC	Linear Accelerator

MgV	Magnesium Vacancy
MNVPE	Metal Nitride Gas Phase Epitaxy
MOCVD	Metal-Organic Chemical Vapor deposition
MOT	Magneto Optical Trap
N.A.	Numerical Aperture
ND	Nanodiamonds
NIC	Negative Ion Cookbook
NMR	Nuclear Magnetic Resonance
NV	Nitrogen Vacancy
ODMR	Optically Detected Magnetic Resonance
PbV	Lead Vacancy
PKA	Primary knock-on Atoms
PL	Photoluminescence
PVT	Physical Vapor Transport
QKD	Quantum Key Distribution
RF	Radiofrequency
RTA	Rapid Thermal Annealing
SEM	Scanning Electron Microscopy
SiC	Silicon Carbide
SiV	Silicon Vacancy
SNICS	Source of Negative Ions by Cesium Sputtering
SPAD	Single- Photon Avalanche Diode
SPS	Single photon source
STED	Stimulated Emission Depletion
STIM	Scanning Transmission Ion Microscopy
STIRAP	Stimulated Raman Adiabatic Passage
TIRF	Total Internal Reflection
ZPL	Zero Phonon Line

Preface

In the past few decades, the use of diamond and other wide bandgap semiconductors as quantum technology platforms has emerged as a promising field of research. One of their more prominent applications is found in the field of quantum sensing, but also in other areas such as quantum computing and communication.

The interest attracted by these platforms, which have been found to be hosts of single-photon sources (SPS), usually referred to as color centers; arises from the possibility of combining compact photonic structures and single-photon sources in the same device, to implement reliable quantum protocols at the nanoscale. Moreover, the majority of these color centers can emit single photons at room temperature, making them even more appealing from the operational point of view.

Among these wide bandgap semiconductors that are been considered for the realization of quantum devices, diamond plays an important role. The large energy gap allows for the incorporation of impurities acting as isolated molecule-like systems. The low density of phononic states present in the crystal at room temperature make the electronic transitions of the hosted impurities display a high quantum efficiency and so reliable for the application as quantum sources. Moreover, diamond is a chemical inert and biocompatible material, which allows for implementation in the biotechnology and nanomedicine fields.

Many different optically active defects have been reported so far in diamond. The Nitrogen vacancy (NV) center is among the most studied ones due to its unique optically addressable spin properties that allow for the implementation of this defect as a sensor for electromagnetic fields, temperatures or even pressure. However, this defect presents some drawbacks such as broad emission, relatively low emission rate and the presence of a metastable level, that limit its implementation in some fields such as quantum information. To overcome these limitations, other impurity-related defects have been reported in recent years with some interesting properties (sharp emission, high emission rate, low radiative lifetime…), such as the Group-IV related emitter (SiV, GeV, SnV and PbV). As part of this research, additional centers have been explored such as the Magnesium vacancy (MgV) center, displaying some properties similarly to the Group-IV centers, but for which further study is still to be done.

One of the most adopted fabrication techniques to produce color centers is based on ion implantation either at keV or MeV energies, followed by a post implantation annealing treatment that allows for the right arrangement of the atoms in the lattice and optical activation of the centers.

Despite being a well stablished technique, the fabrication of reliable sources with optimal properties for the scalability of quantum devices is still a challenge. This thesis dissertation aims to overcome some of the challenges that the fabrication of color centers presents, such as the low creation yield for the majority of the centers, the damage created in the lattice upon high fluences ion implantation that leads to the irreversible graphitization of the diamond or even the pernicious effect that the implantation of heavy ions (Ge, Sn, Pb) has on the properties of the outcoming color centers, due to the suboptimal post-implantation standard annealing techniques.

As part of this objective, during this PhD period part of the work was centered around the commissioning of the 100 keV ion implanter at the Department of Physics in Torino, that allowed to performed part of the experiments that will be discussed in this dissertation, along with many others in collaboration with external users, leading to some outstanding results in other materials, as will be discussed in the conclusions Chapter.

On what regards the fabrication of color centers in diamond, in this dissertation three main experimental works will be discussed. The first one will be centered on the analysis of the single-photon properties of GeV centers upon keV ion implantation and different thermal annealing, including HPHT treatment. The second one will analyze the effect of CW laser irradiation on as implanted diamond for the creation of Sn-related defects. The last one will treat the effects of hot MeV ion implantation on the graphitization threshold of diamond and the formation efficiency of the NV and MgV centers. These three works aim to

find alternative activation methods for the considered color centers in diamond that may pave the way for the reproducible fabrication of quantum devices with integrated single-photon sources (SPS) in diamond.

In addition to the studies based on fabrication of color centers in diamond, during the PhD work several other wide bandgap semiconductors were mannered, in particular the results on the fabrication of centers upon Al keV ions in Aluminum nitride (AlN), will be discussed in detail in the results section. AlN is an interesting material from the photonic perspective, it is of recent discovery the observation of single photon at RT in this material, yet the structural and chemical origin of these emitters is to be explored. In this dissertation the fabrication of such emitters upon keV ion implantation will be discussed.

All this activity has been conducted in the context of the LasIonDef Marie Curie ITN project and the Solid-State Physics group of the University of Turin, leading to a strong interdisciplinary collaboration between researchers of several universities.

The manuscript is organized as follows:

- Chapter 1 introduces the main physical principles of the SPS and their applications in quantum technologies. In particular, the main color centers reported in diamond and other wide bandgap materials will be presented along with a deeper explanation on the main properties of diamond and AlN as the main host materials studied in this thesis.
- Chapter 2 is dedicated to the principles of ion matter interaction and the different techniques that are usually used for the fabrication of SPS in diamond and AlN.
- Chapter 3 includes a detailed description of the different processing tools and experimental characterization setups that have been employed for the studies that were performed during the PhD period.
- Chapter 4 presents the main results obtained during the research work.
- Chapter 5 summarizes the outcomes of the work carried out during the PhD period.

Chapter 1

In this Chapter, the main properties of the single photon sources (SPS) will be explained, along with the main classification of such and the different potential applications they have in quantum technologies. In particular, the discussion will be centered around the solid-state defects as emitters of single photons in several wide bandgap semiconductors. A final explanation on the main materials that will be considered for the fabrication of single photon emitters, i.e. diamond and AlN, will be given, including the main physical properties and the different growth techniques and substrates than can be fabricated.

1.1 Quantum technologies

Quantum technologies is an ever-growing research field that utilizes the fundamental principles of quantum mechanics to achieve certain functionalities more efficiently than classic technologies[2]. The interest in quantum technologies has grown rapidly in recent years, lying mainly in the realization of quantum bits, or as they as referred to usually "*qubits*", as the most elementary unit of quantum information[3].

Qubits have a wide range of applications in the field of quantum technologies, especially in quantum computing and quantum communication as quantum memories and registers[4]. They can be implemented in various systems such as ultra-cold atoms, trapped ions, superconducting arrays, integrated photonic chips, coupled matter-light systems, and solid-state platforms. Among these, those involving quantum states of light, particularly single-photon emitters, seem to be playing a central role in the development of the quantum world[5]. The generation and manipulation of systems emitting single photons is a logical choice for quantum communication[4], computing[6], quantum sensing[7], and metrology[8].

1.1.1 Single-photon sources

Single photons on demand are important resources in various areas of emerging quantum technologies, such as quantum key distribution (QKD) and all-optical quantum information processing[9]. They are a basic prerequisite for unconditional security in QKD protocols and a key ingredient for fault-tolerant quantum computing schemes. In other areas such as metrology, an accurate standard for the luminous intensity, or candela, one of the seven primary SI units, can be built using single photons on demand in well-defined modes[10]. To produce single photons on demand, a source must operate in the deep quantum regime and have a high degree of quantum control. This is necessary to achieve sufficient purity and quantum efficiency of photon production. The following are the required characteristics that a single photon source (SPS) should meet[11]:

- Deterministic emission, the source must deliver only one photon per excitation pulse, avoiding multi-photon emissions, with the photon being emitted shortly after the excitation.
- Monochromaticity, meaning a narrow photoluminescence (PL) linewidth (high Debye factor), requiting low phonon coupling and negligible dephasing or spectral diffusion to exploit Fourier transform limited indistinguishable photons.
- High emission rate, meaning a short, excited lifetime, $\tau \sim$ ns.
- Photostable emission, without blinking or bleaching behavior.
- High quantum efficiency: low probability of non-radiative channels decay.

The types of single photon sources can be categorized following different criteria, although the most common one is separating them into macroscopic probabilistic sources and microscopic deterministic single photon sources[10].

Macroscopic probabilistic sources

These probabilistic sources deliver Poisson distributions of photons (or photon pairs), from which multi-photon events can never be entirely suppressed. In this case the rate of emission of single photons is limited, leading usually to a probability below 1 of obtaining a photon.

This class of sources involves mainly faint laser pulses and parametric down-conversion (among several other ones).

Faint laser pulses. The basis of this single photon source is a pulsed laser attenuated to the single photon level. The probability of finding n photons in such a coherent state follows Poisson statistics[12]:

$$P(m) = \frac{<n>^m}{m!} e^{-<n>} \qquad \textit{Equation 1}$$

Where < n > is the average number of photons. When this number is small, most pulses are empty. In principle, this could be compensated with an increase in the pulsed laser source rate, but usually the detectors' dark counts pose a problem. These types of single photon sources are the most commonly used for the realization of QKD, because of their wavelength convenience and mature technology[13], [14].

Parametric down-conversion. This technique involves using a laser to illuminate a material with a $\chi^{(2)}$ optical nonlinearity, producing two photons while adhering to momentum and energy conservation laws. This constraint has both advantages and limitations. On the one hand, the emission from these sources is highly directional, making it useful for most applications. On the other hand, the inherent dispersion of transparent material is generally uncontrollable, except for the limited control offered by temperature[15].

One downside of $\chi^{(2)}$-based down conversion in crystals is the spatial mode of the photon pairs. The photon pairs are usually created in multi-mode cones surrounding the pump laser, which makes efficient collection by single-mode fibers difficult.

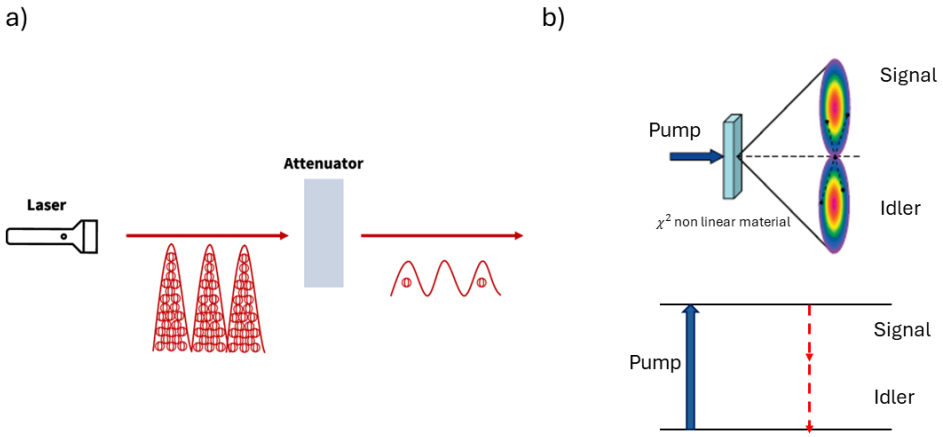

Figure 1 *a) Faint laser pulses system*[16]*, b) Parametric down conversion working principle*[10].

Microscopic deterministic sources

There is a wide variety of systems that have been reported to produce on-demand single photons, among them, we can highlight the semiconductor quantum dots, single cold atoms, and solid-state defects (color centers).

Quantum dots. They are tiny islands of smaller-band-gap semiconductor embedded in a larger-band-gap semiconductor. Their small size results in a discrete energy structure for the electrons and holes. Excitons (electron-hole pairs) can be produced on demand in this structures and their radiative recombination results in single-photon emission. These sources can be excited optically or electrically, providing an interesting platform for the implementation in photonics and electronics. Their main drawback is the fact that quantum dots as single-photon emitters need to operate at cryogenic temperatures, which is still cumbersome. Additionally, they are usually unique structures, as a small difference in the spatial disposition of the quantum dot leads to a different spectral resonance, making the spectral matching of the fabricated quantum dots still an issue and so dimming the potential of practical scalable systems[12], [17], [18].

Single cold atoms. Single-atom emitters are specifically designed to operate in the strong-coupling regime of cavities. In this regime, a single photon has a profound impact on the dynamics of the atom-cavity system, and the optical cavity significantly enhances single-photon emission into a single spatial mode with a Gaussian transverse profile. These atoms are cooled within a magneto-optical trap (MOT). Then, through stimulated Raman adiabatic passage (STIRAP), a single photon is emitted in the cavity mode. As atoms are all identical, atom-based sources could be produced in quantity for a scalable system. However, the experimental overhead required for this would be formidable. Despite these advantages, single-atom emitters have a limited trapping time, and the fluctuating atom-cavity mode coupling can yield decoherence effects, although these effects can be minimized. Additionally, there is a possibility of multi-atom effects[11].

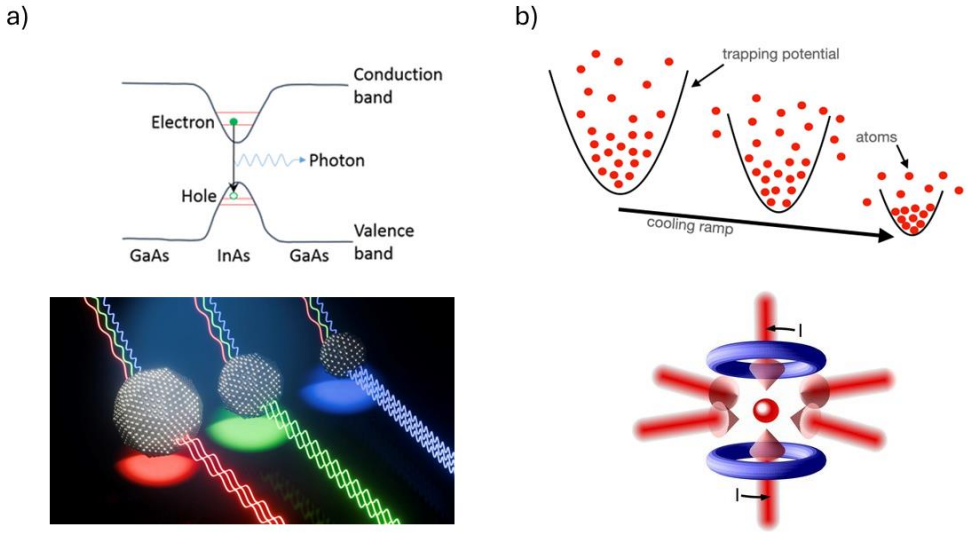

Figure 2 *a) Quantum dot band diagram example* [19]*. b) Cold atoms working principle*[20]

Solid-state defects. These sources produce on-demand single photon sources that can operate at room temperature or at least higher temperatures than in the previous cases. These solid-state platforms are typically semiconductors, and the defects are usually referred to as *color centers*[21]. These color centers arise from localized electronic states around interstitial or substitutional, vacancies or a combination of them. They are usually formed by two states (or three in the case of an intermediate shelving state), a ground and an excited state, that through optical pumping and subsequent radiative decay of an electron leads to the emission of a single photon[10]. The most appealing advantages of this implementation are that usually they are photostable, they can perform in several cases at room temperature although with degraded emission properties and being embedded in a solid-state platform, photonic integrated circuits can be more easily combined with these emitters[22]. Still, the indistinguishability of these sources poses a problem for the majority of the centers studied and reported, due to the challenge in the formation of scalable coherent sources whose environment and structure allow for the identical emission features, although in the past few years, indistinguishability up to 0.73 (for the SiV) has been proved for several types of centers in diamond[23], [24].

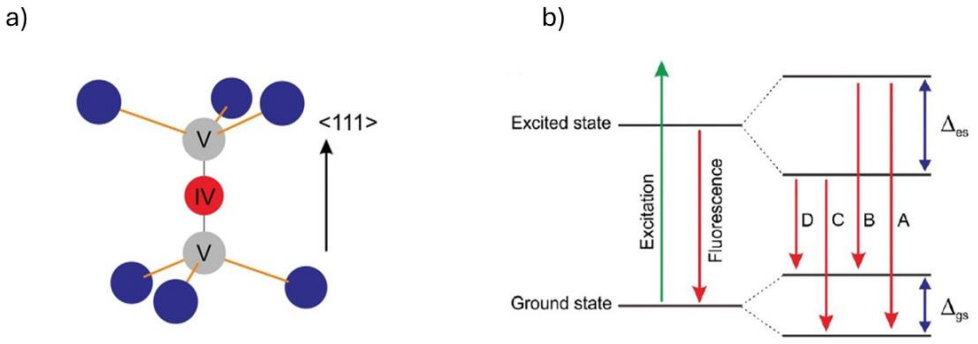

Figure 3 *a) Lattice configuration of group IV color centers in diamond, b) Energy structure of group IV color center at cryogenic temperature* [25].

As has been explained in the previous discussion, there are several well-studied single-photon sources both probabilistic and deterministic. When studying these types of sources, it is important to determine the non-classicality of the emitted photons, in order to classify the systems as single-photon emitters The most common method adopted for this purpose consists of the measurement of the second-order autocorrelation function, traditionally denoted as $g^2(\tau)$, which quantifies the fluctuations of the electromagnetic field of a light beam.

This parameter allows for the interpretation of the below explained types of lights sources and the explanation of a single photon emitter through it. The classical expression of the second-order autocorrelation function [26] is the following:

$$g^2(\tau) = \frac{<I(t)\cdot I(t+\tau)>}{<I(t)>^2} \qquad \textit{Equation 2}$$

Where I(t)=E*(t) E(t) is the electric field intensity and E(t) the electric field amplitude. Making use of the quantum theory, the $g^2(\tau)$ function can be written as a function of photonic creation and annihilation operators as follows[26]:

$$g^2(\tau) = \frac{<\hat{a}^\dagger(t)\,\hat{a}^\dagger(t+\tau)\,\hat{a}(t)\,\hat{a}(t+\tau)>}{<\hat{a}^\dagger(t)\,\hat{a}(t)>^2} \qquad \textit{Equation 3}$$

Therefore, for a specific Fock state ($\hat{a}\,|n> = \sqrt{n}\;|n>$) that fulfils the bosonic commutation relation, the correlation function at zero delay time can be simplified to:

$$g^2(0) = \frac{n(n-1)}{n^2} \qquad \textit{Equation 4}$$

Where n stands for the number of quantum sources. So, in the case in which we are measuring a single photon emitter we will have n=1, and so $g^2(0) = 0$. However, this represents the ideal case, while in the experimental case the measurements are usually affected by the presence of surroundings lights sources, so a value of 0.5 (corresponding to n=2, two single photon emitters) is usually considered as sufficient to verify the quantum nature of the source[26].

The three main types of light and their sources can be characterized by this parameter, as follows (Figure 4)[11], [27]:

1. **Thermal light.** It is also known as chaotic or incoherent. In a more mathematical way, it is referred to as super Poissonian. A thermal light source emits packets of light due to fluctuations of intensity of the source itself. It exhibits $g^2(\tau) = 2$.
2. **Coherent light.** Also referred as to *Poissonian* light, the most representative example of this type of source is a laser source. It exhibits a constant degree of second-order coherence equal to unity for all temporal offsets, $g^2(\tau) = 1$.

3. **Antibunched light.** It is also considered as sub-Poissonian light, showing an increasing second-order coherence monotonically from the initial value $\tau = 0$ out to a some finite temporal offset $\Delta\tau$. $g^2(\Delta\tau) > g^2(0)$.

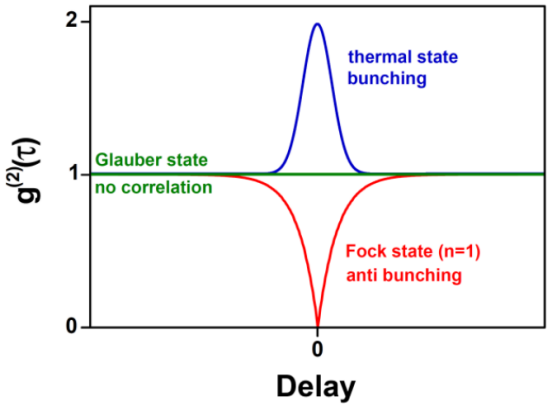

Figure 4 *Second order autocorrelation function for the three types of light sources.*

1.1.2 Quantum technologies applications

While quantum phenomena have been studied for decades, important technologies based on those phenomena have only appeared relatively recently. Some of these technologies offer significant advantages for business, national security, health, and for the study of quantum physics themselves. The infrastructure for research includes quantum computers, quantum communication devices but also quantum sensors, in addition to encryption and software devices. A further insight will be given in this section on mainly quantum sensing, communication, and computing.

Quantum sensing

In recent years, different classes of applications have emerged regarding the employment of quantum mechanical systems as sensors for several physical quantities going from magnetic and electrical fields to temperature and pressure[7]. We can talk of quantum sensing either when using a quantum object to measure a physical quantity, using the quantum coherence of s system to measure a physical quantity, or using the quantum entanglement to improve the sensitivity of a measurement.

The four following criteria must be accomplished by a quantum system to function as a quantum sensor[7]:

1. The quantum system must have discrete, resolvable energy levels ($E=\hbar w_0$, for a two-level system, where w_0 is the frequency related to the energy transition).
2. It must be possible to initialize the quantum system into a well-known state and to read out its state.
3. The quantum system can be coherently manipulated, typically by time-dependent fields (not strictly required).
4. The quantum system interacts with a relevant physical quantity V(t), such as an electric or magnetic field.

One important parameter when talking about a quantum sensor is the sensitivity. On one hand, it is expected that a quantum sensor provides a strong response to the wanted signal, while it should be minimally affected by unwanted noise. The sensitivity can be expressed as[7]:

$$sensitivity \propto \frac{1}{\gamma\sqrt{T}} \qquad \textit{Equation 5}$$

Where γ is a parameter that relates to the changes in the energy of the system (E, for a two-level system) as a function of the external parameter and T is the decoherence or relaxation time (reflecting the immunity of the quantum sensor against noise).

Among the previously discussed single-photon sources, mainly the cold atoms and the solid-state defects can be used as quantum sensors, as they are the ones whose emission properties depend-upon the interaction with some physical entities, such as the magnetic field[7] . Additionally, many other quantum systems that have not been discussed in the above-mentioned single-photon sources explanation, such as trapped ions, Rydberg atoms and superconducting circuits have so far been employed.

Considering this thesis is based on the fabrication of single-photon sources in semiconductors the most extensively studied solid-state defect as a quantum sensor, the NV center is further discussed in the following for clarification.

The NV-center in diamond is a unique color center that has an optically addressable spin state, which can sense magnetic, electric, temperature, and pressure fields at room temperature[28].

The NV center as a defect along with many of its applications in quantum technologies will be explained in detail in the next section, however it is worth mentioning the basis of the NV as a quantum sensor.

The Optically Detected Magnetic Resonance (ODMR) technique when applied to the NV center is based on the fact that the NV center has three main energy levels, the ground state |g>, the excited state |e> and a singlet state |s> (see **Figure 5**). In addition, the ground and excited states are split into a spin-1 subsystem with magnetic spin numbers m_s=0,1,-1 [29].

The m_s= ± 1 states are nearly degenerate upon no external magnetic field and are separated from the 0 state by the zero-field splitting D_g=2.87 GHz. While in the presence of an external magnetic field, according to the Zeeman effect, the m_s= ± 1 states will split by an energy difference dependent on the magnetic field applied, $2\,\hbar\gamma B_{||}$ (see **Figure 5**).

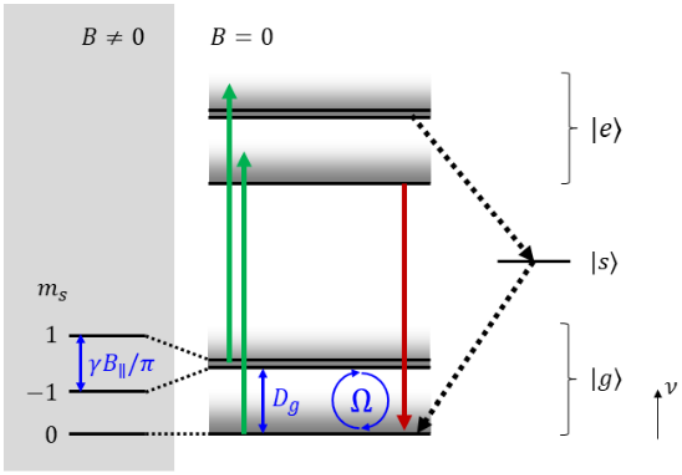

Figure 5 *Energy level system of the NV⁻ center in diamond, with and without induced magnetic field B*

Upon optical pumping of the center, usually employing a green laser (532 nm), the |g,0> state will be excited to |e,0> and mostly decay back to the |g,0> ground state under emission of a photon. The |g,$\pm$1> state on the other hand will be excited to |e,$\pm$1> and predominantly decay through non radiative state |s> to |g,0> leading to a decrease in the fluorescence through the |$\pm$1> state.

Bearing this in mind, experiments can be performed pumping the NV center optically and reading back the photoluminescence, this combined with a radiofrequency of 2.87 GHz leads to a decrease in the signal of the NV as be pointed out in **Figure 6**. As this decrease is linked to the spin state of the center, by Zeeman effect it can be splitted, which is one of the most extended methods to measure the magnetic field. Not only

this transition is sensitive to the magnetic field, but also other effects such as the electric field and temperature may change the Hamiltonian of the system, leading to changes such as the ones plotted in **Figure 7**. Based on this feature of the NV center, many other experiments can be carried out, such as Rabi and Ramsey oscillations, that allow for the measurement of the coherence of the defect.

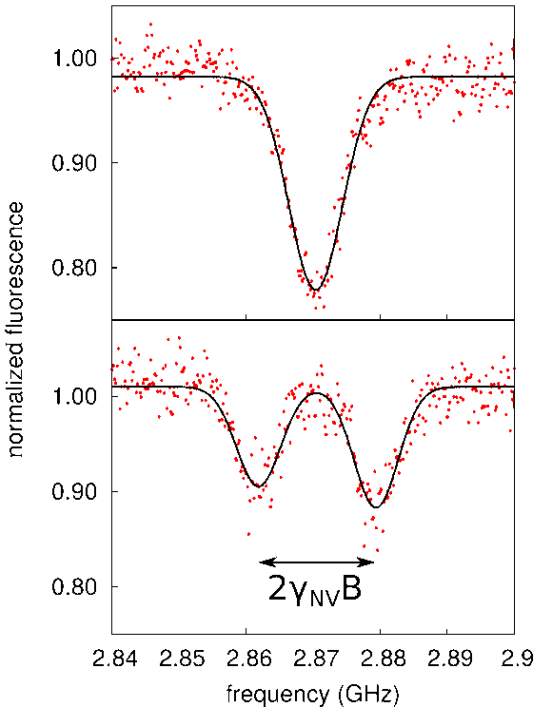

Figure 6 *ODMR signal of NV center, with and wihout magnetic field*[30].

Despite having a shorter coherence time than other quantum sensors, its sensitivity can be compared to that of other atomic counterparts[31]. Moreover, the NV center in diamond has the advantage of being biocompatible and can be found in nanoparticles, allowing in-cell temperature sensing for biosensing purposes and other applications[32], [33].

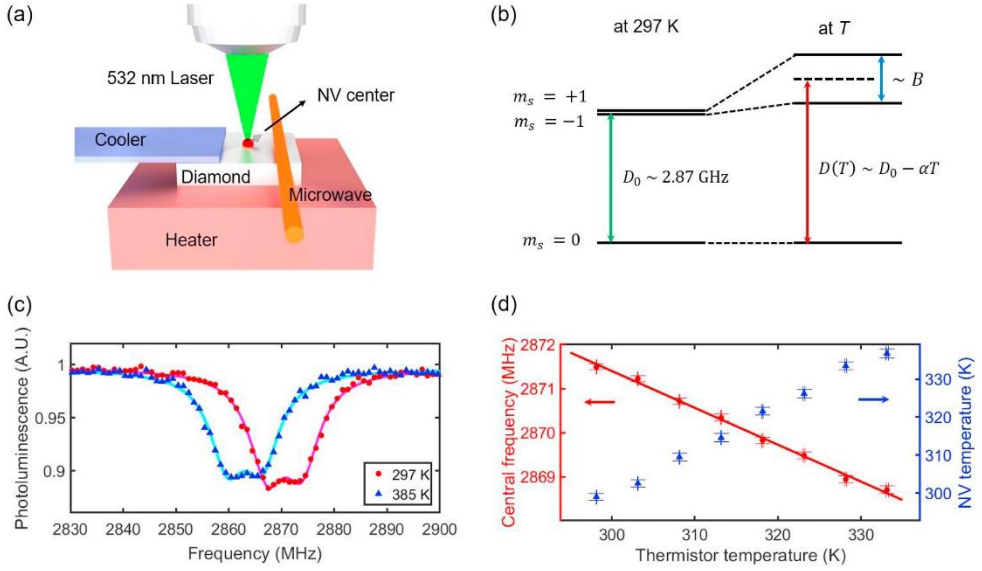

Figure 7 *Example of use of the NV center optically addressable spin state for temperature sensing* [34]

Quantum communication

Quantum communication involves the transfer of a quantum state from one location to another. The fundamental reason behind this is that quantum states encode quantum information in *qubits,* which can enable us to perform tasks that are either impossible or much less efficient when using classical information[4]. The main application of quantum communication are the one presented below.

Quantum teleportation. This technology utilizes the transformation between scattered quantum entanglements and physical information to transfer quantum states to distant locations. It is a vital communication method for transmitting quantum states and serves as the foundation of scalable quantum networks and distributed quantum computing. In quantum teleportation, two parties in remote locations who wish to communicate first share a pair of entangled particles. This system employs three qubits, one of them in an arbitrary state to be teleported, and another two in Bell state[4].

The arbitrary state can be written as:

$$|\chi\rangle_1 = \alpha|0\rangle_1 + \beta\,|1\rangle_1 \qquad \textit{Equation 6}$$

Where $|0\rangle$ and $|1\rangle$ represent the two orthogonal near polarization bases, in this discussion. α and β are two arbitrary complex amplitudes that satisfy the following $|\alpha|^2 + |\beta|^2 = 1$ condition[35].

Then a pair of quantum subsystems $|\psi\rangle_2$ and $|\phi\rangle_3$ in an EPR (Einstein-Podolsky-Rosen) tangled state. As was proved by John Bell for a 2 qubit quantum system there are only four possible entangled stated, called the Bell states[35], [36]:

$$|\Psi^{\pm}\rangle = \frac{1}{\sqrt{2}}(|00\rangle \pm |11\rangle) \qquad \textit{Equation 7}$$

$$|\Phi^{\pm}\rangle = \frac{1}{\sqrt{2}}(|01\rangle \pm |10\rangle) \qquad \textit{Equation 8}$$

Now $|\psi\rangle_2$ is sent to the location of the sender 'A' and $|\phi\rangle_3$ is sent to the location of the receiver 'B'. In order to perform the teleportation 'A' must bring the teleported state $|\chi\rangle_1$ into contact with the entangled state $|\psi\rangle_2$ and perform a Bell state measurement on the combined system $|\chi\rangle_1|\psi\rangle_2$.

The outcome of the Bell state measurements then should be send from 'A' to 'B', using a classical channel. With this information, the receiver 'B' can extract the linear transformations that must be applied to his state $|\phi\rangle_3$ in order to get the exact replica of the state $|\chi\rangle_1$. As couples of entangled pairs are required in order to perform the quantum teleportation, one of the most employed single-photon sources for the experimental realization of it, is the Parametric down-conversion, from which coupled of entangled single photons can be directly generated[35].

Quantum cryptography. It uses quantum states as information carriers and transmits keys between legitimate users via quantum channels. The most famous application of quantum cryptography is quantum key distribution (QKD)[37].

The first protocol established for quantum cryptography was proposed in 1984 and it is referred to as BB84. The protocol is based on three parties, Alice, Bob and Eve. It uses four quantum states, that constitute two bases, for example up, down, left and right. In the first step, Alice sends individual spins to Bob in one of four polarization states chosen at random. The spins can be sent all at once or one after the other, as long as Alice and Bob establish a one-to-one correspondence between the transmitted and received spins. Bob then measures the incoming spins in one of two randomly chosen bases. When they use the same basis, they get perfectly correlated results. However, when they use different bases, they get uncorrelated results[37], [38].

Alice and Bob have a way of determining which bits are perfectly correlated (the ones for which they used the same basis) and which ones are completely uncorrelated (all the other ones). This makes it possible to implement a straightforward error correction scheme: Bob publicly announces the basis he used to measure each bit, but not the result he obtained. Alice then reveals only whether or not the state in which she encoded

that bit is compatible with the basis announced by Bob. If the state is compatible, they keep the bit; if not, they discard it. Using this method, about 50% of the bit string is discarded, and the resulting shorter key obtained after basis reconciliation is called the sifted key. When the third party tries to eavesdrop on the password (Eve), it must be measured in some way, and these measurements will bring detectable anomalies. What Eve does is lowering the bit rate (the number of bits measured by Bob) but not gaining any useful information. A schematic representation of this protocol is represented in **Figure 8**.

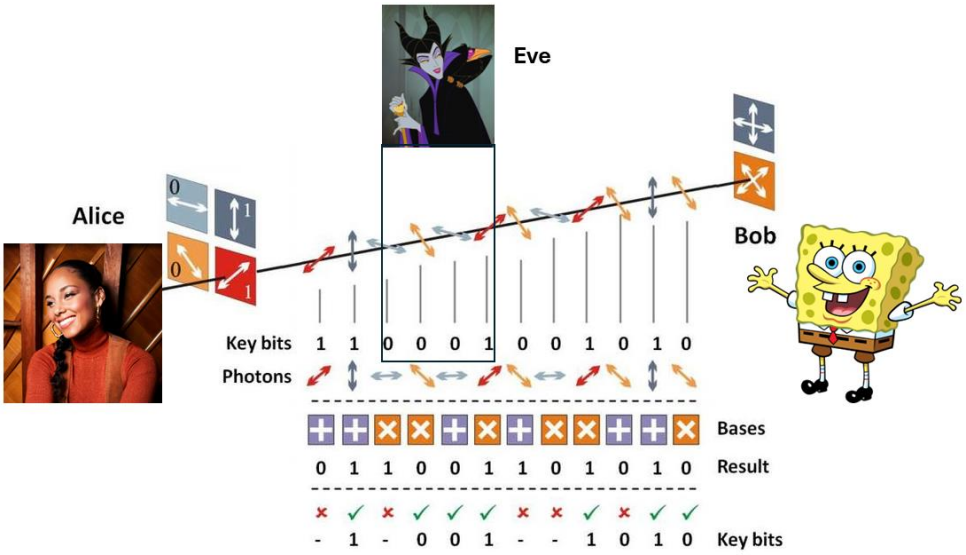

Figure 8 *BB84 protocol exemplification.*

QKD protocols are currently being implemented using mainly laser sources, the wavelengths vary depending on whether a free space or fiber coupled system is being employed. For the detecting part, both superconducting detectors and commercially available APDs (Avalanche PhotoDiodes) are used. On what regards the encoding protocol of the information, the most expanded way is based on polarization of the light as explained for the BB84.

Quantum memories and repeaters. To perform an efficient quantum information network, it is important to count with quantum repeaters and memories. To overcome the distance limitation one needs quantum repeaters, which require both quantum relays and quantum memories. The basic idea is that if the entanglement distribution has succeeded between nodes A and B, but failed between B and C, one stores the A-B entanglement in quantum memories and restarts the B-C entanglement distribution. A quantum memory that can store a qubit for a period sufficient to allow several rounds of communication between nearby nodes is crucial. One of the best quantum memories is a simple fiber loop, but in the past decade the implementation of quantum memories in systems like solid state defects (NV center)[29] has already been proved[4].

The three main requirements for a quantum platform to be implemented as a quantum node are the following[39]:

- The ability to connect at least one qubit with optical photons in order to create remote entanglements at high speeds.
- The capacity to store quantum states during entanglement generation with coherence times that exceed the entanglement generation time between the nodes.
- The capability to store multiple entangled states per node and perform high-fidelity operations between them to facilitate multiqubit protocols like error correction.

The NV center in diamond satisfies most of these requirements, as it contains an individually controllable optically active spin with access to several long-lived nuclear spins in its surrounding, its internal level structure is suited to generate remote entanglement, its optical emission is bright and can be collected with high efficiency and as diamond is a solid-state material, it potentially enables the nanophotonic device fabrication at a large scale. These properties are in general also common to the Group IV color centers, presenting a much more appealing performance on what regards the bright optical emission and quick optical response, although the coherence times achieved with these centers have been so far reported to be much lower than for the NV case[40], [41].

Thanks to these properties the NV center as well as other color centers in diamond, have or have been hypothesized to be useful platforms for the realization of quantum nodes.

An example of the experimental realization of a quantum network node based on color centers in diamond is shown along with a simplified optical level scheme in **Figure 9**. It consists of an optical active qubit (purple spin) embedded in an optical cavity (two highly reflective mirror) to enhance the interaction strength of the photon with the qubit. The state of the color center qubit can be swapped onto long-lived nuclear spin (memory) qubits that are located in the surroundings of such (yellow spins) using high-fidelity gates that employ microwave or RF pulses delivered via dedicated lines (gray)[39].

In this scenario, network nodes can be optimized for frequency operation by applying a static electric field using electrodes (depicted as yellow beams). The frequency conversion process (depicted as a black box) can be utilized to lower the frequency of entangled photons to match telecommunication wavelengths, which minimizes photon transmission losses. Furthermore, the color center allows for spin-resolved optical transitions between an optical ground state (GS) and an excited state (ES), facilitating optically mediated remote entanglement generation as illustrated in **Figure 9**[39].

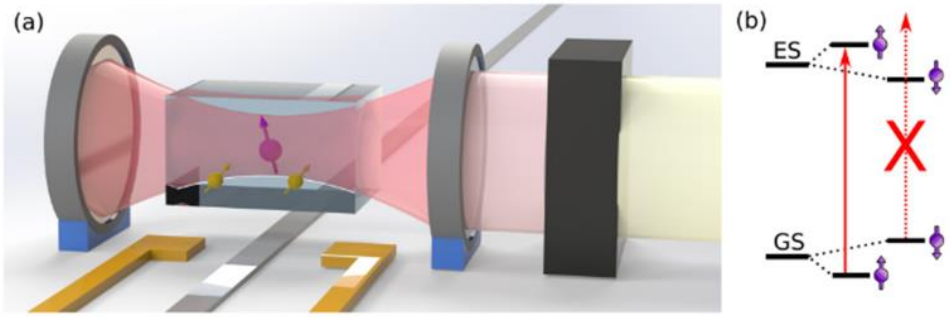

Figure 9 *a) Simplified schematic of a quantum node in diamond. b) Simplified optical two level system energy levels*[39].

Quantum computing

In the past few decades, there has been tremendous progress in the experimental development of a quantum computer: a machine known for been able to exploit the full complexity of a many-particle quantum wavefunction to solve a computational problem[6].

Quantum computers have a unique feature called the 'closed box' requirement. This means that the internal operation of a quantum computer must be isolated from the rest of the universe, except when the programmer has control over it. Leakage of information from the box can cause disturbances in the fragile quantum mechanical waves that the computer depends on, leading to a destructive process known as 'decoherence'. There are several forms of decoherence, such as the interference phenomena that occur in quantum mechanical waves like light from a laser or the oscillations of the components in quantum

computers. These phenomena disappear in repeated experiments. Quantum computers also face other challenges, such as operating in a Hilbert space whose dimensions can grow exponentially without an exponential cost in resources such as time, space, or energy. Additionally, the computer's entropy must be extractable to maintain its quantum state[6].

Several platforms have been used for the realization of this quantum computers; among them the most developed one is the one based on superconducting qubits by IBM company. Additionally, regarding the solid-state defects, NV based quantum computers have nowadays been developed[29], although the qubit scalable fabrication and addressability of the several NV qubits is still an ongoing research field[42]

In this first section, the different types of single-photon sources and the different potential applications in the quantum technologies fields have been assessed. In this dissertation, however, the discussion will be centered mainly in one of these types, the solid-state defects.

The main defects in several wide bandgap semiconductors will be deeply discussed in the next section, as well as the most expanded fabrication methods of such. A special dedication will be given to diamond's case, as it is the material in which the majority of experiments related to this thesis work were performed, along with the aluminum nitride, although in this case, the literature available on color centers is much less extended.

1.2 Color centers in bulk semiconductors

Solid state defects or color centers as they will be referred as to from now on, are optically active defects embedded in the crystal lattice that have their own energy structure within the hosting material bandgap[22], allowing for addressability by visible light. In the case of diamond, for example, the high concentration of these defects is what usually gives the diamond gemstones their several characteristic colors [20][36], [37][37][36].
Numerous wide bandgap semiconductors have been reported to host single photon sources [22], both occurring natively or as a result of the introduction of impurities. In this Chapter, several of the most commonly studied and appealing color centers platforms will be presented, along with the most studied single-photon sources that have been reported for each of them.

After discussing the several single photon emitters reported for these platforms, it is important to understand how these sources are fabricated [43], [44]. The systematic fabrication process of these sources is important for the scalability of the quantum systems, in addition to the formation with suitable properties for their application as single photon sources, especially the coherence times and stability of the centers.

1.2.1 Color centers in diamond

Optically active defects can be formed by impurities that are naturally present during the crystal's growth, such as nitrogen or silicon, in the diamond case. They can also be intentionally introduced during or after growth, such as tin or germanium. These defects can also be formed by vacancies, which occur when there is an absence of a carbon atom in the lattice. Usually, it is the combination of both impurities and vacancies that leads to the formation of optically active defects[22].

It is worth noting that not every impurity introduced into the diamond lattice leads to the formation of an optically active color center, because although it introduces localized energy levels due to the change in the electronic configuration of the lattice around it, the energy levels may have non radiative decay paths that don't lead to luminescence effects[45], [46].

In the same way, regarding the impurities or defect systems that form color centers, not all of them form single photon sources[46]. As it has been explained in the previous section, solid-state defects form isolated

electronic structures, that lead to individual energy levels (usually two-level systems) that can be single photon sources. Unfortunately, not every luminescent defect in diamond can be isolated at the single photon emitter level, some of them just form clusters of color centers that decay in a radiative way with more of a bunching behavior or their spontaneous emission lifetime is too low to get single photon reliably emerging from the background [45]. In this section, we will concentrate on the single-photon sources in diamond, as these are the useful ones for the realization of quantum technologies which is the main topic of this thesis.

Even though many color centers in diamond have been reported to have a single photon emission upon laser excitation, none of them meets all the requirements of a good single-photon source[47]. Despite these drawbacks, many of them are nowadays extensively studied and have already been implemented in quantum devices. The presented centers include both more mature and recently discovered centers that have appealing properties for future use in quantum technologies.

NV center

The NV center can be considered the most historically studied center in diamond. It was first reported as an individual luminescent center in 1997[48], [49], [50], since then it has been widely studied. It consists of a nitrogen substitutional atom and adjacent vacancy (a missing carbon atom). It has two charge state configurations, NV^0 with the ZPL (Zero Phonon Line) at 575 nm and NV- with the ZPL at 639 nm, among them the most scientifically appealing is the negative one because of its spin properties.

This NV^- center has an optically addressable spin state at room temperature. As it can be pointed out in **Figure 10**b this defect can be addressed with a green laser and by using the right microwave signal it can change spin state, leading to a change in its PL (photoluminescence) signal [51], [52]. As we are talking about spin states, they can be split by the use of a magnetic field (Zeeman effect) making it a perfect sensor of magnetic fields. In the same way, these splitting is dependent on the pressure, temperature and electric fields, which makes the NV- center a great sensor also for these type of fields.

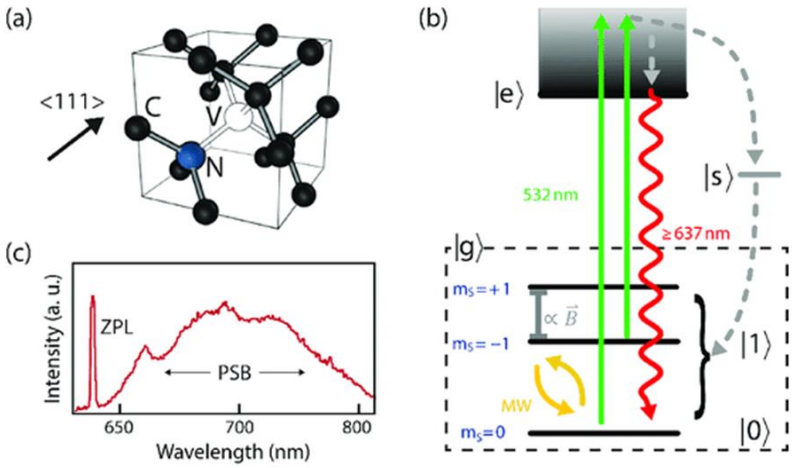

Figure 10 *a) Lattice structure of NV center. b) Energy diagram of the NV- center. c) Photoluminescence spectrum of the NV- center.*

This center is optically very stable and has a high quantum efficiency at room temperature. However, it has some drawbacks, such as the strong electron-phonon interaction that results in a very broad emission spectrum as can be noticed in **Figure 10**c, with a really low Debye-Waller factor (emission into the ZPL) at room temperature. This is a problem for the implementation of this center in quantum communication where monochromaticity is required, nevertheless it has been overcome with the use of cryogenic temperatures and the use of this center as a quantum node has already been demonstrated[53].

The creation of individual NV^- close enough to perform entanglement operations between them is still a challenge although recent works published in the past few years have demonstrated the use of molecular ion implantation for this purpose and on the coupling of third party quantum system, such as C^{13} atoms in the diamond lattice, for the spin state control[54], [55].

Regarding the use of the NV center as a quantum sensor, there are many implementations for which different configurations of the defect, intended as the location and arrangement within the sample, are necessary. As an example, high ensembles of NV^- are necessary in bulk diamond close to the surface, in order to perform high contrast enough fields sensing, as the sensitivity of the systems scales with $\sqrt{N}$, being N the number of independent systems, in this case NV centers [56]. While for instance, in the case of nano-NMR experiments the use of array place single NV^- centers is much more convenient, as each single NV is supposed to be addressed independently to detect NMR signals coming from volumes in the order of magnitude of the defect size itself [57]. Both applications need still of improvement in the fabrication process of the centers, in terms of efficiency of creation, scalability and coherence of the systems fabricated, as both the problems of deterministically positioning of the single NV centers with the same surrounding environment that doesn't affect the properties of such and the formation of high-density ensembles that allow for an increase in sensitivity of the quantum sensor without sacrificing the volume of such, have not yet been successfully overcome, although the research carried out in both these two fields in the past few years have shown promising results[40], [58], [59], [60], [61].

Group-IV centers

As part of the ongoing research for the quantum emitter that fits all the requirements for quantum communication, such as high Debye-Waller factor, short lifetime and negligible spectral diffusion, the group IV color centers (G4V) have been reported to have more suitable properties compared to the NV^- center[62].

These centers are mainly SiV, GeV, SnV and PbV, and they are formed by one atom of the Group IV of the periodic table in an interstitial position in the middle of two vacancies, as it is usually referred as to, in split-vacancy configuration. In **Figure 11**a this split-vacancy configuration is represented[25], [63]. This configuration is an intrinsic inversion-symmetric structure, that allows for the outstanding spectral stability of these G4V centers. The referenced symmetry is called D_{3d} symmetry and makes the G4V center's emission properties less dependent on surrounding electromagnetic fields.

One important characteristic of all of these centers is that they have a sharp ZPL and stable emission at room temperature, as it can be pointed out in **Figure 11**b, where the characteristic photoluminescence spectra for each of these centers is summarized. A further property that makes them interesting for the application in quantum communication is the low lifetime in the order of a few ns[63], [64].

Additionally, all of them have a four-level energy system that can be addressed at cryogenic temperatures, thanks to the spin-orbital coupling and Jahn-Teller effect. The ground state splitting of these system is directly proportional to the mass of the atom from which it is form, so the higher ground state splitting is observed for the PbV center while the SiV has the smallest one. Therefore, in order to coherently control this systems and operate them as quantum systems, the required operation temperatures range between a few mK in the case of SiV to around 10 K in the case of PbV. This energy structure at cryogenic temperatures is represented in **Figure 11**c[25], [64], [65].

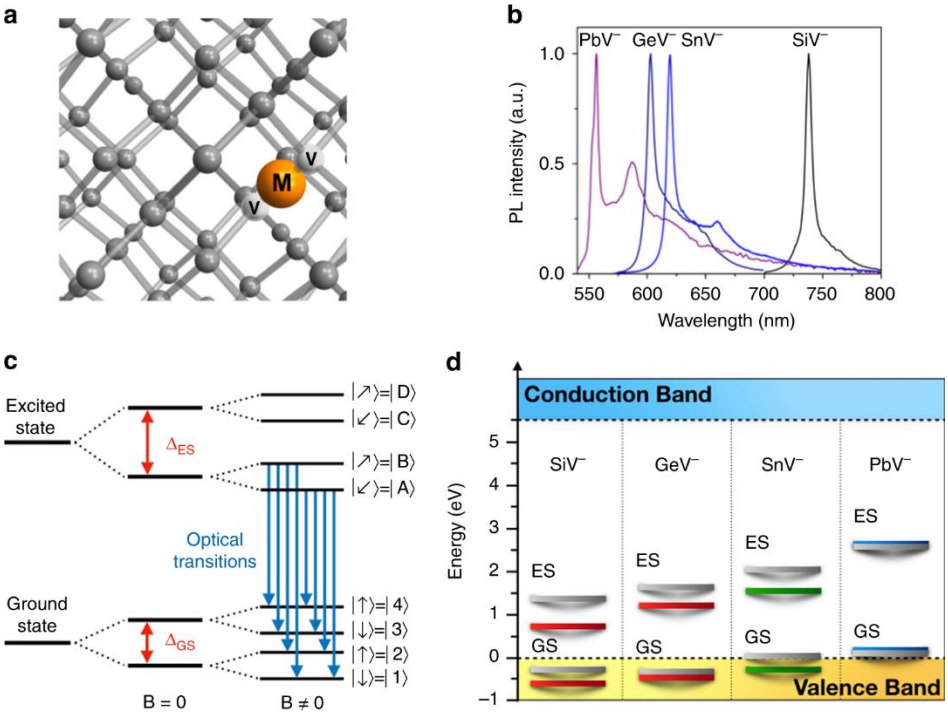

Figure 11 *a) Split-vacancy configuration for the Group-IV color centers in the lattice. b) PL spectra of the four color centers. C) Energy diagram for G4V color centers at cryogenic temperatures. D) Position of the energy levels inside the bandgap of the diamond*[63].

For each of these cases, the negative charge state of the center is mainly the one studied for the application in quantum technologies. The position of these charge states inside the diamond bandgap is represented in **Figure 11**d.

The main features of each of these centers are summarized in the following

Silicon vacancy center (SiV). The SiV color center exits in two charge states, the neutral SiV^0 (ZPL is ~946 nm). and the negatively charged SiV^- (ZPL is ~738 nm)[66]. The most widely used and studied is the negatively charged, because of its addressable ½ spin state at cryogenic temperatures. Silicon, along with nitrogen is one of the most common impurities in synthetic diamonds, which. The use of ion implantation has been reported as a really useful tool for the in bulk fabrication of these single photon sources with accurate position[48]. While in the case of nanodiamonds, the grown SiV are usually the most extensively studied[67], [68].

This center has shown potentiality in electroluminescence applications and for the implementation in quantum communication as a qubit, among other quantum fields. This center below a temperature below 500 mK, allows for a coherent control for around 13 ms while reaching even lower temperatures, the coherence times can go up to 1 s[23], [69].

Germanium vacancy center (GeV). The GeV^- center has a prominent ZPL at 602 nm and a phonon sideband roughly up to 670 nm. It has a Debye-Factor of around 0.6 (a little bit lower than for the SiV, for which has been reported to be around 0.7)[63], [70]. Its radiative lifetime (in the range of 1.4-6.6 ns) is comparable to that of the other group IV centers in diamond, while in the case of the ground state splitting is around 150 GHz. This means that the temperature necessary to optically address it as a qubit, is still under the 1 K[71]. So far the longest coherence times achieved with this center, have been reported to exceed 20 ms, paving the way for the successful implementation as a quantum node[72].

On what regards the fabrication of this center at a single emitter level, it is mainly based on the use of ion implantation[73], but due to the large mass of the ion, its activation with optimal optical properties is still

a challenge[70], [71], [73]. However, some possible useful activation tools have been reported to work pretty well, as will be discussed in the results section of this thesis[74].

Tin vacancy center (SnV). The tin vacancy color center in diamond is an extensively studied single photon source with a ZPL at 620 nm[75]. Among the group IV color centers it shows a large ground state splitting, that allows for the coherent control at temperatures up to around 6 K[76]. Moreover, it has been observed transform-limited emission of these centers in nanopillars that in addition to the advancements in fabrication and charge stability demonstrate that these SnV centers are a suitable spin-photon interface for quantum networking and measurement-based computation[25], [77], [78].

Additionally, the optical coherence of the emitted photons, often referred to as 'indistinguishability' , was recently demonstrated up to 0.64 and the microwave spin control of a tin-vacancy based qubit was reported[24], [79].

Considering, all these application and reports, it is worth noting that a reproducible fabrication method of these color centers is necessary for the scalability of the technique. In the past ten years, many technique have been developed on this field, so far the one that leads to the centers with the best optical properties is the combination of ion implantation plus HPHT treatment[80]. However, this technique is quite invasive, so the research for less invasive technique that may lead to high formation yields with optimal properties is still ongoing.

Lead vacancy center (PbV). The optical transition energy of the PbV center has not yet been determined consistently, values have been reported both at ~550 and ~520 nm[81], [82]. As the heavier atom among the group-IV elements of the periodic table and taking into account the behavior of the other three already reported regarding the temperature dependence of the ground state splitting, it is predicted to exhibit a millisecond spin coherence time at 9 K, making it more appealing from the energetic consuming point of view, decreasing the necessity of continuous flow type of cryostats Recently, the transform-limited photon emission from a lead-vacancy center in diamond at 16 K has been reported, demonstrating its high-temperature robustness compared to other color centers in diamond[83].

On what regards this center, extensive work has still to be carried out in order to understand both the structure of the center, along with its charge state and electronic configuration, and the formation process, as the repeatable fabrication of this type of centers is considered as a challenge due partially to the damage induced by the large nucleus as it is introduced into the diamond lattice, that may lead to the formation of unwilling structures around the center. [84].

Magnesium vacancy center (MgV)

As part of the quest of additional color centers in diamond that may display suitable properties for the implementation in several fields within the quantum technologies, the magnesium vacancy center was recently reported as a single photon emitter in diamond.. It is based on an Mg atom in an interstitial position in between two carbon vacancies, in the same way as for the G4V color centers, it has a split-vacancy configuration[85]. Consequently, it has an inversion symmetry that makes it less dependent on the surrounding electric and magnetic fields. It presents a ZPL at 557.6 nm at room temperature, and some other intense peaks at cryogenic temperature that have not been completely understood yet. It has high Debye- Factor, high quantum efficiency, with intensity values at saturation > 1 Mcps and saturation powers in the order of 0.5-3 mW, and low radiative lifetime (2-3 ns)[47].

So far the fabrication of this center has been carried out through ion implantation and subsequent high-temperature annealing leading to creation yields in the order of 5-10% without any additional irradiation or doping technique [85]

Its optical properties along with its implementation in quantum technologies have not yet been extensively reported and need further study.

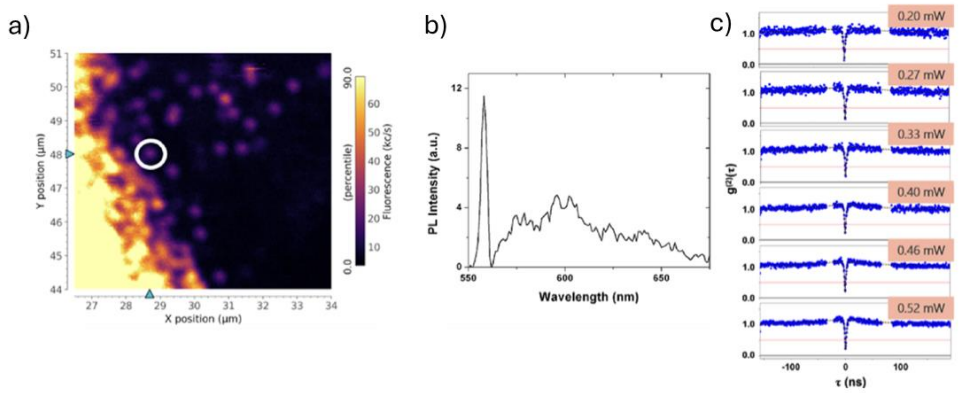

Figure 12 *a)PL map of the implanted Mg region, b) PL spectrum of the MgV defect, c) g2 measurements performed at different excitation powers.* [47]

Apart from diamond, which is one of the most studied solid-state platforms as a host of single emitters, there are several other wide bandgap semiconductors which are increasingly been studied because of their interesting properties for implementation as quantum platforms. There are several reasons why there is a growing interest in alternative platforms to diamond. One reason is the difficulty in using diamond as a photonic platform, particularly in fabricating structures like low-loss waveguides, which remains a challenge[86]. In contrast, photonic integrated technology is much more advanced in other semiconductors such as silicon or III-nitrides[87], [88]. Additionally, most color centers found in diamond emit light in the visible range, so there has been increasing research in other platforms where defects can emit light in the telecom range. This is aimed at directly implementing the photon sources in quantum communication technologies, without the need for frequency transformers like in the case of nowadays diamond-based quantum repeaters[39].

Some of the platforms that have been reported to host single-photon emitters in the past few years both at room and cryogenic temperature have been: silicon carbide (SiC), silicon (Si), gallium nitride (GaN) and aluminum nitride (AlN); an overview of the main color centers reported for each of them will be presented in the following sections.

1.2.2 Silicon Carbide (SiC)

Silicon Carbide (SiC) is a wide bandgap semiconductor, with 3.26 eV as bandgap energy. This high energy allows for the generation of single photons at room temperature[89]. As a transparent material, it reports similar optical properties to diamond[90], [91]. The SiC fabrication can be considered as a mature industrial technique at the wafer scale growth and processing technology of it, as its use for power electronics has been notably increased in the past decades.

This material exists as many different structural polytypes, however the most studied ones as host of single photon sources are the 4H and 6H-SiC, as they are two of the three (aalso 3H- SiC) more mature fabricated polytypes were the first ones that garnered interest regarding the identification of single-photon sources[89], [92].

The most studied single photon defect in SiC is the Silicon-vacancy center (V_{Si}), a lattice defect characterized by the absence of a Si atom in its intended lattice site. V_{Si} has been recently proposed as a novel sensor for quantum thermometry and magnetometry applications[90], [93], [94], [95]. Additionally, the V_{Si} center can be addressed in the electroluminescence regime.

Another promising single-photon emitting defect is the Carbon anti-site–vacancy pair ($C_{Si}V_C$ center), which consists of a C atom occupying a Si lattice site (anti-site defect) coupled with a C vacancy. Both the V_{Si} and the $C_{Si}V_C$ centers are intrinsic defects[96]. They can be fabricated simply by introducing radiation damage in the host crystal via interaction with energetic ion, electron, or photon beams. A subsequent high-

temperature annealing is responsible for the formation of a stable defective configuration in the crystal lattice.

Extrinsic color centers generated by the incorporation of external chemical species have been so far demonstrated for a limited set of impurities. Color centers fabricated upon ion implantation at the single-photon emitter level include the nitrogen-vacancy center (N_CV_{Si})[97], which exhibits single-photon emission in the telecom band (emission lines in the 1150–1350 nm range in 4H-SiC, depending on the configuration of the lattice site) with a 2 ns excited state lifetime, and the substitutional vanadium-related V^{4+} center (1279–1387 nm ZPLs, emission lifetime above 70 ns)[98]. Despite the material still needing to reach full maturity for applications in quantum technologies, SiC has also been extensively explored as a potential host material for integrated photonics[99].

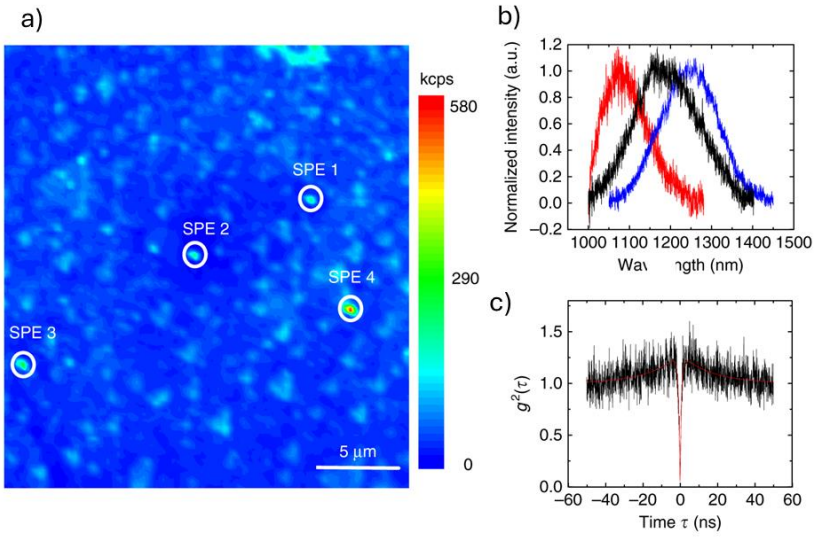

Figure 13 *Single emitetrs in the telecom range in SiC. a) PL map of the spots. b) Spectra of the different single emitetrs. c) g2 measurement for one of the SPS*[100].

1.2.3 Silicon

Color centers in silicon (Si) offer an interesting alternative to the more established types of quantum emitters. Despite its indirect band gap, silicon has shown potential for integrating photon-emitting components with CMOS technology, thanks to photoluminescence and electroluminescence from various optically active defects[101], [102]. However, it was only in 2020 that the first single-photon emission at cryogenic temperatures from a silicon point defect (the G center) was demonstrated, sparking renewed interest in luminescent centers in silicon for developing next-generation technologies for the second quantum revolution [103].

Another single-photon source of similar brightness (2-6 kcps emission intensity at saturation) is the intrinsic complex known as the W center, a tri-interstitial complex that occurs as a typical radiation-induced defect in silicon[104], [105]. Recent theoretical studies have also shown that carbon- and oxygen-related radiation damage defects called C centers have potential for implementing optically-readable quantum memories. While they have not yet been demonstrated as single-photon sources, the ZPL at 1570 nm (0.79 eV) experimentally observed at the ensemble level in irradiated Czochralski silicon samples could pave the way for the implementation of telecom quantum networks, which benefit from minimal losses in commercial optical fibers.

On what regards the most studied center, the G center, it has been already systematically fabricated using ion implantation and standard annealing, laser annealing and laser fabrication[106].

Since the first reports on single-photon emission in silicon, this material has become among the most appealing ones for the development of solid-state quantum technologies. It has some appealing features with respect to other platforms, such as the maturity of both the photonic and electronic devices fabrication, the maturity of the industrial-level wafer fabrication[22], [107]. Not only it shows captivating properties from the point of view of the material, but also the single photon emitters so far reported in it have a spectral emission in the telecom window, which increases the interest for its application in quantum communication[22]. However, among its main drawbacks is the necessity of operation at cryogenic temperatures, while in the case of the other platforms reported in this section the single-photon generation can be obtained at room temperature[104].

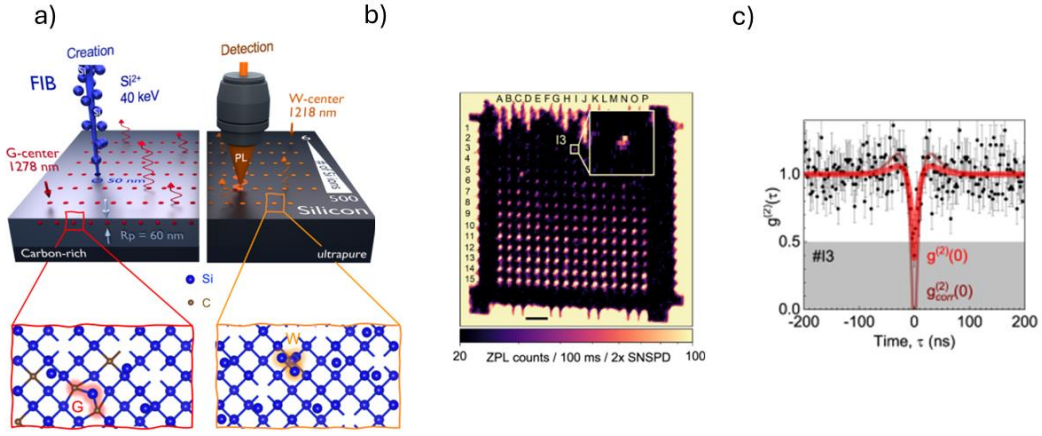

Figure 14 *a) Schematic of FIB implantation for the formation of the SPS. b) Confocal PL map od the implanted points. c) g2 measurement for the highlighted spots in b)*[108].

1.2.4 Gallium nitride (GaN)

GaN is a direct-wide-bandgap semiconductor that has been used in the past few decades mainly for LEDs and high-power electronics[109], [110], [111]. The material has also received attention for developing photonics structures and optoelectronics at the nanoscale, indicating a high degree of maturity for the uptake of single-photon sources in integrated devices. The first report on single-photon sources in GaN dates to 2017, when a class of native single-photon emitters was discovered. The emission was denoted by a sharp zero-phonon line (ZPL) with a large emitter-dependent variability in the 600–700 nm spectral range[112]. It exhibited an excited state lifetime of about a nanosecond and high room-temperature emission intensity at saturation (1–5 × 10^5 photons/s). Since then, these emitters have been integrated into photonic structures and GaN substrates' layered growth[113], [114].

An additional class of bright color centers emitting single photons at telecom wavelengths (1100–1300 nm) was identified in 2018. These emitters operate at room temperature with rates up to 5 × 10^5 photons/s and have been integrated into photonic structures for further emission enhancement[115]. However, the reported classes of emitters were found natively in GaN, and their unambiguous attribution to a specific defective complex is still missing, currently limiting the perspective of a controlled fabrication process for integration in quantum photonic circuits.

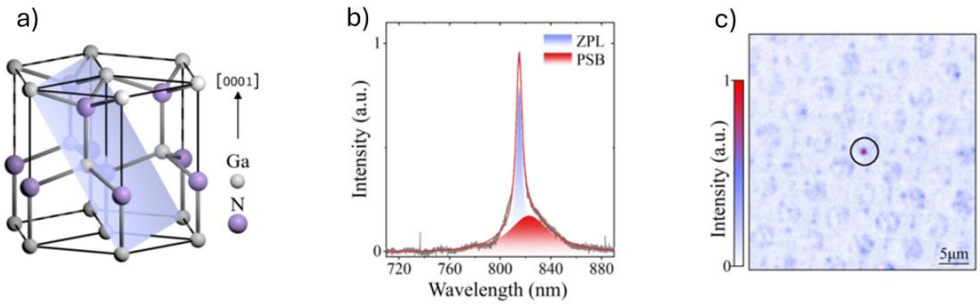

Figure 15 *a) Structural configuration of GaN. b) PL spectrum of the single emitters in c. c) PL map with a single emitter*[116].

1.2.5 Aluminum nitride (AlN)

AlN is a semiconductor with a wide bandgap of 6.03 eV. It is widely used in high-power electronics and as a piezoelectric material. AlN is also used as a substrate layer for the growth of GaN in photonics[117]. In 2020, single-photon emission from native defects in AlN was experimentally demonstrated. Individual defects were identified in thin AlN films, and they exhibited room-temperature-linear-polarized emission from the visible to the infrared range, with count rates up to 5×10^5 photons/s and a 2-3 ns excited state lifetime[118]. The nature of these emitters has not been conclusively attributed yet, which is why the single-photon sources in this material were studied more deeply during the work of this thesis. The observed emission lines could be related to different classes of color centers or different site symmetries of the same point defect. The large spectral variability observed in the literature could originate from the interaction with the crystal lattice environment in a piezoelectric material[119], [120], [121]. In this thesis, it will be shown that individual color centers in the 550-650 nm range can be formed by the controlled introduction of radiation-induced lattice damage through Al-ion implantation and subsequent thermal annealing up to 600 °C[122]. This offers a convenient pathway for their manufacturing. These results, along with the theoretical prediction of point defects with optically addressable spin properties[123], highlight the potentially seamless integration of AlN emitters into integrated platforms for quantum photonics. The efficient registration of single-photon sources into integrated circuits has already been proved in 2020 with the integration of a quantum emitter into a waveguide by means of grating couplers[124].

Additionally, several other papers have recently reported the creation of single emitters both by femtosecond laser writing and by implantation of other species, such as Zr[125], [126]. The experimental validation and confirmation of the reliability of these fabrication tools would allow for the scalability of single photon emitters combined with the integration in photonics for quantum technology applications in this material.

The prevalence of AlN in high-power and solid-state lighting makes it a promising platform to investigate. It presents an established route to cost-effective and commercial-scale fabrication, with epitaxial material available at a low cost. Apart from the already reported photonic integrated structures in this material, the several DFT (density functional theory) predictions of defects displaying similar spin properties to the NV center in diamond, have also attracted the interest of this platform. Based on these reports, this material was chosen as one of the studied materials, along with diamond, for the fabrication of single-photon emitters.

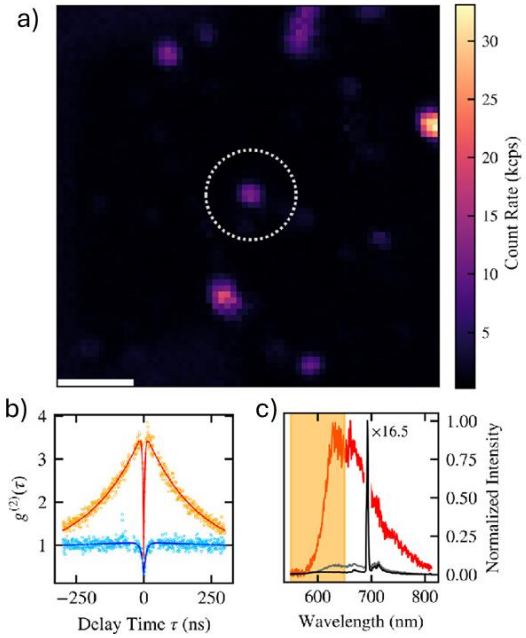

Figure 16 *a) PL map of a single emitter. b) g2 measurements at different powers for the SPS. c) Room temperature spectrum of the single spot*[119].

1.2.6 Fabrication processes

The main fabrication processes of color centers in the above-mentioned materials, but more specifically in the two main materials studied in this dissertation work: diamond and AlN that so far have resulted in successful systematic fabrication of such are the presented following ones.

Incorporation during the growth of the substrate

The first reports of single-photon emitter in all of the semiconductors described in the previous sections were based on defects found in just-grown substrates without any post-growth introduction of impurities[22], [27], [114], [120].

For the diamond case, which as has been stated before the color center study is among the most mature, the first reports of single emitters , came from the individualization of nitrogen impurities that had been incorporated into the diamond during the growth unintentionally[127]. As a more *contaminated* method (considering the atmosphere in which it takes place), the HPHT (high-pressure high-temperature) growing process usually leads to diamond full of color centers, where the address of a single impurity becomes harder. The use of CVD (chemical vapor deposition) technique is nowadays much more expanded for the incorporation of impurities while growing either bulk diamonds or nanodiamonds[128], [129].

One of the advantages of this technique is that it allows for the formation of stable centers in an undamaged environment without requiring further treatments, resulting in longer coherence times[48], [130]. However, a major drawback is the lack of control over the lateral position of the centers within the sample. This presents a problem for quantum technologies where the position of the array of centers is crucial (for qubit scalation)[42], as well as for quantum sensing where high density of centers in a specific location is sometimes important[59]. However, this formation process is usually the most commonly adopted for the formation of color centers in nanodiamonds[131]. The position of the color center is not a critical factor in this formation process, and the incorporation of impurities such as silicon has been found to be effective. It should be noted that not all color centers have been successfully created using this method in nanodiamonds, but research in this area is ongoing.

Regarding the in-grown color centers in AlN, the majority of center so far reported for this material have been found in as grown substrates grown on two main materials: sapphire and silicon[119], [120]. Still the

origin of these defects, i.e. whether they are related to any introduced impurity during the growth or any combination of vacancies in the crystal, is a field under study.

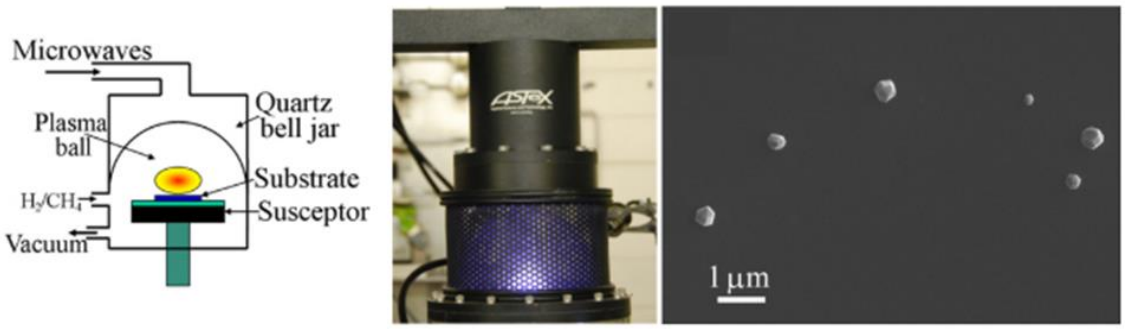

Figure 17 *CVD example growth of nanodiamonds with embedded SiV color centers* [132]

Laser writing

This technique can be considered as the most recent one and it is based on the femtosecond laser irradiation of the semiconductor that leads to the formation of vacancies. These vacancies upon a chosen annealing method (either furnace or laser-induced) diffuse and stabilize to form an energetically stable color center. In diamond case, so far the laser writing of impurities has been centered in the formation of NV color centers, by producing vacancies close to present N atom in the crystal in order to promote the formation of the defect[133], [134]. It is considered as an efficient process, with a high position control given by the diffraction limit. One other advantage that it presents is the fact that the formation of this defects is usually a few micrometers below the surface which for coherence purposes presents as an interesting point.

One major drawback of this method is that it can only fabricate defects related to impurities introduced in the material by other means, such as synthesis or ion implantation, as it is based only on the vacancy creation, so the color center creation can be considered as a combination of the first method and this second one. Additionally, the process requires annealing to activate the center properly, which traditionally entails applying the process to the entire diamond. This whole device annealing may be considered as a potential problem when talking about photonic devices where all the components may not stand the annealing treatment for potential photonic devices. Fortunately, it has been demonstrated that by using the same laser at lower powers, the region can be heated to a sufficient temperature to create the desired centers[133], [135].

In AlN case, this method has been reported to lead to outstanding outcomes, resulting in the production of single-photon emitters with consistent and reproducible optical properties[125].

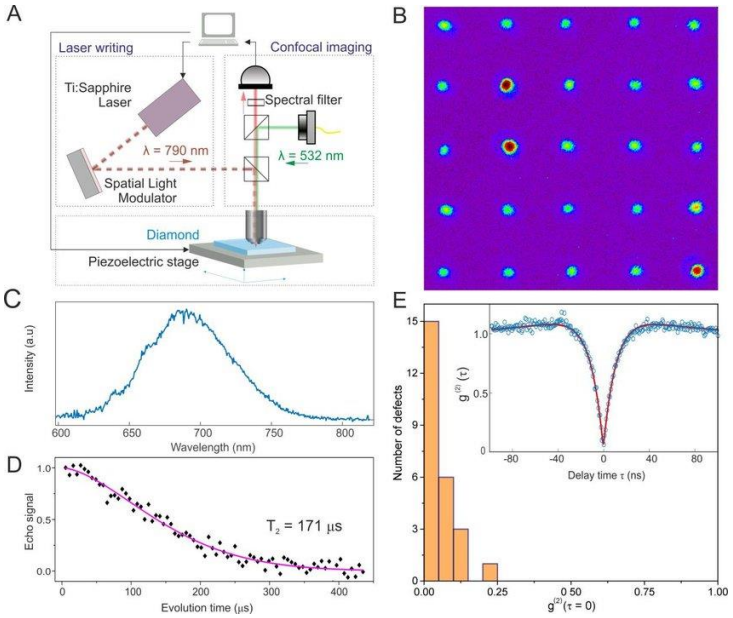

Figure 18 *Deterministic laser writing of NV color centers in diamond. a) experimental apparatus. b) PL image of the fabricated spots. c) Typical PL spectrum. d) Measured spin echo from a color center. e) Histogram of $g^2(0)$ values for the centers fabricated*[134]*,*

Electron irradiation

In the same way as femtosecond laser irradiation, this technique consists of the irradiation of the substrate with an electron beam to promote the formation of vacancies. In diamond, this technique allows for the formation of intrinsic defects related to vacancies or other defects like NV centers, thanks to the previous presence of nitrogen in the substrate. It usually is employed for the creation of high-density ensembles of NV centers for sensing applications[136].

It also requires a thermal annealing to promote the diffusion of vacancies in the crystal and form the color centers, but also to repair the lattice and minimize the decoherence that could be produced by the damage induced in the surroundings. In the diamond case, the minimum electron energy for which an electron is able to move the carbon atom from its position in the lattice and it is equivalent to an acceleration energy of the electron beam of at least 145 keV[137]. From that threshold energy, the increase of the electron energy leads to an influence of the irradiation at larger depths within the material, while the fluence of electrons introduced into the diamond is what makes the difference in terms of vacancies creation.

Ion implantation

Ion implantation of defects is a well-known technique for the fabrication of electronic devices in semiconductors in general [138] and over the past few decades has become also one of the main techniques for the fabrication of color centers in diamond [139], [140]. It is based on the introduction of the willing spice for the formation of the defects. The passing of the ion through the diamond lattice produces the vacancies necessary for the formation of the center.

It allows for the localized introduction of impurities in the diamond, with precise control in the quantity and depth (depending on the energy)[61], [141] . Most of the color centers based on extrinsic impurities in diamond are fabricated using this method, whose main drawback is the need for a thermal annealing of the sample in order to activate the centers and repair the damage caused by the ion passing through.

This method will be explained in detail in the next Chapter, considering that it is the main fabrication strategy employed in this thesis work for the formation of color centers.

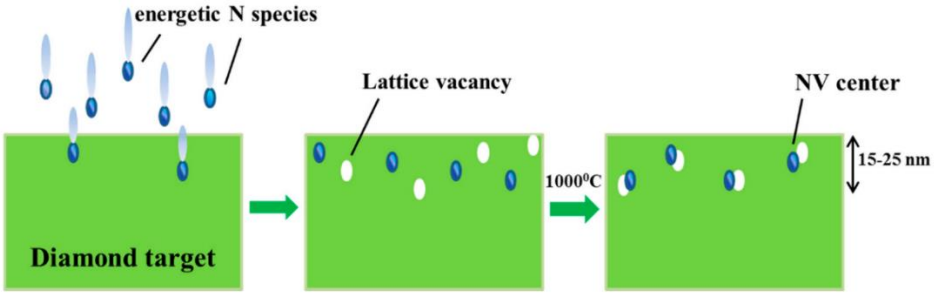

Figure 19 *Formation of NV center using ion implantation*[49].

1.3 Materials

In this dissertation, the fabrication of color centers was centered in two main materials: diamond and AlN. For this reason, in this section the main physical properties of each of them will be described in detail.

1.3.1 Diamond

Diamond is a well-known material, valued not only for its use as a gemstone but also for its exceptional optical and physical properties[142], [143]. Naturally, diamonds are formed below the Earth's surface through the high-pressure and high-temperature conditions that carbon atoms are subjected to. The main crystallographic component of diamond is carbon, a non-metallic atom from group IV and period II with an electronic configuration of [He] $2s^2 2p^2$. Diamond is one of several allotropic forms carbon can take, including graphite, fullerene-like structures, and a wide variety of stable amorphous phases such as glassy carbon and tetrahedral amorphous carbon. Graphite is the most stable form of carbon, and for many years, it has been the most extensively studied form, along with diamond. However, a new form of carbon, graphene, has been identified in recent years. Graphene is an allotrope of carbon consisting of a single graphite layer with extraordinary physical properties, although it is not the focus of this work [144], [145].

As shown in **Figure 20**, diamond is synthesized under extreme conditions, while graphite is the stable form under normal environmental conditions. Diamond is considered "metastable," since the energy barrier required to break the bond is too high to occur under normal conditions [146].

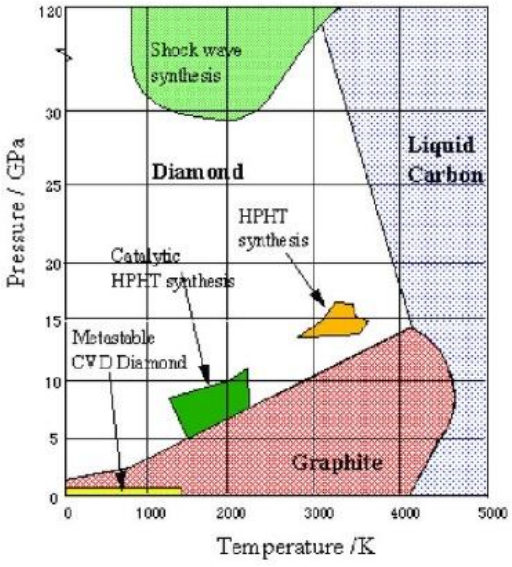

Figure 20 *Phase diagram of carbon* [147]

Crystallographic structure

Diamond is an allotrope of carbon arranged in a tetrahedral structure. This structure is formed by the hybridization of the s and p external orbitals in a sp^3 configuration, which allows each carbon atom to be covalently bonded to four other carbon atoms at a bond distance of 1.54 Å in the (111) direction. The lattice configuration of diamond is a face-centered cubic (FCC) with two carbons in the base at (0,0,0) and a (1/4, 1/4, 1/4) displacement. This is equivalent to two interpenetrating FCC lattices displaced by 1/4 along the diagonal and a lattice constant of 3.57 Å.

Diamond has a high atomic density of 1.77 x 10^23 atoms/cm3, which leads to a very high mass density of 3.54 g/cm3 [143].

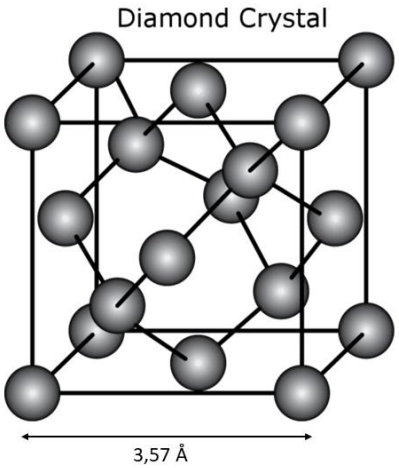

Figure 21 *Crystallographic structure of diamond.*

Mechanical properties

Diamond is the hardest natural material, and it ranks as a 10 on the Mohs scale. The binding energy between carbon atoms in diamond is 7.62 eV[148], which is a high value if we compare it to the silicon one (4.63 eV[149]). This feature is the basis of several interesting macroscopic properties such as the high Young's module (1220 GPa), high Debye temperature (2000 K)[150], chemical inertia and excellent biocompatibility[151].

Diamond is an excellent material for various technological applications, thanks to its impressive thermal and electrical properties. At room temperature, diamond has a low density of phonons, resulting in fewer collisions between phonons and higher thermal conduction compared to other crystals. Its thermal conductivity is 25 W·cm-1·K-1[46], which is significantly higher than most other solids. Additionally, diamond has a high electron mobility due to the small amount of phonon scattering. These unique properties make diamond a promising material for developing miniaturized heat sinks and high-power electronics.

Electronic properties

Diamond has a band structure that is similar to silicon and germanium. The four orbitals produce eight sub-bands, out of which four are filled and correspond to bonding states. The valence band consists of these four sub-bands. The remaining four sub-bands are called "conduction sub-bands" and correspond to anti-bonding states (see **Figure 22**). In diamond, the valence and conduction bands have an indirect gap of 5.45 eV (see **Figure 22**), which is significantly higher than that of silicon (1.12 eV) and germanium (0.66 eV)[149]. This gap is mainly due to the smaller interatomic distance between carbon atoms. The high value of the gap makes diamond an excellent insulator at room temperature, or as it is usually referred as to a semiconductor with a very high energy gap.

Diamond is transparent over a broad spectrum of light, from near ultra-violet to far infrared, because of its insulating behavior. The coloration present in some diamonds is due to impurities. For example, many diamonds appear yellow due to nitrogen impurities, which introduce an absorption band in the blue spectral range[127].

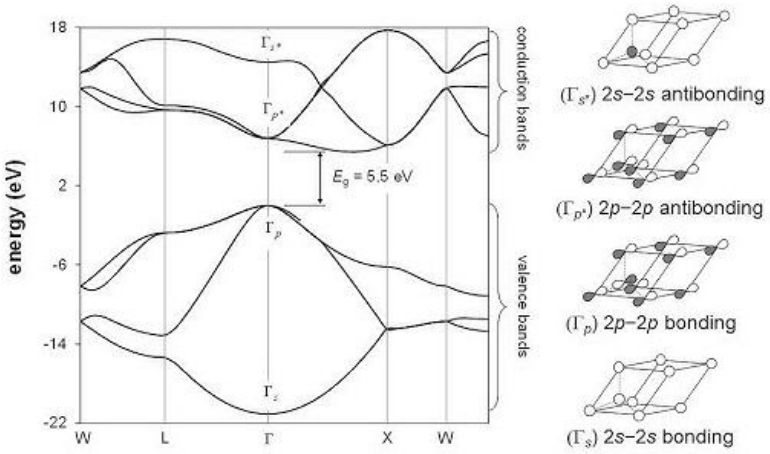

Figure 22 *Diamond band diagram*

The electrical resistivity of diamond is approximately 10^15 Ω cm at room temperature. This property is due to its wide gap. As a result, diamond is an excellent candidate for electronic applications when compared to silicon and germanium. Unlike semiconductor detectors, diamond's high resistivity eliminates the need for inversely polarized p-n junctions, which can cause thermally generated dispersion currents and their fluctuations that affect the amplitude of the applied electric field.

Moreover, as a semiconductor, diamond dopants can play a significant role. They can be introduced through chemical synthesis or ion implantation followed by thermal annealing[149]. Boron and phosphorus are the most used dopants, with boron being p-type and phosphorus being n-type[152]. However, incorporating these dopants in the crystal lattice can be challenging, especially in the case of phosphorus. The acceptor and donor energy levels for boron and phosphorus are 0.37 eV above the valence band and 0.56 eV below the conduction band, respectively[153]. These same elements act as dopants in silicon, but with much lower energy levels of 0.045 eV and 0.044 eV, respectively, which leads to vastly different resistivity in the doped materials, especially for n-type conduction[154].

The electrical conduction properties of diamond can be significantly altered by modifying its surface. When hydrogen is used to terminate diamond, it creates a p-type conductive surface layer[155]. Furthermore, the low ionization energy caused by the electron affinity of the hydrogen-terminated diamond surface promotes the transfer of electrons from the valence band to physiosorbed adsorbates such as water. On the other hand, the oxidized surface of diamond is insulating.

Optical properties

Diamond as a wide bandgap semiconductor is transparent from wavelengths around ~225 nm towards the infrared. Absorption in the IR is weak in this material because it is a purely covalent crystal that does not possess a permanent dipole moment[46]. Given this low absorption, which is two orders of magnitude weaker than in ionic crystals, diamond is also employed in IR spectroscopy and in particular for TIRF (Total Internal ReFlection) technique, where a high refractive index like the diamond one is needed for the experimental setup.

The presence of nitrogen impurities can lead to a continuum absorption in the visible spectrum, more intense in the blue spectral region and very weak in the red, resulting in the yellow coloration of nitrogen-rich diamonds (such as those synthesized by high-pressure high-temperature technique)[46].

As a material that has high density and polarizability, it presents one of the highest refractive index values among transparent materials in the visible range[46]. Its average value over the visible spectrum is n = 2.42. Due to this high refractive index, the reflectance coefficient R reaches 17%, which makes diamond an ideal material for use in jewelry. It is also worth mentioning that ion-damaged diamond shows an increased refractive index compared to the majority of optical materials that behave oppositely.

Additionally, the First-order Raman scattering occurs at 1332.5 cm-1, with a high cross-section compared to other ionic crystals and a sharp spectral line (FWHM is typically below 5 cm-1)[46].

Synthesis and classification

Unlike the gemstone diamond, that mainly is classified using the 'Four C's' (cut, clarity, color and carat), the most expanded criteria for the classification of diamonds are their content of nitrogen and boron impurities. The majority of natural diamonds can be classified as 'Type I' diamonds containing notable concentrations of nitrogen impurities. 'Type II' diamonds, on the other hand, have very low nitrogen concentration. The type of diamond can be more deeply classified as follows [156]:

- **Type Ia:** Most natural single crystals belong to this type. They contain nitrogen impurities ranging from 100 to several thousands of ppm. Nitrogen is usually present in A and B aggregates, which are only detectable in the IR and UV absorption spectra, making them nearly transparent in the visible range. These diamonds are commonly used in jewelry.
- **Type Ib:** This type is rarely found in nature; most high-pressure synthetized diamonds are of this type. The nitrogen concentration in this case is between 100-500 ppm, partially on isolated substitutional sites. The absorption spectrum of these diamonds increases towards the end of the blue range, which makes them yellowish.
- **Type IIa:** This type is also very rare to be found in nature, its concentration of nitrogen goes from 10 to 100 ppm, not enough to be detected as IR or UV features.
- **Type IIb:** In this case, substitutional boron acceptors play a role due to the lack of nitrogen donors (almost no concentration) and the material displays a notable p-type semiconductivity. Moreover, the boron impurities cause an absorption of light towards the end of the red range of the spectrum, making the diamond look bluish.

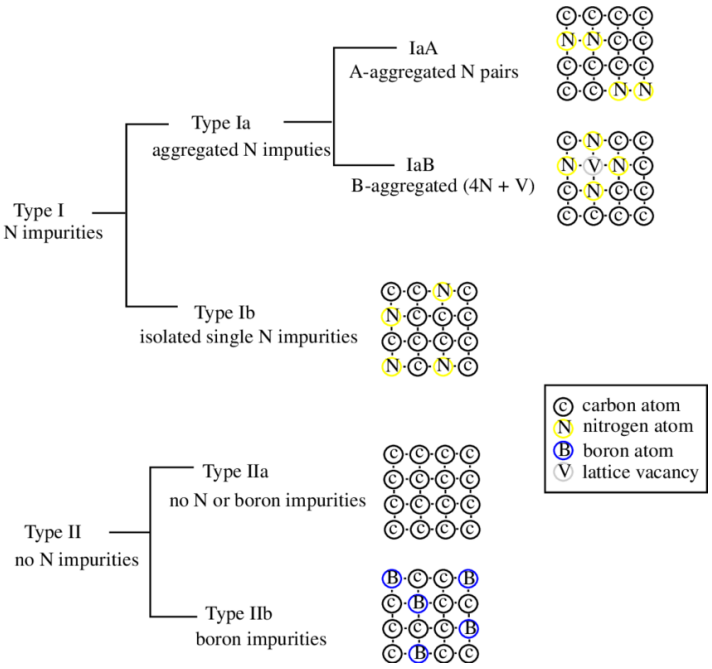

Figure 23 *Classification of diamond* [156]

Diamond, as it has been already explained, can be classified mainly in four types of which just one is mainly present in nature, the rest of them are usually synthetized to improve the quality and increase its availability for engineering applications.

In the last century, several synthesis techniques have been developed and ameliorated to allow systematic reproducibility. The most widespread techniques so far are the following ones:

High-pressure High temperature (HPHT)

This technique, developed in the 1950s [157], aims to replicate the natural conditions under which diamonds form. It is a fast process that can produce large crystals. The process involves starting with a small diamond (called a "seed") and placing it in a mixture of melt metal (the catalyst) and graphite grains. The system is then put under pressure (about 5 GPa) and heated to above 1500 ºC. The catalyst allows carbon to dissolve from the graphite inside the metal, and the diamond seed begins to grow at different rates depending on the surface orientation[158].
The resulting sample is monocrystalline but has several zones due to the different surface orientations from the original seed, where the concentration of impurities is higher. These impurities, particularly nitrogen, pose a significant problem for this type of grown diamond. Apart from making them appear yellow.
High-pressure high-temperature (HPHT) diamonds are commonly used as cutting tools and indentations. They are often used as a substrate for epitaxial chemical vapor deposition (CVD) growth of electronic diamond layers, as they have fewer dislocations compared to CVD-grown diamonds and thanks to their cost-effectiveness.

Chemical Vapor deposition (CVD)

In the case of CVD growth, unlike the HPHT technique, a metastable process takes place instead of a process that follows the thermodynamical laws. During the diamond CVD synthesis process, the pressure is usually below atmospheric pressure typically between 1-200 Torr. The synthesis is carried out using hydrogen and hydrocarbon as starting materials. The hydrocarbon is usually present in small doses of between 1% and 5% of the gas, and it provides the carbon source needed to form the diamond. The precursors are pyrolyzed on the substrate using a hot filament of plasma.

To obtain a pure diamond, it is essential to control the pristine vapor phase and vacuum contaminations. CVD crystals are usually purer than HPHT ones, but the main contamination is still nitrogen. Silicon is also commonly found in CVD samples and comes from the quartz windows of the vacuum chamber. It can be accommodated in the crystal structure.

The main limitation of this production method is the growth rate, which restricts the amount of crystal that can be deposited over the substrate. Therefore, CVD diamonds are usually large but thin. CVD technique can also yield polycrystalline diamonds, which are cheaper and less technically difficult to produce. This polycrystalline material can be deposited over many substrates, such as silicon electronic devices, to act as a heat sink. However, the optical and electric properties of polycrystalline diamonds are grain-size dependent and generally worse than those of single-crystal diamonds[159].

Nanodiamonds (ND)

Diamond nanocrystals can be synthesized in sealed chambers by detonating highly explosive carbon-containing compounds such as trinitrotoluene (TNT) and cyclotrimethylenetrinitramine (RDX) mixtures. The high pressures and temperatures reached during the detonation wavefront provide the necessary conditions for the synthesis of nanodiamonds. These processes produce nanodiamonds with sizes down to a couple of nanometers, while nanocrystals in the range of 20 to 200 nm can be directly fabricated by milling of CVD or HPHT crystals[160].

1.3.2 Aluminum nitride (AlN)

Aluminum nitride is a type of ceramic material that is composed of nitrogen and aluminum. Although it was first synthesized in 1877, it wasn't until the mid-1980s that its potential application in microelectronics was realized, thanks to its relatively high thermal conductivity and electrical insulating ceramic behavior. Since then, it has been increasingly used in a wide range of thermal management and electrical applications. It exists in two different crystallographic forms: hexagonal wurtzite and cubic zincblende. In this section, we will discuss the hexagonal wurtzite which behaves as an insulator with a wide band gap of 6 eV. This material can be made more interesting for the semiconductor industry by doping the structure and changing its electrical properties. On the other hand, the cubic zincblende phase of aluminum nitride is a metastable structure that has been hypothesized to exhibit superconductivity behavior under high-pressure conditions [161].

Crystallographic structure

In 1924, Heinrich Otto, first reported AlN to have a wurtzite crystal structure. Each Al atom is bonded to for equivalent nitrogen atoms to form corner-sharing AlN tetrahedra. In the same way, the N is bonded to four equivalent Al atoms to form corner-sharing NAl tetrahedra (as represented in **Figure 24**). Its lattice constants are approximately 3.11 Å for a, and 4.978 Å for c.

The basis vectors that form the unit cell are (0,0,0), (a/$\sqrt{\mathbf{3}}$, 9, c/2), (a/$\sqrt{\mathbf{3}}$, 0, c/8), (0,0,5c/8), where a is the length of the hexagonal side and c is the distance along the z direction[162].

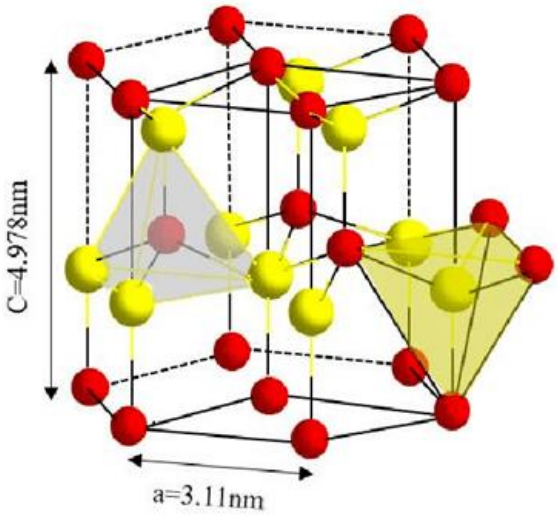

Figure 24 *Crystallographic structure Aluminum nitride (red points correspond to Al atoms, yellow ones to N)*[163]

Mechanical properties

Aluminum nitride is a material that is resistant to attack by most molten metals and salts. This means that it has a high abrasion resistance. It possesses properties such as high thermal conductivity for a ceramic material (second only to beryllia), high volume resistivity, and high dielectric strength. Table 1 summarizes its main physical and mechanical properties, showing some suitable characteristics for its application in high power electronics [161]. For example, its stable operating temperature and high thermal conductivity allow for great heat dissipation. It is also important to consider the mechanical properties of thin film AlN, which is widely used in photonics and electronics, in addition to its bulk form properties. The fracture

strength of AlN films is influenced by the deposition method, with higher temperature deposition leading to stronger films due to higher quality crystal formation. The Young's modulus of AlN films is generally similar to that of bulk AlN, and dependent on the crystallinity of the film[164].

Property	Value
Density (g cm^{-3})	3.32
Modulus of rupture (MPa)	300 – 350
Modulus of elasticity (GPa)	310
Fracture toughness (MPa $m^{-1/2}$)	3.35
Coeff of thermal expansion RT 1000ºC (x 10^{-6} K^{-1})	5.6
Thermal conductivity (W/mK)	140 – 177
Specific Heat (J kg K^{-1})	780
Volume resistivity (ohm cm)	10^{10}
Operating Temperature	Stable up to 2200 ºC
Dielectric Strength (kV mm^{-1})	>20

Table 1 *Mechanical and physical properties of AlN*[1]

Electronic properties

The band structure of AlN is similar to the ones of CdS, CdSe and ZnO. It has a direct band gap of 6.2 eV (see **Figure 25**) at room temperature, which is among the widest semiconductors in general diamond (5.5 eV), silicon (1.12 eV), and wider than its competitors in the electronic industry: GaN (3.4 eV) and SiC (3.3 eV). The valence band of AlN is divided into two subbands. The first subband is formed by the 2s levels of the nitrogen atoms, while the second subband is mainly attributed to the 2p levels of nitrogen. On the other hand, the bottom of the conduction band arises from the hybridization of aluminum's s and p orbitals[117].

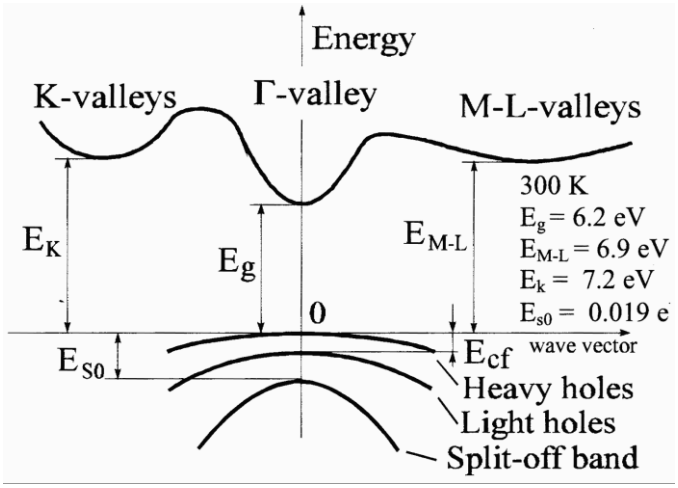

Figure 25 *Band diagram of AlN. Important minima of the conduction band and maxima of the valence band* [165]

Thanks to this wide bandgap, AlN is transparent in a wide range of wavelengths, a property that combined with its large thermal conductivity makes a great electrical isolation and thermal dissipation.

AlN, like other ceramics, has high electrical resistivity in the range of 10^{10} - 10^{16} Ω cm, although lower than that of diamond. It has a relatively high dielectric constant of ~8.9, which is lower than SiC. AlN also has a high breakdown electric field and its piezoelectric properties allow it to convert mechanical strain into an electric signal or vice versa [166].

AlN as a material with semiconductor properties, similarly to what discussed for diamond, can be controlled by introducing dopants. According to reports, introducing Mg dopant can enhance the piezoelectric

response of the material. However, doping both P type and N type of AlN poses specific difficulties. In the case of P type doping, a high concentration of dopants is required to reduce the distance between the acceptor levels and the valence band[167].

For N type doping, dopants from the upper part of the periodic table such as Beryllium (Be), Magnesium (Mg), and Zinc (Zn) are usually more effective. Lithium (Li) is mainly used for N type doping[167]. These doped substrates of Aluminum Nitride are good candidates for the realization of MEMS (MicroElectrocMechanical System) resonators and microwave filter, due to their large piezoelectric coefficient.

Optical properties

AlN is one of the largest bandgap semiconductor materials, with a bandgap of 6.2 eV at room temperature. The wide transparency window of AlN, covering from UV up to MIR, making it an interesting material for photonic integrated circuits, which have already been demonstrated. These circuits include micro-ring resonators (UV and MIR range) and waveguides, beam splitters and interferometers in the MIR rage. The refractive index of AlN is around 2.1 up to 1550 nm, which enables index contrast with some interesting materials like SiO2, for mode confinement in optical waveguide[87].

Furthermore, this material displays both second-order and third-order optical nonlinearities, which enable second-harmonic generation and parametric down-conversion. When used in quantum optics, like many other wide band gap semiconductors, it can also act as a host for single photon sources at room temperature. More information on this topic will be provided in the following sections [87].

Moreover, the Raman effect of AlN has been utilized to extend the optical frequency comb wavelength range and to demonstrate the Raman-based laser.

Synthesis

Aluminum nitride can be synthesized in many ways. They can be mainly divided in the growth of bulk aluminum nitride and on-substrate aluminum nitride, although some of them are common for both substrates.

On what regards the growth of bulk diamond, the three main methods are the following.

Physical vapor transport (PVT)

To grow AlN crystals using the PVT or sublimation method, AlN powder is heated above 2000 ºC in a nitrogen atmosphere. Aluminum and nitrogen atoms from the powder recondense on a seed crystal due to a temperature gradient between the source and seed, forming an AlN bulk crystal. However, one of the challenges of this method is finding a material for heating the AlN powder by induction that can withstand extremely high temperatures without melting. Currently, the most suitable options are made of tungsten and TaC[168].

Hydride vapor phase epitaxy (HVPE)

Thick AlN layers can be grown in HVPE through a chemical reaction of aluminum chloride gas and ammonia. This process was demonstrated by various groups and takes place in a temperature-controlled furnace at a relatively low temperature of 900-1000°C. The resulting AlN deposits are of high purity, and it's easier to control unwanted impurities due to the lower deposition temperature. Although the growth rate by this method is about one-tenth of that obtained by PVT, it proves to be a reliable method for high-purity AlN deposition[168].

Solution growth method

The solution-growth method involves introducing a seed into a solution containing Al and N, usually in a nitrogen atmosphere. This method produces high-quality AlN crystals due to the growth occurring close to

thermal equilibrium. However, few efforts have been made to grow AlN using this method, resulting in small crystals. The seed, mounted on a rotating shaft, is dipped into the solution, allowing Al and nitrogen atoms to deposit onto it. The growth temperature for solution growth is typically much lower than that of sublimation growth, which reduces demands and stress on the experimental setup. However, in cases where a higher temperature is desired to improve crystal quality, growth temperatures of up to 1600º C may be applied. Despite its thermodynamic appeal, the solution-growth method faces several unresolved challenges. It is the least developed of the three growth methods discussed in this review, and future work is needed to find practical solutions to all the challenges and ultimately prove its potential[168].

Concerning the growth of AlN on top of a substrate, the most expanded methods are again PVT, HVPE and the two following ones.

Metal-organic chemical vapor deposition (MOCVD)

This method is currently the most advanced technique for growing low-cost AlN templates with sapphire substrates. The most commonly used precursors in this process are trimethyl-aluminum (TMA) and triethyl-aluminum (TEA) as the aluminum source, and ammonia (NH3) as the nitrogen source. These precursors are delivered to the substrate's surface in a reaction or growth chamber using nitrogen or hydrogen as a push gas. The growth process typically involves a 2-step process: a low-temperature (950°C) pulsed process followed by a high-temperature (1250°C) continuous growth step[169].

Metal nitride gas phase epitaxy (MNVPE)

In this growing setup, there are two separate induction zones. One of them is used to deposit Al pellets, which creates Al vapor. The other zone is used to heat the substrate. As the Al is heated and vaporized, it is carried by a pushing gas (commonly Ar gas) to the substrate region. Here, it reacts with nitrogen that is also introduced as a gas flux and deposits onto the substrate. This process is usually carried out in several steps, similar to MOCVD. Each step uses several gas fluxes with increasing temperatures.

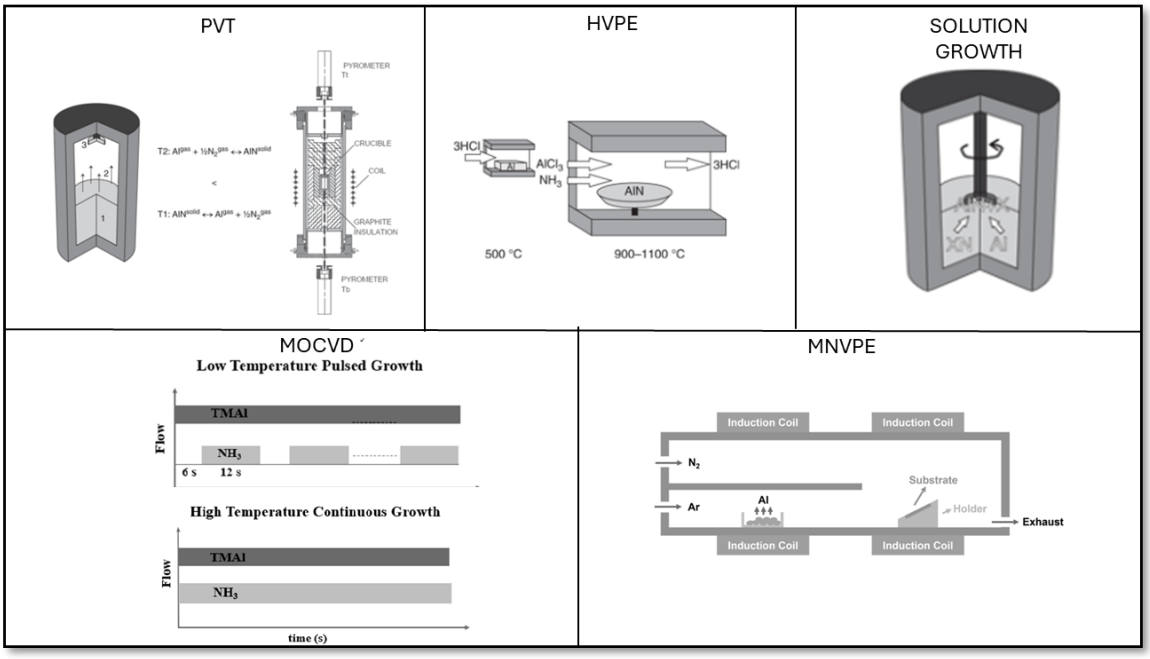

Figure 26 *Synthesis processes of AlN*[168], [170], [171], [172], [173].

Chapter 2

In this second Chapter, the principles of ion-matter interaction will be extensively discussed. In this line, the main parameters that are usually studied in this ion-matter interaction field will be analyzed, along with the known effects of ion irradiation in both considered materials, diamond and AlN. In addition, several implantation methods usually employed for the irradiation of semiconductors and in particular for the creation of color centers, such as keV and MeV ion implantation, will be presented.

Finally, the several post-implantation activation methods that so far have been used in the research field for the creation of color centers, will be discussed, showing the working principles, benefits and drawbacks of each of them.

2.1 Ion-matter interaction

Ion beam processing of materials involves the introduction of external atoms into a solid substrate by bombarding the solid with ions in the energy range of eV to MeV. The success of ion beam processing depends on factors such as the distribution of the energetic ions, the amount and type of lattice disorder created, and the location of the energetic ions within the crystal lattice[174].

2.1.1 Stopping power

To understand the distribution of the ions within the material, one must study the interaction between the material and the incoming ions. The Coulomb interaction between the target nuclei and the ions defines the trajectory of the ions and leads to an energy loss, while the ionization of electrons leads only to the loss of energy[174].

Considering these two mechanisms of energy loss, the nuclear collisions and the electronic collisions, the total energy loss can be expressed as follows[174]:

$$\frac{dE}{dx} = \frac{dE}{dx}\Big|_n + \frac{dE}{dx}\Big|_e \qquad \textit{Equation 9}$$

Where n and e denote the nuclear and electronic components, respectively.

In addition to the energy-loss rate, it is also customary to speak of the stopping cross-section $\boldsymbol{S}$, which can be defined as:

$$S = \frac{\frac{dE}{dx}}{N} \qquad \textit{Equation 10}$$

Where N is the volume atomic density.

Nuclear Stopping power

In the nuclear stopping term, the average energy loss that results from elastic collisions with target atoms is quantified. The nuclear stopping power or nuclear energy loss rate is the energy lost by a moving particle due to elastic collisions per unit length traveled in the target and it can be described by kinematics[174]. If the elastic collision occurs with a target atom initially at rest, the conservation of energy and momentum yields a transferred energy *T*:

$$T = \frac{4M_1M_2E}{(M_1+M_2)^2} sin^2\frac{\theta_c}{2} \qquad \textit{Equation 11}$$

Where E is the initial energy and θ_c the scattering angle in the center of mass and M_1 and M_2 are the atomic mass numbers of the ion and target atom, respectively. The maximum energy transfer (T_{max}) is obtained in a head-on collision, resulting from an angle of 180º. The schematics in two different reference system is represented in **Figure 27**.

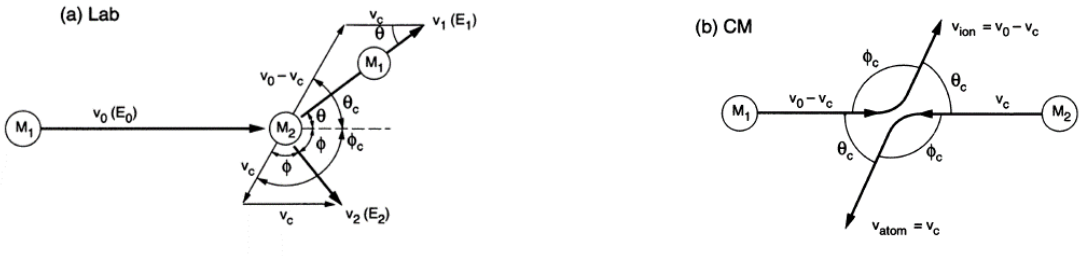

Figure 27 *Collision diagram of two different masses in a) lab reference system b) center of mass reference system*[174]

The cross-section for ion-atom interaction is given by the Rutherford formula:

$$\frac{d\sigma}{d\Omega} = \left(\frac{Z_1 Z_2 e^2}{4E}\right)^2 \frac{4}{sin^4\,\theta_c} \qquad \textit{Equation 12}$$

Where Z_1 and Z_2 are the atomic numbers of the ion and target atoms respectively, dΩ is the differential solid angle and e is the elementary charge.

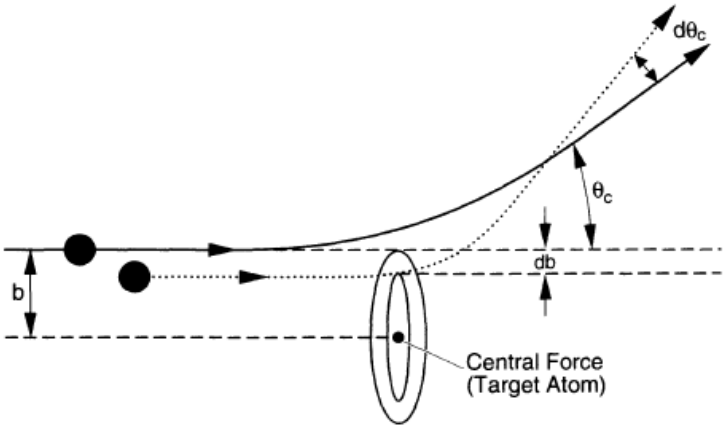

Figure 28 *Scattering of a particle that approaches a nucleus with an impact parameter, b*[174].

It should also be considered the scattering angle θ_c dependence on the interatomic potential, that can be written as follows (where b is the impact parameter, see **Figure 28**):

$$\theta_c = \pi - 2b \int_{Rmin}^{\infty} \frac{dr}{r^2\left[1-\frac{V(r)}{E_c}-\left(\frac{b}{r}\right)^2\right]^{\frac{1}{2}}} \qquad \textit{Equation 13}$$

The form of the repulsive potential V(r) used for this calculation is the one of a screened Coulomb potential due to the screening of the bare nuclei of the ion and target atoms by their electron clouds:

$$V(r) = \frac{Z_1\, Z_2\, e^2}{4\,\pi\,\epsilon_0\, r}\,\chi(x) \qquad \textit{Equation 14}$$

Where $\chi(x)$ is the screening potential. An approximate analytical expression for the universal screening potential is plotted in **Figure 28**, along with other classical screening functions.

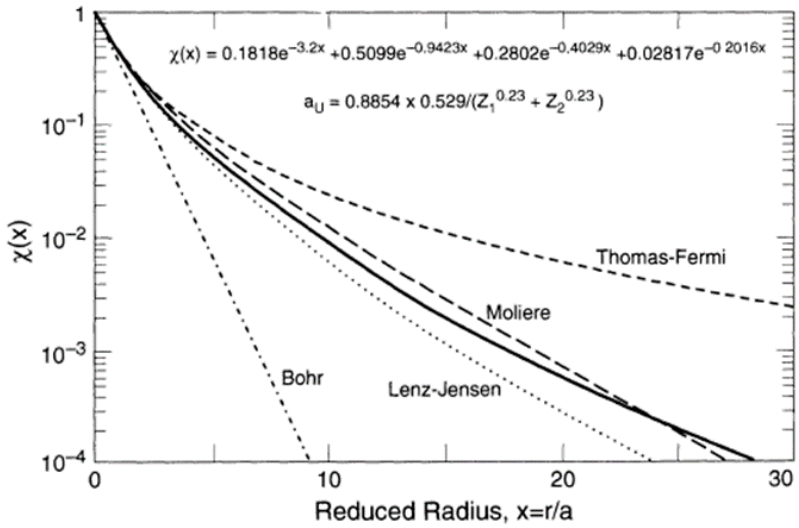

Figure 29 *Reduced screening potential functions, as a function of x= r/a, where a is the universal screening length*[174]

Once the interatomic potential function has been introduced, it is possible to derive the average nuclear stopping power S_n (E) which defines the average energy that is transferred by the projectile at each nuclear collision. S_n (E) can be calculated by integrating the energy transfer of a nuclear collision event over all the possible impact parameters b:

$$S_n(E) = \int_0^\infty T\, d\sigma = 2\,\pi\, \frac{4\,M_1M_2E}{(M_1+M_2)^2} E \int_0^\infty sin^2\frac{\theta}{2}\, b\, db \qquad \textit{Equation 15}$$

A reduced energy expression was suggested by Lindlhard to solve the **Equation 15**. The reduced energy ϵdescribes the dependence of the nuclear stopping power on the masses (M_1 and M_2) and the charges (Z_1 and Z_2) of the atoms involved in the scattering process and introduces the universal screening length a_u:

$$\epsilon = \frac{E_0\, a_U}{Z_1\, Z_2 e^2 (M_1+M_2)} \qquad \textit{Equation 16}$$

$$a_U = \frac{0.8853\ \ a_0}{Z_1^{0.23}\ \ Z_2^{0.23}} \qquad \textit{Equation 17}$$

Where a_0 is the Bohr radius and E_0 is the initial energy of the M_1 in the laboratory reference system (see **Figure 27**a). Using this reduced variable, it is possible to obtain the universal stopping power S_n:

$$S_n(E_0) = \frac{8.462 \times 10^{-15} Z_1 Z_2 M_1 S_n(\epsilon)}{(M_1+M_2)(Z_1^{0.23}+Z_2^{0.23})} \left[\frac{eV\ cm^2}{atom}\right] \qquad \textit{Equation 18}$$

This nuclear stopping power dependence with the reduced energy is plotted in **Figure 30**.

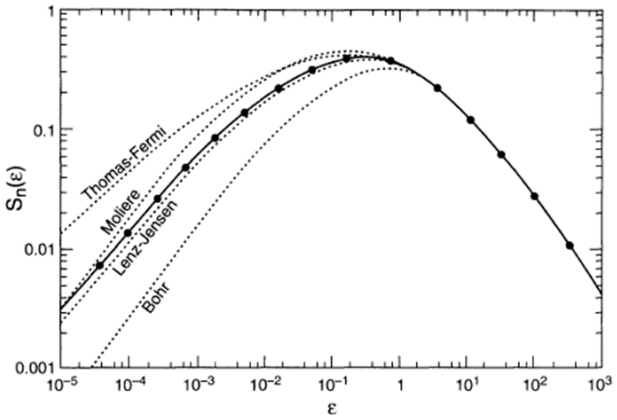

Figure 30 *Universal nuclear stopping power calculations as a function of the reduced energy. Other nuclear-stopping power calculations based on four classical atomic models are represented*[174].

The quantity S_n just presented is a key parameter to understand the effect of the ion pass through and the final position of the ion in the material, when in low energy regime, as it will be more extensively discussed in the following.

Electronic Stopping power

As it has been presented at the beginning of the section, two parameters play a role in the energy loss of the ion introduced in the material: the nuclear stopping power (explained above) and the electronic stopping power.

The electronic energy loss is defined as the inelastic energy loss of the incident ion as it moves through the cloud of electrons of a target material. The interaction between the projectile and the electrons still correspond to a Coulomb process[174].

Electrons can undergo three different effects: they can be excited to higher discrete energy levels, they can be ejected (ionization) or they can be excited in collective motion (plasmons). The prevalence of one contribution over the other depends on the ion velocity with respect to that of the target electrons.

In the low velocity regime, when $v < v_0 Z_1^{2/3}$ (v being the projectile ion, v_0 the Bohr velocity of an electron in the innermost orbit of a hydrogen atom and Z_1 been the atomic number of the ion), the electronic energy loss is proportional to the ion velocity. The interaction arises from the scattering of electrons that are no longer attached to any specific atoms but form a gas in which the positive charge is embedded. For this regime the Lindhard- Scharff model derived the formula[174]:

$$S_e(\epsilon) = \left(\frac{d\epsilon}{dx}\right)\Big|_e = k\,\epsilon^{\frac{1}{2}} \qquad \textit{Equation 19}$$

where

$$k = \frac{Z_1^{\frac{2}{3}} Z_2^{\frac{1}{2}} \left(1+\frac{M_2}{M_1}\right)^{\frac{3}{2}}}{12.6\left(Z_1^{\frac{2}{3}}+Z_2^{\frac{2}{3}}\right)^{\frac{3}{4}} M_2^{1/2}} \qquad \textit{Equation 20}$$

Where M_1 and Z_1 are the mass and atomic number of the projectile ion, while M_2 and Z_2 are the mass and atomic number of the target stom. This formula depends on the nuclear term and cannot be described by a universal curve. The electronic stopping power is proportional to the ion velocity for energies below 1 MeV. It reaches a maximum when the ion velocity is comparable to the average velocity of the outer electrons,

maximizing the interaction time and reaching a maximum energy transfer between the projectile and the target electrons.

The shape of the electronic stopping power profile depends on the detailed electronic structure of the target atoms. As a consequence, there is an increase in the shell effect for this low energy regime and the stopping cross section varies not monotonically with the target atomic number.

At higher velocities, the excitation and ionization of core electrons becomes the dominant effect, and the collective excitation of the electron gas takes place. In this range, the cross-section falls with energy and the target becomes progressively more transparent [174].

For high ion velocities, the ion has a high probability of losing all the electrons, and so the formula proposed by Bethe and Bloch becomes valid:

$$\frac{dE}{dx} = \frac{8\,\pi\ Z_1^2\ e^4}{I_0\,\epsilon} ln\left(1 + \epsilon\ + \frac{5}{\epsilon}\right) \qquad \textit{Equation 21}$$

$$\epsilon = \frac{4\ E\ \frac{m_e}{M_1\ m_0}}{I_0\ Z_2} \qquad \textit{Equation 22}$$

Where Z_1 and Z_2 are the core charges of the ion and the target, e is the elementary charge, m_e is the electron mass, m_0 the atomic mass unit, M_1 is the relative atom mass of the ion, and I_0 is the so-called Bloch constant expressed in eV units (**Figure 31**).

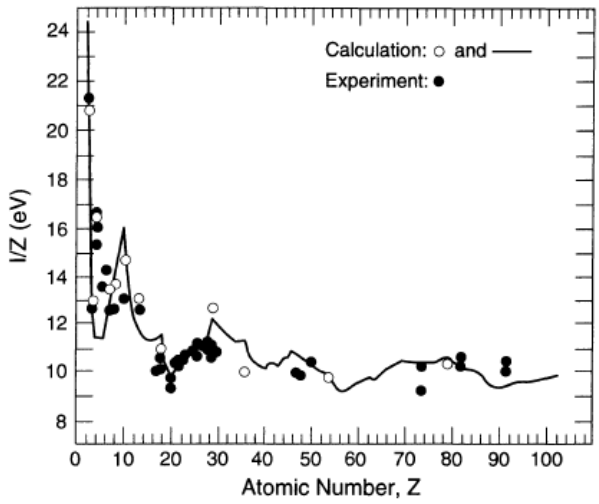

Figure 31 *Representation of the Bloch constant (I/Z) as a function of the atomic number of the target atoms.*

As anticipated before, the nuclear-stopping power is the most important process at low energies, reaching its maximum value around $\epsilon = 0.35$ and then falling off with increasing energy. However, the electronic stopping power increases linearly with ion velocity and becomes the dominant energy loss process for energies greater than $\epsilon \cong 3$.

2.1.2 Ion range and distribution – Straggling

In the previous section, it was explained how an implanted ion in a material loses energy through both nuclear and electronic interactions with the substrate atoms. The nuclear interaction involves individual elastic collisions between the ion and target-atom nuclei, while the electronic interactions can be seen as a continuous viscous drag phenomenon between the injected ion and the sea of electrons surrounding the target nuclei[174].

Considering that the stopping of an ion is a stochastic process, the sequence of collisions and subsequent ion deflection, as well as the total path length of the ions in coming to rest, vary randomly from ion to ion. Therefore, a statistical approach is necessary.

In this sense, the depth distribution of implanted ions, N(x), normalized for an ion implantation dose ϕ_i (total number of ions introduced into a certain fixed area of material) , is given by the expression[174]:

$$N(x) = \frac{\phi_i}{\Delta R_p\,(2\,\pi)^{1/2}}\,exp\left[-\frac{1}{2}\left(\frac{x-R_p}{\Delta R_p}\right)^2\right] \qquad \textit{Equation 23}$$

Where R_p stands for the projected range of the ion and ΔR_p is the projected range straggling.

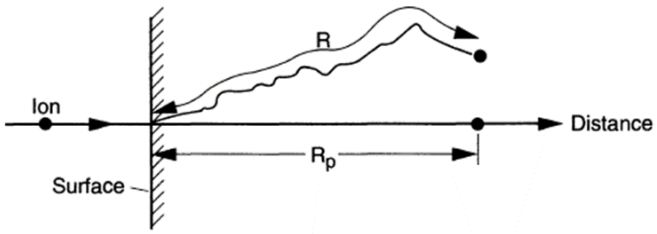

Figure 32 *Ion impinging into a semiconductor, with a projected range Rp*[174]

If we assume all the implanted ions are retained, the dose is related to the ion depth distribution as follows:

$$\phi_i = \int_{-\infty}^{\infty} N\,(x)dx \qquad \textit{Equation 24}$$

The gaussian approximation is useful to gain a simple physical picture of the implanted ion profile. It should be noted that the profile shown in the **Equation 23** ignores the diffusion processes which may take place during the implantation, in the same way, the channeling events are not considered. Furthermore, longitudinal and lateral straggling (the average fluctuation in the projected range of the ion in depth and XY plane, respectively) are also present, affecting the ion position in the orthogonal plane to the ion beam direction, as it is visible in **Figure 33**.

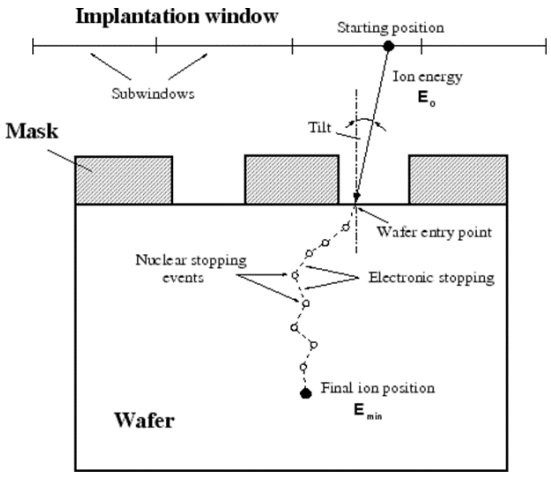

Figure 33 *Interaction ion-matter upon implantation in a semiconductor and trajectory of the implanted ion*[175].

2.1.3 Radiation damage

As an ion slows down and comes to rest in a crystal, it makes a number of collisions with the lattice atoms. In these collisions, sufficient energy may be transferred from the ion to displace an atom from its lattice

site. Electronic stopping will usually not create extensive damage to the host crystal, except in cases where the electronic excitation may break the interatomic bonds, leading to some structural rearrangement.

Lattice atoms displaced by incident ions are called primary knock-on atoms (PKA)[174]. The PKA, during its motion, can collide and displace other atoms (secondary knock-on atoms, tertiary knock-ons, etc.), creating a cascade of atomic collisions (see **Figure 34**). This results in the distribution of vacancies, interstitial atoms, and other types of lattice disorder in the region at the end of the ion range.

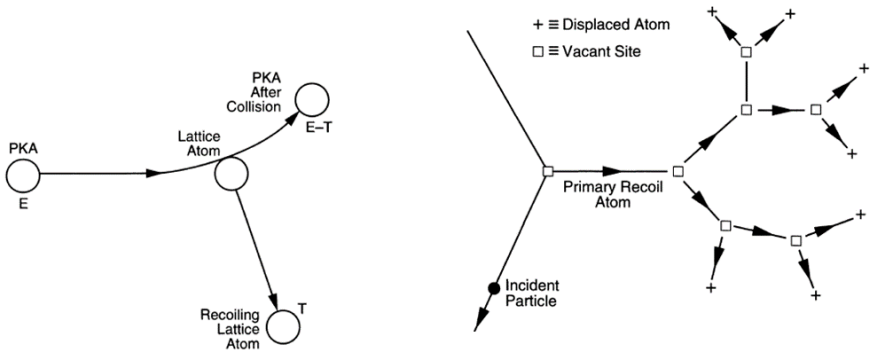

Figure 34 *PKA energy loss working principle and subsequent displacements taking place in the cascade*[176], [177].

The energy required to displace the lattice atom is called displacement energy, E_D. If the energy transfer to the lattice atom during a collision is less than E_D, the struck atom undergoes large amplitude vibrations without leaving its lattice position. However, if the energy transfer is greater than E_D, the struck atom can move out of the lattice site, leaving a vacancy and occupying an interstitial site in the lattice. These effects occur when the incoming ion has low energy[177]. If the ion has MeV energy before interacting with the target atoms, it will lose energy by electronic interaction. As a result, the damaged layer is produced mostly at the end of the ion range[176], [177].

2.1.4 Dynamics simulation

Considering the stochastic behavior of ions upon arrival in the material, simulating processes within the semiconductor seems like an intriguing and beneficial concept. Thee SRIM program allows for the simulation of this stochastic ion's behavior inside the material.[178].

This software is a Monte Carlo program that calculates the interaction of energetic ions with an amorphous target (the directional properties of the lattice are neglected). The input parameters to the program are the ion type and energy, the composition and density of the target material, and the energy required to displace a target atom from its lattice site creating a vacancy.

The program simulates the process of an ion entering a target and continuously losing energy through electronic interaction until it collides with a target atom. SRIM simulates the collisions in an statistical way allowing the ion to make jumps between calculated collisions and them averaging the collisions results over the intervening gap. Once all recoil nuclei have energy below a certain cut-off, the program resumes following the motion of the implanted ion. The ion continues with its new energy and direction until another statistical collision occurs, and this process continues until the ion's energy is below the energy required to create a vacancy, at which point it cannot dislodge any more atoms and comes to rest. The program stores the history of the first projectile and all secondary events, and then a new ion is shot into the target[178].

The parameters required to understand the ion effect and trajectory in the material have been previously discussed. These can be obtained by simulating the ion species, the material target, and the energy using SRIM. This provides a clearer understanding of the physics mentioned earlier.

Stopping power simulation

In **Figure 35**, the results of two different irradiations in the same material (in this case, diamond) were analyzed using the SRIM simulator. In both cases the stopping power dependence with the projectile energy is plotted in a range from 10 keV to 10 MeV. The difference between the simulations is the mass of the irradiation ion, for **Figure 35**a it is a light ion, H, while for the **Figure 35**b, Ge ions were used.

As anticipated before, for light ions, the dominant stopping power is in any case, the electronic one, which has an increasing behavior in the low energy range (keV range) and decreasing at increasing energy after ~150 keV.

When talking about heavy ions, the nuclear stopping power plays the most important role for low energies while at increasing energies it starts losing its effect and the electronic stopping power becomes dominant.

Comparing both graphs, it can be pointed out how the increasing behavior with energy of the heavy ion electronic stopping power reaches values much higher (not even plotted) than in the case of light ions, for which the increasing behavior goes up to a few hundreds of keV.

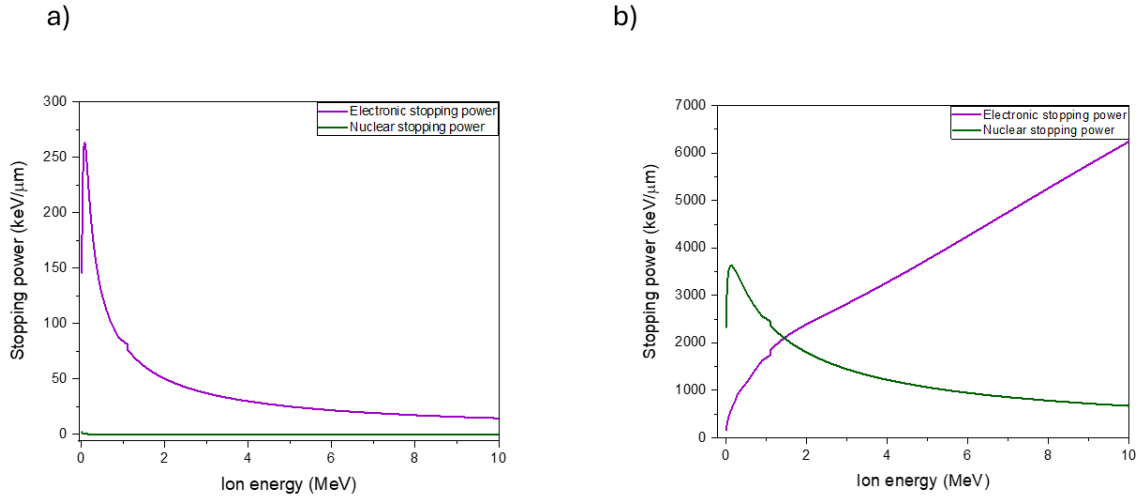

Figure 35 *SRIM simulation of the stopping power as a function of the energy of the ion for a) H ions, b) Ge ions.*

Range and distribution simulation

In **Figure 36**, the ion implantation profiles in the target material for different ions and different energies are plotted.

In **Figure 36**a the deposition profiles for H ions in diamond for energies between 50 keV and 700 keV are plotted. It can be pointed out how the higher the energy of the ion the deeper the ions reach inside the material, but also the wider the ions profile is (larger Bragg's peak) and so more uncertainty in the depth we have. In **Figure 36**b, where the same profiles were simulated in this case for Ge ions, it is visible how the depth range is already much smaller, because the larger the ion the lower the implantation depth. In this case it is also worth pointing out how the Bragg's peaks are wider for all the energies, so the ions will be placed in much wider regions.

In **Figure 37**, the visual of the trajectory of H ions in diamond from different perspectives and different energies is reported. For this particular case, it can be pointed out both the lateral and depth straggling of the ions, demonstrating how the larger the ion energy, in this case 500 keV (**Figure 37** a. and b.), the deeper the depth but the larger the straggling. While for energies of around 50 keV (**Figure 37** c. and d.), in the same conditions, the straggling is much lower, leading to a much higher precision of the implantation. As was pointed out before, the straggling of the ions is due to the collisions of the projectile ions with the target atoms. For this reason, the lower the energy of the projectile the lower the number of collisions and so the less it deviates from its projected trajectory.

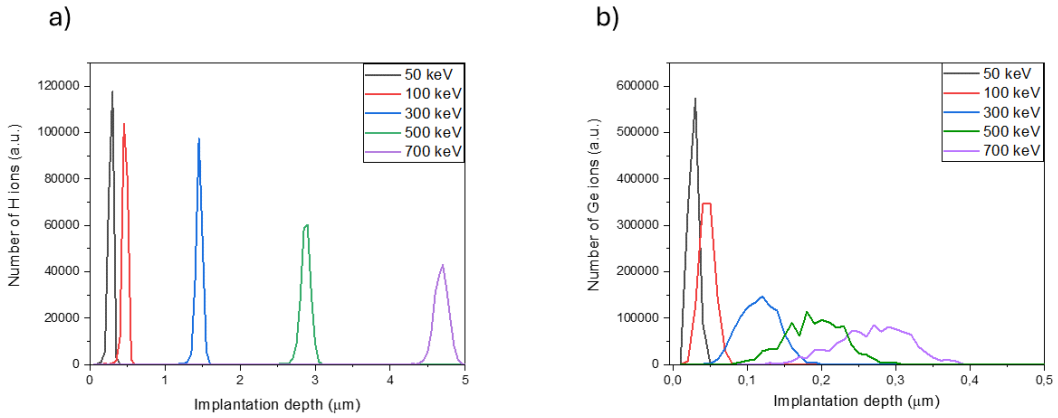

Figure 36 *SRIM simulation of the deposition of the ions inside the targets for different energies: a) H ions, b) Ge ions.*

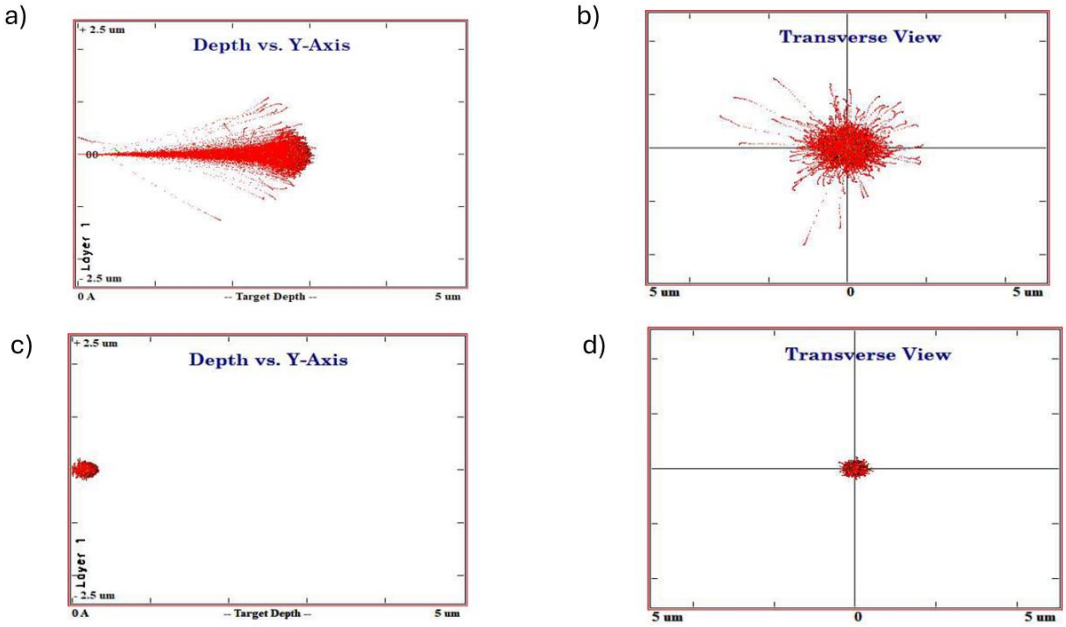

Figure 37 *SRIM simulation of the straggling of the ions from the xy plane and xz plane, for a), b) high energy H ions and c), d) low energy H ions.*

Radiation damage simulation

In **Figure 38**, a representation of the vacancies (damage) created by a heavy and a light ion is shown. It is worth noting that the heavier the ion, the higher the induced damage. This induced damage usually shows the same profile of ion implantation, but it shifted towards the surface of the sample, meaning that the damage is created upon the passing through of the ion that leads to the displacement of a host atom, but as the projectile ion comes to rest it doesn't have enough energy to damage the target material.

In the case of light ions implantation, the induced damage is always deeper and usually more localized as it is the ion profile (see **Figure 38**).

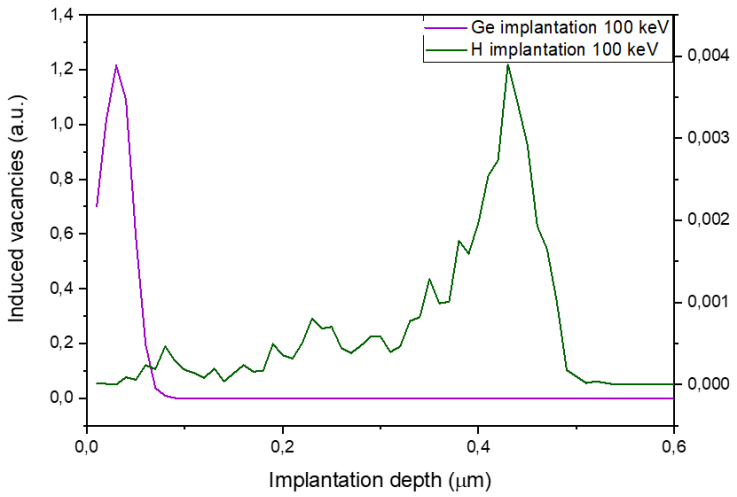

Figure 38 *Damage events created upon ion implantation with two different ions*

2.2 Ion beam modification

In the previous section, the physical principles of the ion-matter interaction were explained in detail, including the simulation software that is usually used for the planification of experiments and understanding of the ion behavior.

In this section, the principal effects of ion beam irradiation in the two materials that are studied in this thesis will be explained, along with the main limitations that ion implantation presents nowadays as a technique for the fabrication of color centers.

2.2.1 Structural modification

Diamond

Implanted ions release energy in the target material, often enough to break chemical bonds and create lattice defects. If this damage effect occurs in a crystalline material, such as silicon, it induces only amorphization[177]. However, in metastable materials, such as diamond, it can promote the conversion of to its stable phase, graphite[179]. This conversion occurs due to the defects induced in the lattice that promote the formation of an amorphous network of sp^2/sp^3 carbon atoms. The damage peak occurs at the end of the ions' penetration range, which is a few micrometers below the sample surface in the case of implanted ions with energy in the MeV range[180].

Thermal annealing plays an important role on damaged diamond: the high temperature provides the kinetic energy necessary to promote the rearrangement of the atoms and a partial recombination of vacancies with interstitial atoms. If the number of such defects is below a certain threshold value (usually referred to as the "graphitization threshold"), the implanted region can re-convert to pristine diamond. When a more heavily damaged diamond is annealed, it creates a larger number of defects such as small clusters of sp2 atoms or graphitic regions[180]. In this case, annealing will have the effect of inducing a complete transition to the graphitic phase. As a result, it is possible to obtain graphite-like buried structures inside diamond by means of ion-induced structural damage. This graphitization threshold has been extensively studied over the years and it has been reported to vary as a function of the energy of depth of implantation. For shallow implantation an induced vacancy creation of around $1x10^{21}$ vacancies/cm^2 is enough to amorphized the implanted layer, while in the case of deep implantation the induced damage is almost an order of magnitude higher $\sim 9x10^{22}\ vacancies/cm^2$[179]. The difference between the two energy ranges is due to the distance to the surface from one case to the other. As in the low energy range the damage is induced in the

first layers of the diamond closer to the surface, where the amount of inherent structure defects is higher, the creation of sp^2 clusters is easier than for the high energy case[181].

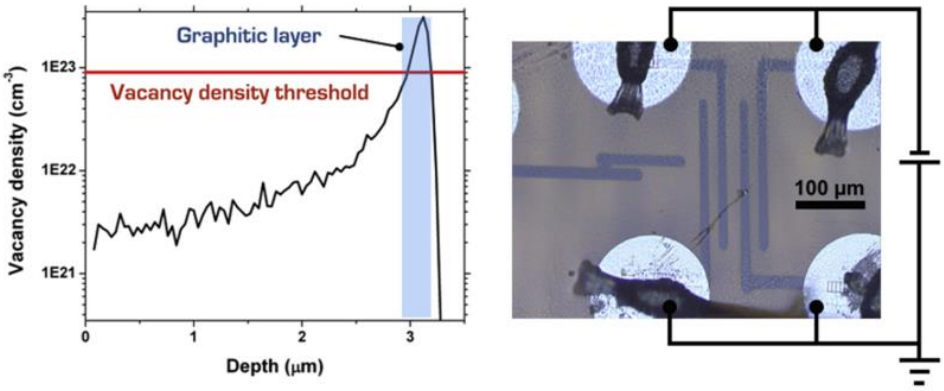

Figure 39 *Vacancy density profile induced by ion implantation of light ions in diamond and produced graphitic pattern*[182].

Aluminum nitride (AlN)

As it was previously explained, in the case of crystalline compounds that don't constitute a metastable material, the main effect of the ion implantation is the amorphization of the crystal.

It has been reported that no preferential surface disordering is observed in AlN upon implantation either at low temperatures or room temperatures, unlike the case of GaN where a preferential site is present for amorphization[183]. The damage produced by heavy ion bombardment increases with the ion dose, as in the case of diamond and reaches the randomized level at fluences of $\sim 10^{16}\ ions/cm^2$ for heavy ions, such as Au[183]. However, no saturation damage has been reported in AlN films upon high doses, meaning that even if upon high doses the crystal becomes heavily damaged it doesn't get amorphous like in the diamond case[10]. This result indicates extremely high radiation resistance (intended as the minimum amount of damage needed to amorphized the crystal) of AlN and a large mobility of ion-beam-generated point defects.

The effect of annealing on these highly damage regions is usually low, as it has been reported the use of RTA (Rapid Thermal Annealing) at temperatures of around 1000ºC for 1 min results in a negligible reduction of the ion-beam-produced disorder. Indeed, as a rule, temperatures of around 2/3 of the melting point are required to remove the ion-beam-produced extended defects in semiconductors, suggesting that temperatures of > 1900ºC may be needed to anneal out implantation-produced damage in AlN[183].

2.2.2 Electronic modification

As semiconductors, both materials' electronic properties can be modified by the introduction of dopants. These dopants can be introduced as ions into the crystal lattice and by several annealing methods they can be optimally activated, leading to both P and N doped regions in the material[167], [184], [185].

For diamond's case, the two most used dopants are B and P, for both P and N doping respectively. The fabrication of P type regions is achieving a maturity level[186] that allows for the systematic fabrication of devices, while in the case of N type regions the activation of P ions in the diamond as a dopant is still a challenge[187], [188]. Additionally, the fabrication of graphitic electrodes by high doses ion implantation allows for the electrical addressability of specific regions inside the diamond. These graphitic electrodes represent an electrically sensitive tool embedded in a biocompatible and inert material, that can be used for biosensing purposes[182], [189], [190].

On what regards AlN, the introduction of Mg dopants is extensively used for the fabrication of LEDs, by creating high performance P type regions[191]. Moreover, the high fluence implantation of AlN substrates has been studied to undergo a strain and compositionally induced polarity change, that leads to the piezoelectric coefficient decrease[192].

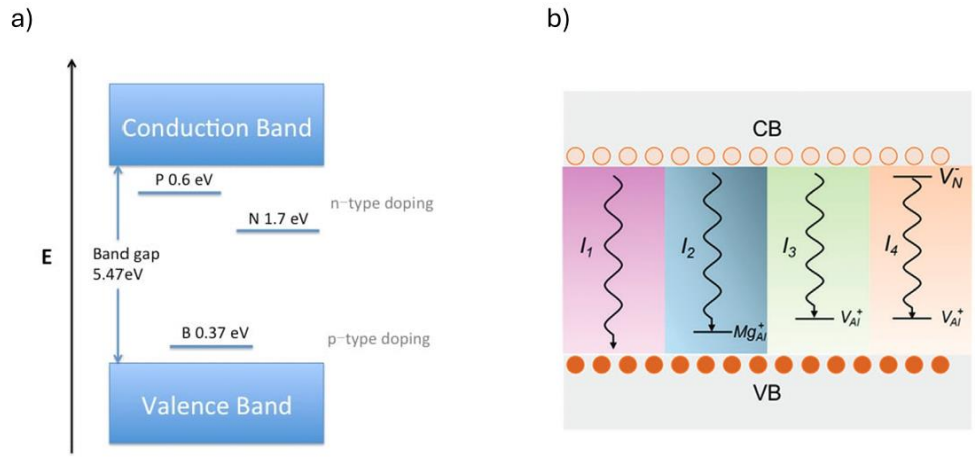

Figure 40 *a) Activation energy levels of the two most expanded dopants in diamond. b) Energy levels of the Mg dopant in AlN and the two types of single vacancies*[191], [193].

2.2.3 Fabrication of color centers

The creation of color centers in wide bandgap semiconductors can be achieved through ion implantation, as anticipated in Sect. 2.6 of Chapter 1. The process of defect engineering by ion implantation typically involves two subsequent steps: namely, the ion bombardment of the semiconductor, followed by activation through annealing treatment to correctly arrange the atoms in the lattice and form the emitting color center[194].

One key parameter when studying the fabrication of color centers is the number of ions that are introduced in the material per surface unit, or as it is usually referred to: 'fluence'. It can be experimentally expressed by[195]:

$$\Phi = \frac{\int I\, dt}{Q\, A}\ [cm^{-2}] \qquad \textit{Equation 25}$$

Where I is the current measured with the amperemeter used in the experiment, t is the time of the implantation, Q is the charge state of the implanted ion and A is the area of irradiation.

Typical fluences values for the functionalization of semiconductors range from 10^8 to 10^{18} cm^{-2}, depending on the purpose of the implantation. For the case of color centers fabrication usually lower fluences are used aimed for single ion implantation, however, as was discussed in Section 1.2.6, regarding the quantum sensing the use of high ensembles of color centers is sometimes required[138].

For the case of diamond, as one of the most extensively studied host platforms of color centers, the influence of different ion implantation fluences in the formation of single-color centers has been widely reported and analyzed[196], [197], [198]. Ideally, it would be enough to implant one ion per diffraction-limited spot (~10^8 cm^{-2}), however, up to now there has not been reported a 100 % efficiency of formation for any color center in diamond[52]. This means that it is necessary a combination of several ions in the same spot to form an isolated single emitter with adequate annealing conditions.[23]. On what regards the higher fluences ion implantation, it was already pointed out before, that the creation of too many vacancies may lead to the graphitization of diamond, so the creation of high-density ensembles of color centers is also a

challenge[199], because of the irreversible graphitization of the implanted region upon high fluences implantation.

On what regards the ion implantation of AlN for the fabrication of color centers, no extensive studies have yet been performed. However, a couple of them, one of which will be discussed in the results section of this thesis, have shown how the ion fluences that may lead to the creation of single emitters are between 2 and three orders of magnitude higher than in the case of diamond[122]. Additionally, the effect of annealing after ion implantation in these defects is still not fully understood, considering also the much higher mobility of defects and vacancies in this semiconductor with respect to diamond.

Fabrication challenges

On what regards the fabrication of color centers, many challenges must be overcome before the technology can be considered mature enough to be systematically and mass-produced.

One of the main objectives of the fabrication of color centers in semiconductors is the achievement of a deterministic process, meaning that both the number of emitters and the position within the sample should be controlled. In order to achieve this control over the fabrication of emitters, it is necessary to have a high efficiency of formation intended as the number of emitters created over the number of ions introduced in the semiconductor. Additionally, the number of ions that are introduced into the substrate should be measured in a precise way as well as the position of such ions in the substrate.

The fabrication process of color centers either in diamond or AlN, has still significant drawbacks at the state of the art that can be summarized as follows:

- *Low creation efficiency*. The efficiency of formation of color centers is reported to be very low, usually below 10%. This low conversion rate of individual impurities into structurally stable optically active defects requires the implantation of several hundreds of ions to form a single-color center. This results in a Poissonian-type uncertainty in the formation of the single emitters.
- *Ion straggling*. The interaction of the implanted ion with the atoms in the host lattice, leads to straggling of the impinging ion and so also some uncertainty in the position must be considered in this sense. The lowering of the implantation energy usually leads to the lowering of the straggling, and so a much more precise implantation.
- *Single ion implantation*. Low enough fluence implantations are achievable by employing the state-of-art ion implanters, being able to reach current in the range of fA. However, the single ion delivery needs for an accurate measurement of these low currents (which is still a challenge) and the precise position of the deliverable ion.
- *Single ion detection*. The measurement of a single ion is a very challenging technique, many techniques are being developed in the past decades, including the measurement before the implantation or inside the semiconductor by the induced charge of the ion (laborious in wide-bandgap semiconductors)

These challenges are currently trying to be overcome by the exploration of several techniques, some of which will be more extensively explained in the next section:

- *Hot implantation.* The heat-up of the host substrate while the implantation is being performed may lead to the increase in the formation efficiency, thanks to the movement of the vacancies while they are being created, that may lead to the decrease in the formation of clusters[200]. This technique will be extensively studied in this thesis, aiming to overcome the low creation efficiency of color centers.
- *Low energy implantation.* The use of low energy ions, as was anticipated before, corresponds to a smaller straggling of the implanted ions[194], which allows for much more precision within the semiconductor.
- *Focused ion beam (FIB) and nano masking.* The use of FIB ion implantation techniques allows for the nm scale precision (diminishing the effect of the ion straggling) in the ion beam

precision[201], [202], Additionally, the use of nanometric masks on the samples allows also for a high precision in the implantation. Still, these techniques need of improvement as it will be explained in the next section.

- *Single ion counting detectors.* The development of several detection techniques, such as charge imaged detectors, electron-hole pair detectors, and secondary electrons detectors, has marked a significant advancement in the field of single ion implantation. Some of these techniques are based on IBIC (Ion Beam Induced Charge) methods[203], while others rely on measuring secondary electrons produced by the ion impacting the substrate. Additionally, detectors like the charge image detectors are based on inducing a current as the ion passes through before the implantation. The single ion counting technology nowadays is much more mature for high-energy ions[204], [205]. This is in contrast to the use of low-energy implantation, so it is necessary to research single ion counting at low energies.

Many other challenges need to be overcome, still, the color center fabrication field can be considered as a quite studied field, with many ongoing research[61], [206], [207], [208], [209], [210] seeking for the repeatable fabrication of single emitters for the realization of the quantum technologies.

2.3 Implantation methods

In this section, we will provide a general overview of the types of implantations currently used for fabrication. Additionally, we will make an initial distinction between keV and MeV implanters.

2.3.1 Ion implanters – keV and MeV

The fabrication of color centers partially relies on the use of an ion implanter. The depth control of the implanted defects is a critical parameter depending on the application so different ion energies are required.

Independently of the energy, the main parts that constitute an ion implanter are:

- *Ion source.* The first part of an ion implanter is always the ion source. Generally, the different classes of ion sources do not depend on the energy of the ion implanter, but the final aim of the implanter may be an important factor in the choice of the source. Some sources are based on the production of plasma upon the introduction of a gas precursor, so only the gas-based elements can be accelerated (RF ion source in **Figure 41**.b)[211]. In other cases, both solid (upon pressing of a solid powder) and gas-based elements can be accelerated, but the limiting factor is the charge of the exiting ions (SNICS source in **Figure 41**.a), leading to only the creation of either negative or positive ions (as will be explained in Chapter 3, depending on the electronegativity of the atom, it is possible to form it as a negative or as a positive ion, but no both). The SNICS source will be described much more in detail in the following Chapter, as it is the base of the ion implanter mainly used for the development of the experiments. Apart from the presented ion sources in this section, many others are used both in industry and research such as laser pulsed sources, multipole

confinement sources, field ionization sources, surface ionization sources, arc discharge sources, etc[211], [212], [213], [214].

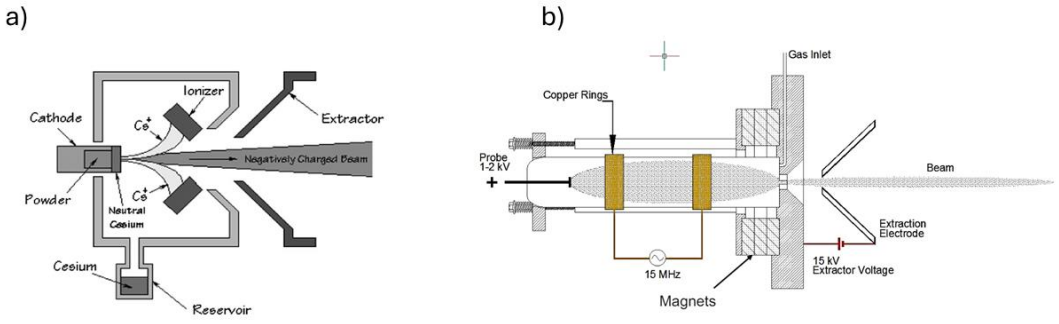

Figure 41 *a) SNICS source* [215] *b) Radio Frequency ion source.*

- *Acceleration stage.* This element is the one that determines whether a high energy or low energy accelerator has been considered as it is where the energy of the ions is set. Regarding the lower energies accelerators (<200 keV), it is mainly based on what is usually referred to as electrostatic accelerators while in the higher energies range the most extended is the tandem accelerator [211].

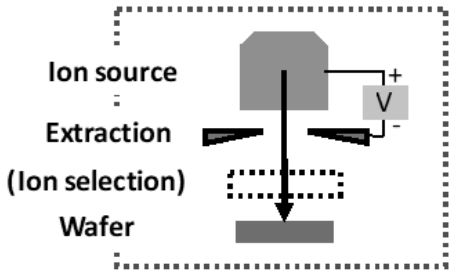

Figure 42 *Single stage acceleration implanter*[211]

- *Mass spectrometer.* Generally, more than one ion species extracted from the source is accelerated at the same time. Therefore, it is then important to have a tool that allows the selection of the ion desired as projectile. This selection process is based on the Lorentz law, and it is usually achievable by the use of tunable magnets in current[211].
- *Focusing elements.* They are usually magnetic lenses based on quadrupoles or octupoles, aiming to adjust the ion beam divergence and direction[211]. They will be extensively explained in the ion implanter section 3.1.

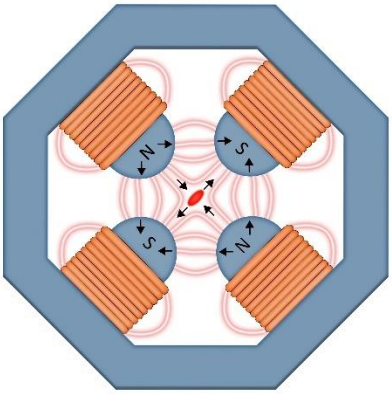

Figure 43 *Quadrupole scheme.*

- *Steering elements.* As in the case of the focusing elements, these steerers are based on magnetic or electric fields that allow the deviation of the ion beam as desired. These steering elements aim to correct the deviations of the beam inside the beamline to carry it towards the irradiation chamber, where the implantation takes place. They can also be used as scanning elements, lowering the need for mechanical positioners.

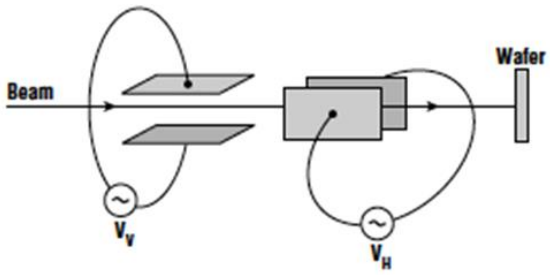

Figure 44 *Electric steerers' diagram*[211].

- *Ion beam monitoring elements.* The ion monitoring elements are a crucial part of the beamline of an ion implanter as they allow for the aligning of the ion beam and the correct focalization of it, in addition to giving the ion current that is being delivered to the target. The most common tool for the measure of the ion current in the beamline is the Faraday cup, which consists of a metal cup that is connected to an amperemeter [216]. Other type of monitoring elements are sometimes used, such as silicon diodes[217] or scintillator monitor systems[218].

The previously explained elements are as has already been pointed out common to most ion implanters and they will be extensively explained in the experimental methods Chapter, as part of the 100 keV ion implanter section 3.1.

Nevertheless, it is important to properly present the two main type of ion implanters that have been employed in the experiments of this thesis, the keV and the MeV.

keV implanter

The ion energies required for the realization of a keV ion implanter are mainly obtained with electrostatic accelerators. The high voltage is usually generated with a Cockroft-Walton generator in which low AC voltages are converted to high DC voltages by means of a series of diodes and capacitors[211].

In the case of low energy ions, the most common schemes of accelerator that are usually employed are the ones shown in **Figure 45**: either there is just one acceleration stage after which the ion selection and the implantation takes place, or a second acceleration/deceleration stage takes place after the ion selection. This second arrangement is common when the required implantation energies are around 1 keV or less.

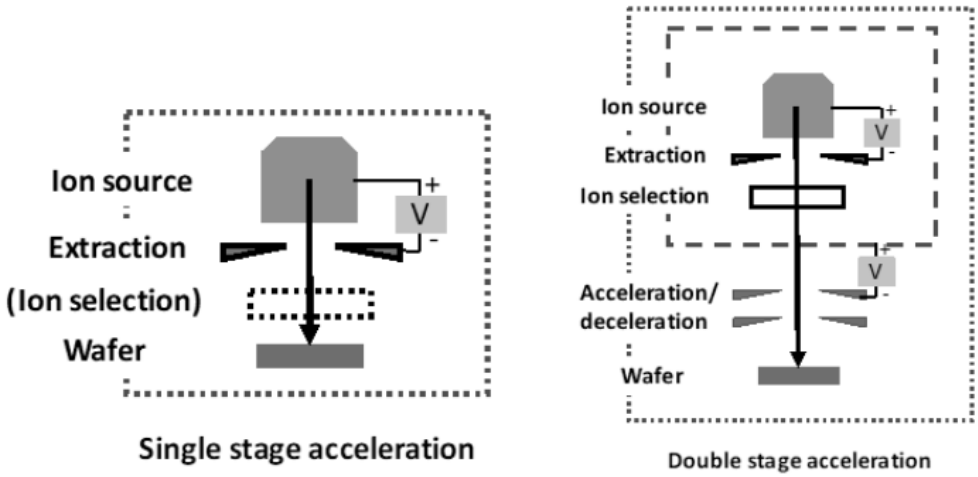

Figure 45 *Sketch of the major elements of a single and double stage acceleration beam lines*[211].

Most of the experiments that were carried out during this thesis were performed using two different 100 keV ion implanters, whose acceleration stage was based on an ion source connected to an extractor, followed by a higher acceleration stage, after which the ion selection was carried out (unlike in **Figure 45**b, where the ion selection is performed before the second acceleration stage). The use of a double-stage acceleration has the advantage of allowing to change the energy without sacrificing the extraction of ions from the source, which is more sensitive to the extraction and cathode voltages[219], [220]. This type of accelerator, including the physical working principle of each of its components, will be explained in the next Chapter.

The use of these types of implanters for the fabrication of color centers can be considered as widely applied technique. The ion implantation technique allows for ion implantation resolutions down to 50 nm[194]. Regarding the dependence of the ion straggling with the energy of the ions, low energies are needed to improve the spatial resolution in the defect localization. However, it has been proved that in general the creation efficiency as well as the coherence of the shallows centers is usually lower that the deep ones because of the effect of the surrounding surface[221], [222], [223]. The exposure of the surface to functionalization treatments along with some highly invasive annealing techniques, such as HPHT, that me damage the surface, show the necessity of using higher energies implantation, more in the MeV range for some specific applications.

MeV implanter

To achieve higher implantation energies, the use of MeV implanters is required. For few MeV acceleration energy, the use of a Van de Graff accelerator is sufficient[219]. However, if higher energies want to be achieved either a LINAC (linear accelerator) or a Tandem one is needed (the sketches are shown in **Figure 46**)[211]. Among these two, only the second one was employed for the carrying out of experiments related to this thesis. Therefore, it will be explained in detail in the following.

A Tandem accelerator is based on extracting positive or negative ions using one of the previously presented sources. The ions are then either stripped of electrons or charged to reach the opposite charge of the initial one before undergoing another static acceleration. The most commonly used technique involves a charge exchange section where gas is present[224] . In these types of accelerators, multiple charge states are

usually present after the exchange, resulting in a wide energy spectrum for each element. However, lighter elements have fewer available charge states, making tandems less effective when accelerating them [224] .

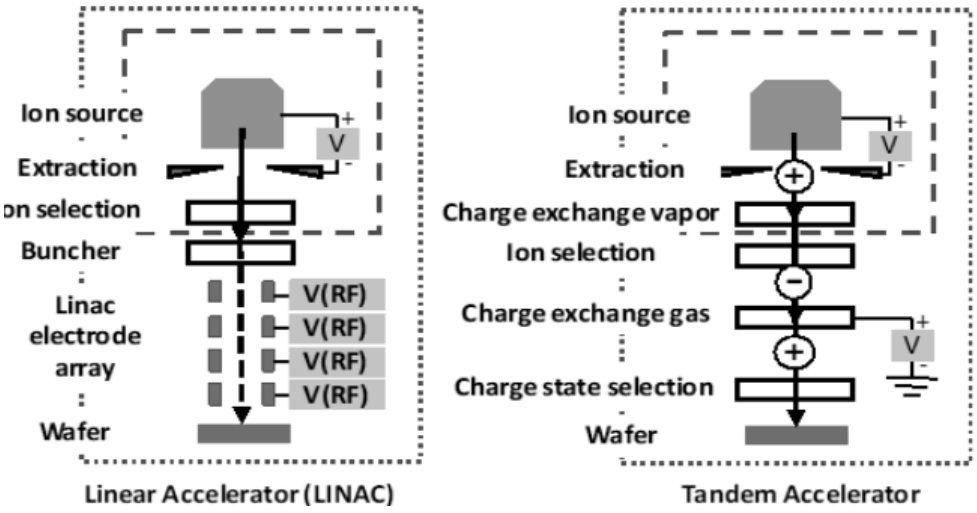

Figure 46 *Sketch of major elements of two MeV types of accelerators: LINAC and Tandem*[211].

As anticipated before the use of MeV accelerator for the formation of color centers may present some drawbacks regarding the positioning, it is important for the achievement of deep emitters and when the sample has to undergo extreme invasive post-implantation treatments. In this thesis, the tandem accelerator located at the Laboratory for Ion Beam Interaction of the Ruđer Bošković Institute (Zagreb) was employed for the study of hot implantation effect on the formation of color centers.

2.3.2 Ion implantation techniques

After the explanation of the basic parts of an ion implanter have been explained and the differences between keV and MeV acceleration have been reported, some of the most widely employed techniques for the localized creation of defects will be presented in this section. Depending on the type of beam that is being employed they can be classified in two different types: broad beam implantation and focalized ion beam techniques.

Broad beam techniques

In this case, the broad beam ion technique refers to the use of few focalizing elements in the beamline that results in a broad beam delivered to the irradiation chamber where the target is usually mounted[225], [226]. When this is the case, it is a widespread technique to use several masking techniques either before the sample or on top of the sample[85]. Several other innovative techniques have been reported in the last decades such as the use of AFM tips[206]. The use of these tools leads to much more simplicity in the preparation of the ion beam by sacrificing in some cases accuracy[85]..

The collimated beam technique is a widely extended technique based on the positioning of a mask in front of the sample or on top of it, thick enough not to let the ions pass through it where the holes are not present. The collimated beam technique can be implemented with the use of several masking tools, explained in the following.

Micrometer-sized foil masks

The use of micrometer-sized foil (i.e. aluminum foil) is based on the placement of this mask close enough to it, so the straggling of the ions in the mask doesn't lead to the irradiation of a much wider region on the sample.

These types of masks can be mounted on piezoelectric nanopositioners allowing for high-precision patterns on the sample irradiated[74], [85], [122], [227]. Regarding the implantation of ensembles of color centers, it can be considered one of the most widely used techniques and it allows normally even in the high fluences case for the individualization of single emitters in the edges of the regions implanted[228], because of the straggling of the ions with the mask. It is not the most precise technique so far studied for the fabrication of single-color centers, however, it allows for the easy and low time-consuming fabrication of ensembles and provides a useful tool for the exploration of new color centers. This technique is the one adopted for the majority of the experiments carried out in this thesis and an example of an implantation using it is represented in **Figure 47**.

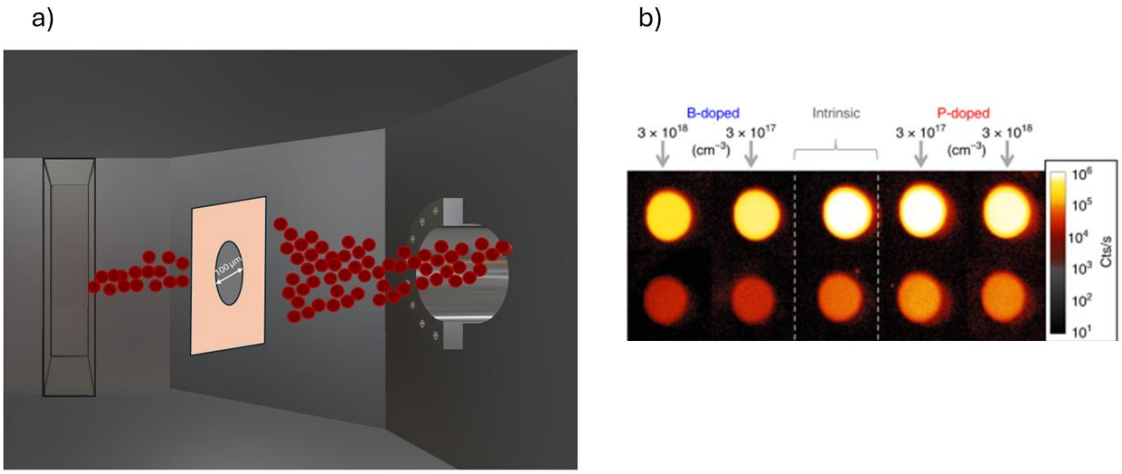

***Figure 47** a) Sketch of collimated implantation using a broad beam. b) Example of N implanted regions in diamond using a system similar to a)*[85].

PMMA nano masking

This technique consists on the ion implantation though an array of apertures that was patterned in a PMMA layer initially deposited on top of the host substrate[229]. It allows for the parallel implantation of any impurity inside a large number of targeted spots, with a resolution defined by the diameter of the aperture. This diameter is always limited by the energy of implanted ion, mainly because the higher the energy the thicker the PMMA substrate has to be to avoid the implantation of the target outside the holes and the thicker the PMMA the larger the holes need to be (limiting of the electron beam lithography that is usually employed for the hole making)[230] . In **Figure 48** an example of the creation of single NV spots created by the patterning of 80 nm diameter holes is reported, by analyzing the PL map after the irradiation, **Figure 48** f, it can be seen how this approach results in a statistical process, because not every aperture will receive the same amount of ions as the beam used is considered as a Poissonian beam and is measured in a much wider surface. This can be considered as the main drawback, nevertheless, it has proved to be a useful tool for the repeatable fabrication of color centers in different semiconductors with nm scale resolution, especially in the keV range[229], [231].

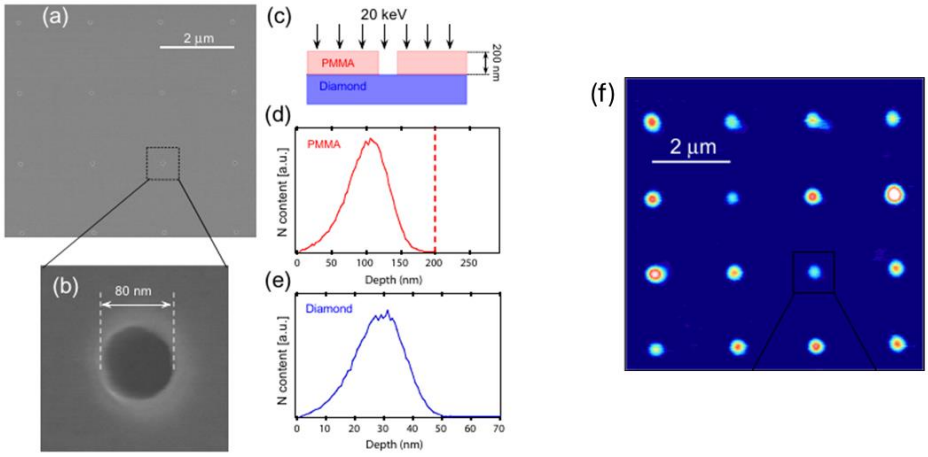

Figure 48 *a) PMMA pattern optical image, b) zoom in one of the holes fabricated with EBL, c) implantation scheme, d) SRIM simulation of the ion range in PMMA, e) SRIM simulation of the ion range in diamond, f) PL map of the fabricated spots*[198].

AFM tip

This technique was first reported in 2008[194] and it allows for the mask-less implantation of single ions at low kinetic energy with nm resolution. It is based on the use of a FIB pierced AFM tip, that acts as a collimator system in the nm range. The spatial resolution of the implantation is given by the size of the hole and they usually can go down to 30 nm diameter, giving even a better resolution than the previously exposed method. However, the complexity of the system may represent a problem, in addition to the coupling of the source to the implantation system that leads to the limitation of both the ion availability and the energy of it, which is so far limited to a few keV. In **Figure 49**, the experimental setup used to carry out this first experiment back in 2008 is represented along with a STED map of the centers created[194], [232].

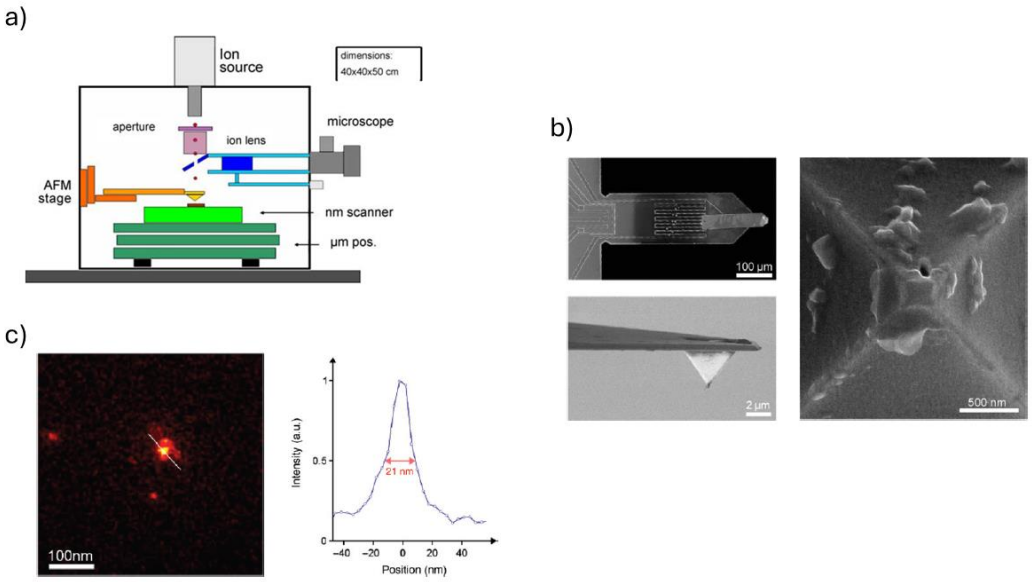

Figure 49 *a) Sketch of the ion implantation set-up, b) AFM SEM images including the tip, c) STED map of the centers created*[194], [229]

Focused beam techniques

The use of focalized beams for the localized fabrication of color centers in wide bandgap semiconductors is increasingly being implemented in the research field. Both keV and MeV ions can be focalized, but the minimum dimension that can be achieved depends on the type of ion that is accelerated and its energy. The magnetic rigidity R [233]:

$$R = B\rho = \frac{mv}{q} \qquad \textit{Equation 26}$$

Where B is the magnetic field and ρ is the radius of curvature of the ion. The magnetic rigidity depends on the mass m of the ion, its velocity v, and its charge state q. This parameter is a measure of how difficult it is to bend charged particles through a given radius in a magnetic field[233]. Considering this parameter, the explanation can be divided into two different ranges, the keV and the MeV.

Focused keV ion beams (FIB)

The FIB implanter are usually working at low energy values, between 25 and 50 kV. This technique is widely known for the fabrication of nanostructures in different materials, mainly by the use of a Gallium source[233]. However, recently the scientific community has started to implement its use for the fabrication matrixes of color centers with nanometric precision [137], [196], [201], [202], [222].

A representative schematic of the internal parts of a FIB machine is represented in **Figure 50**b. In this case the ion source is typically a metal ion source (LMIS)[234], which is composed of a tungsten needle towards which the heated metal melts. From there, the ions are extracted and lead into the focusing part. In some cases the FIB column is provided with a Wein filter that allows to perform the mass selection and the charge state selection[233]. Once extracted the beam passes through different electrostatic lenses that aim to define the beam size and focus on the target. The readback of the current is usually performed in a Faraday cup, while the imaging of the sample can be done either optically or by SEM technique (see **Figure 50**c) as the FIB is commonly combined with a SEM system. This technique has achieved beams' spot sizes in the order of 10-100 nm, in line with what has been achieved for some of the other abovementioned techniques, in terms of resolution (nano masking and AFM tips)[196], [235].

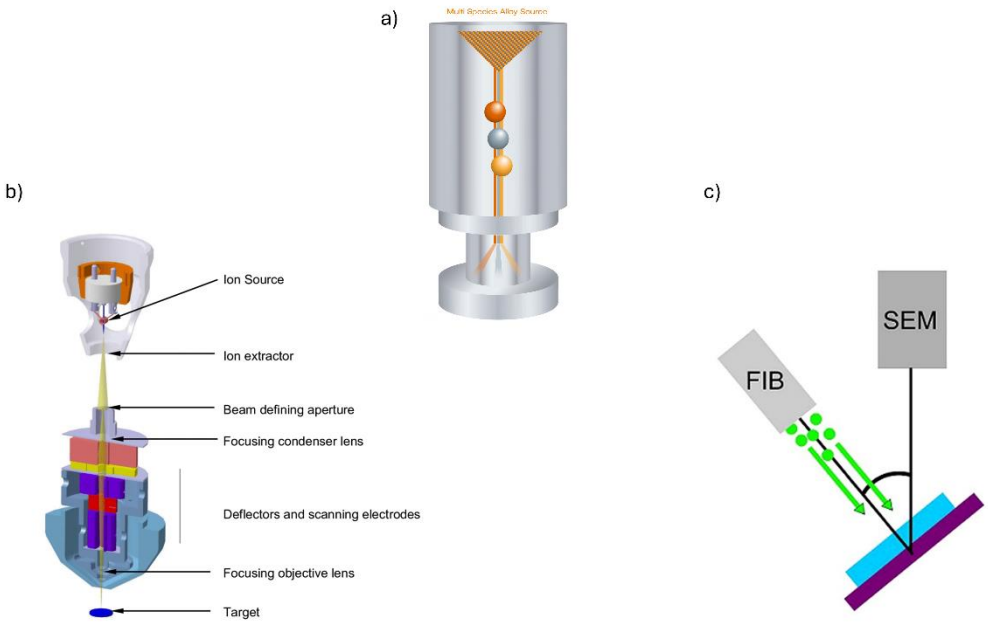

Figure 50 *a) Metal-alloy source scheme of a FIB b) Column sketch of a FIB*[236] *. c) FIB and SEM combination schematics*[237]

Another important advantage that this technique presents is the possibility of easily reaching single ion implantation, by lowering the ion current, in addition to the extremely spatially resolved implantation[222], [238]. However, the fabrication of repeatable arrays of single emitters in semiconductors with this technique is still under study, many emitters have already been fabricated meanly in diamond and silicon. The small availability of ion species and the challenging focalization of some ions species, place this technique as an interesting technique for the fabrication of single emitters, although research must still be carried out in this field.

Focused MeV ion beams (Nuclear Microprobe technology)

On what regards MeV focused ion beams, the main parts of the accelerator have been already explained in Section 2.3.1. In contrast to the FIB case, for the Focused MeV ion beam the accelerator must be a tandem accelerator with a dedicated ion beam.. In this specific case, the difference relies in the introduction of a quadrupole triplet before the sample (see **Figure 51**) that allows for the focusing of the beam[233]. Because of the high ion momentum, the same magnetic solenoid lenses used in the FIB case are not sufficient to bend the ion trajectory. The quadrupole lenses have much stronger focusing action, but this technique requires greater lens complexity and difficulties of construction to the required precision.

The working principle of three consecutive quadrupoles lies on the combination of focusing and defocusing effects of the sequence of the three magnetic lenses that allows for the minimization of the beam spot size. This types of implanters are widely used for ERDA, IBIC, STIM and many other ion beam analysis techniques[239], [240], [241] and are currently being implemented for the fabrication of color center[236]s. The main drawback is that the energy of the ions leads to a larger beam spot size compared to the use of keV FIBs. Additionally, the majority of ions used for the fabrication of color centers are not light ions such as H or He, which further degrades the resolution limit[194].

Still, dimensions of less than 1 μm^2 can be routinely achieved at several facilities worldwide, [242] , however the intrinsic straggling related to the use of high energies inside the substrate is still a drawback of this technique.[194], [205], [243].

The use of focused MeV ion beams is sometimes combined with the steering elements of the beamline in order to perform scanning patterns in the sample irradiated, to define homogeneous irradiation areas[244], [245]

On what regards the experiments carried out for this dissertation, the microbeam facilities of Ruđer Bošković Institute were used for the fabrication of both NV and MgV centers, allowing for the maskless fabrication of color centers.

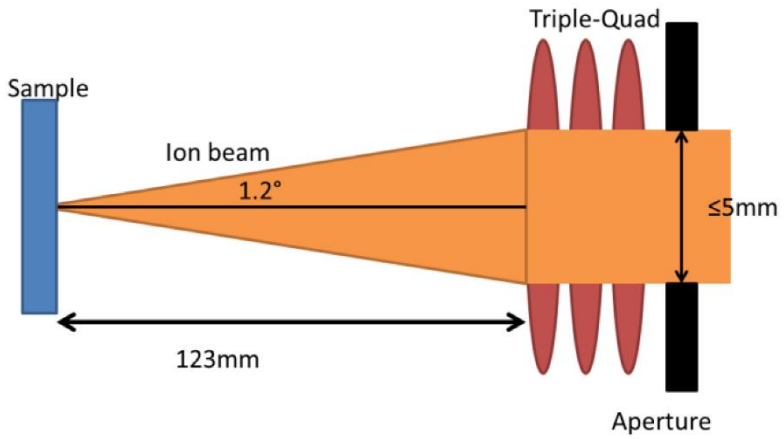

Figure 51 *Quadrupole triplet for microbeam techniques*[246].

In this section, we discussed some of the most common techniques for creating color centers through localized fabrication. However, it's important to note that these techniques may not guarantee the delivery of just a single atom. Therefore, it's crucial to consider detection techniques, as well as specific methods

for isolate single ions, such as Paul's trap[247]. However, delving into these specific techniques is beyond the scope of this thesis.

2.4 Activation methods

The fabrication of color centers via ion implantation in wide bandgap semiconductors is based in two different processes: the ion irradiation and the subsequent annealing treatment. The different types of ion implantation techniques have been discussed in the previous section. The main different types of annealing treatments that have been commonly explored for the activation of color centers, mainly in diamond and AlN, are analyzed separately in the following. Different annealing treatments or different parameters of the same treatment might lead in fact to different results regarding the formation efficiency of center (number of centers formed per number of ions implanted), their quantum properties and stability, among other properties.

2.4.1 Furnace annealing

Thermal annealing has historically been the most used method to activate dopants in semiconductors. Similarly, after ion implantation, color centers typically require thermal energy input to move vacancies and set the optical centers in their most stable configuration[122], [248].

Upon the ion irradiation, the lattice structure can get damaged. To fix this, high temperatures are used to repair the lattice. Furnace annealing is a technique where samples are heated to temperatures between 300-1500 ºC (i.e. in the diamond case) in controlled atmospheric conditions, for a long amount of time, usually from 30 min to a few hours[47].

When annealing diamond, it is common to use furnace annealing in high vacuum conditions ($< 10^{-6}$ mbar) to prevent impurities from reacting with the diamond surface and causing damage. Color centers in diamond are activated at temperatures above 600°C[249], as this is when vacancies in diamond become mobile. It's important to consider the phase diagram of diamond, as beyond a certain temperature, it begins to turn into graphite, making low pressure high temperature a concern, as can be pointed out in the phase diagram in **Figure 20** of Chapter 1. In general, thermal annealing below 1500°C is feasible under these conditions for a couple of hours without risking the integrity of the diamond.

As for the efficiency of activating color centers in diamond through this type of annealing, in general the increasing of the temperature of annealing leads to an increasing in the stability and formation of centers. However, this *optimal temperature* is dependent on the type of center that want to be formed, for NV center is usually between 1200-1300 ºC[250], for centers such as ST1 temperatures below 1000 ºC [251]are needed and in the case of larger nuclei such as the majority of Group IV centers higher temperatures are needed to repair the lattice and make the centers indistinguishable[75].

For AlN color centers the studies so far reported on this topic are not sufficient to understand the effect of this treatment, however during one of the works that are presented in this thesis this technique was employed for the annealing between 300 and 700 ºC of the implanted AlN samples with a successful result[122]. These annealing treatments were performed in an N_2 atmosphere, based on several works that state the convenience of performing AlN films high-temperature annealing in a controlled N_2 atmosphere to properly repair the lattice and promote the nitridation of the AlN outer surface, reducing the vacancies.

An example of a furnace annealing set-up is presented in **Figure 52**. It usually is based on a plate that is heated by the flow of an electrical current through a resistance. The heating component is located inside a sealed chamber in which the atmosphere can be controlled. In the left part an inert gas feed for processes in controlled atmosphere is represented, while in the right part the working principle of high vacuum annealing is represented. It should be highlighted that for reaching the high vacuum conditions, not only a scroller pump is needed but also a turbomolecular pump is required.

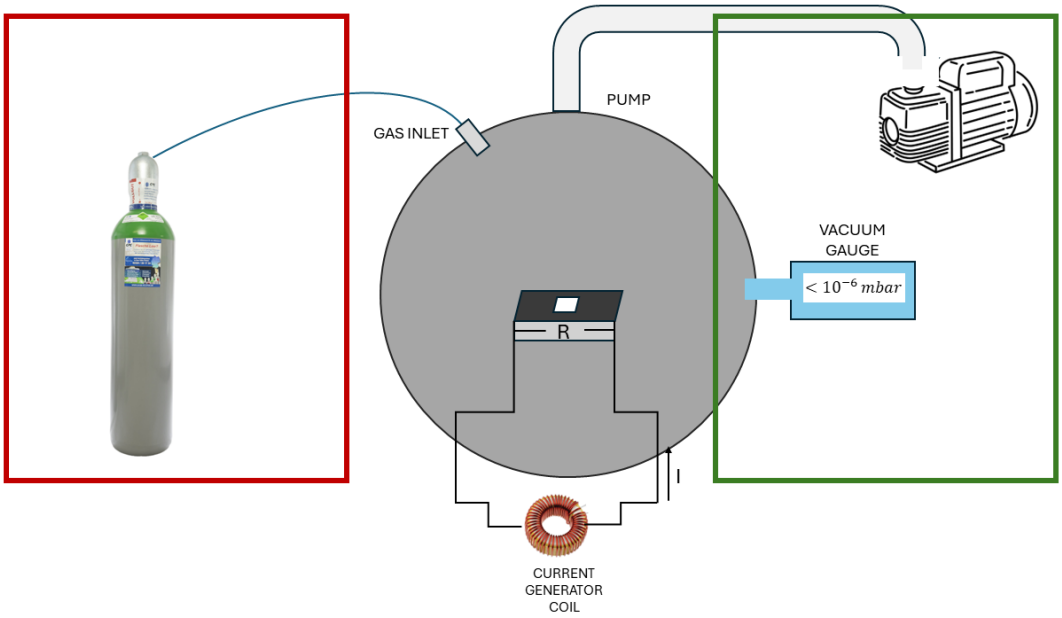

Figure 52 *Furnace annealing schematics, red squared part regards the controlled atmosphere with an inert gas, while green surrounded is the case in which high vacuum conditions are present.*

2.4.2 RTA (Rapid Thermal Annealing)

The Rapid Thermal Annealing, typically referred as RTA, is based on the limitation of the exposure time to heat of the sample. The exposure times usually are in the millisecond and second range[252]. It is also possible to heat for longer periods of time and just perform the ramping up and down in the seconds range, to guarantee the annealing at a fix temperature (not as in furnace annealing that usually heats slowly up). This technique is widely used in the activation of dopants in the silicon industry[252], among other semiconductors, to prevent the diffusion of dopants due to their high mobility in the substrate[252], [253], [254].

In the case of diamond, considering the low diffusion coefficient of the impurities, it is usually not employed, based on the absence of advantages shown with respect to the common furnace annealing.

However, regarding other type of platforms, as anticipated before, the diffusion of the defects may play a key role. The RTA treatment is it is widely used for the activation of implanted atoms and activation of color centers and electrical dopants [89], [113], [114], [253].

In **Figure 53** an image of an RTA chamber is presented[255], in this case, the heating processing occurs thanks to the exposure to an IR lamp, for few seconds up to temperatures of 1200 ºC. The atmosphere in this case is usually an inert gas such as Ar or N, although it can be also performed in high vacuum conditions.

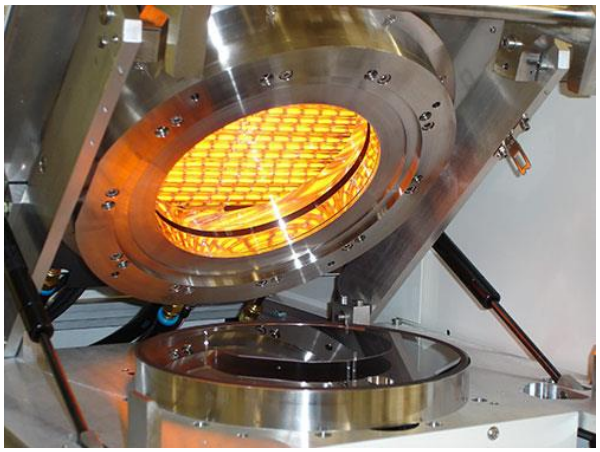

Figure 53 *RTA processing chamber*[255].

2.4.3 High- Pressure High-Temperature (HPHT)

The treatment is based on the natural conditions in which a diamond is formed (see **Figure 20** in Chapter 1). As was explained for the furnace annealing, high vacuum conditions are only an optimal activation method below a certain temperature threshold around 1500 ºC, because above that temperature the phase transition promotes the formation of the graphitic phase or carbon below the diamond one[256]. In addition, the HPHT annealing condition is located in the thermodynamically stable region for diamond in the diagram phase and is, therefore, much more efficient for the recovery of implantation-induced damage and for the activation of ion-implanted dopants than thermal annealing in vacuum.

It is so based in the introduction of the diamond in a press at pressures at above 5 GPa and temperatures usually above 2000 ºC. However, the process is affected by the challenging control of the surrounding atmosphere and the presence of unwanted impurities in the press anvils, which could lead to the formation of inclusions or specific defect classes. Moreover, the diamond is usually damaged after this process and its roughness increases, which may lead to the necessity of further polishing with the removal of surface layers. This damage produced in the first surface layers of the diamond might prevent the keV implantation from being effective, as it can lead to destroy of the diamond part where the defect is fabricated.

This necessity depends usually on the final purpose of the centers, in the case of quantum technologies it is usually crucial to have the best surrounding environment and accessibility to the center possible. Based on these drawbacks, the most adopted technique for the fabrication of the centers that later will undergo a HPHT treatment is the use of high energy ions, to separate them from the surface. Another more recent technique is the use of keV ions and the overgrowth of cvd diamond on top of the implanted layer[257], before performing the HPHT treatment.

In general, this technique is used just for the activation of large nuclei, such as the majority of Group IV because it allows for the stabilization of the ion the right split vacancy position and the properties of the centers formed improve, as it will be shown in the results section[74], [80], [84].

In addition, it allows for the anneal out of some impurities in diamond thanks to the high temperatures, for example nitrogen, making the concentration of native color centers in diamonds much smaller after HPHT annealing.

In **Figure 54**, an example of a BARS HPHT press is shown[258] . The system is based on two stage compression mechanisms: a set of six anvils (usually made of tool-steel) distribute force on the faces on a cubic arrangement of eight corner truncated cubes (made of tungsten-carbide). These cubes are the ones that press the diamond making it undergo pressures in the order of 5 GPa (up to 25 GPa)[258].

Figure 54 *Mult anvil HPHT press* [258].

2.4.4 Hot implantation

Hot implantation of dopants is a well-known technique in the silicon industry as a way to improve the performance of the doped region in semiconductors[200].

Bearing in mind this improvement in the performance of the fabricated doped regions of semiconductors, it seems like a straightforward process to try to apply it to the formation of color centers. Although contemporary reports have reported similar results regarding the NV center formation[259], in this dissertation work the novel results on formation of NV and MgV center upon hot ion implantation at MeV energies will be presented in the results Chapter.

The improvement obtained with this technique is supposed to arrive from the possibility of moving the vacancies and defects created in the irradiated substrate at the same time they are been created.

In this case, both the furnace annealing setup and the ion irradiation chamber are combines in high vacuum conditions and usually the sample is attached to a ceramic heater that is powered with a current generator.

2.4.5 Laser annealing

Laser annealing based on femtosecond and nanosecond lasers is a widespread technique for repristinating irradiated semiconductors such as silicon and silicon carbide[260], [261], [262]. Additionally, the successful creation of color centers in semiconductors based on the irradiation with the femtosecond laser has already been demonstrated, as discussed in the first Chapter. This process involves creating vacancies in the crystal structure, which then combine with impurities already present in the material. Subsequent thermal annealing leads to the formation of color centers.

On what regards the laser annealing used for the formation of color centers; it is mainly based on the localized heating of the material in a previously implanted region. The differences in thermal capacity and diffusion coefficient in the target material led to the use of different lasers for this purpose[262].

So far, the most widely employed laser for the activation of color centers in semiconductors is the femtosecond laser[263], however, the use of nanosecond ones has recently shown really good results for the activation in silicon of IR emitting color centers[106].

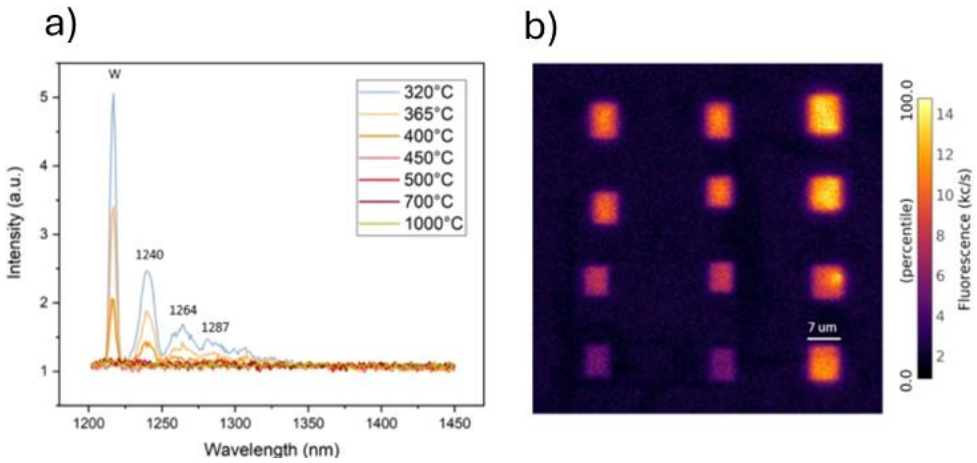

Figure 55 *a) Spectrum of laser-activated spots. b) PL map of laser-activated spots in silicon* [106] .

The laser annealing activation provides a useful advantage for the localized activation of color centers, avoiding treating the whole substrate. It allows additionally for the diffraction-limited activation, which may lower the need for single ion implantation. Considering an activation efficiency of implanted centers upon laser annealing much lower than 100 %, the activation of a single diffraction-limited spot (in the middle of a ensemble implantation) that can be individually assessed may simplify the process with respect to the localized single ion implantation of defects. However, the use of this tool has so far not proved the activation of all color centers, for example in diamond and the correct parameters need to be investigated[263]. On what regards AlN, the heating of the substrate for activation of color centers has not yet been reported.

Chapter 3

In this Chapter, an introduction to the most relevant scientific instrumentation developed and exploited in the course of the PhD activities will be presented.

In particular, the setting up and commissioning of the 100 keV ion implanter at the Department of Physics of the University of Turin will be discussed in detail. The working principle of each of its components will be presented, to highlight the features that the facility offered for the deployment of several of the experiments presented in Chapter 4. As part of the fabrication process, the annealing furnaces used for the fabrication of color centers will be also introduced, together with the nanosecond high-power laser that was employed for the realization of implantation masks.

Finally, an overview of the of the main characterization technique adopted for the optical characterization of point defects, photoluminescence confocal microscopy, will be presented.

3.1 Setting-up of a 100 keV ion implanter

During the PhD period, the setting up of a 100 keV ion implanter at the University of Turin was carried out, aiming to explore the effect of ion implantation in different materials. This ion implanter allowed for the implantation of many semiconductors and the fabrication of several color centers, that will be explained in the results section of this dissertation.

This 100 keV ion implanter, is an electrostatic accelerator based on an SNICS (Source of Negative Ion by Cesium Sputtering) source connected to an acceleration stage that increases the ions energy up to 115 keV. The selection of the implanted ion is performed through a mass spectrometer based on a 90º magnet. Several steering and focusing components allow for the beam transport to the irradiation chamber, where the samples are implanted. Each of these elements will be explained in detail in this section. In **Figure 56**, a 2D model of the ion implanter is represented, including all the parts that will be described.

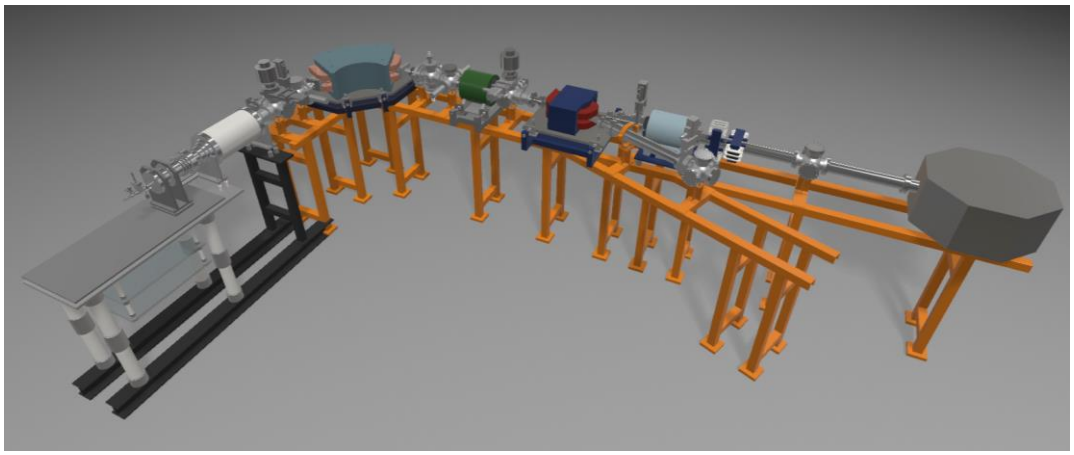

Figure 56 *2D representation of the 100 keV ion implanter at the University of Turin*

3.1.1 SNICS source

As was presented in Chapter 2, a central part of an ion implanter is the source of ions, as it determines the species that can be extracted, the efficiency of extraction of these ions, and their charge state.

The SNICs, Source of Negative Ions by Cesium Sputtering, is a source of negative ions [212]. The working principle of this ion source can be explained by looking at **Figure 57**. It is composed by a cesium reservoir that is heated up to around 140 ºC to evaporate the Cs into the source chamber. As it evaporates, a thin layer

is deposited on top of the cathode, as neutral Cs. Part of the Cs reaches the ionizer that is formed by two hot plates (heated by the pass of currents around 20 A), and it ionizes as Cs^+ by contact with these plates. These positive ions are then attracted towards the cathode which is polarized at a negative voltage of maximum 6 kV (for this specific implanter), and it is based on a copper cylinder into which the powder of the desired element for the implantation is pressed. Considering the high temperatures that this cathode can reach inside the chamber, it is connected to a petrol cooling system in order to prevent its melting inside the vacuum chamber. Due to its negative polarization, the cathode is bombarded by positive Cs^+ ions that are attracted towards it, resulting in the sputtering of negative ions of the pressed material that is present inside the cathode cylinder. The extracted negative ions are then accelerated by the positive extractor voltage which is around 10 kV allowing the extraction of much more current of ions from the ion source to the subsequent acceleration stage.

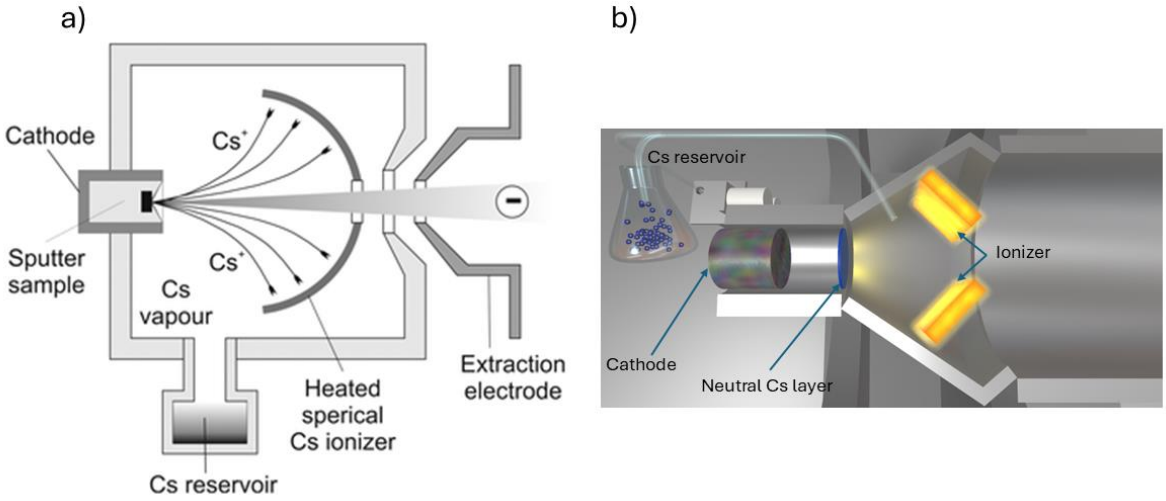

Figure 57 *a) SNICS source working principle, b) 2D scheme of the source at the University of Turin*

Based on the operational principle of the SNIC source, where the electron added to cathode atoms in order to create negative ions comes from the charge exchange with Cs, it can be pointed out how the maximum charge state of the ions produced is -1.

Each element in the periodic table has a characteristic parameter that allows to distinguish the feasibility to produce a negative ion out a neutral atom, such a parameter is the binding energy of the added electron or the so-called *electron affinity*[264]. This affinity must be positive in order to form a metastable negative ion state. In **Figure 58** the ionization potential and the electron affinity of some elements of the periodic table are presented, in particular, the ones surrounded by a red circle are the ones that cannot be accelerated as single negative ions. However, many of these ions can be accelerated as negatively charged molecules, which might be interesting from the acceleration point of view, as several elements can be implanted at the same time.

IA	IIA	IIIA	IVA	VA	VIA	VIIA	VIIIA
$_{1}$H 13.59 0.754	Ionization Potential Electron Affinity						$_{2}$He 24.48 0.078*
$_{3}$Li 5.39 0.618	$_{4}$Be 9.32 0.195*	$_{5}$B 8.30 0.277	$_{6}$C 11.26 1.263	$_{7}$N 14.53 -0.07	$_{8}$O 13.61 1.461	$_{9}$F 17.42 3.399	$_{10}$Ne 21.56 < 0
$_{11}$Na 5.14 0.548	$_{12}$Mg 7.64 < 0	$_{13}$Al 5.98 0.441	$_{14}$Si 8.15 1.385	$_{15}$P 10.48 0.747	$_{16}$S 10.36 2.077	$_{17}$Cl 13.01 3.617	$_{18}$Ar 15.76 < 0
$_{19}$K 4.34 0.501	$_{20}$Ca 6.11 0.043	$_{31}$Ga 6.00 0.30	$_{32}$Ge 7.90 1.2	$_{33}$As 9.81 0.81	$_{34}$Se 9.75 2.021	$_{35}$Br 11.81 3.365	$_{36}$Kr 14.00 < 0
$_{37}$Rb 4.18 0.486	$_{39}$Sr 5.70 < 0	$_{49}$In 5.79 0.3	$_{50}$Sn 7.34 1.2	$_{51}$Sb 8.64 1.07	$_{52}$Te 9.01 1.971	$_{53}$I 10.45 3.059	$_{54}$Xe 12.13 < 0
$_{55}$Cs 3.89 0.472	$_{56}$Ba 5.21 < 0	$_{81}$Tl 6.11 0.2	$_{82}$Pb 7.42 0.364	$_{83}$Bi 7.29 0.946	$_{84}$Po 8.42 1.9	$_{85}$At 9.5 2.8	$_{86}$Rn 10.75 < 0

Figure 58 *Ionization potential and electron affinity of some elements in the periodic table*[264].

In **Figure 59**, a picture of the SNICS source of the ion implanter that was set up at the Department of Physics is presented. The cooling tubes connected to the cathode are visible at the left part of the picture, the cathode is only partially visible as its main volume is installed inside the chamber in high vacuum conditions. The Cs reservoir is shown in the bottom part and the extractor in the left side of the source picture. Next to the extractor, the source contains also a focusing Einzel lens that allows for the focusing of the beam into the magnet. Both the extractor and focus are inside the vacuum chamber, however, what is visible from outside are the resistors that allow for their powering.

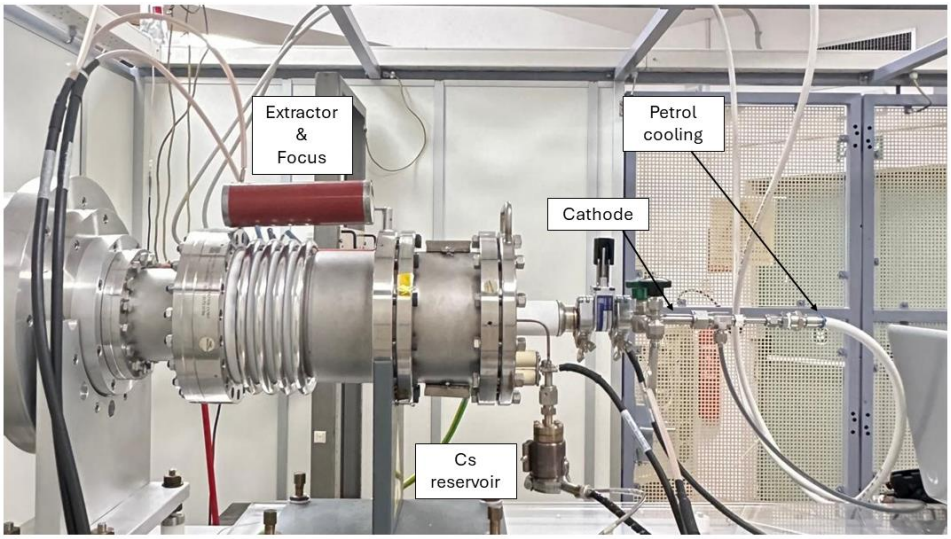

Figure 59 *Picture of the source of the ion implanter with the names of the main visible parts.*

After the ions are produced in the SNICS source, they can be accelerated up to 115 keV, for this purpose the acceleration tube presented in **Figure 60** is necessary. A difference in electrostatic potential is generated between the two sides of the accelerating tube, which allows for the introduction of the ions at a given energy, given by the sum of the cathode potential, the extractor potential and the high voltage one, into the beamline.

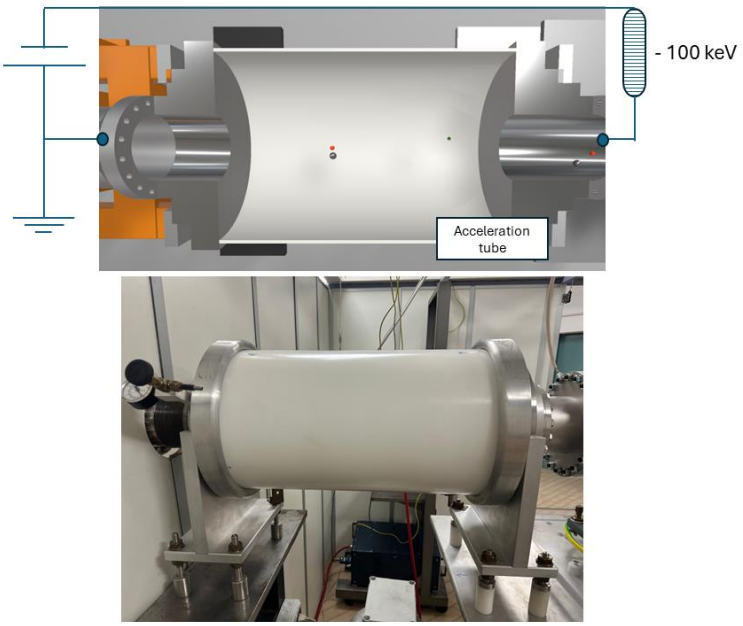

Figure 60 *Acceleration tube schematics and real picture.*

All these components are placed inside a Faraday cage, to provide electrical insulation from the rest of the working place.

3.1.2 Mass spectrometer

The mass spectrometer in the ion implanter allows for the selection of the desired implanting ion into the substrate. The core of the mass spectrometer is a bending magnet with an angle of 90º. A picture of the magnet is shown in **Figure 61**.

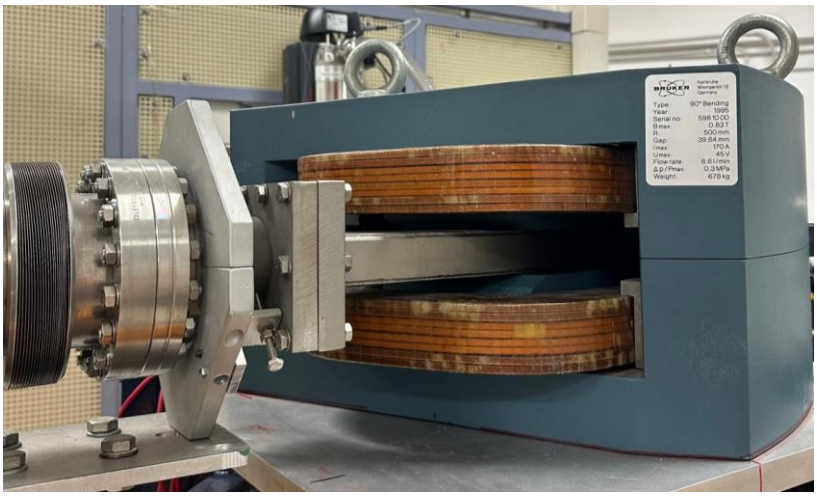

Figure 61 *90º bending magnet.*

The working principle of the mass spectrometer using the bending magnet is the Lorentz force. Considering the passing of an ion with charge state **Q** and mass **m** in a magnetic field **B** perpendicular to the ion velocity vector **v,** in a magnet of radius **r**, the force necessary to bend the ion can be written as follows[265]:

$$F = QevB = \frac{mv^2}{r} \qquad \textit{Equation 27}$$

The energy of the accelerated ions is the implanter can be written as:

$$E = Qe\ \Delta V = \frac{1}{2}mv^2 \qquad \textit{Equation 28}$$

Where **ΔV** represents the accelerating potential and **e** the elementary charge. By combining both equations 1 and 2, it is possible to obtain the relation between the dependence between the magnetic field and the applied voltage and mass of the ion (the mass of the ion **m** can be expressed as **m=AM**, where A is the atomic mass of the ion and **M** nucleon mass):

$$B = \sqrt{\frac{2A\ M\ \Delta V}{r^2 Qe}} \qquad \textit{Equation 29}$$

Now, for this specific magnet represented in **Figure 61**, the company provided dependence of the magnetic field B on the current passing through the coils follows the expression:

$$B\ [T] = (4.903\ \pm 0.007) \cdot 10^{-3} \left[\frac{T}{A}\right] \cdot I[A] + (1.8\ \pm 0.7) \cdot 10^{-3}[T] \qquad \textit{Equation 30}$$

Now, considering the radius **r** of the magnet is 500 mm, the mass of the nucleon **M** is $1.63\ \cdot 10^{-27}\ kg$, it is possible to extract the dependence of the current passing through the coils of the magnet I as a function of the ion energy and the mass of it (considering that Q is always 1 in our case):

$$I\ [A] = 0.059\ \sqrt{A\ \Delta V} - 0.36 \qquad \textit{Equation 31}$$

This formula is based on the specifications of the magnet and the theoretical formulas, and it is already visible how the higher the atomic number of the ion we are accelerating, the higher the current that must be given to the magnet, the same in the case of the accelerating potential. At a fixed energy, for the same magnetic field, the heavier the ion the less it bends and the lighter, the more it bends, as it is represented in **Figure 62**.

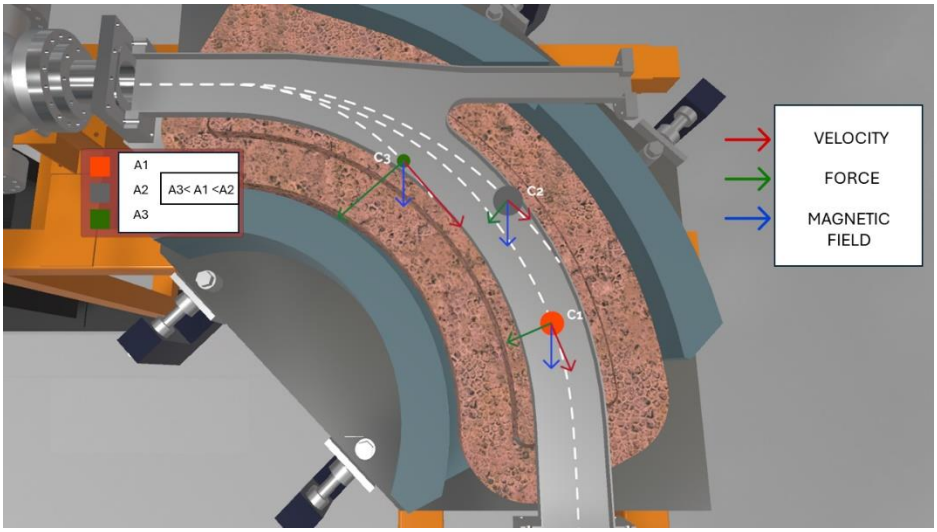

Figure 62 *Lorentz force working principle inside the magnet.*

To properly calibrate the magnet, in order to use it for the in-site implantations, several mass spectra were acquired at different energies for different cathode powders with known compositional contents. In these spectra, the ion current measured at the exit of the magnet was plotted as a function of the current passing through the magnet's coils. In this sense, for a fixed energy of the ions, each of the peaks presented in the acquired spectra should correspond to a different ion mass, selected by the magnet. To help with the understanding of the spectra acquired, the *Negative Ion Cookbook (NIC)*[264] was used, which provides a systematic study of the mass spectra for most of the elements of the periodic table accelerated as negative ions, providing specific information on the isotopes that can be accelerated for each of the ions and how prolific they should be.

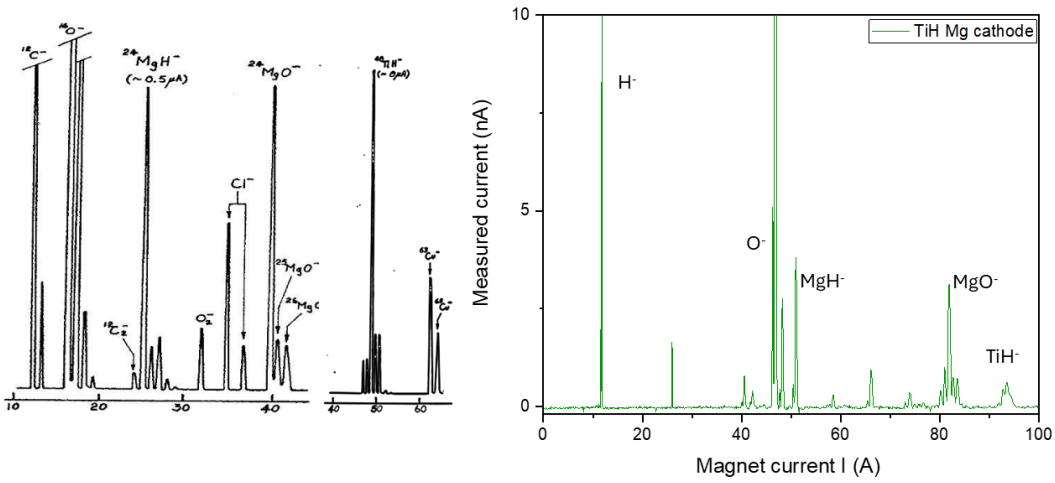

Figure 63 *Ti H Mg cathode experimental spectrum acquired from the negative ion cookbook left) and lab-acquired spectrum (right)*

In **Figure 63**, an example of the expected spectrum of two different cathodes is shown (left), magnesium and titanium hydride. It is already visible from these experimental NIC spectra that the magnesium negative ion is not prolific enough to be extracted from this type of sources, and the molecules that are more prolific are the MgH^- and MgO^-. The same happens in the case of titanium, where the most prolific ion is the TiH^-. Considering this, the spectrum of the cathode of compressed magnesium and titanium hydride powder prepared in the lab was acquired (reported in **Figure 63**, right), showing the hydrogen, oxygen, magnesium hydride, magnesium oxide and titanium hydride ions, among other ions that were not considered in the study. By the knowledge of the energy of these ions and the mass of each of them, a calibration curve between the current of the magnet and the mass of the ions was extracted, see **Figure 64**.

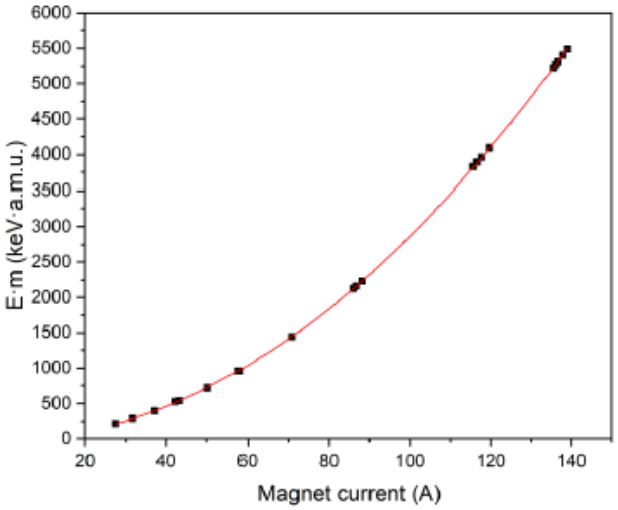

Figure 64 *Fit extracted from the acquired spectra in the lab, dependence of the energy and mass of the ion as a function of the magnet current*

As it can be seen in **Figure 64**, the dependence of these parameters can be fitted with a quadratic dependence as follows:

$$E \cdot m = a \cdot I^2 + b \cdot I + c \qquad \textit{Equation 32}$$

$$a = (0.27592 \pm 0.00162)\frac{keV\ amu}{A^2} \qquad \textit{Equation 33}$$

$$b = (1.46905 \pm 0.27832)\frac{keV\ amu}{A} \qquad \textit{Equation 34}$$

$$c = (-38.5588 \pm 9.83347)\ keV\ amu \qquad \textit{Equation 35}$$

Where E is the energy of the ions, m the mass of the ions and I the magnet current.

Aiming to increase the reliability of this calibration, many other spectra were acquired, some of which are reported in **Figure 65** and **Figure 66**. In **Figure 65** a spectrum of a Sn cathode (prepared by pressing Sn powder) is presented (right), where almost all the isotopes predicted (left) are present.

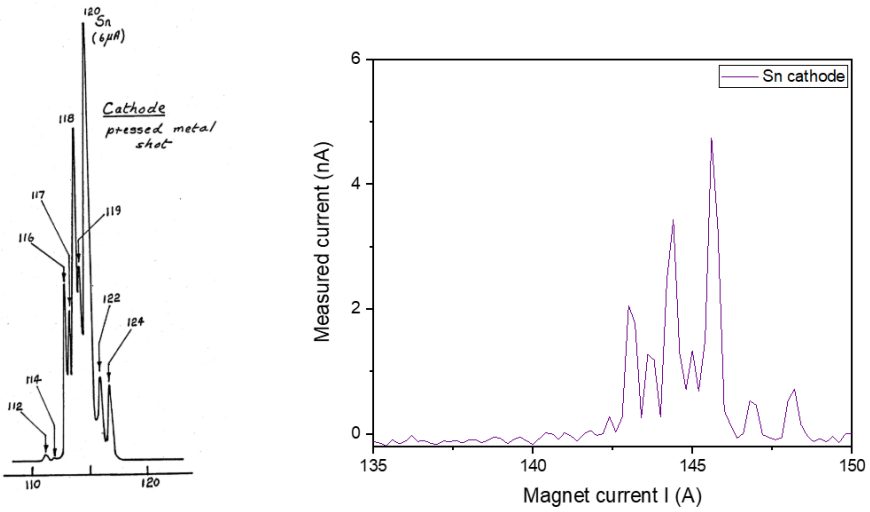

Figure 65 *Sn cathode experimental spectrum acquired from the negative ion cookbook spectrum (left) and lab-acquired one (right).*

In **Figure 66**, the expected spectra from germanium and silicon cathodes are represented, showing also how prolific both of them are as negative single ions, especially silicon. The spectrum was then acquired for the magnet in the implanter and as it is represented in the center of the figure, both the ^{28}Si and all the three ^{70}Ge, ^{72}Ge, ^{74}Ge, are clearly present in the spectrum.

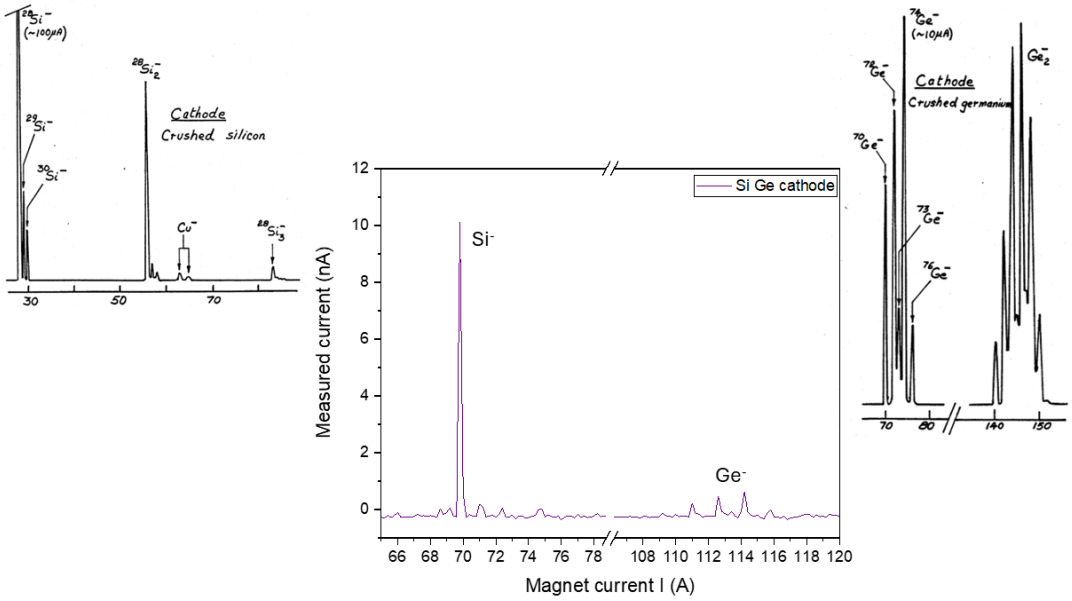

Figure 66 *Si and Ge expected spectra (left and right) and acquired one (center).*

As it is expected, not all the ions can be addressed at every energy. The main limitation relays in the magnet current limit, as at maximum it can be 170 A, and this states a limit mainly for heavy ions. For example, for the case of Pb the maximum energy at which it can be implanted is around 25 keV, as the magnet wouldn't be able to bend it at higher energies.

3.1.3 Beam shaping

Once the desired ions exit the magnet, a set of beams shaping elements are present in the beamline that allow to correctly carry the ions to the irradiation chamber. These elements go from electric steering elements, that allow for the alignment of the beam at the center of the beamline, to electromagnetic focusing, that allow for the reduction of the beam size, and steering ones, which are used both for scanning purposes and centering of the beam on the sample.

Electric steerer

After the magnet, the first element present in the beamline is the electric steerer. It is used for changing the vertical position of the ion beam inside the line. It allows for the vertical correction of the beam, which is also crucial for the focusing elements that come afterward. The electric steerer is formed by two parallel plates (see **Figure 67**) to which a difference of voltage is applied, depending on how they are polarized the ion beam can be shifted up or down. These plates are polarized using a voltage supply that can supply up to 5 kV.

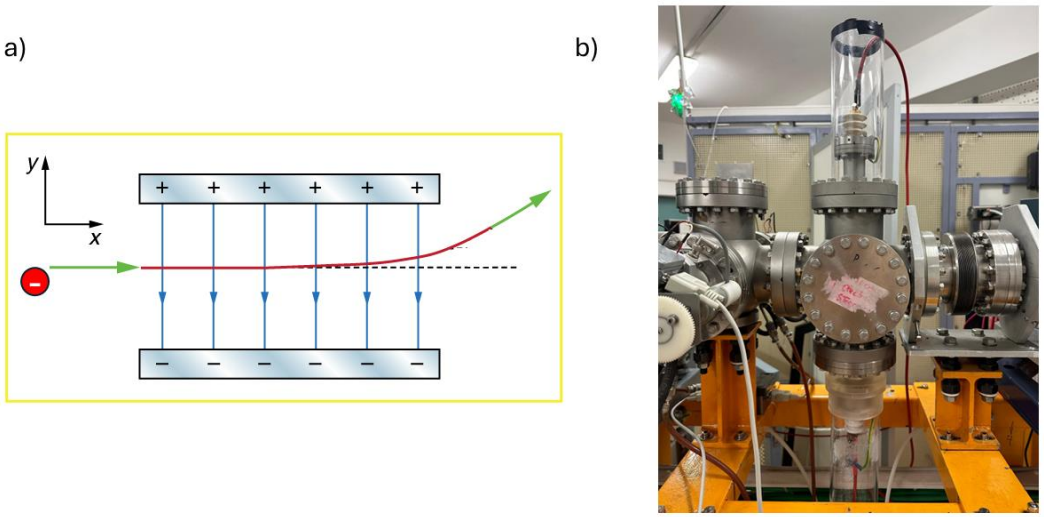

Figure 67 a) Working principle of the electric steerer. b) Picture of the electric steerer from outside in the lab.

Focusing quadrupoles

The main focusing elements that were installed in the beamline, apart from the Einzel lens (in the source) and the magnet itself (which focalizes also the beam), are the quadrupoles. A quadrupole consists of a system with 4 poles, each being opposite in polarity with the adjacent one generating a hyperbolic profile, as depicted in **Figure 68**a. As it can be highlighted in **Figure 68**, these quadrupoles are typically used in pairs (**Figure 68**b) as the use of only one of them would focus only on one direction. The working principle of these quadrupoles is shown in **Figure 68**a and it is based on the Lorentz force, which allows for the focus on one axis and the defocus in the second axis.

In **Figure 68**c a picture of one of the two quadrupoles present in the beamline is shown, it is formed by four coils through which a set current flows, leading to an induced magnetic field around it dependent on the current supplied. The current supply is provided through two current generators that allow to reach 25 A.

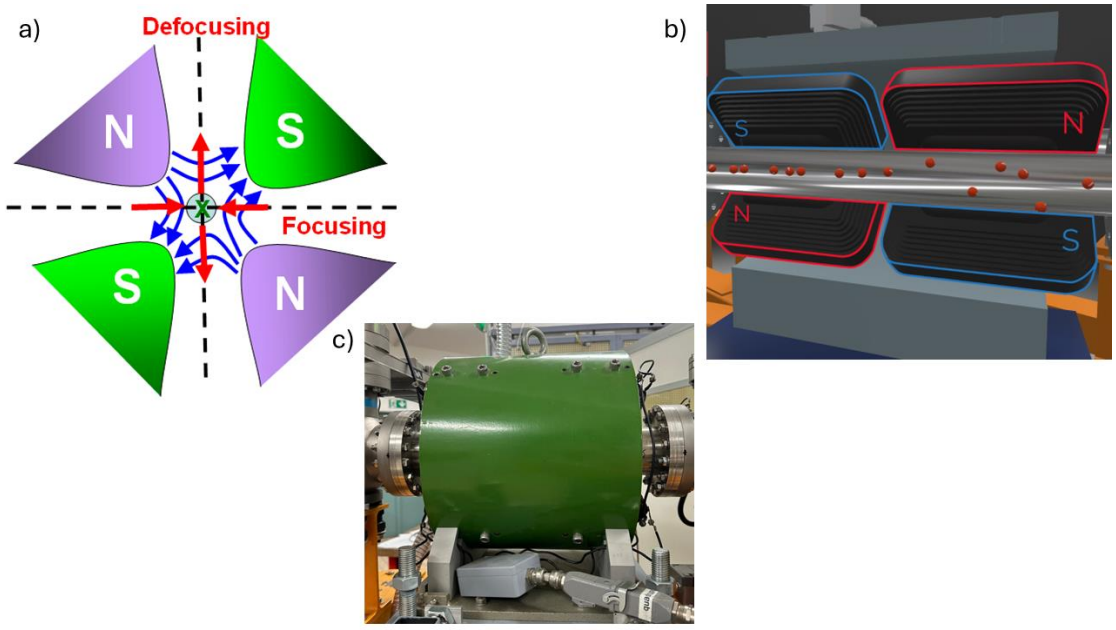

Figure 68 *a) Working principle of a quadrupole*[266]. *b) Schematics of the focalization of the quadrupole in the lab (open in a half). c) Picture of one of the two quadrupoles present in the ion implanter.*

Magnetic steerers

The magnetic steerer target function is the same as the electric steerer, it allows to reach the target positioned in the irradiation chamber. Its physical working principle is the Lorentz force. Two coils are positioned around the tube where the ion passes, with opposite polarities and by introducing a certain current in the coils a magnetic field is induced, which can steer the trajectory of the ions passing in the middle. As it is visible in **Figure 69**, in our case, we have three magnetic steerer, one horizontal that allows for the x shift of the beam, one in vertical, allowing the y shift of the beam and a third one at 45º to shift the origin. The main advantage that these steerers present with respect to the electrical one is the possibility of placing them outside the vacuum tube, in addition to the possibility of choosing their exact orientation and in consequence, the direction towards which the steering wants to be done.

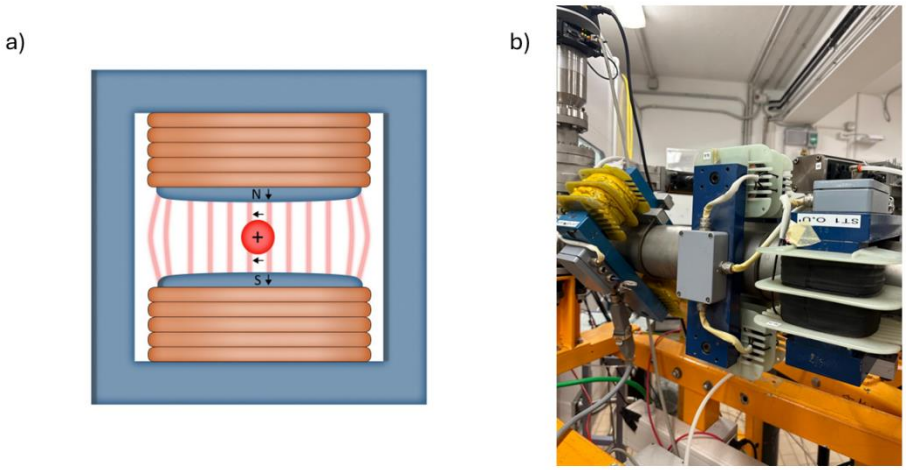

Figure 69 *a) Schematics of magnetic steerers. b) Picture of three magnetic steerers in the ion implanter in the lab.*

3.1.4 Measurement tools

Apart from the set of elements that allow for the shaping of the beam and ion selection , it is important to measure the position of the ion beam inside the beamline.. In order to understand this, the measurement of the ion current is performed using a homemade Faraday Cup. The Faraday cup design is shown in **Figure 70** it is composed of the readout part (represented by 2 and 3 in the figure) where the ions arrive and the amperemeter (in our case a Keithley 6485) is connected to, and the electron suppression part. The electron suppression part is a plate positioned before the plate of the ion collection, that is connected to a potential difference of -220 V with respect to ground. This electron suppression allows for the charge balance inside the Faraday cup, that may be affected by the detection of secondary electrons produced upon the irradiation of the measurement plate (copper plate) with the ion beam. In our beamline, a Faraday cup was mounted after the magnet, allowing to perform the spectra shown in the previous section. The second one is placed in the irradiation chamber and allows to understand how many ions will be implanted on the sample.

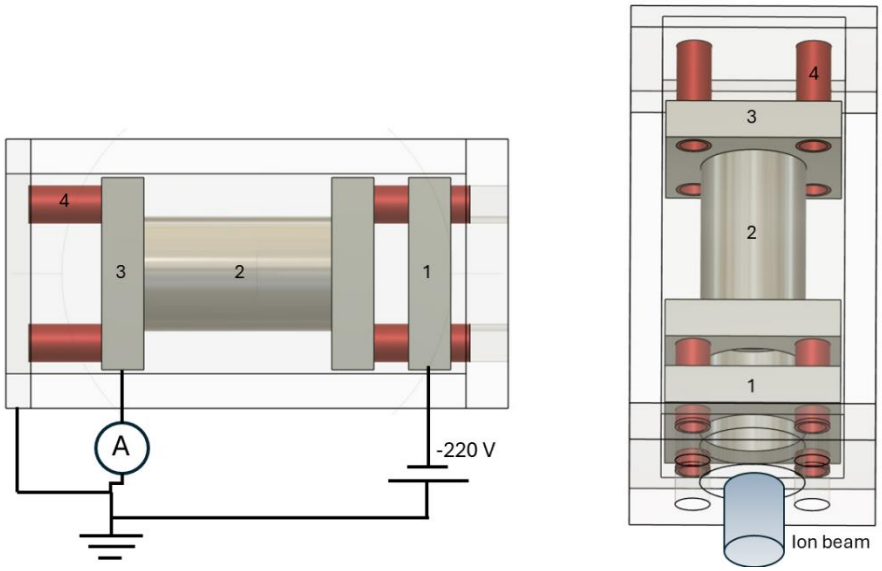

Figure 70 *Schematics of one of the homemade Faraday cups that is present at the ion implanter. The 1 part is a plate connected to -220 V and it is called electron suppressor, 2 is a tube that improves the readout of the beam current, 3 is the plate where the amperemeter for the readout of the current is connected and 4 represents the isolating tubes that allow for the grounding and not short circuit of the faraday cup.*

Apart from the analytic measurement that provides a pretty accurate knowledge of the number of ions that are being accelerated and implanted, it is sometimes useful to use scintillators materials that under ion beam irradiation produces ionoluminescence providing information on the shape and position of the beam. It can be positions in the irradiation chamber (useful for the implantation beam) or as it is presented in **Figure 71**, in the back part of the magnet to see how aligned the ion beam is in exit of the source.

Figure 71 *Picture of the luminescence produced by the ion beam on Cesium hydride in the exit of the source.*

3.1.5 Irradiation chamber

The irradiation chamber is the last part of the ion implanter, as it is where the samples that will be implanted are mounted and irradiated. It is the only part that is necessary to vent, meaning that the high vacuum conditions must be broken each time a sample wants to be implanted, putting the chamber in atmospheric pressure conditions, as it needs to be mounted on the sample holder. The rest of the ion implanter is always in high vacuum conditions, meaning $< 5 \cdot 10^{-6}\ mbar$.

A picture of the inside of the irradiation chamber is reported in **Figure 72**. The irradiation chamber has a cylindrical geometry, with 12 feedthroughs on the side walls allowing to interface the instruments inside with the different control software, for example, BNC connectors for the current measurement, 15-pin connectors for the different steppers or optical feedthrough for the optical addressability of the system.

As can be pointed out in **Figure 72**, several sections are present inside the irradiation chamber.

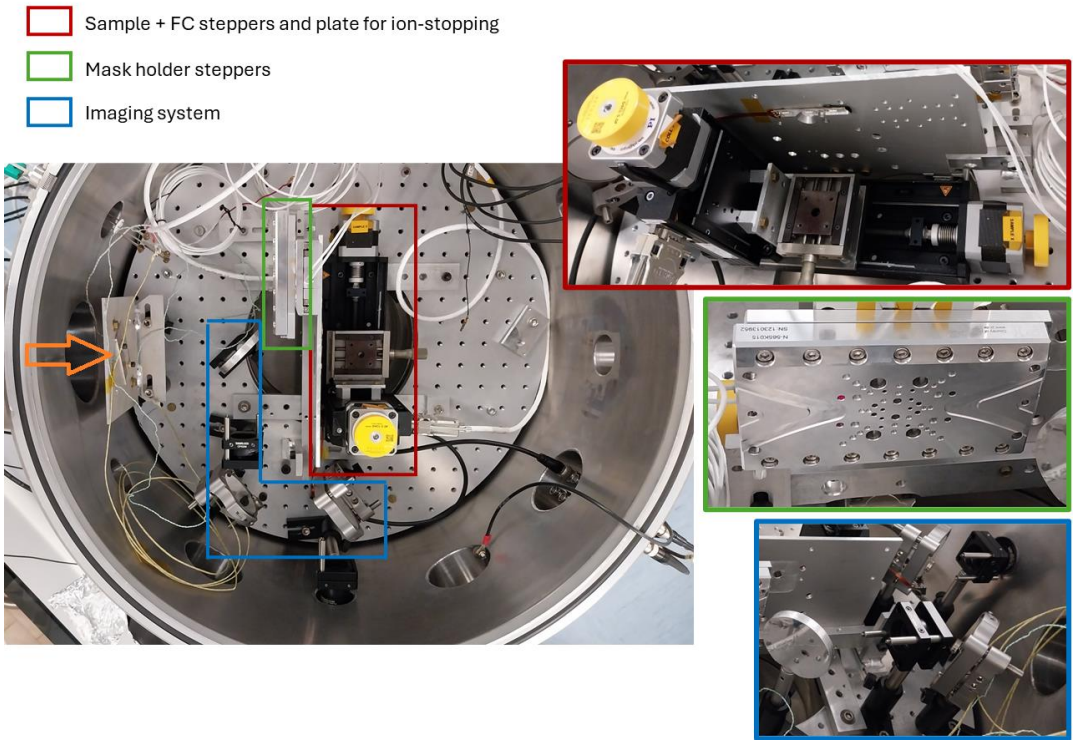

Figure 72 *Picture of irradiation chamber where main systems are highlighted, the entrance of the ion beam is the left-center part hole (orange arrow)*

Imaging system

The blue highlighted region in **Figure 72** shows the imaging system of the irradiation chamber, which allows for optically understanding of the position of the sample. Its components are presented more deeply in **Figure 73**. It is composed of a CMOS camera, attached to a small microscope outside of the chamber. Inside the chamber, to increase the magnification of the image a system with two piano convex lenses was installed and some mirrors to allow for the in-line imaging of the sample. In front of the sample a flat mirror with a passing-through hole in the middle, allows for both the imaging and the passing of the ions towards the sample.

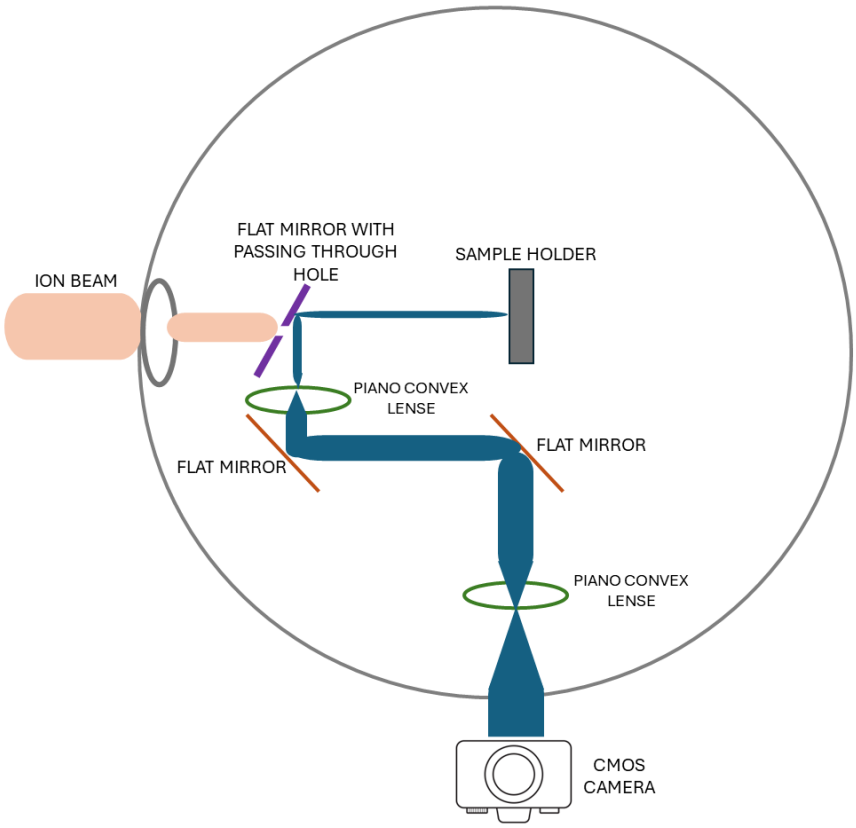

Figure 73 *Schematic representation of the imaging system mounted in the irradiation chamber.*

Masking system

The masking system, which is highlighted in green in **Figure 72**, is based on two nano positioners from Physik Intrumente (Model N-565K015) guided by two Mercury cards (Model E-861). The range for both steppers is of 26 mm and they allow for the movement of the mask holder in the xy plane (the same as the sample). By connecting a mask holder where the desired implantation masks are placed, to the positioners, it is possible to precisely decide the position of the implanted region within the sample or even to perform different patterning.

Sample + FC scanning

Lastly, one of the most important parts is the sample and Faraday cup mounting and scanning system, which is circled in **Figure 72** in red.

This scanning part of the sample and Faraday cup is based on two micrometric precision steppers from Physik Intrumente (Model 6230V6400 and 6230V1000) controlled remotely by Mercury cards (Model C-

663) and a third one controlled manually. As it is shown in **Figure 74**, the vertical position has a range of 25 mm while the horizontal position can be changed over a range of 100 mm.

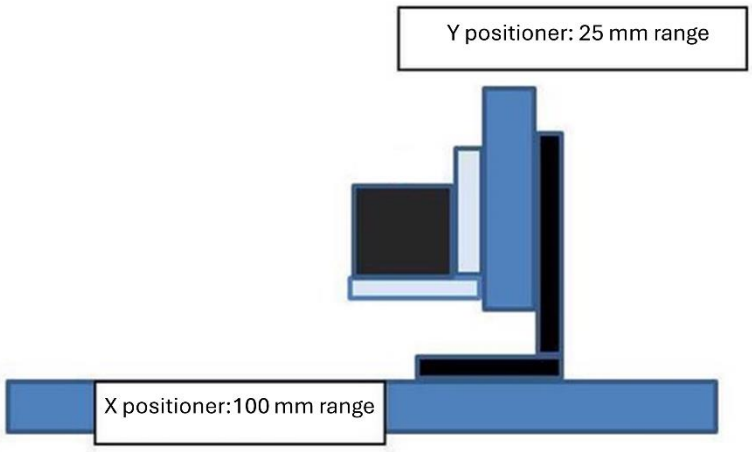

Figure 74 *Sample holder positioners scheme. The blue parts represent the two steppers, while the black square represents the sample holder,*

Mounted on the positioners is the sample holder presented in **Figure 75**. In the blue highlighted region, the samples are positioned with double size scotch in order to hold them vertically. The orange highlighted area represents where the Faraday Cup (FC) is placed. The size of the cup is miniaturized to allow for a precise current measurement in plane with the sample position. The FC is linked to a picoammeter (Model Keithley 6485) as well as the electron suppressor via BNC feedthrough.

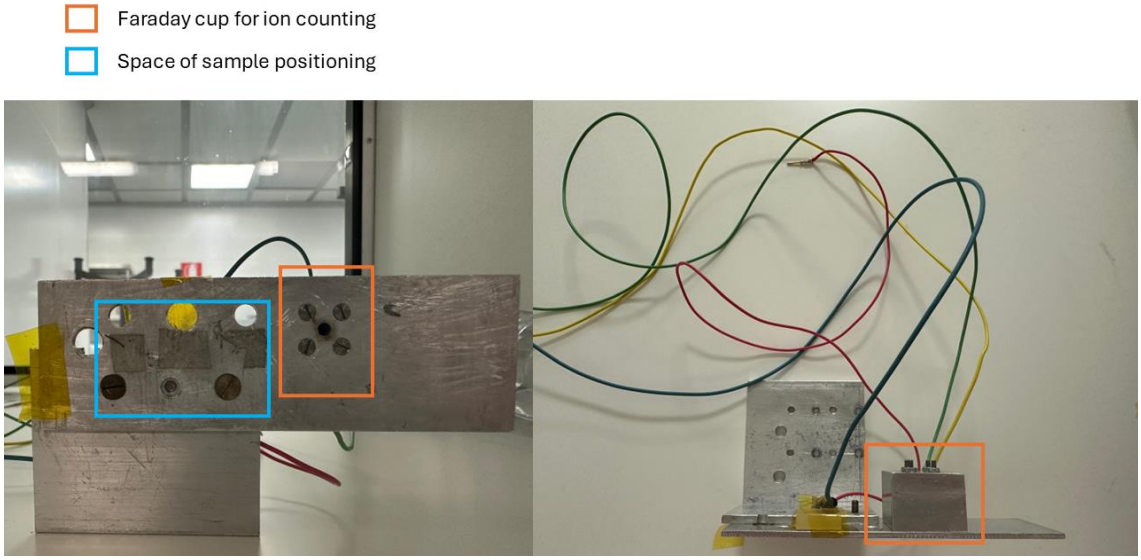

Figure 75 *Sample and Faraday cup holder.*

Finally, it is important to highlight the interest of having the Faraday cup and the sample mounted in the sample holder with a fixed known positioned. As the holder is attached to two steppers controlled remotely, it is possible making use of a homemade Labview program to do a scan of the beam that is arriving to the Faraday cup (FC) and so to define the exact position of the ion beam and the amount of ions that are arriving to it. An example of an acquired scan is reported in **Figure 76**, where the maximum current is centered in the center of the FC as a negative value (as we are counting negative ions). With this information, it is possible to easily extract the time of implantation, intended as the exposure time of the desired region to the ion beam, the desired position of the masks of implantation and the of the sample that wants to be implanted. The exposure of the sample to the ion beam is controlled with the entering and exiting of the

Faraday cup system in the middle of the beamline, which is controlled by a LabVIEW program and a mechanical air compressed system.

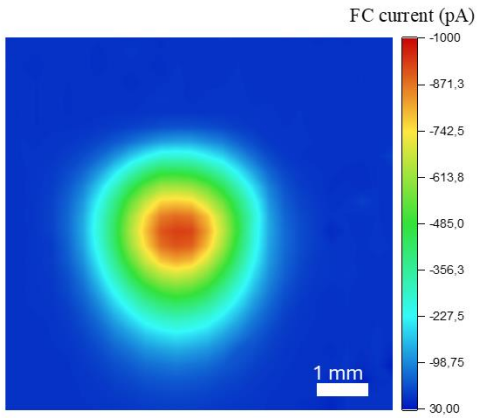

Figure 76 *Intensity plot of the scan of the FC mounted on the sample holder, acquired with a pixel size of 50x50 μm².*

3.2 Furnace annealing

During the experiments of this thesis, several annealing treatments were employed to activate color centers, both in diamond and AlN. In this section, the ones used for the experiments in Section 4.4 of this thesis will be explained, mainly a tubular furnace and an annealing chamber with a heating plate.

3.2.1 Tubular furnace

The tubular furnace employed for the treatment of AlN was a ThermoConcept ROT 60/200/12 tubular oven. The system can reach a maximum temperature of 1200°C with a power of 3 kW. The control system enables the programming of treatment ramps based on the desired process protocol. Samples are placed inside the tube in an inert alumina crucible.

In particular, a continuous laminar flow of inert gas (Ar or N_2 supplied by gas cylinders) is established inside the tube for the treatments at high temperature and inert atmosphere. In the case of AlN, the maximum temperature reached was 600 ºC and the process was performed under N_2 atmosphere. To control the flow of nitrogen, a pressure regulator and a bottle of water with a plastic tube are connected to the annealing tube at the entrance and exit.

Figure 77 *Tubular thermal furnace in the lab.*

3.2.2 High-temperature annealing chamber

The high-temperature annealing chamber is a homemade vacuum chamber, based on a steel cross composed of 5 flanges to which several components can be connected. As can be highlighted in **Figure 78**, in the chamber present in the lab, a turbo pump is connected with a CF type of flange (right side of the cross) to guarantee pressure below $< 5 \cdot 10^{-6}$ mbar , a vacuum gauge (left side of the cross) to monitor the vacuum level inside the chamber, the flange to which is connected the heating plate is located at the bottom. This flange (see **Figure 78**b) is composed of two feedthroughs, one for the current supply and the other for the thermocouple that allows for the temperature reading. The current is then directed towards a resistance that heats up a ceramic plate where the samples can be positioned as it is shown in the picture. The power supply allows to reach temperatures up to 1500ºC and the ramping up of the plate is controlled by a PID (Proportional Integral Derivative) controller whose objective is to reach the final temperature set, without large oscillations.

This annealing chamber was extensively used for the work carried in the lab, as it allows for the high temperature annealing of samples at high vacuum conditions for many hours (up to 10 h annealings were performed). This annealing chamber is additionally equipped with a water chiller and an air fan that allow for the heat dissipation in the steel cross, which can get high due to the radiation emitted by the heated plate.

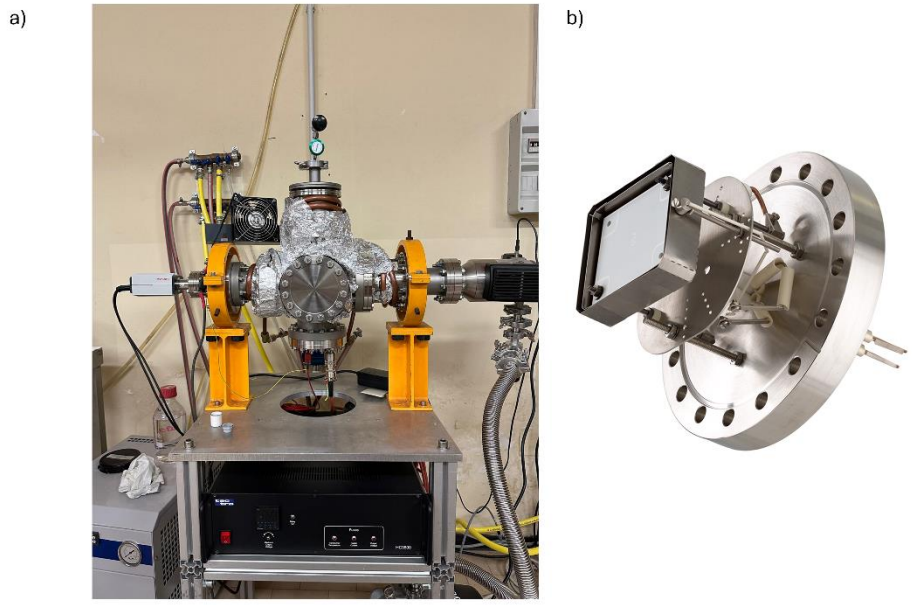

Figure 78 *High-temperature annealing setup in the lab.*

3.3 Nanosecond laser

The nanosecond laser is a EzLaze 3 instrument from New Wave Research. It is a Nd: YAG (neodymium-doped yttrium aluminum garnet, Nd:$Y_3Al_5O_{12}$) pulsed laser operating in "Q-switching" mode, meaning the emission is enables after the maximum population inversion is achieved. The maximum obtained output energy is 0.6 mJ with a pulse duration of 4 ns. The maximum dimension of the aperture is 2.5 x2.5 mm^2, leading to a maximum power density of 2.4 MW cm^{-2} before any objective.

This laser has the possibility of performing lithographic patterns by using a Labview program. It has three different wavelengths: green, UV and IR (**Figure 79**). They allow for the performing of different experimental activities such as laser annealing of material such as silicon[106], the lithographic patterning of semiconductors, the markering of materials such as diamond or even the drilling of materials for the fabrication of implantation/evaporation masks.

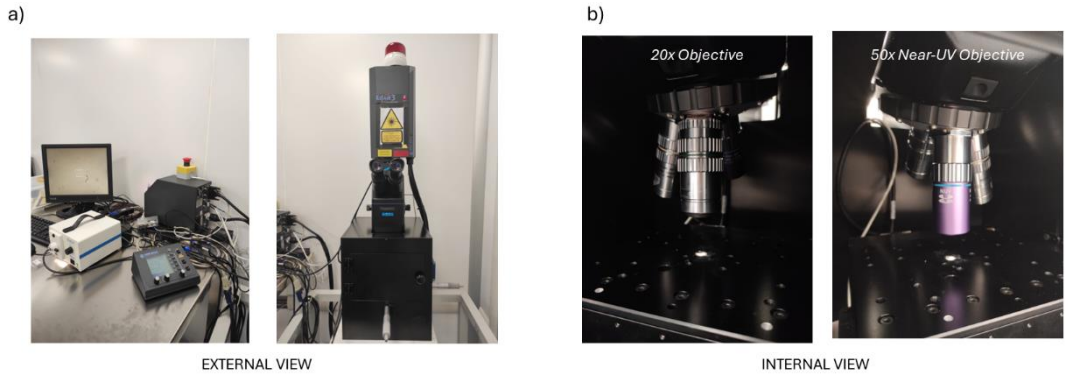

Figure 79 *a) External view of the nanosecond pulsed lase. b) Internal view of the pulsed laser.*

For the experiments carried out in this thesis work, the laser was mainly used using the green wavelength at high powers to perform both micrometer size markering of diamond and AlN and aluminum foil drilling for creating masks for the ion implantation chamber. As it can be pointed out in **Figure 80**, the dimension of the laser beam can be adjusted using an XY shutter and it can be shrunk down to a dimension of 2.5 x 2.5 μm^2. Additionally, in **Figure 80**b it can be observed an SEM image of a mask fabricated with the laser in aluminum foil for the use in the ion implanter as a collimated mask.

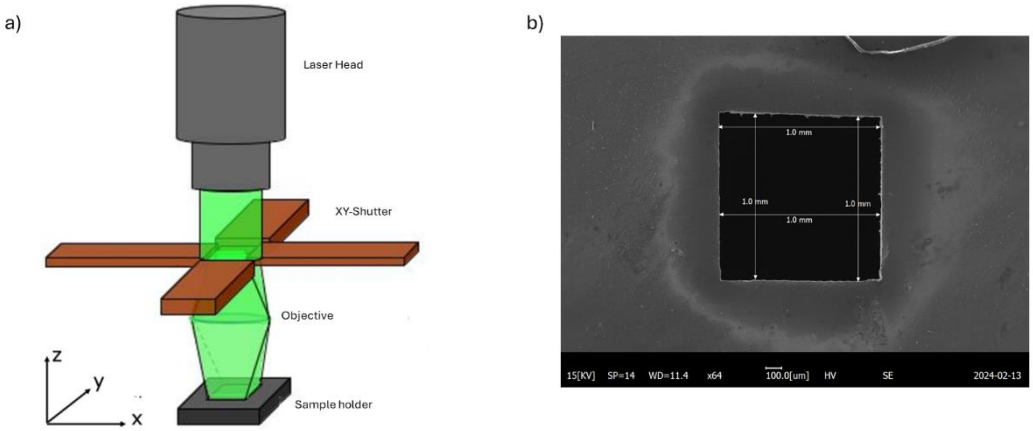

Figure 80 *a) Schematics of the laser working, b) SEM image of an aluminum mask fabricated with the laser.*

3.4 Confocal microscope

Confocal microscopy was the technique adopted for the characterization of the color centers studied in this thesis. This experimental technique represents an essential technique in photoluminescence measurements for characterizing single photon sources (SPS) both an ensemble and single-emitter level. The main advantages that it presents with respect other microscopy techniques are[267]:

- Better lateral resolution with respect to conventional microscopy.
- A depth resolution sufficient to allow optical sectioning.
- High contrast due to the removal of the signal not originating from the addressed focal plane.
- The possibility of combining it with other interesting techniques such as spectral analysis or interferometry.

The confocal microscope system uses a laser to trigger emission from defects in a crystal lattice, as shown in **Figure 81**. Here's how it works: the laser light (shown as a blue beam) passes onto the sample through a dichroic mirror, which acts as a filter with a specific cutoff wavelength. The sample absorbs the laser light and emits fluorescence (green beam), which then passes through the dichroic mirror to the light collection path. Since the objective lens has a high numerical aperture, the excited volume is small, but fluorescence can still come from optical planes that are not in focus. A pinhole is placed in the collection path to address this issue to remove out-of-focus fluorescence, creating optical sectioning along with the point-like excitation.

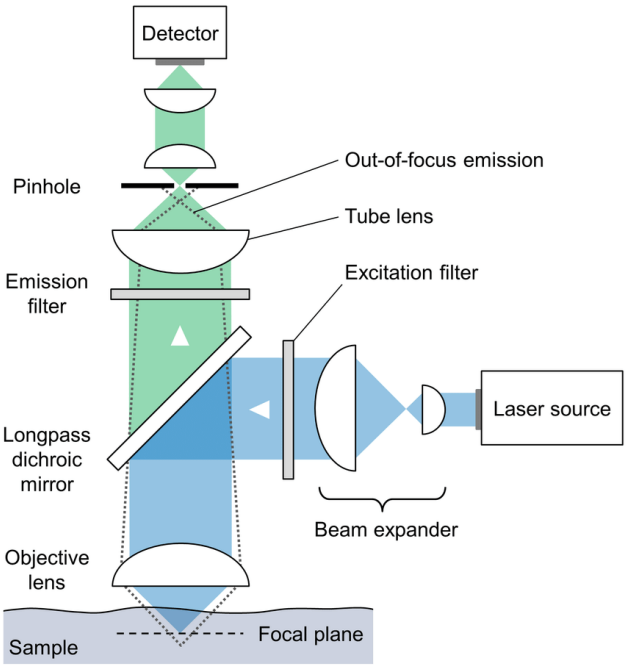

Figure 81 *Schematic representation of a confocal microscope. The blue beam represents the laser excitation, while the green beam stays for the fluorescence coming from the sample*[268].

It is important to analyze the spatial resolution and the optical sectioning that a confocal microscope can present, to know the limits of the experiment. The optical resolution of a microscope is usually limited by aberrations and diffraction. Aberrations are related to the chromatic and non-paraxial conditions in the alignment of the setup, and they result in image distortion. Aberrations can be minimized by using carefully selected optical components and aligning the setup carefully. Diffraction is a physical limit that arises because light, due to its wave-like nature, produces diffraction phenomena while interacting with the lenses in the system.

The limiting effect of diffraction can be understood by considering a point-like object on the focal plane of an objective, as shown in **Figure 82** (Diffraction pattern produced by a circular aperture). Under this assumption, the light collected by the objective and focused onto the image plane forms a two-dimensional circular pattern consisting of a central disk (referred to as Airy Disk) surrounded by concentric rings[267].

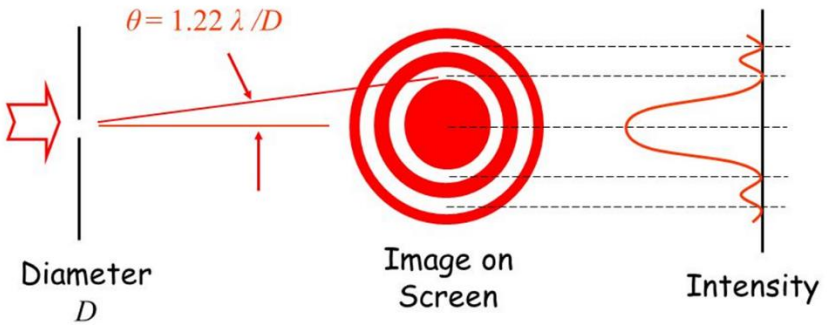

Figure 82 *Diffraction pattern through a circular aperture.*

As shown in **Figure 82**, in the absence of aberration and distortion, the resolution limit of the system is described by the Abbe equation:

$$d = \frac{0.61 \cdot \lambda}{N.A} \qquad \textit{Equation 36}$$

Where d is the resolvable feature size and N.A. is the numerical aperture of the objective.

The axial and transversal dimensions of a point-like object can be estimated by calculating the amplitude of the electric field on the optical axis. This calculation is known as the Point Spread Function (PSF). In every microscope, the image is produced by the convolution of the image function (the two dimensional function of an image) and the PSF.

The PSF allows to measure the efficiency of an optical system and is defined as the square of the amplitude H(ν). This amplitude represents the transverse spatial variation of the image amplitude produced on the focal plane when the lens is illuminated by a perfectly point-like source. Diffraction, combined with any aberrations, causes the formation of an image of the point-like source with finite transverse dimensions at the focal plane. For a circular converging lens, in the absence of aberrations and under the paraxial approximation, the PSF is represented by the Airy disk, and therefore its amplitude is given by[267]:

$$H(\nu) = \frac{2\,J_1(\nu)}{\nu} \qquad \textit{Equation 37}$$

where J_1 is the first order Bessel function and the optical distance $\nu = 2\pi ar/\lambda f$ where a is the lens radius, f its focal length and r is the radial distance from the optical axis.

It is possible to calculate the intensity distribution in terms of the amplitude of the PSF, h(x,y), and the amplitude of the object's transmittance function, t(x,y), for the confocal microscopy case[267]:

$$I_c = |t \otimes H^2|^2 \qquad \textit{Equation 38}$$

Given the geometric response of a confocal microscope to a point-like object, $\mathbf{I_c}$ in **Equation 38** can be expressed as follows:

$$I_c = |H|^4 \qquad \textit{Equation 39}$$

Therefore, it can be concluded that the PSF, in the case of a circular aperture (in the absence of aberration and under paraxial approximation), for a confocal microscope is given by the square of the Airy disk and hence is substantially narrower than in other types of microscopes and has very weak sidelobes[267].

The resolution of an optical system is defined as the minimum distance required between two-point sources for them to be distinguished as separate points. This is determined by the Rayleigh criterion, which states that the resolution limit occurs when the peak of the Airy disk created by one point coincides with the first minimum of the Airy disk created by the other point[267]. In confocal microscopy, the Rayleigh distance can be calculated as follows:

$$d = \frac{0.56 \cdot \lambda}{N.A.}$$ *Equation 40*

The Rayleigh distance in the case if confocal microscopy is lower than in the case of conventional microscope. The mathematical expressions discussed above show how diffraction sets the intrinsic limit of the optical microscope. The smallest angular separation that can be measured with an optical system is proportional to the wavelength of the electromagnetic radiation and inversely proportional to the numerical aperture of the optical components used.

Apart from the above-mentioned spatial resolution, the confocal microscope's unique advantage for characterizing SPSs lies in its optical sectioning capability, which is comparable o its spatial resolution. By using a pinhole, the instrument filters out fluorescence light not originating from the focal plane, resulting in a reconstructed image with improved resolution. Additionally, the possibility to perform additional measurements at the diffraction limit, as will be explained in the following sections, makes it even more appealing from the characterization point of view.

3.4.1 Experimental implementation

During the thesis work, different confocal microscopes were built and used. In **Figure 83** it is reported one of the adopted configurations for the confocal microscope based on a supercontinuum pulsed laser (SuperK Varia) from NKT photonics, with a wavelength range going from 400 to 850 nm. In this case, as the scheme in the picture shows, the photoluminescence scanning of the samples is performed using a galvo mirror (model GVS212 from Thorlabs). This confocal uses a 4x objective for the collimation of the laser beam, then the beam is redirected to a dichroic mirror (whose cutoff wavelength is changed depending on the center studied). From there, the beam is reflected to the galvo mirrors that move the beam in the x and y direction, always making it pass through a 4f (collimating beam lenses) system and arriving to a 100x objective with a N.A. of 0.9. This objective then allows for the focalization of the laser beam into a focal plane of the sample, that is mounted on a one axis piezoelectric positioner, whose allows for the precise adjusting of the focal depth at which the optical sectioning is performed.

The photoluminescence (PL) coming from the illuminated spots is collimated by the same 100x objective, passes through the 4f system and galvo mirror, arriving to the dichroic mirror, whose cutoff wavelength is chosen low enough to reflect the emission of the laser and let pass most of the PL signal. Afterwards, the PL signal arrives to an achromatic lens that focuses it into a pinhole of 50 μm diameter, connected to a multimode fiber with 50 μm diameter core.

This multimode fiber is usually connected to single-photon avalanche diodes (SPAD) that allow for the single photon counting coming from the single photon emitters. Additionally, they can be connected (in our case) to the interferometer system that will be explained in the next section in which the nature of the light emitted is analyzed or to a spectrometer, for the spectral analysis.

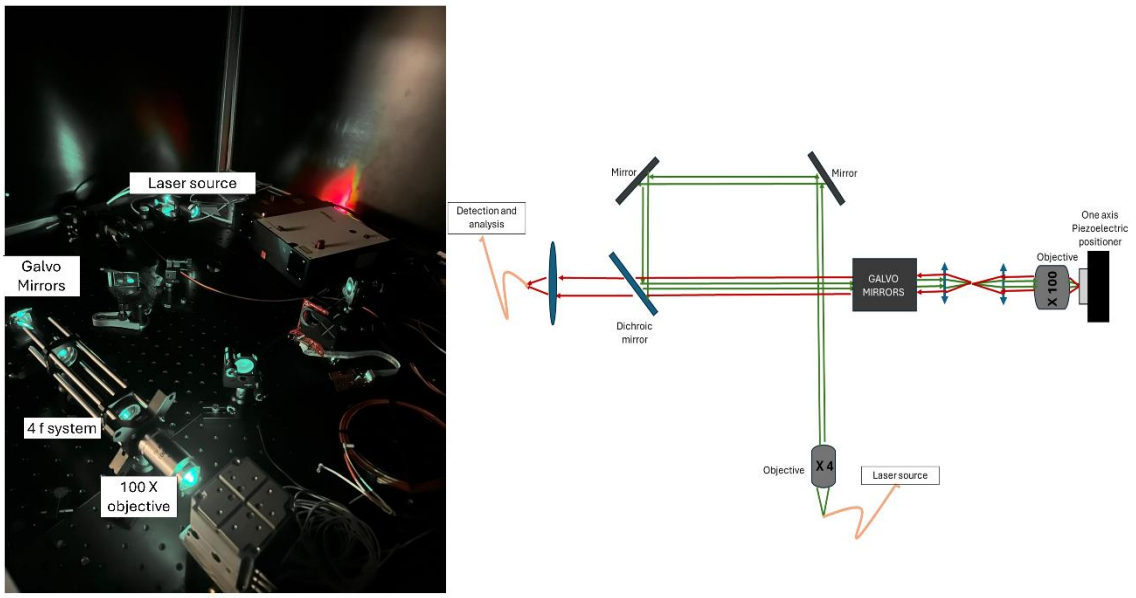

Figure 83 *Tunable laser confocal microscope with galvo mirror scanning system.*

Another example of confocal microscope used during the work carried out, always at room temperature, is the one shown in **Figure 84**. In this case, the peculiarity that differentiate it from the first one reported is the double laser excitation. In this confocal setup, several CW (continuous wave) lasers were combined at several wavelengths: 405, 445, 505, 520 and 595, to address several centers contemporaneously. The collimation objective of the laser is the same type as for the other confocal, allowing to perform overfill of the focalizing objective and in this case, the positioner is a 3-axis piezoelectric with nanometric precision, that allows for the scanning of the sample over a region of 100x100x100 μm^3

In both systems, before the achromatic focusing lens several filters (longpass and shortpass filters) are usually places to select the spectral region that wants to be analyzed.

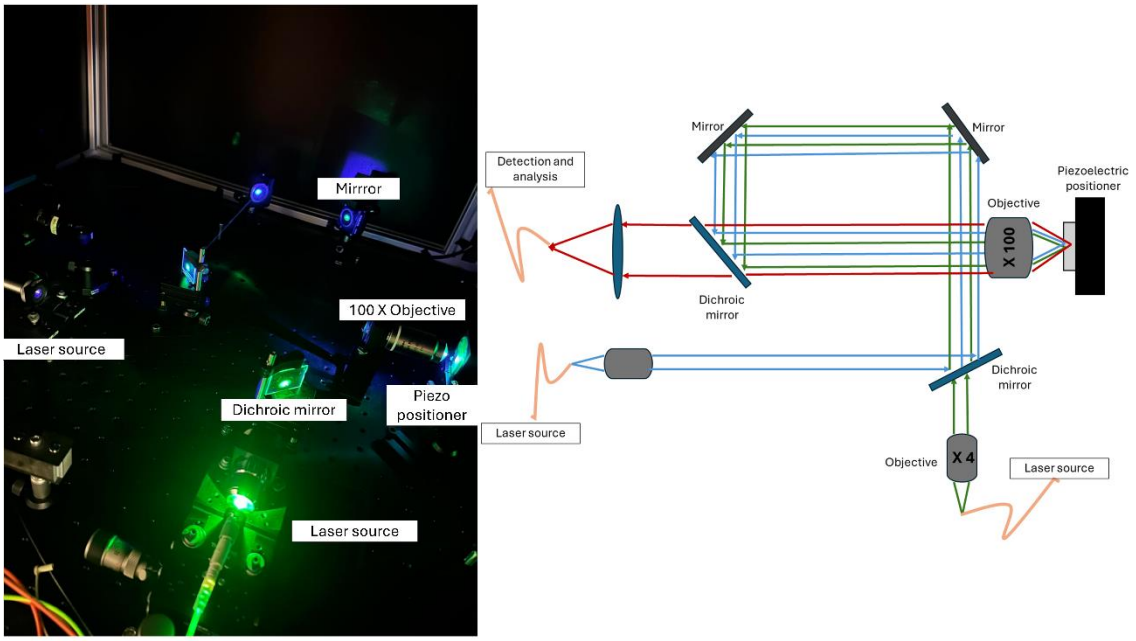

Figure 84 *Confocal microscope with double excitation laser and piezoelectric scanning.*

3.4.2 Hanbury-Brown and Twiss Interferometer

As was already anticipated in the first Chapter one of the most expanded techniques for the analysis of the emission statistics of color centers is the Hanbury-Brown and Twiss interferometer. It allows for the differentiation of the non-classical single-photon emission from thermal or coherent light. From the experimental point of view, the light source is directly sent onto a beam splitter, which divides the emission into two paths, each linked to a single-photon-sensitive detector, as shown in **Figure 85**a.

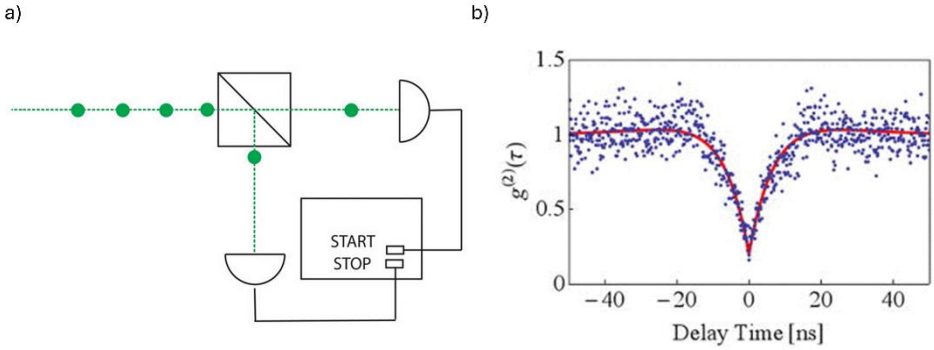

Figure 85 *a) Schematics of a Hanbury- Brown and Twiss interferometer. b) Second-order autocorrelation function plotting for CW photoluminescence experiments*[269].

The main idea is to compare the changes in intensity between the two beamsplitters. Each detector produces a pulse when it detects a photon. These pulses are used as input signals for two separate acquisition channels of a time tagger (refer to **Figure 86**). The time tagger then measures the coincidence time between the two signals, creating a histogram of events based on the time delay (**Figure 85**b). This histogram represents the interferogram showing the time differences between pairs of detection events at the two detectors. The START channel is the one used to measure the time delay. When a photon is detected in the START channel, it starts an internal timer. This timer is then stopped when the STOP detector absorbs a second photon. The time interval between these two events is used to generate a histogram of the measured delay events through a time-to-digital conversion operation. This histogram represents the second-order autocorrelation function $g^2(\tau)$, where the value at zero-time delay is an important measure for assessing the non-classical nature of the source. In particular, the measured histogram c(t) represents the second-order autocorrelation function upon the following normalization:

$$g_{exp}^{(2)}(\tau) = \frac{c(t)}{R_1 R_2 w T} \qquad \textit{Equation 41}$$

where R1 and R2 represent the count rate of the two detectors, w is the bin width, and T is the acquisition time. A lack of event pairs recorded at t = 0 results in an anti-bunching signature in the $g^2(\tau)$ histogram, indicating emission from an ideal single-photon source. As expected, the measured signal is the sum of the emitted photons (i.e., the real signal, S) and the background (B) (i.e., dark counts, reflected laser radiation, or non-classical spurious photoluminescence). Therefore, according to **Equation 2**, the measured $g^2(\tau)$, denoted as $g^2_{exp}(\tau)$, is defined as follows:

$$g_{exp}^{(2)} = \frac{\langle (S(t)+B(t))(S(t+\tau)+B(t+\tau)) \rangle}{\langle S(t)+B(t) \rangle^2} \qquad \textit{Equation 42}$$

Considering:

$$g^2(\tau) = \frac{\langle S(t)S(t+\tau) \rangle}{\langle S(t) \rangle^2} \qquad \textit{Equation 43}$$

We can write the corrected function as follows:

$$g^{(2)}_{corr}(\tau) = \frac{g^{(2)}_{exp}(\tau)+\rho^2-1}{\rho^2} \qquad \textit{Equation 44}$$

Where $\rho = \frac{\langle S \rangle}{\langle S+B \rangle}$.

In **Figure 86** the main components necessary for the experimental realization of the Hanbury-Brown and Twiss interferometer at the lab are presented. First, the multimodal fiber beamsplitter is connected to the collecting part of the confocal microscope from one side and from the other side to two SPAD detectors. These detectors are connected to the Swabian Time tagger presented in the figure, in such a mode, that upon the arrival of photons, it converts the pulses to TTL signals that can be read by the multichannel analyzer and generate the histogram as a function of the amplitude received from each of the detectors. An example of such type of histogram for the single emitter case is plotted in the left part of **Figure 86**, as it can be highlighted there is an antibunching, that is not located at 0 delay time just because an electronic delay was introduced into the system. This antibunching behavior corresponds to the single photon source nature of the emitter analyzed. Additionally, other two bunching peaks are visible in the histogram, these two are due to the reflection of the photons in the connectors of the fibers with the detectors and are usually referred to as backflashes.

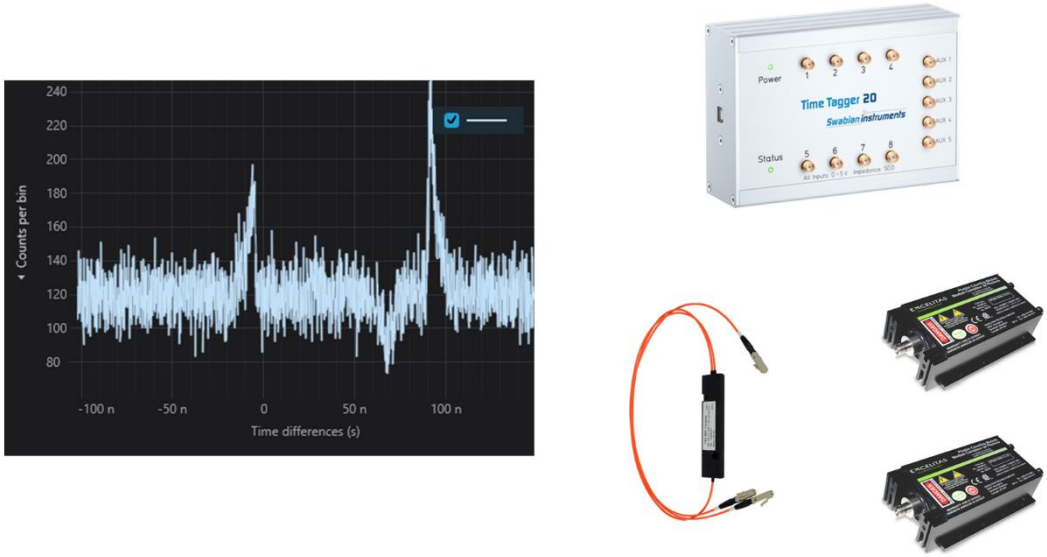

Figure 86 *Experimental components for the realization of the interferometer.*

3.4.3 Spectral analysis

Apart from the identification of the nature of the source through the statistical analysis of its photon emission, the spectral analysis of the color centers represents an important study to understand the spectral footprint of the center and understand the monochromaticity of such. For the understanding then of the emission of the center in our case, we use a Spectrometer like the one presented in **Figure 87**. In this case, the fiber coming from the collecting pinhole of the confocal is introduced into the spectrometer, and by using a diffraction grating (as shown in the figure) the different wavelengths are separated and focalized into a high sensitivity array, reported to be around 300 ke, (see bottom of **Figure 87**) in which each pixel of the array corresponds to a different wavelength. It allows for the resolution of down to ~0.2 nm of spectral peaks for wavelengths between 400 nm and 1000 nm.

Figure 87 *Spectrometer schematics of the experimental setup used for the experiments.*

Chapter 4

In the upcoming Chapter, I will outline the primary outcomes attained from creating and activating color centers in both diamond and AlN. First, I will delve into the findings regarding group IV color centers in diamond, specifically GeV and SnV. Additionally, I will share the progress made in creating large ensembles of NV and MgV centers. Lastly, I will discuss the work done in fabricating vacancy-related defects in AlN..

4.1 Efficiency optimization of GeV quantum emitters in single-crystal diamond through ion implantation and HPHT annealing

In this section, a systematic analysis of the effects on the single-photon emission properties of GeV centers in HPHT treated diamond with respect to conventional thermal annealing will be presented. More precisely, the physical parameters needed to maximize the emission efficiency, in terms of optical excitation power and emission intensity, will be deeply emphasized.

The reason for this study was the significant challenges faced when creating group-IV related emitters due to the impact of keV ion implantation and standard post-implantation annealing processes[70], [270], [271]. When atomically large impurities are incorporated into the dense diamond crystal, they cause significant lattice distortion and residual radiation damage[82], [84], [272], [273]. This damage affects the environment of the color center formed, leading to a deterioration of its optical properties. One potential solution to this problem was suggested for the SnV and PbV centers by using a HPHT post-implantation annealing process[75], [84]. In both cases, treating the keV-ion implanted diamond at temperatures above >2000ºC and pressures around 7 GPa resulted in an improvement of the spectral emission properties by reducing the contribution from competing impurity-related defect configurations.

4.1.1 Samples preparation

The experiments were conducted on three single-crystal type-IIa diamond samples supplied by ElementSix. Samples **1** and **2** consisted of 2x2x0.5 mm^3 *electronic grade* quality substrates, characterized by a <5 ppb substitutional N and B concentrations, while sample **3** was a 3x3x0.3 mm^3 *optical grade* sample type, for which the nominal substitutional concentrations are N < 1 ppm and B < 0.05 ppm.

These samples were implanted at an energy of 40 keV with Ge^- ions at the low-energy accelerator of the University of Leipzig[74]. Four different regions of 200x200 μm^2 area were implanted for each of the samples at four different fluences between $1x10^{10}$ cm^{-2} and $1x10^{13}$ cm^{-2} using broad implantation with a collimating mask. Although the lower implantation fluences may be low enough to address the individual GeV centers, considering the formation efficiency of GeV centers is usually below 1% upon keV ion implantation and standard high temperature annealing treatment [274], the photoluminescence analysis was performed in the edges of the irradiated regions where individual centers could be easily individualized thanks to the scattering of the ions with the collimating mask that results on a lower density of ions in those borders[47].

On what regards the different treatments performed in each of the samples to understand the effects of each annealing process on the optical properties of the centers, the following conditions were studied:

- **Sample 1** underwent two subsequent post-implantation annealing processes in high vacuum conditions (< 5 x 10^{-6} mbar), one at 900 ºC for 2h and the following one at 1000 ºC for 10 h.
- **Sample 2** was treated at 1500 ºC for 1 h in high vacuum conditions.

- **Sample 3** was processed first at 950 ºC in high vacuum (after which no individual GeV centers could be individualized) and afterward, a 15 min annealing was performed at 2000 ºC under 6 GPa or HPHT treatment.

After each of these treatments (except for the 950 ºC in sample 3, where no individual centers were observed) the single-photon emission analysis was performed, including the analysis of the saturation parameters and the radiative lifetime of the centers.

4.1.2 HPHT treatment effects

As explained in Chapter 2.4.3 of this thesis, the HPHT treatment is quite an invasive annealing treatment for the diamond, as it undergoes the natural extreme conditions for its formation which may lead to an increase in the surface roughness or the introduction of undesired defects. That's why, it is important to explain the parameters and the effects that this annealing had on the studied sample.

The HPHT treatment was carried out at the V.S. Sobolev Institute of Geology and Mineralogy of the Siberian Branch of the RAS (Novosibirsk) under s stabilizing pressure of ~6 GPa via split-sphere multi-anvil apparatus (BARS)[74]. The pressure-transmitting medium employed for the annealing was cesium chloride (CsCl) which is a solid at ambient conditions but becomes a liquid under high-pressure conditions and provides quasi-hydrostatic conditions of annealing. The sample was then heated up to ~2000 ºC for 15 min.

A detailed examination of the sample surface using SEM imaging was conducted because it was expected the surface roughness to increase. As shown in **Figure 88**a, the surface displays uneven increase in roughness due to the formation of micron-sized seeds because of the HPHT conversion to diamond, as well as surface etching caused by high temperatures.

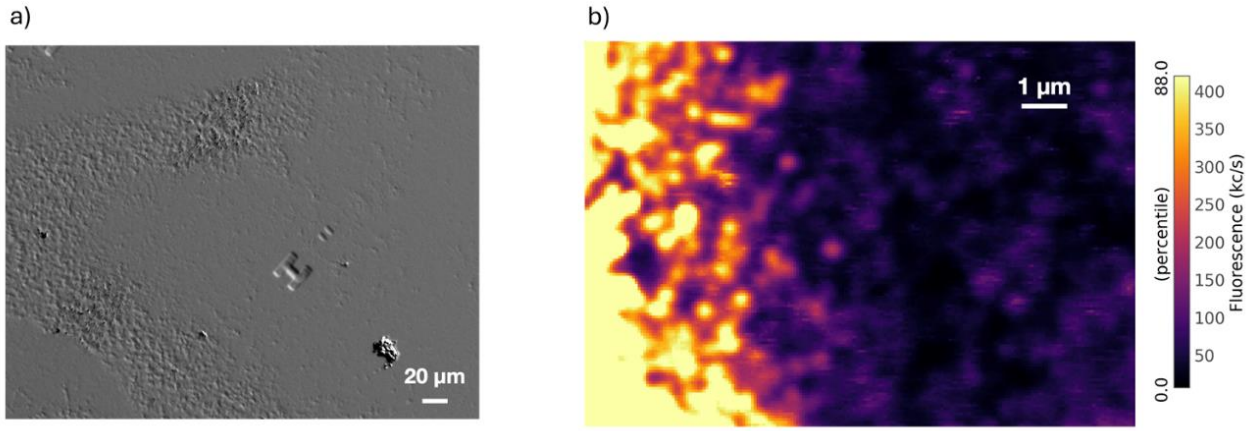

Figure 88 *a) SEM image of the HPHT treated sample, b) PL confocal microscopy map of the same region.*

If now we compare the surface roughness of Sample 3 displayed in **Figure 88**a with the one of Sample 1 after 900 ºC annealing treatment (shown in **Figure 89**a), it is apparent that the high temperature high vacuum treated sample didn't result in any apparent decrease inhomogeneity. However, looking at the corresponding PL maps performed using confocal microscopy for the Sample 3 in **Figure 88**b and **Figure**

89b no apparent effect of this surface roughness seems to affect the formation of stable single-photon emitters.

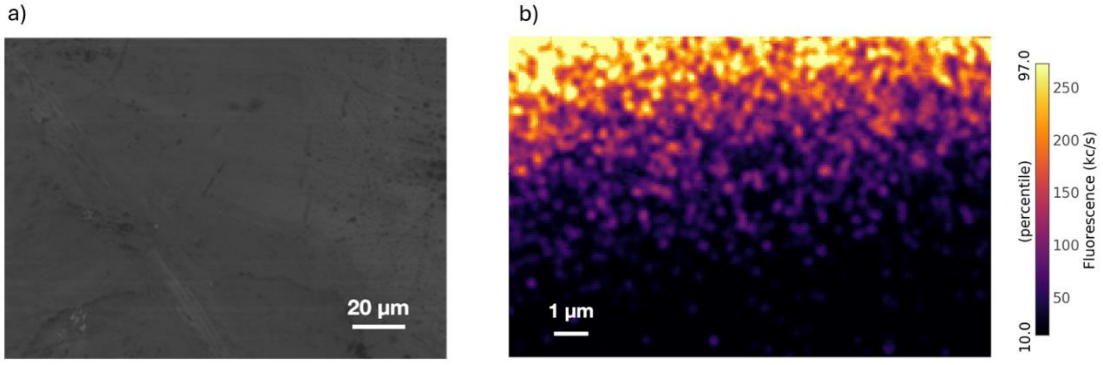

Figure 89 *a) SEM image of the Sample 1 after 900 ºC annealing, b) PL confocal microscopy map of the same region.*

Apart from the surface analysis, a PL ensemble spectral analysis was performed on the GeV region. The reason for this study was mainly based on the fact that the sample implanted, as has been previously stated, was an optical grade diamond, meaning the concentration of nitrogen impurities was quite high, leading to the difficulty of individualizing the single GeV center due to the high NV center background signal.

The photoluminescence (PL) spectra were captured at a temperature of liquid nitrogen (77 K) from the area that was implanted at a fluence of 3 x 10^{12} cm^{-2} before and after treatment. This was done using a custom-built setup relying on a Horiba JY iHR320 monochromator equipped with a Syncerity CCD detector, this preliminary spectral analysis was carried out by the researchers at the Sobolev Institute of Novosibirsk.

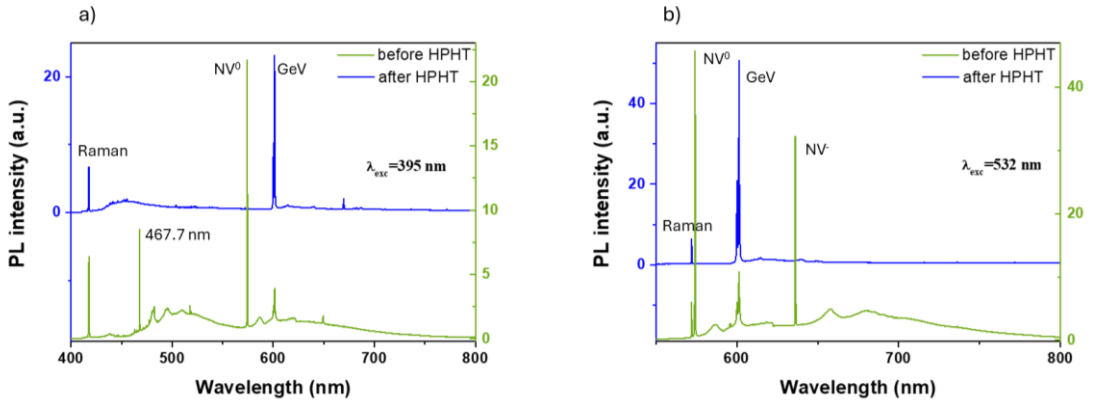

Figure 90 *PL spectra acquired from Sample 3 under a) 395 nm and b) 532 nm laser excitation before (green line) and after (blue line) HPHT annealing.*

As plotted in **Figure 90**, the PL spectra were acquired under both 393 nm (**Figure 90**a) and 532 nm (**Figure 90**b) CW laser excitation before and after the HPHT processing. Before the HPHT process, the spectra (green lines) mainly comprise native NV center emissions with zero-phonon lines at 575 nm and 637 nm[275]. The intensity of the NV centers is much higher than that of the GeV centers (ZPL at 602 nm). Additionally, an emission band with a ZPL at 467.7 nm (2.65 eV) and phonon replicas with 73 meV energy was observed in the spectrum excited with 395 nm. This band is probably attributed to intrinsic vacancy-related defects[46].

After the HPHT treatment, the PL spectra from the same area (blue line in **Figure 90**a and 90b) showed the complete disappearance of both the 467.7 nm feature and the NV-center-related emissions. This outcome is consistent with previous reports indicating the disaggregation of the NV and 467.7 nm[48] centers at temperatures 1500-1700 °C and ~1900 °C, respectively.

These results already provide a check for the HPHT annealing process as a functional tool for activating GeV defects at the ensemble level by lowering the amount of undesired impurities in the diamond (NV). However, we were still interested on the analysis of the properties at a single emitter level of GeV center as will be explained in the next section.

4.1.3 PL Single-photon emission analysis

The systematic characterization of single GeV emitters was carried out after each of the above-mentioned annealing treatments in the PL regime. The confocal microscope used was like the one described in the experimental methods section, using a 520 nm CW laser excitation and a dichroic mirror and a long pass filter at 550 nm. The spectral analysis, in this case, was carried out using a single grating monochromator (1200 grooves mm^{-1}, 600 nm blaze, ~4 nm spectral resolution) out-coupled via multimode fibers to a SPAD detector. The single photon emission was checked using the HBT interferometer, which was explained in the experimental section.

The assessment of the dependence of the emission properties of the GeV centers from the post-implantation treatment was then performed based on the following sampling: 15 GeV centers in Sample 1 after the 900 ºC and after the 1000 ºC annealing in high vacuum conditions; 13 GeV centers in Sample 2 after the 1500 ºC in high vacuum annealing, finally 15 centers were assessed in Sample 3 after the HPHT treatment.

The experimental approach that was adopted for the comparison of the optical properties of the studied centers was the following for all the exposed annealing conditions. Firstly, a PL mapping of the outer edges of the Ge^- implanted regions, to identify bright emission spots as potential single-photon sources. An example of a PL map where many spots can be individualized is plotted in **Figure 91**a. Secondly, after one diffraction limited spot was selected (i.e. the white circled one in **Figure 91**a), its spectrum was acquired in order to understand whether it was a GeV center or another type of color center. As can be seen in **Figure 91**b (black line), the individual GeV center showed a sharp ZPL (zero phonon line) at 602 nm with a low phonon sideband. It was always compared with the spectrum of the surrounding background aiming to understand if any of the signal collected was due to any other defect (red line), as can be pointed out the only thing present in the background spectrum is the first-order Raman peak from diamond

Afterwards, the single photon nature of the source was addressed utilizing HBT interferometry, acquiring different $g^{(2)}$ histograms at different excitation powers of the same center (**Figure 91**c). It is worth noting that all of these coincidence histograms are background corrected.

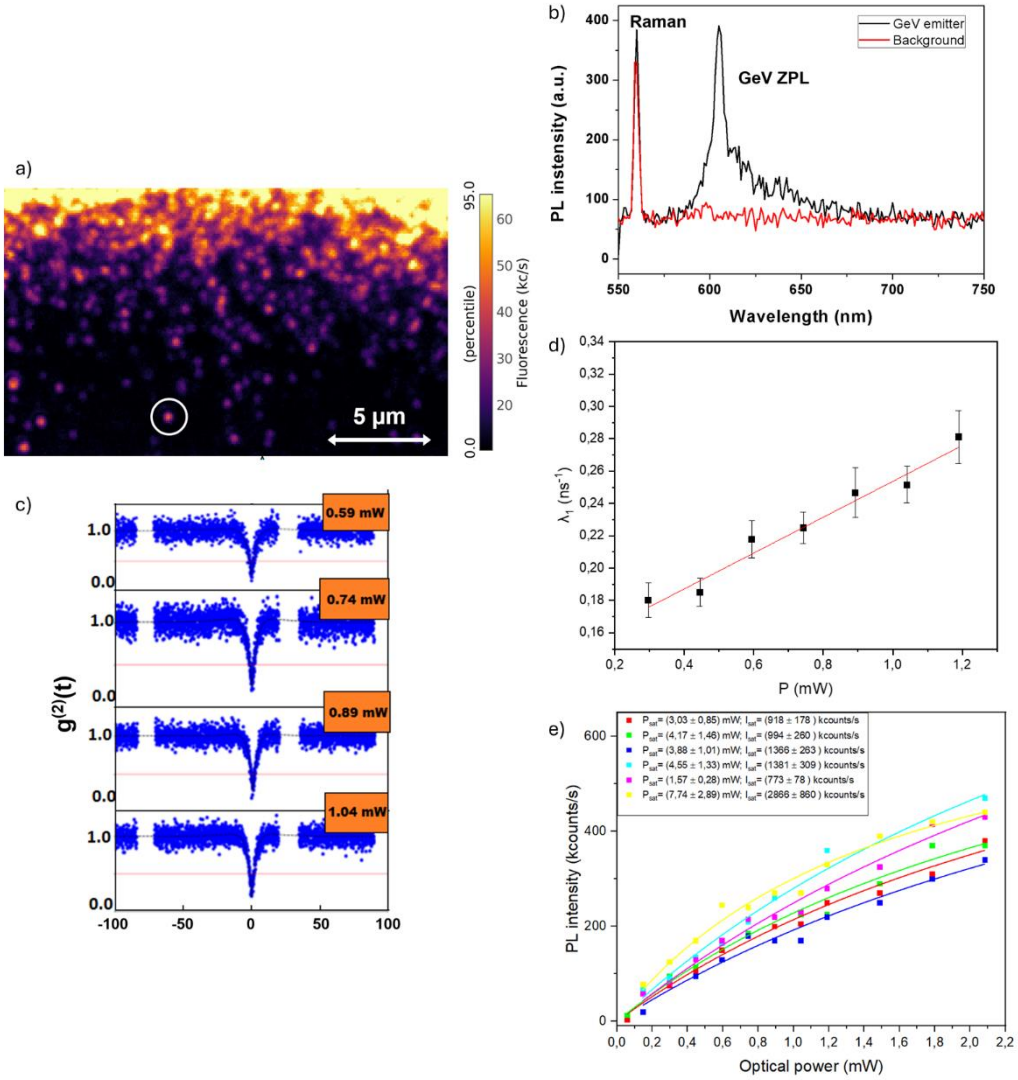

Figure 91 *Exemplary analysis in the systematic investigation of individual GeV centers formed by ion implantation and annealing a) PL map of the edge of a region implanted at a fluence of 2 x 10^{13} cm^{-2} after 900 ºC annealing, b) PL spectrum acquired under 520 nm laser excitation of a single spot circled in white in a), c) Second-order-auto-correlation histograms acquired from the same spot under several excitation powers (the removed parts correspond to the backflashes coming from the fibers), d) Linear regression of the λ_1 fitting parameter as a function of the optical excitation power and e) Intensity saturation curves of 6 individual GeV center acquired in Sample 1 after 900 ºC annealing treatment.*

After the second-order auto-correlation histograms ($g^{(2)}(t)$) were acquired, they were all fitted according to the expression for a three-level system[47]:

$$g^{(2)}(t) = 1 - A_1 \cdot exp(-\lambda_1 \cdot |t|) + A_2 \cdot exp(-\lambda_2 \cdot |t|) \qquad \textbf{Equation 45}$$

Where A_1 parameter quantifies the antibunching effect at t=0 delay while λ_1 parameter, is the reciprocal of the characteristic time constant of the center and depends on the optical excitation power *P* through a linear coefficient α as follows[270]:

$$\lambda_1 = \lambda_1(P) = \alpha \cdot P + \tau_1^{-1} \qquad \textbf{Equation 46}$$

Where the parameter τ_1 represents the lifetime of the excited state of each GeV center. Bearing this in mind, the criterion adopted in this work, was the assumption that a value $g^{(2)}(0) < 0.5$ confirmed the single-photon emission of the diffraction-limited spot[112], [276]. Considering this criterion, for each of these cases, the fitting was performed centering the attention on the λ_1 parameter and leaving the study of the power

dependence of the λ_2 parameter out of the scope of the work, considering the overall weak bunching that could be observed in all the studied emitters.

As can be pointed out in **Figure 91**d, the extracted λ_1 parameters from the curves were plotted with their corresponding excitation power giving place to a linear regression from which the lifetime of the center could be extracted, as the inverse of the origin of the regression $\tau = \lambda_1(P = 0)^{-1}$[81], [196], [277].

Finally, the assessment of the intensity saturation emission parameters was performed for the individual GeV centers. This measurement was carried out by acquiring the PL count rate *I* as a function of the optical excitation power *P,* upon subtraction of the background count rate acquired from the unimplanted surrounding region. In **Figure 91**e, the saturation curves of several individual GeV centers acquired from the map shown in **Figure 91**a are plotted. All these curves were fitted according to the saturation model[47]:

$$I(P) = \frac{I_{sat} \cdot P}{(P + P_{sat})} \qquad \textit{Equation 47}$$

Where I_{sat} and P_{sat} are the saturation emission intensity and optical power, respectively, they represent the maximum number of photons the center can emit and the laser excitation power required for reaching that intensity value , so the emission efficiency of the system is encrypted in these two parameters.

The experimental analysis above described was applied to investigate the statistical distribution of the key parameters for single-photon emission plotted in **Figure 92**: emission lifetime (**Figure 92**a), saturation excitation power (**Figure 92**b) and saturation emission intensity (**Figure 92**c).

The lifetime values of the emitters did not show a clear trend based on the annealing process (**Figure 92**a). The median values for the 900°C and 100°C processes (4.8 ± 1.9 ns and 5.9 ± 1.6 ns, respectively) are similar to the results from the samples treated at 1500 °C (3.0 ±0 .6 ns) and HPHT (7.0 ± 0.9 ns). Moreover, it is worth highlighting that the results from the HPHT-treated crystal are consistent with the ones observed at lower annealing temperatures (except for the 1500 ºC case). This suggests that using an "optical grade" sample does not lead to environment-dependent changes in the emission properties compared to using an "electronic grade" diamond. As a result, the HPHT treatment allows for the use of less expensive material substrates for GeV-based technological applications, this is also supported as will be explained afterward by the increase in the efficiency of the GeV defect emission upon HPHT annealing.

Although no specific trend was observed, to the best of my knowledge it was the first time a systematic assessment of the GeV emission radiative lifetime based on a statistical analysis was performed. Additionally, all the lifetime values reported in this work were ranged between 1.4-6.6 ns has previous reports had stated previously in literature[70], [72], [73], [278].

Concerning the statistical distribution of the optical excitation powers at saturation, we can point out in **Figure 92**c. The data indicates that there are no significant differences in the P_{sat} parameter for the 900 °C (3.0 ± 1.2 mW) and 1000 °C (3.1 ± 1.4 mW) annealing processes, consistent with previous reports. However, the saturation power decreases noticeably when the annealing temperature is raised to 1500 °C (1.2 ± 0.5 mW) and further decreases to (0.9 ± 0.3 mW) upon HPHT treatment. This can be attributed to the reduction of divacancy defects, which are a byproduct of the ion implantation process used to create GeV centers. If we consider the divacancy as the optically active defect that interferes with the charge state stability of GeV centers then high-pressure annealing efficiently promotes the disaggregation of these defects, leading to improved emission efficiency of the GeV center.

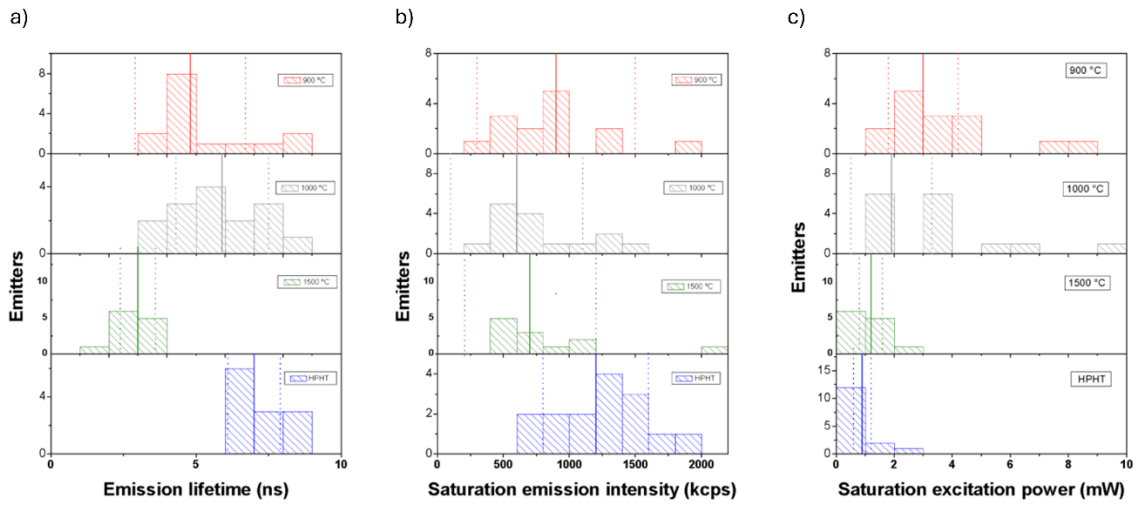

Figure 92 *Histograms of the results of a) emission lifetime b) saturation excitation power and c) saturation excitation power among a set of 57 single-photon emitters grouped by post-implantation annealing treatment. The vertical continuous lines indicate the median value of each distribution, while the dashed ones indicate the standard deviation.*

Regarding the saturation emission intensity (**Figure 92**c), the median I_{sat} values obtained for the four different annealing conditions (900 ± 600 kcps, 600 ± 500 kcps, 650 ±350 kcps, and 1200 ± 400 kcps) are fully compatible. However, the 900 °C and 1000 °C processes lead to a wide variability in the I_{sat} parameter. It's important to note that the >600 kcps values reported for each of these datasets provide strong experimental evidence of the promising quantum-optical performance of this system, especially when compared to the results of previous room-temperature characterization (in the 178±4 kcps - 790±20 kcps range). Additionally, previous works have identified several individual emitters exceeding 1 Mcps emission rates [70], [71], [73], [279], [280], which could be partially explained by assuming different detection efficiencies for the experimental setup.

While the overall data variability didn't allow for the identification of any significant trend based on the annealing temperature, it's worth mentioning that 60% of the emitters studied in the HPHT-treated sample exhibited >1 Mcps intensity at saturation, indicating a substantial positive effect of the process on the opto-physical properties of the GeV center.

All these median values are presented in Table 1 with the corresponding type of diamond and post-implantation treatment that it underwent before the analysis. The error shown corresponds to the standard deviation assuming a normal distribution.

Already from these highlighted data, one could state some conclusions:

- The radiative lifetime didn’t show any particular trend with the temperature neither with the type of sample that is being used (was not affected by the light N type doping caused by the high concentration of nitrogen).
- The median values for the emission intensity at saturation didn’t show any particular trend, however if looking at the distribution in the case of HPHT treatment, most of these saturation intensities stand above >1 Mcps, which is a value confrontable to the one reported for SnV centers under HPHT treatment.
- The saturation power values seem to have a decaying trend at increasing annealing temperature. In particular, upon the HPHT treatment most of the centers showed a a saturation value <1 mW.

Post-implantation treatment	Crystal quality	Median excited state radiative lifetime (ns)	Emission intensity at saturation (kcps)	Optical excitation power at saturation (mW)
900 °C 2 h	Electronic grade	4.8±1.9	900±600	3.0 ± 1.2
1000 °C 10 h	Electronic grade	5.9±1.6	600 ± 500	3.1 ± 1.4
1500 °C 1 h	Electronic grade	3.0 ± 0.6	650 ± 350	1.2 ± 0.5
HPHT (2000 °C, 6 GPa)	Optical grade	7.0 ± 0.9	1200 ± 400	0.9 ± 0.3

Table 2 *Table of the median values of excited radiative lifetime, saturation emission intensity, and excitation power acquired after each treatment.*

Finally, it has already been explained the effect of the annealing on all the parameters independently, however, it is important to analyze the dependence of the saturation parameters together. As every setup in which this analysis may be done may have a different collection and excitation efficiency, the analysis of power and intensity of saturation as independent variables may not be quite convincing as a result.

However, the performance of GeV centers as single-photon emitters can be evaluated by considering the ratio of the saturation optical excitation power to the emission intensity at saturation, $E_{sat} = P_{sat}/I_{sat}$. This ratio is inversely proportional to the system quantum efficiency and indicates the effectiveness of the optical excitation and radiative response of the system. Lower values of E_{sat} indicate lower energy required for single-photon emission[10], [41], [281], leading to a higher efficiency in the excitation-emission process. Achieving low E_{sat} values is crucial to enhancing emission intensity with minimal optical power consumption, enabling ultra-bright emission from individual GeV centers. **Figure 93** shows box chart plots summarizing the distributions of the E_{sat} parameters evaluated for the populations of emitters under investigation. The trend of decreasing E_{sat} at increasing annealing temperatures is evident, with the 1500 °C (1.5 ± 0.3 μJ/kcps) and the HPHT (0.5 ± 0.3 μJ/kcps) treatments leading to 2.6 and 7.8 times increase compared to the 900 °C annealing process (3.9 ± 1.6 μJ/kcps), respectively.

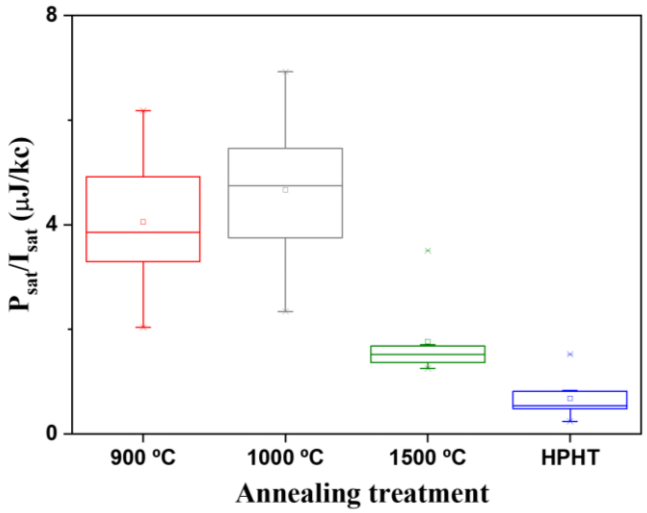

Figure 93 *Chart-box of the reciprocal of the quantum efficiency of the centers as a function of the annealing temperature undergone by the centers.*

4.2 CW laser activation of Sn-related defects in as implanted diamond.

In this section, an activation protocol of Sn-related defects using CW laser will be presented. In particular, in this study, the focus will be put on activating the 595 nm emission line related to the Sn ion implantation. In Chapter 1, the main characteristics of the SnV center were discussed, it was explained how the main emission (ZPL) of this center is at 620 nm. However, this center has been reported to display several other emission lines at 595 nm, 631 nm, 647 nm and 663 nm, whose origin and properties have not yet been fully understood. In this work, the main emission that will be analyzed will be the 595 nm spectral peak.

In the introductory part of this dissertation, it was explained how the most commonly used method of introducing defects in diamond involves ion implantation followed by high-temperature annealing for promoting the formation of stable defects in the desired structural configuration. However, the formation efficiency, as mentioned before, has been reported to be low for SnV upon conventional thermal annealing[85].

Recent emission channeling experiments have reported that the structural formation efficiency, intended as the fraction of implanted ions that result in a bond-centered configuration of the defect in the lattice, exceeds 40% for the SnV implanted samples without any further thermal process [282]. This bond-centered configuration is related to the split-vacancy configuration (see **Figure 94**c) of the SnV defect but doesn't consider the number of vacancies that are linked to the impurity[282]. Despite this difference, a non-negligible number of centers in the split-vacancy configuration can be hypothesized upon ion implantation. However, the photon emission coming from these color centers does seem to require a further activation step, as no emission has been reported up to this work coming from this color center before any further annealing[22], [283]. This further step is commonly achieved by thermal annealing, however, in this work, the laser activation of this defect was addressed aiming to stabilize the defect into the right electronic configuration.

4.2.1 Sample preparation

The experiments were performed on a type IIa single crystal, *electronic grade* type of diamond. The sample was implanted using the 100 keV ion implanter presented in the experimental Section 3.1. The ions implanted were Sn^- at an energy of 56 keV, reaching a depth in the diamond of around 20 nm[178]. The implantation scheme is presented in **Figure 94**a, in this case, an aluminum mask with a hole drilled with the high-power laser of 200 x 200 μm^2, was used to collimate the beam and limit the region of implantation. The chosen fluence was $1x10^{12}$ ions/cm^2, as the study was planned to be performed at the ensemble level and not centered at the single-photon level activation.

After the implantation, the sample was not treated, meaning that no annealing or surface termination was induced on it. The photoactivation study and the photoluminescence readout of the centers activated were both performed in the same confocal setup, reported in **Figure 84** of Chapter 3.

The characterization of the PL signal coming from the sample was performed using a 522 nm laser diode (probing laser) at a fixed optical power of 100 μW on the sample surface. The choice of this optical power was based on the use of a low enough power to not give rise to the photoactivation of any centers in the implanted region.

On what regards the photoactivation of Sn-related emission in the as-implanted sample, several processing wavelengths were considered. For this activation process, four different continuous wave (CW) lasers (processing lasers) emitting at 405 nm, 445 nm, 509.5 nm and 522 were employed. The confocal combination of the probing and processing lasers was implemented by the use of a dichroic mirror with a cutoff wavelength at 520 nm (see **Figure 84** of Chapter 3).

An investigation was conducted to examine the impact of optical power and duration of laser exposure on the photoactivation for each processing wavelength. The study involved the processing of the implanted region of the sample by creating a grid of spots (see Figure 7b) with different laser irradiation parameters. This included varying optical powers (ranging from 1 to 25 mW) and exposure times (ranging from 1 to 75 minutes) for each activation wavelength. Through this setup, we were able to determine the relationship between photoactivation efficiency and the energy delivered to the sample through laser irradiation. Additionally, longer irradiation periods (10 hours) were performed at the maximum power available for each activation wavelength to identify the asymptotic behavior of the photoactivation process.

The assessment of the irradiated grids by PL mapping was carried out before and after the laser irradiation, by exploiting a 550 nm dichroic mirror and a long-pass filter at 550 nm to cut the reflection from the laser source. Additionally, the spectral analysis was centered in the 580-680 nm spectral window, as the two spectral features of interest (595 nm and 620 nm) were englobed in this range[75]. To compare the spectra acquired, a background (signal coming from the unirradiated area of the sample) subtraction was performed along with a normalization to the first-order Raman peak intensity.

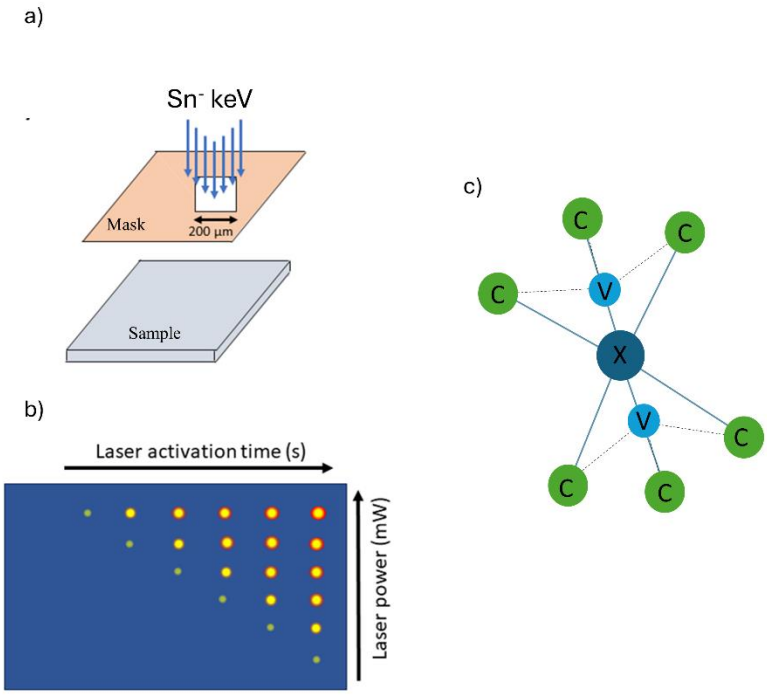

Figure 94 *a) Implantation scheme of the sample, including the mask with a 200 um hole and the diamond, b) Laser irradiation scheme implemented, c) Split-vacancy configuration of the tin-vacancy center.*

4.2.2 Laser irradiation power and exposure time analysis

An exemplary PL map after the laser irradiation and spectrum acquired from the white-circled point are reported in **Figure 95**. The PL map presented in **Figure 95**a, corresponding to an irradiation wavelength of 405 nm, shows the grid of regularly spaced spots under different optical power (increasing arrows, from bottom to top) and different exposure times (increasing columns, from left to right). To analyze the activation of these spots, that show an increase in PL signal with respect to the not processed area, a systematic spectral analysis was conducted. An exemplary spectrum of one of the activated spots is shown in **Figure 95**b, denoting a sharp 595 n Sn-related peak. This peak, despite not being the well-known 620 nm ZPL of the SnV[80], [284], has been previously reported by Iwasaki et al[75], which hypothesized it to be a Sn-based center in a not exact split-vacancy configuration, so either the Sn atom is not placed exactly in the middle of the two vacancies, or the vacancy configuration is not the one desired. No further studies have reported on this PL peak up to this work, so information on the energy levels of the system is still missing in order to fully understand the process that is taking place. However, the study was mainly based

on the activation of this 595 nm peak, although some results on the 620 nm ZPL of SnV will be presented[75].

Along with the 595 nm peak spectrum, in **Figure 95**b, a spectrum of the background surrounding the activated spot is presented (orange curve), evidencing the lack of this 595 nm spectral signature and the sole presence of the first-order Raman peak (1332 cm^{-1}).

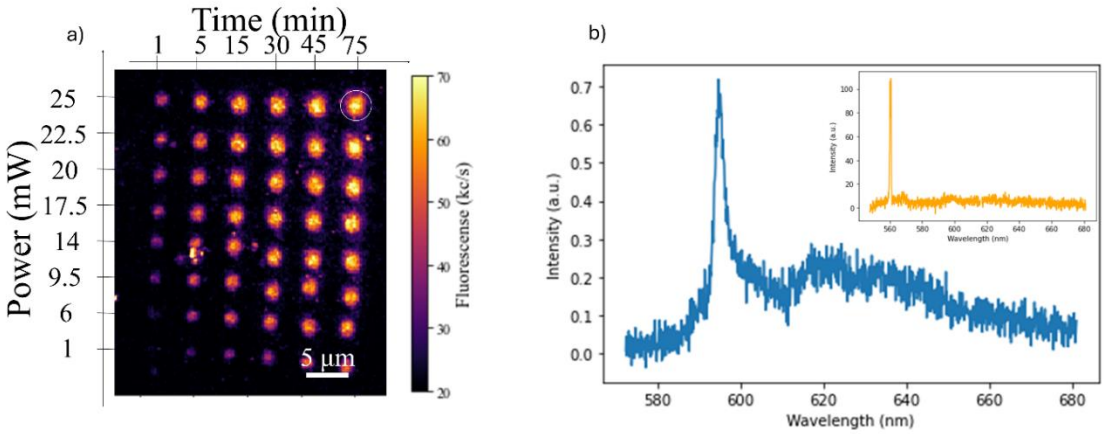

Figure 95 *a) PL map of the laser-irradiated region ,implanted with Sn ions, at different exposures times and optical powers of the 405 nm laser. b) Exemplary spectrum of the white-circled spots in a).*

The PL emission rate increased as the optical power of the processing laser increased, indicating a clear correlation between the sample exposure and the activation yield of color centers. This correlation can be seen in **Figure 96**a, where the area underlying the emission spectra profiles is plotted against the 405 nm processing optical power for two exposure times (1 min and 75 min). The data shows a clear increasing trend with saturation behavior at high optical powers. In addition to studying the power dependence, the PL emission rate's dependence on the lasing exposure time was investigated for each optical power. **Figure 96**b shows the intensity of each activated spot of Sn-related emitters under different time exposures with a 405 nm processing laser wavelength under two different optical powers. An increasing trend with exposure time is observed in all cases, without apparent saturation behavior for the high-power case.

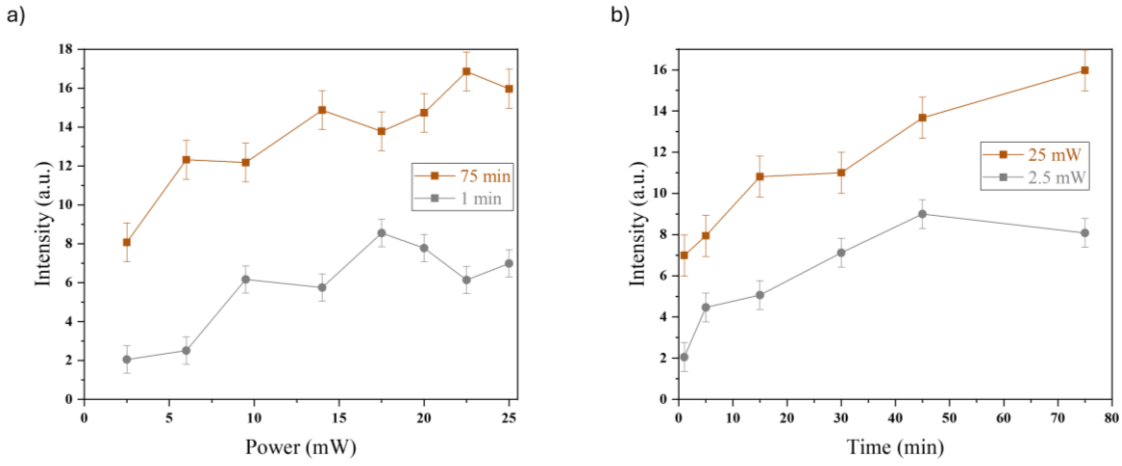

Figure 96 *c) Emission intensity of the 595 nm peak extracted from the area under the emission spectra between 580-680 nm as a function of the optical power of the 405 nm irradiation laser for 75 min irradiation time and 1 min irradiation time, b) Emission intensity under the same processing wavelength of the 595 nm peak as a function of irradiation time for 2.5 mW and 25 mW of power laser.*

After the independent analysis of the power and time of exposure was carried out, both parameters were combined, aiming to understand the dependence of the PL intensity on the energy delivered to each of the

processed spots (see **Figure 97**). The asymptotic behavior of the process is reported, corresponding to the point irradiated at maximum power (25 mW) for 10 h.

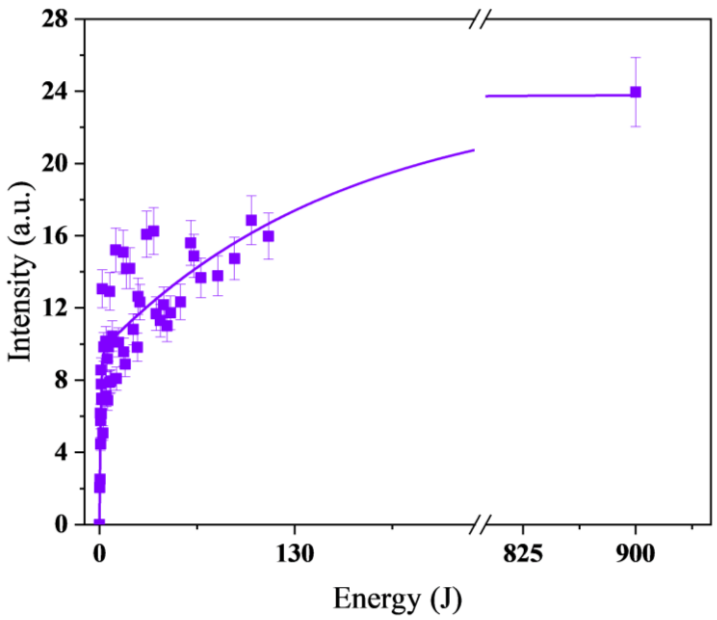

Figure 97 *Emission intensity coming from the irradiated spots (405 nm irradiation) and readback with 522 nm laser as a function of the energy delivered to the spots.*

In order to understand these results, a theoretical model was hypothesized, considering the following assumptions. The process observed was interpreted as a laser-induced optical activation of an ensemble of defects which are already available in the diamond lattice in the bond centered configuration, as was above mentioned, but are denoted by an electronic configuration associated with a dark state of the defect. This assumption was taken since the considered wavelengths and instantaneous optical powers were not sufficient to introduce any thermal-related structural modification comparable with the typical annealing temperatures required for vacancy diffusion[285], [286].

The total number of Sn-related centers in the bond-centered configuration N_{BC} is given by the sum of those that are in the active and inactive configuration[287].

The total density number of Sn-containing bond-centered defects N_{BC} is given by the sum of between the active N_A and inactive N_{IA} configurations:

$$N_{BC} = N_A + N_{IA} \qquad \textit{Equation 48}$$

The photoinduced conversion between those two can be thus described by the following time dependent rate equation:

$$\frac{dN_A(t)}{dt} = r_{21}N_A(t) - r_{12}N_{IA}(t) \qquad \textit{Equation 49}$$

Where r_{21} (r_{12}) indicates the activation (deactivation) rate related to the conversion from (to N_{IA} to (from) N_A. By combining) **Equation 48** and **Equation 49** and implementing the constraint that the N_A, is 0 at time 0 as has been seen in the data reported previously, the expression for the density of Sn-related active centers as a function of the exposure time to the processing laser can be written as follows[287]:

$$N_A(t) = \frac{r_{21}}{r_{21}+r_{12}} N_{BC}\left(1 - e^{-t(r_{21}+r_{1t})}\right) \qquad \textit{Equation 50}$$

Here, r_{21} *and* r_{12} can be regarded in general as transition rates dependent on the wavelength λ and power P. The asymptotic behavior at t→∞ is indicative of the maximum fraction $r_{21}/(r_{21}+r_{12})$ of bond centered centers that can be converted to Sn-related defects.

If the photoactivation is considered as a one-photon absorption process, the transition rates can be described in simple terms as $r_{21} = a_{21}(\lambda)P$ and $r_{12} = a_{12}(\lambda)P$[287].

Considering this dependence, the number of centers activated can be written in terms of the total energy E deposited within the diffraction-limited focal point of the optical objective:

$$N_A(E) = \frac{a_{21}}{a_{21}+a_{12}} N_{BC}\left(1 - e^{-E(a_{21}+a_{1t})}\right) \qquad \textit{Equation 51}$$

The intensity coming from the activated spots *I*, should be directly proportional to the number of centers activated and so the intensity coming from the center as a function of laser irradiation energy:

$$I(E) = I_0 e^{-E(a_{21}+a_{1t})} = I_0(1 - e^{-E/\alpha}) \qquad \textit{Equation 52}$$

Where α is inversely proportional to the sump of the transition rates and I_0 is the intensity at saturation of the activation process. The fitting curve in **Equation 52** however, didn't fit the data reported in **Figure 97**, as it does with the other wavelengths studied: 445,509.5 and 522 nm. A reasonable agreement was found for the data fitting by adding a second exponential term to the fitting function, as follows:

$$I(E) = I_0\left(1 - a\, e^{-\frac{E}{\alpha}} - b\, e^{-\frac{E}{\beta}}\right) \qquad \textit{Equation 53}$$

Where α and β are dependent on the activation and inactivation of the centers and represent how fast the process is in terms of energy. I_0 represents the amount of intensity at saturation upon this activation process, while a and b are the saturation parameters for each of the activation parameters α and β, respectively. The introduction of the second exponential is based on the hypothesis that two independent processes are occurring, these two exponential expressions has two independent energy terms, α and β, each of one corresponding to the energy scale at which each of the processes becomes more probable.

Each of these parameters was extracted from the curve fitting, obtaining the following results:

$$I_0 = 23{,}83 \pm 2{,}22\ a.u. \qquad \textit{Equation 54}$$

$$a = 0.392 \pm 0.037\ a.u. \qquad \textit{Equation 55}$$

$$b = 0.599 \pm 0.038\ a.u. \qquad \textit{Equation 56}$$

$$\alpha = 0.86 \pm 0.29\ J \qquad \textit{Equation 57}$$

$$\beta = 163.16 \pm 48.62\ J \qquad \textit{Equation 58}$$

As can be pointed out from these results, two processes are present, one of which (the one related to α) seems to have a high increasing velocity, characterized by a low $\alpha < 1$ parameter, this behavior can be also appreciated in **Figure 97** by looking at the abrupt increase in the first part of the curve. The second parameter β however is much higher, characterizing a much slower process, as it can be also pointed out in the second part of **Figure 97**.

This double-process behavior was observed along with the presence of the 620 nm peak in some of the spectra acquired after the laser irradiation in this region, as can be seen in **Figure 98**b. This data suggests the presence of a first activation process related to the 595 nm peak coming from the ionization of the defect and probably due to a charge state change, followed by a much less probable activation process, related to the SnV already in split-vacancy configuration, that is probably also present in a different charge state and required the photo pumping of carriers into the defect to change its charge state to the optically active one at 620 nm. This second peak activation, related to the SnV, was not extensively studied as no particular

trend was observed as a function of the energy induced, and further research would be needed to understand the optimal formation of the SnV defect.

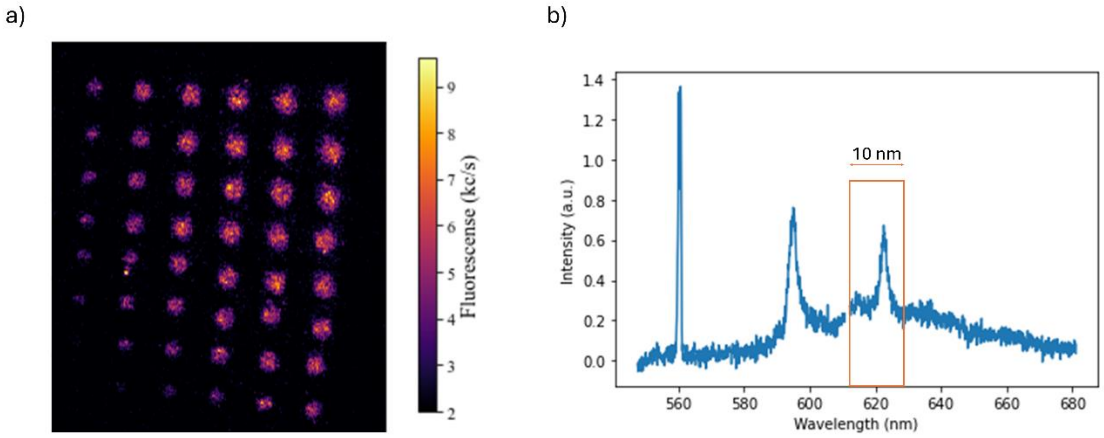

Figure 98 *a) PL map of the region activated with 405 nm laser with BP 620 (10 nm width) c) Spectrum acquired without BP where the ZPL of SnV centers can be seen along with the 595 nm peak.*

4.2.3 Laser irradiation wavelength analysis

The same analysis explained in the previous section was carried out for three additional laser irradiation wavelengths: 445, 509.5 and 522 nm. The parameters used for each of the irradiation wavelengths varied in terms of optical power, depending on the limitations of the laser used, while the times used were the same as for the 405 (1-75 min). The deposited energy range studied for each of the lasers is reported in Table 2. For the 405, 445 and 509.5 nm the point at maximum power for 10 h was performed, while in the case of 522 it was not possible to do it, due to a problem with the laser diode, whose emission was not stable anymore.

Processing laser wavelength (nm)	Processing optical power range (mW)	Deposited energy range (J)
405	1.0-25.0	0.1-900.0
445	0.8-5.0	0.1-136.8
509.5	1.0-18.0	0.1-648.0
522	1.5-7.7	0.1-35

Table 3 *Laser irradiation parameters of time and power for each of the processing lasers*

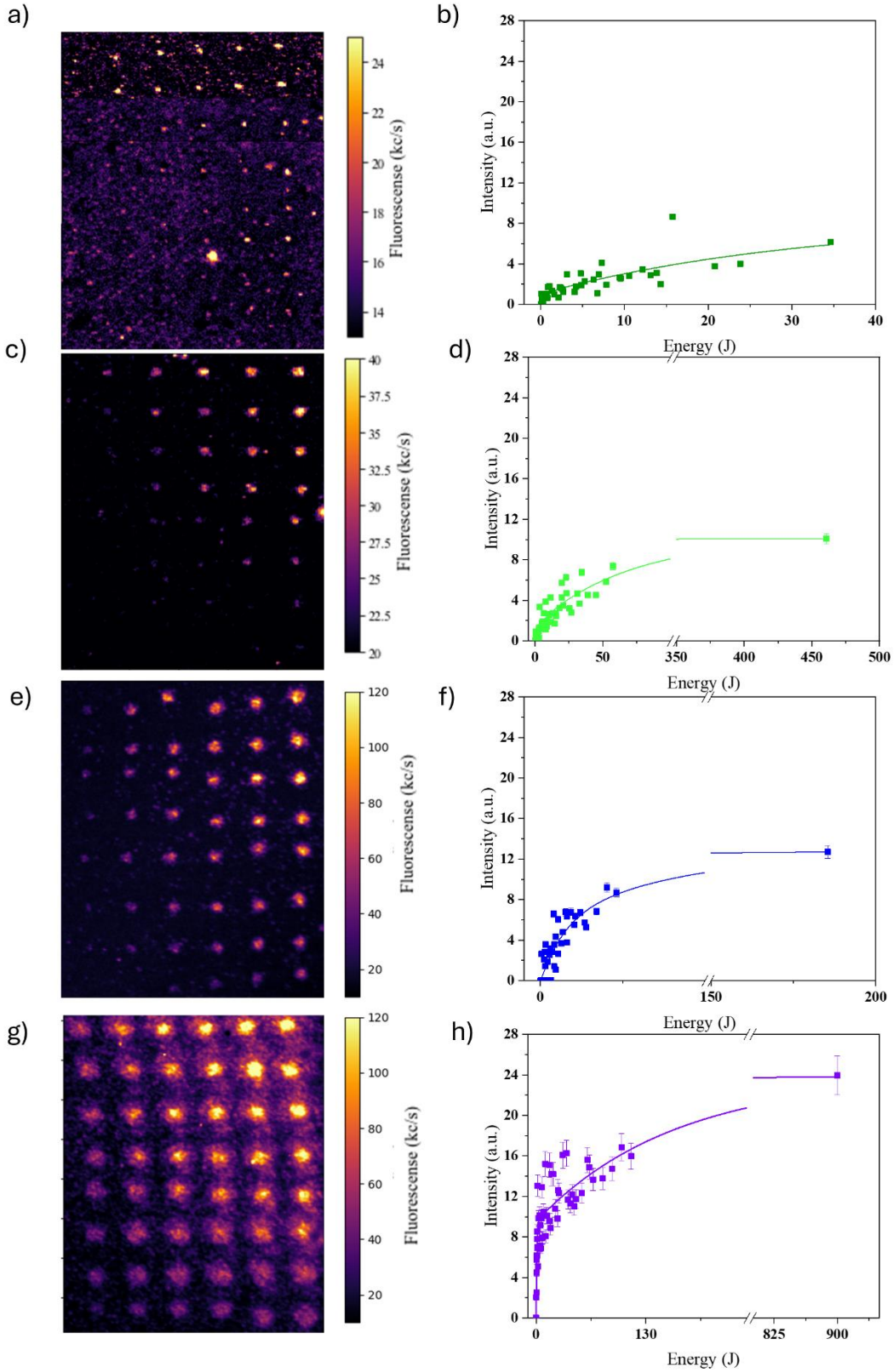

Figure 99 *First column includes the PL maps of the irradiated regions with different laser, readback at 100 uW with 522 nm laser: a) 522 nm, c) 509.5 nm, e) 445 nm and g) 405 nm. Second column reports the intensity coming from each of the spots as a function of the energy delivered with each of the lasers: b) 522 nm, d) 509.5 nm, f) 445 nm and h) 405 nm.*

In **Figure 99**, the PL maps acquired in each of the laser irradiated regions along with the intensity of each of the irradiated spots, extracted from the area under the spectral curve of the spots normalized to the first-order Raman and background subtracted, as in the 405 nm case. For each of the lasers presented in this figure an increase of PL signal can be appreciated after the irradiation with respect to the non-laser irradiated area, so the model explained in **Equation 52 and Equation 53** was applied for each of them. Additionally, a higher wavelength of irradiation was use as processing laser, 593 nm laser source, however this laser didn't give rise to any visible increase in PL, suggesting an energy threshold to this phenomenon[287], [288].

The curves plotted in **Figure 99** were fitted according to the model described in **Equations 52 and 53**. Except for the 405 nm case, as has been mentioned above, the use of a single-exponential was enough to describe the process (**Equation 52**), indicating the photoactivation process involved the ionization of a single dark charge state into the optically-active 595 nm emission. Unlike the 405 nm laser processing, no apparent activation of the 620 nm peak could be observed, confirming the relation of the second exponential to the activation of the 620 nm ZPL of SnV.

In **Figure 100**a, the emission intensity at saturation I_0 is plotted as a function of the irradiation wavelength. As can be observed, I_0 decreased as the processing photon energies increased, indicating a higher activation efficiency as lower wavelengths. On what regards the α parameter, it appears to be similar (see **Figure 100**b) for the three higher wavelengths that were fitted with a sole exponential, while in the 405 nm this parameter is one order of magnitude lower, indicating a quicker process in terms of energy. This lower α parameter is accompanied by a much higher β parameter indicating a much slower process, possibly related to the 620 nm peak activation.

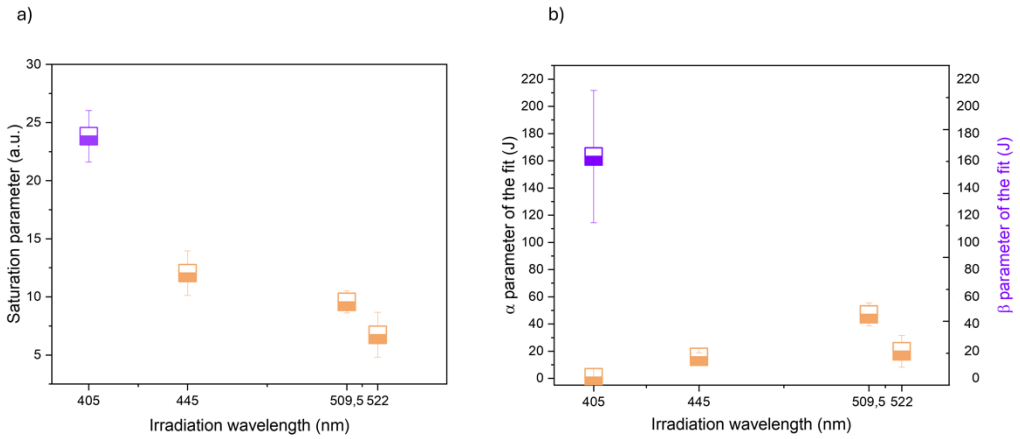

Figure 100 *a) Asymptotic PL intensity of the Sn-related defects fabricated as a function of the processing laser wavelength, as extracted from the curve in Eq.52. b) Dependence of the α and β from Eq.53. extracted from the curves in Figure 99, as a function of the processing laser wavelength.*

Finally, we estimated the formation efficiency of the process. This was achieved by identifying several single emitters with the 595 nm ZPL around the irradiated spots. We then performed second-order autocorrelation measurements to confirm that they were indeed single-photon sources. This information is presented in **Figure 101**b. After identifying the single emitters, we extracted the area under the curve of the spectrum shown in **Figure 101**b. We did this to compare it with the intensity emanating from the array spots.

In **Figure 101**c, the intensity dependence from the spots is plotted for four irradiation wavelengths. It is shown as a function of the energy that is introduced through the laser into the defect. As we've mentioned earlier, the 405 nm laser is the most efficient, while the 520 nm shows the least intensity coming from the spots.

Considering the number N_i of Sn ions introduced by ion implantation in the confocal volume as the product between the implantation fluence F=1 x10^{12} cm^{-2} and the confocal spot size given by the diffraction limit (A=7x10^{-2} μm^2) and the number of ions activated N_{act} as the ratio between the area under the spectral curve of a single ion (**Figure 101**b) and the area under the curve of the activated ensemble spot (left values of **Figure 101**b). The ratio N_{act}/N_i offered a direct assessment of the Sn-related centers formation efficiency for the process, defined as the number of optically active emitters per implanted ion. These values are shown in the right vertical axis of **Figure 101**c.

In this energy range, we obtain almost a 4.2% formation efficiency in the case of a 405 nm laser. Although the reported formation efficiency in literature for most centers is higher than what we are reporting here for the 595 nm activation, it is important to note that we did not use high temperature annealing to activate these centers. This raises an interesting opportunity for future research, particularly in terms of enhancing the formation of the 620 nm ZPL of the SnV. However, conducting a thorough investigation on this would require more time than is available within the scope of the PhD thesis. Nonetheless, the presented study yields interesting initial findings that could offer a technique for directly creating color centers in ion-implanted diamond.

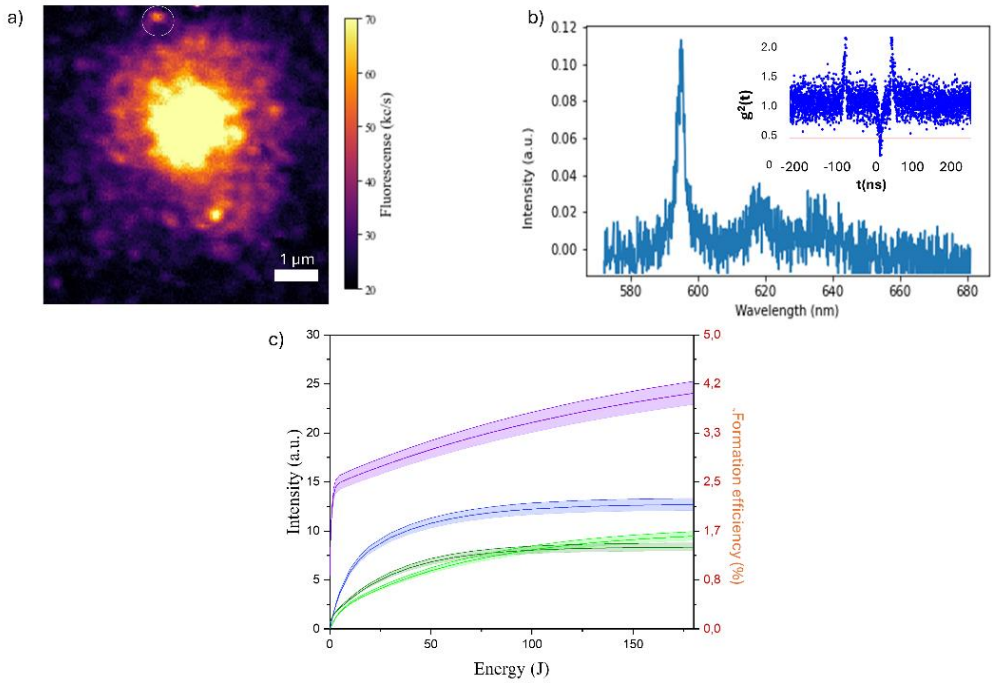

Figure 101 *a) 10 h irradiated spot under 405 nm processing laser, with single emitter circled in white, b) Spectrum of 595 nm peak center with g2 background corrected, c) Intensity as a function of the energy introduced into the region in black and formation efficiency calculated extracting the area under the curve of the spectra in b), in red.*

4.3 Creation of high-density color center ensembles efficiently by utilizing ion implantation on a heated diamond substrate.

After the study presented in the second chapter showing a new activation method for Sn-related defects, in this section, the heating of the diamond while the ion implantation is being performed for the formation of two different centers, NV and MgV, will be discussed.

As previously mentioned, the most direct way to create localized color centers is by using ion implantation followed by high-temperature annealing[85]. Specifically, NV centers can be easily created by introducing nitrogen ions into the crystal lattice, allowing for precise control of the volume density, ranging from individual ions to high-density ensembles of emitters[61], [199]. However, there is a limit to the density of NV centers due to radiation damage that can cause the diamond to become amorphous at high doses[179], [289]. Additionally, the efficiency of forming optically active color centers from implanted ions is typically below 10%, unless co-implantation of dopants or additional irradiation is carried out for both NV and MgV[85].

Both the graphitization threshold and the sub-optimal conversion efficiency concur to determine the maximum density of color centers that can be produced in diamond through conventional ion implantation at room temperature. In this section, the effects of MeV nitrogen implantation in a heated diamond substrate (500 ºC and 750 ºC) compared to room temperature implantation will be explored, using various ion fluences around the graphitization threshold of diamond. Additionally, the creation of ensembles of MgV centers through heated implantation at different temperatures (300 ºC, 500 ºC, and 700 ºC) in comparison with room temperature conditions will be studied[245].

4.3.1 Samples preparation

The experiments were conducted on two different samples, one for the NV and the other one for the MgV fabrication. The first sample, from now on referred to as ***Sample 1***, was an *optical grade* type of sample for the N^+ implantation while for the second sample, ***Sample 2,*** an *electronic grade* was employed for performing the Mg^+ implantation. Both implantations were carried out at the microbeam MeV line of the accelerator in Ruđer Bošković Institute.

Prior to ion implantation, both samples were masked with a thick metal layer (> 150 μm thickness), in which several apertures of 100 x 200 μm^2 were milled to define the regions of the same where each implantation at each temperature was performed, thus enabling their homogeneous assessment and comparison after the implantation. In this case, the implantation beam was a micro-sized MeV (~10 μm diameter) beam that was scanned over the regions of interest instead of a broad beam with collimated masks. The schematics of the implantation are presented in **Figure 102**.

For ***Sample 1***, the implantations were performed with 2 MeV energy N^{2+} ions at 4 different fluences. The chosen fluences: 1×10^{15} cm^{-2}, 5×10^{15} cm^{-2}, 1×10^{16} cm^{-2}, and 2.5×10^{16} cm^{-2}, were selected all around the graphitization threshold of diamond at the given energy, meaning the number of vacancies created by the implantation were all around the amorphization threshold, as calculated using the Monte-Carlo simulation software SRIM (see **Figure 103**).

Three regions were implanted for each of the fluences, differing for the temperature at which the diamond substrate was held. The temperatures adopted were the following: first the room temperature (22 ºC) implantations took place, followed by the 550 ºC irradiation and lastly the three last regions were fabricated at a fixed temperature of 750 ºC. In this way, at the end of the implantation processes, all of them were processed at the same maximum temperature. The timescale at which the ion implantation was performed was defined in order to avoid the introduction of the radiation damage in the crystal lattice at a too high

rate, in this way, all the implantations were performed on a timescale of 1 hour by adjusting the ion current of the beam accordingly, in a range between 50 and 150 pA.

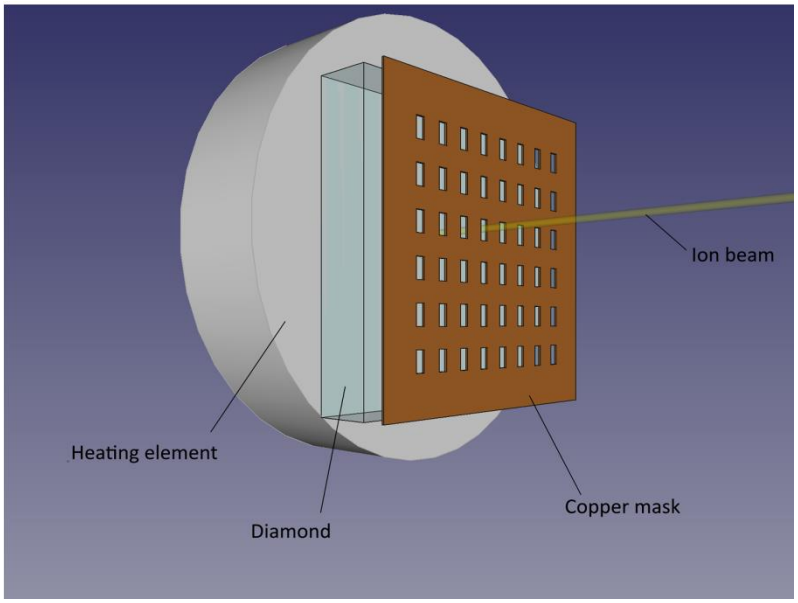

Figure 102 *Schematic representation of the implantation set-up including the heating element and the copper mask.*

Sample 2 was implanted using the same implantation scheme represented in **Figure 102**. In this case, the implantations were all performed at a fixed fluence of $1x10^{14}$ cm^{-2} way below the graphitization threshold, aiming to study the ensemble formation of the centers. The beam consisted of 2 MeV Mg^{+} ions that were focused down the to 10 µm diameter spot size, as for Sample 1. In this case, a single region was implanted for each temperature, and in total 4 different temperatures were assessed. Both the effects of the in-situ annealing and the lowest temperature at which these emitters were optically activated wanted to be understood, so in this case first the 700 ºC implantation took place, followed by the 500ºC, 300 ºC and lastly the room temperature one (22 ºC).

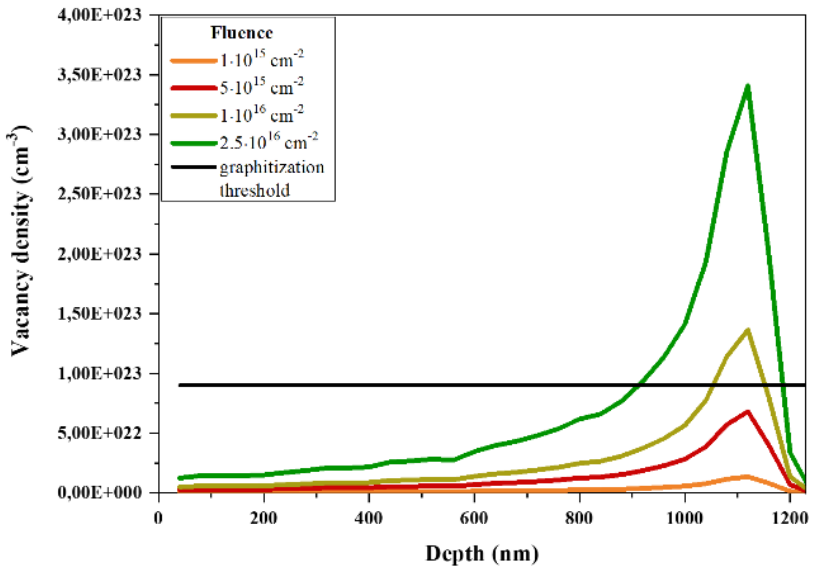

Figure 103 *Vacancy density introduced into the diamond at different fluences and the graphitization threshold at MeV energies.*

After the ion irradiation, the first sample was characterized using photoluminescence (PL) before any subsequent thermal annealing process. The characterization was performed using confocal Raman

spectroscopy with a Horiba-Jobin-Yvon LabRam HR-VIS instrument equipped with a Peltier-cooled CCD detector array. The process involved 532 nm laser excitation with a power of 21.6 mW and a 20x air objective. The same set-up was employed for the post-annealing characterization of both samples.

For the second sample, after the ion irradiation, the signal coming from the implanted regions was not high enough to address it with the previously explained setup, so a homemade confocal microscope coupled to a monochromator (see Section 4.1.1) was used, under 200 µW 520 nm CW laser excitation.

Additionally, ***Sample 1*** underwent a 950 ºC annealing in high vacuum conditions (< 5x 10^{-6} mbar) for a total processing time of 12 hours. The annealing time was chosen one order of magnitude larger than the initial implantation time in order to understand whether at long time scales of post implantation annealing, the hot annealed regions displayed any difference with respect to the room temperature implanted ones.

Sample 2 was similarly processed, however, in this case, the sample was heated up to 900 ºC four times with a process duration of 2h, 4h, 3 h and 3h, so in total the sample underwent a 12 h process. After each of these treatments, the sample was characterized using the same confocal Raman spectroscopy as for the NV sample.

4.3.2 NV center formation and graphitization

In the previous section, we explained the selection of four implantation fluences around the known graphitization threshold of diamond for MeV ion irradiation[179]. **Figure 103** highlights that the first two fluences did not result in a vacancy density profile exceeding this threshold, while the Bragg peak of the last two suggest the formation of an amorphous layer at the end of the ions range that would be irreversible converted in graphited upon thermal annealing above 800 ºC if the ion implantation occurred at room temperature.

In **Figure 104**a, an optical micrograph of the areas implanted at different temperatures in ***Sample 1*** before any ex-situ annealing, is presented. As expected, in the first column (the one implanted at room temperature) the highest implantation fluences exhibit a significant optical opacity, that indicates the amorphization of the irradiated areas. If we observe the two right columns, the ones implanted at 550 ºC and 750 ºC, none of these high-dosed regions show the same opacity, suggesting an increase in the graphitization threshold.

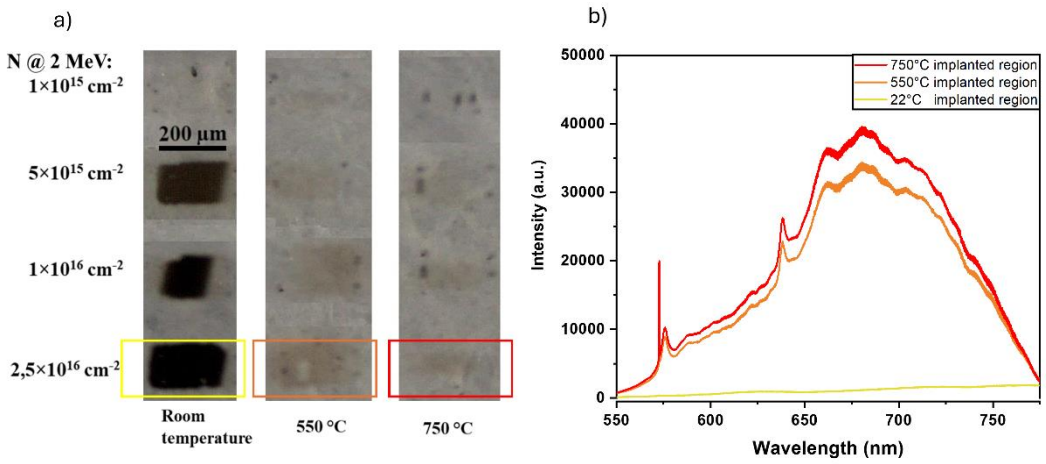

Figure 104 *a) Optical micrograph of the areas implanted at different temperatures before ex-situ thermal annealing in Sample 1. b) PL spectra acquired from the three regions implanted at the highest fluence 2.5 x 10^{16} cm^{-2} at different temperatures after the ex-situ thermal process.*

It is however convenient to analytically analyze this data, both aiming to understand the formation of NV centers and the graphitization threshold. **Figure 104**b, shows the highlighted set of PL spectra in **Figure 104**a, after the additional thermal annealing of 12 h at 950 ºC. Considering all the spectra were taken in the same atmospheric and experimental conditions, several features can be remarked. First for the red (750 ºC) and orange (550 ºC) lines, the first-order Raman scattering at 572.6 nm [290] under 532 nm laser excitation

is present in the spectra and both the ZPLs of the neutral (575 nm) and the negative (638 nm) charge state of the NV center with their corresponding phonon replicas at higher wavelengths [30]. Additionally, none of these features is visible in the room temperature implanted region (yellow line), demonstrating how the graphitization of diamond leads to a decrease in the NV formation.

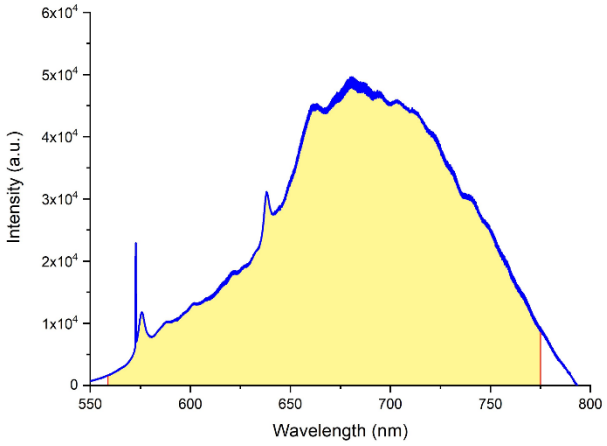

Figure 105 *PL spectrum acquired from the region implanted at room temperature with a fluence of 10^{16} cm^{-2}, the yellow-colored region shows the integration area for the PL activation calculation.*

A quantitative comparison was then performed by integrating the whole PL spectrum related to the NV emission (560-775 nm range, as highlighted in **Figure 105**). Assuming the same conditions during the characterization, the integral of this area was then assumed to be proportional to the NV concentration in the probed sample volume, around 20 μm^3. All the acquired data from the spectra corresponding to each of the regions as implanted and after the 12 h at 950 ºC annealing is plotted in **Figure 106**.

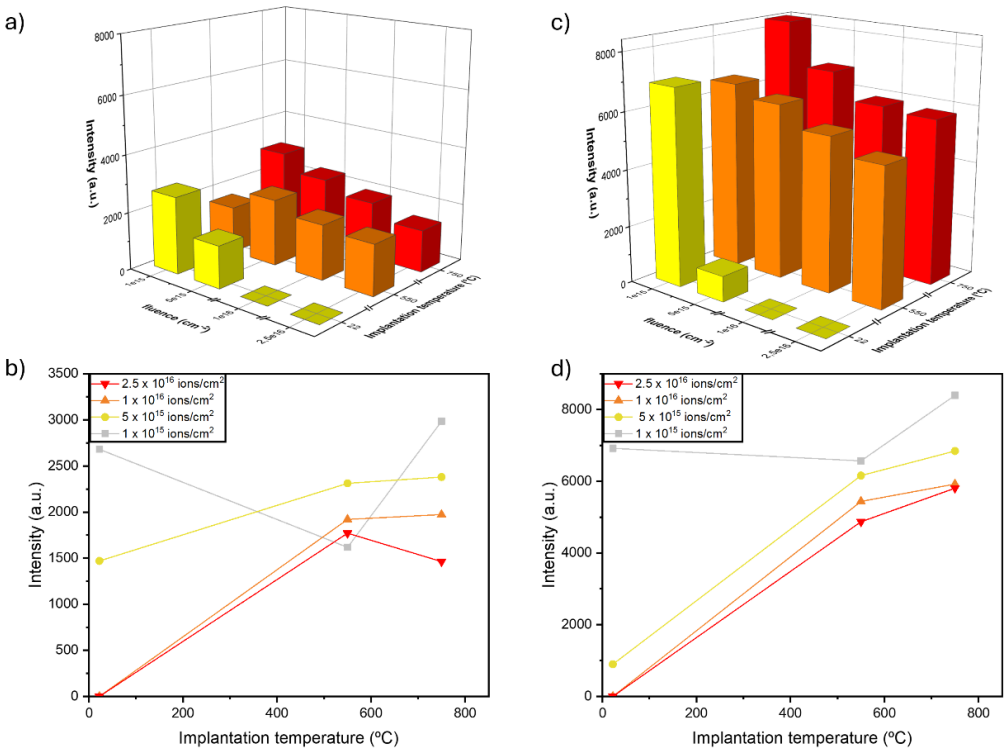

Figure 106 *a)3D representation of the integrated intensity of the NV spectra for each of the regions as implanted. b) 2D representation of the integrated intensity as a function of the implantation temperature for each of the fluences*

before any post-implantation annealing. c) 3D representation of the integrated intensity of the NV spectra for each of the regions after the 12 h annealing. d) 2D plotting of the integrated intensity as a function of the implantation temperature for each of the fluences after the 12 h annealing.

On what regards the 'as implanted' sample intensities, plotted in **Figure 106** a. and b. the intensity of the NV emission is higher in the regions implanted at the lowest ion fluence considered (10^{15} cm^{-2}). This observation aligns with already reported findings that state there is a decrease in the quantum efficiency when a higher density of NV centers is present in the region[52]. This decrease is linked to a '*self-absorption'* process where photons emitted by closely located color centers may be absorbed by neighboring emitters[291].

It is worth highlighting also that the higher the temperature of implantation the higher the observed NV signal. The lack of NV emission coming from the two highest fluences, both before and after the post-implantation annealing treatment of 12 h, can be interpreted as the effect of the amorphization of the crystal (before the annealing) and into graphite (upon the post-implantation annealing). This result is consistent with what typically is reported as implantation fluences above the graphitization threshold[179]. Conversely, implantation at 550 ºC and 750 ºC resulted in in-situ recovery of the crystal lattice, significantly increasing the graphitization threshold.

The differences between the as-implanted intensities (**Figure 106**a and b) and the post-annealed ones (**Figure 106**c and d) are mainly the further increase in PL coming from the non-graphitized regions and a clearer trend with the temperature of implantation, showing a slightly higher intensity for all the region implanted upon 750 ºC compared to the 550 ºC implantation.

In addition to the graphitization threshold, in this work the absolute creation yield of the NV centers was assessed. To determine the absolute creation yield, we obtained the photoluminescence (PL) spectrum from a non-implanted area of the sample. This specific area had a nominal N concentration of < 1 ppm and an upper limit concentration of NV centers of 5 ppb [292] (~ 9×10^{14} cm^{-3}). Since the spectrum solely consisted of the NV center's spectral features, we were able to normalize all the acquired spectra to estimate the yield for each of the N-implanted regions.

Considering the PL spectrum from the area implanted at room temperature with a fluence of 1×10^{15} cm^{-2}, we observed that the PL increased by a factor of 5.6 compared to the non-implanted area. This resulted in a concentration of NV centers of ~5×10^{15} cm^{-3}.

As the optical setup used for the study (Horiba-Jobin-Yvon LabRam HR-VIS instrument, explained in the samples preparation Section 4.3.1) was composed of a 20x objective lens with a 0.4 numerical aperture , considering the resolution formulas explained in the experimental Chapter, the volume under investigation was ~ 18 μm^3, but only a fraction of this volume, estimated to be 0.64 μm^3, is occupied by the fabricated NV centers. This estimation was made assuming the in-depth distribution of the implanted ions to be ≈ 200 nm, corresponding to the width of the Bragg peak of the ions' penetration range in diamond, obtained by the SRIM simulation.

Considering this fraction of the fluorescence originating from the fabricated ensemble of NV centers, we calculated a creation efficiency of ~ 3.6% for the considered region ($1x10^{15}$ cm^{-2}). This value increases to 4.4% for the area implanted with the same fluence (1×10^{15} cm^{-2}) at 750 °C, but drops significantly for the areas implanted with higher N^{2+} ions fluences, down to ≈ 0.1% for 2.5×10^{16} cm^{-2} implanted at 550 °C. It must be reported that previous literature papers reported significantly higher values (up to 50%) for this ion implantation energy [52], however these values are associated with the fabrication of individual NV centers obtained with low implantation fluences of ~10^{10} cm^{-2}.

To summarize the most relevant results coming from the hot implantation of N^{2+} MeV ions were firstly, an increased graphitization threshold above the 3.5 x 10^{23} cm^{-3} vacancy density value at both 550 ºC and 750 ºC implantation temperatures. Secondly, the progressively increasing PL intensity at increasing implantation temperature for the same implantation fluences showed an increase in the creation efficiency of the NV centers at higher temperatures.

4.3.3 MgV spectral characterization

In addition to the NV study, a separate investigation on the formation of the MgV centers in ***Sample 2*** under hot implantation conditions was performed. As has been stated before, in this case the 'as implanted' characterization was performed in a different single photon sensitive setup with a much lower excitation power (200 μW)

The PL spectra shown in **Figure 107** indicate that only the region implanted at 700 °C exhibits the characteristic features of the MgV center[47], which include a sharp zero-phonon line (ZPL) at 557 nm along with its phonon replicas in the 560-650 nm range. The hot implantation at 500 °C results in a weak emission at 557 nm (MgV ZPL) [47]and a stronger photoluminescence signal at 741 nm (GR1 band related to the neutral vacancy emission[187], [293]). This is because the GR1 center has the highest formation yield [187]in this temperature range. On the other hand, the PL spectra obtained from the regions implanted at 300 °C and room temperature show only the presence of the GR1 emission, without any noticeable contribution related to the MgV center. This is consistent with the common experimental protocols for creating various diamond color centers, where the conversion into stable optically active defects requires the recombination of the implanted impurities with the lattice vacancies introduced during ion implantation[276], [294]. This process is activated by providing sufficiently high thermal energy to achieve vacancy diffusion and leads to the disappearance of the GR1 spectral feature at temperatures above 600 °C.

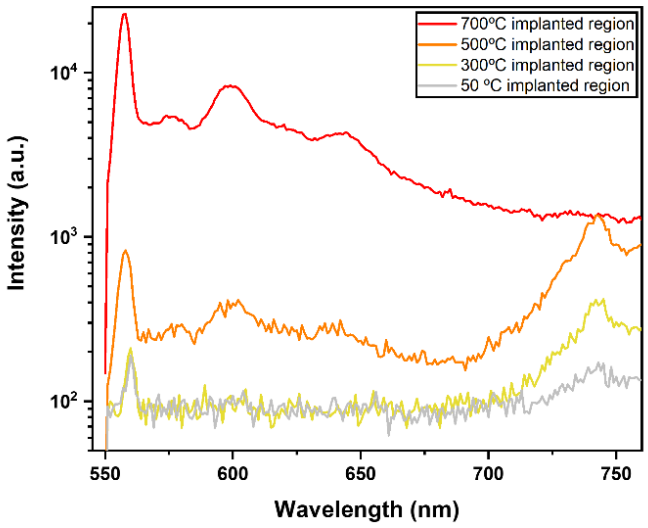

Figure 107 *PL spectra under 520 nm laser excitation from Sample 2 following Mg ion implantation. The four spectra refer to the different implantation temperatures: 50ºC (grey line), 300 ºC (yellow line), 500 ºC (orange line) and 700 ºC (red line).*

In the same way as for Sample 1, the diamond was thermally processed for a total amount of 12 h. The PL spectra after these processes, were all acquired using the same Raman spectroscopy setup as in the first sample, leading in this case to a spectrum like the one reported in **Figure 108**. The range studied in this case, went from 530-700 nm in order to neglect the contribution of the GR1 center, although after 900 ºC no presence of it was visible in the spectra taken.

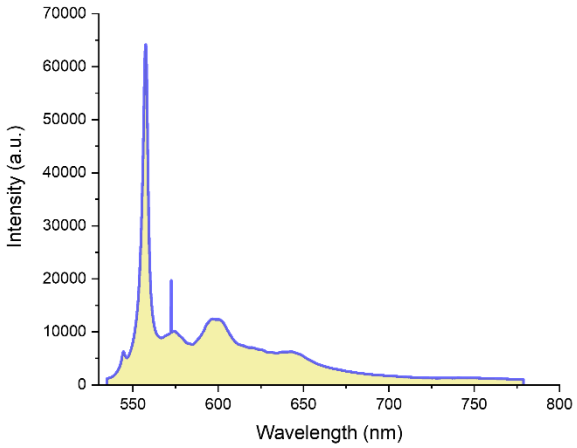

Figure 108 *PL spectrum of the MgV in the 700 ºC processed region with the integration range colored in yellow.*

Now, looking at the results shown in **Figure 109**, it is clear that the sample area implanted at 700 °C (red triangles in **Figure 109**b) shows the highest PL intensity among all the annealing durations. Specifically, after 12 hours of thermal annealing, the photoluminescence for the 700 °C implantation exhibits an increase of approximately 20% compared to the area implanted at 500 °C. On the other hand, the areas implanted at lower temperatures do not show a significant dependence on the implantation temperature itself. The implanted regions at 50 °C, 300 °C, and 500 °C all demonstrate comparable emission intensities at each post-implantation annealing step (**Figure 109**b). This suggests that all implantation temperatures below 500 °C are insufficient to enhance the formation efficiency of the MgV center, indicating that ion fluence is the only relevant processing parameter at implantation temperatures below 500 °C.

These results indicate the advantage of ion implantation on a hot substrate over the same process at room temperature to achieve better defect formation rates, particularly at higher temperatures. Similarly, well-established procedures for dopant activation in other semiconductors demonstrate that hot implantation results in better electronic properties and overall higher crystal quality. Furthermore, the reported benefits of this technique pave the way for optimizing the fabrication of highly dense ensembles of color centers and contribute to further studies on hot implantation processes applied to optical defect engineering in semiconductors and their optical activation.

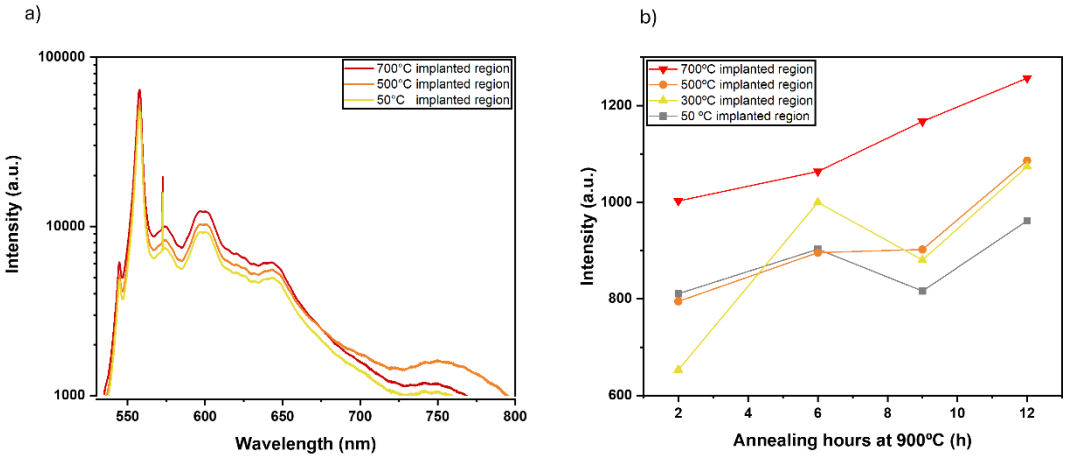

Figure 109 *a) PL spectra acquired from the Mg^+ implanted regions at increasing temperatures*

4.4 Color center fabrication in aluminum nitride epilayer on sapphire via Al-ion implantation and thermal annealing.

In this last section of the Chapter, the fabrication of color centers in AlN upon keV irradiation with Al^- will be presented. As explained in the first Chapter, single-photon sources in AlN were first reported a couple of years ago. The composition and a repeatable fabrication method for such sources are still under study.[120].

Aiming to establish a fabrication method of single photon emitters in this material, in this work we investigated the manufacturability of these AlN thin films grown on sapphire by means of Al^- ion implantation and subsequent thermal annealing. The choice of Al as the species introduced into the lattice was based on the objective of promoting the formation of lattice vacancies without introducing any further extrinsic defects into the material[119].

In this work, several implantation fluences were assessed in order to investigate the dependence between the defect introduced into the lattice and the overall PL emission intensity coming from the irradiated area, not considering however the contribution of the previously present emitters in the crystal. In addition, the effect of post-implantation thermal annealing was studied aiming both to activate more defects and to reduce the radiation-induced background emission.

4.4.1 Sample fabrication

The experiments were carried out on a 1 μm thick MOCVD-grown AlN epilayer on sapphire. The fabrication process performed on the sample is summarized in **Figure 110**a. It shows how first the Al^- ions were implanted into the sample to induce the formation of lattice vacancies. Then using thermal annealing, the diffusion and recombination of these vacancies takes place, leading to the formation of optically active defects[122].

In particular, the sample was implanted with 60 keV Al^- using 100 keV ion implanter presented in Section 3.1. This energy led to an implantation profile of the ions (blue line) and the creation of vacancies (red line) like the ones presented in **Figure 110**b, suggesting the implantation-induced color centers were formed within 100 nm from the surface. The implantation was performed using a broad beam with a collimated mask of 1 mm diameter and the fluences were in the $1x10^{12}$-$1x10^{14}$ cm^{-2} range. Two post-implantation annealing treatments were performed on the sample using the tubular furnace (Chapter 3.2.1), first at 400 ºC and a subsequent one at 600 ºC, both for 30 min in N_2 atmosphere.

After the implantation and after each of the post-implantation treatments, the sample was characterized by means of PL confocal microscopy in order to assess the effects of ion implantation and annealing on the formation of optically active centers.

The areas where the different doses of ions had been implanted were marked using high-power laser milling (using the nanosecond laser introduced in Section 3.3) to allow for the examination of the same light-emitting areas after each subsequent treatment on the sample[106]. The analysis of the light emission was conducted using the custom fiber-coupled microscope described in Section 3.4. A 522 nm laser diode was used for optical excitation.

During all measurements, a set of spectral filters defined a 550-650 nm detection range ensuring the elimination of background coming from the chromium line of sapphire but leading to an abrupt interruption of the spectra acquired. Second-order autocorrelation histograms were obtained from isolated light-emitting spots using the HBT interferometer, aiming to determine whether the emitters that were been fabricated were single photon sources. The density of created centers was determined by comparing the number of isolated spots found in the implanted areas through PL mapping with those in a reference pristine area.

Finally, a spectral analysis at room temperature was conducted on all the considered areas using a Princeton Instruments PIXIS spectrometer (see Section 3.4.3).

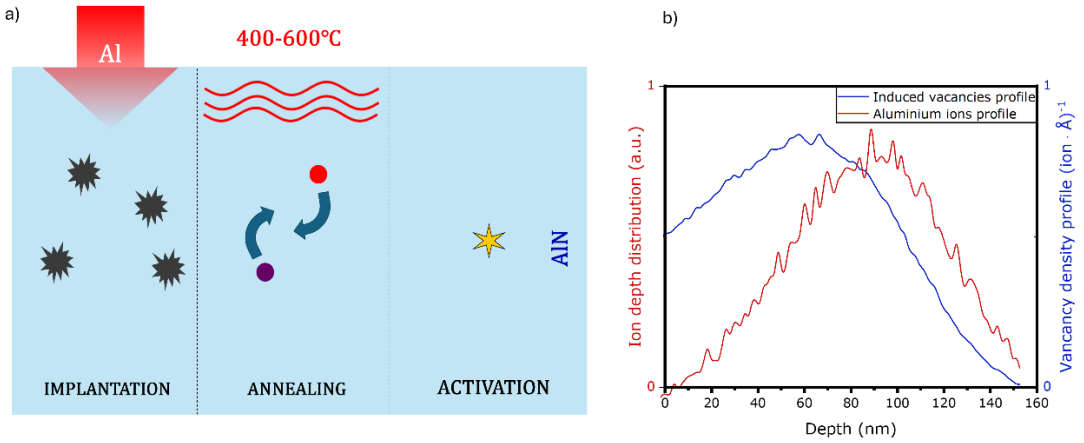

Figure 110 *a) Schematics of the experimental fabrication steps. b) Vacancy density profile (blue line) and implanted Al ion distribution (red line) simulated via SRIM for 60 keV Al implantation.*

4.4.2 Density of emitters analysis

The formation of color centers in AlN as an effect of the ion-induced damage was investigated as a function of both the implantation fluence and the post-implantation annealing temperature. This study was based on the PL mapping of the same regions after each thermal treatment. As it can be pointed out in **Figure 111**, the same regions (20 x 20 μm^2): unimplanted region, $1x10^{12}$ cm^{-2}, $1x10^{13}$ cm^{-2} and $1x10^{14}$ cm^{-2} were assessed after each of the thermal treatments, always at the same excitation power (2 mW).

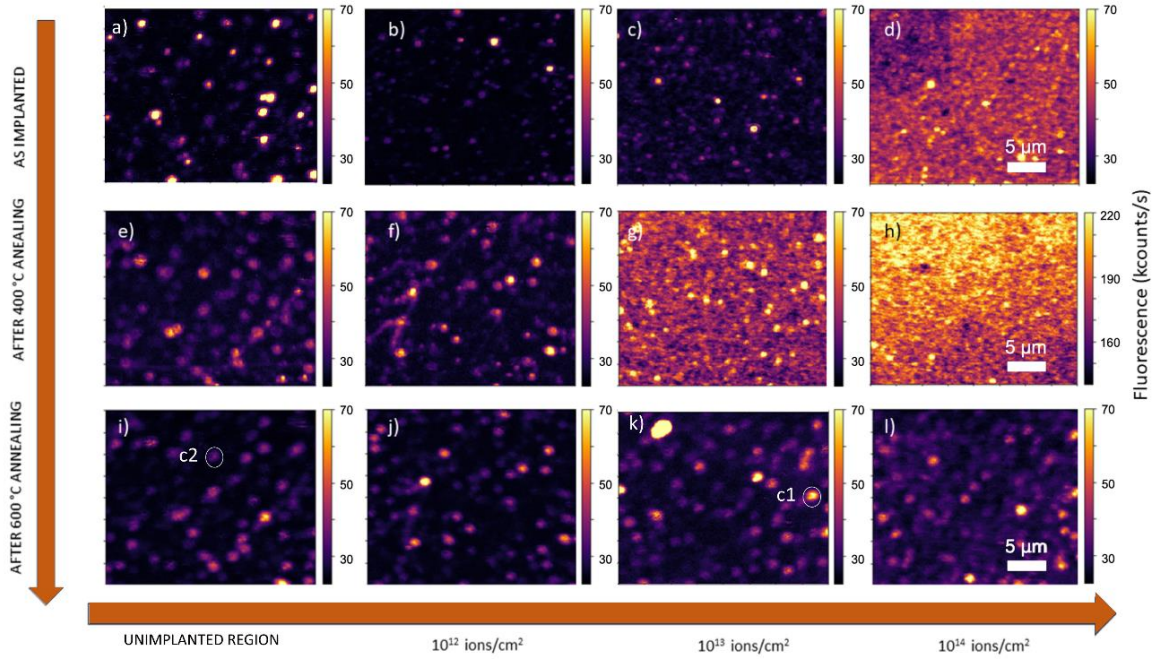

Figure 111 *PL confocal mapping of the same implanted regions (20 x 20 μm^2) upon different thermal annealing steps, under 520 nm laser excitation and collection window between 550-650 nm. The color scale encodes the number of photons from the studied point at the diffraction limit.*

The maps acquired prior to any thermal treatment, plotted in the first row of **Figure 111**a-d, show already a difference in the number of bright spots present in the studied regions. The pristine region (first column) exhibits a low density of single emitters, calculated to be around ~0.075 μm^{-2}, considering the number of

individual spots (with medium emission intensity ~50 kcps) with respect to the background originating from the surrounding region (~2 kcps). If now we compare it with the region implanted at $1x10^{12}$ cm^{-2} (**Figure 111**b), it doesn't seem to have any increase in the density of emitters, ~0.08 μm^{-2} in this region. However, compared to the $1x10^{13}$ cm^{-2} region, a notable increase can be appreciated (~0.37 μm^{-2}), considering the spots with similar photon count rates with respect to the pristine region. This observation indicates an effect of the ion implantation on the creation of optically active defects. Moreover, the further intensity increase coming from the region implanted at $1x10^{14}$ cm^{-2} , where no individual emitter can be however individualized because of the high ensemble PL, confirms this effect.

After the 400 ºC annealing treatment, shown in **Figure 111** e-h, the same of increasing PL intensity with increasing ion fluence can be highlighted. For the pristine region, no change in the emitter density could be observed, while the annealing led to a noticeable increase in the $1x10^{12}$ cm^{-2} (~0.2 μm^{-2}) implanted region. For the $1x10^{13}$ cm^{-2} implanted region, a high increase in the PL intensity could be appreciated, accompanied by a noticeable increase in the background, not making it possible to distinguish any single spots. The region implanted at $1x10^{14}$ cm^{-2} exhibited a three-fold increase in the PL intensity, indicating the formation of a large ensemble of optically active intrinsic defects, making it also not possible to assess the individual emitters.

The subsequent treatment at 600 ºC, lead to the results shown in **Figure 111** i-l. The density of emitters in the pristine region was not altered by the annealing, if compared to the previous treatments. For the implanted regions, this annealing resulted in the substantial suppression of the PL background emission that was observed after the 400 ºC annealing for 10^{13}-10^{14} cm^{-2} fluences, resulting in this case in a distribution of single emitters with much more visibility and giving place to densities of 0.2 and 0.25 $\mu m^{-2,}$ respectively.

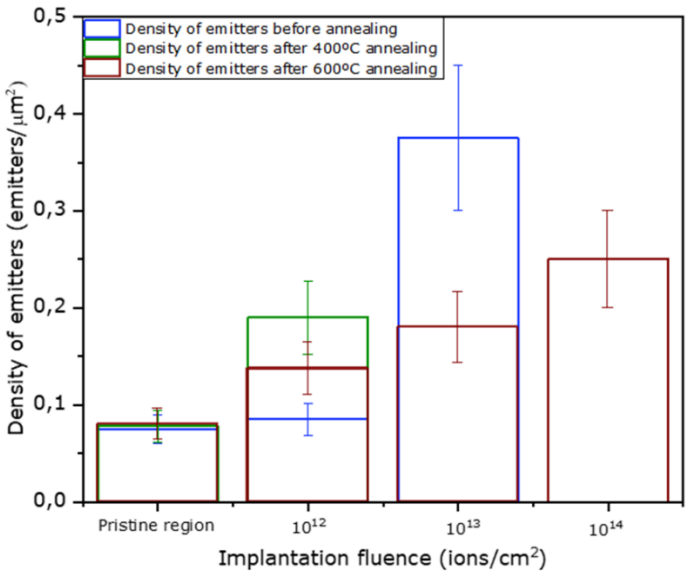

Figure 112 *Box chart of the density of emitters extracted for each of the regions after each annealing treatment. Before annealing (blue box), after 400 ºC annealing (green box), and 600 ºC annealing (brown box).*

The emitters' densities are displayed in **Figure 112** plot. The highest density of individual emitters that could be individualized was reported for the $1x10^{13}$ cm^{-2} region before any thermal treatment, 0.4 μm^{-2}. After annealing at 400°C, the emitter density moderately increases (up to 0.2 μm^{-2}) for the $1x10^{12}$ cm^{-2} fluence. However, at higher fluences, there is a significant increase in background PL, leading to the impossibility of identifying single emitters. Annealing at 600°C resulted in a slight decrease in emitter density (0.15 μm^{-2}), which is lower than the corresponding value at 400°C for a fluence of 10^{12} cm^{-2}. With the highest implantation fluence ($1x10^{14}$ cm^{-2}) and annealing at 600°C, individual emitters are formed. In

some cases, it is difficult to quantify the density of individual emitters due to high levels of PL from entire regions, indicating the formation of ensembles of centers that cannot be individually resolved. That's why the data coming from the region implanted at $1x10^{14}$ cm^{-2} before annealing and after 400ºC annealing and the ones coming from $1x10^{13}$ cm^{-2} after 400 ºC annealing, was left out of the graph in **Figure 112**.

4.4.3 Spectral analysis of the emitters

After the density of individual spots has been assessed, the spectral features of the AlN emitters studied can be investigated. In **Figure 113**, a set of exemplary spectra acquired from individual diffraction-limited spots from the maps in **Figure 111** are reported. This figure shows the three main types of emitters that could be individualized during the study: the ones with the ZPL falling around 560 nm, highlighted by a green bar (**Figure 113** a-c), the yellow marked ones show a ZPL more in the 580-600 nm range (**Figure 113** d-f) and lastly the orange marked ones showing the ZPL after 600 nm (**Figure 113** g-i). From all of these emitters, it can already be pointed out how the emission band at room temperature is quite broad suggesting a quite important phonon mediation in the emission process. Additionally, these spectra are in good agreement with what has been previously reported in literature as single-photon sources in AlN[119], [120], [295].

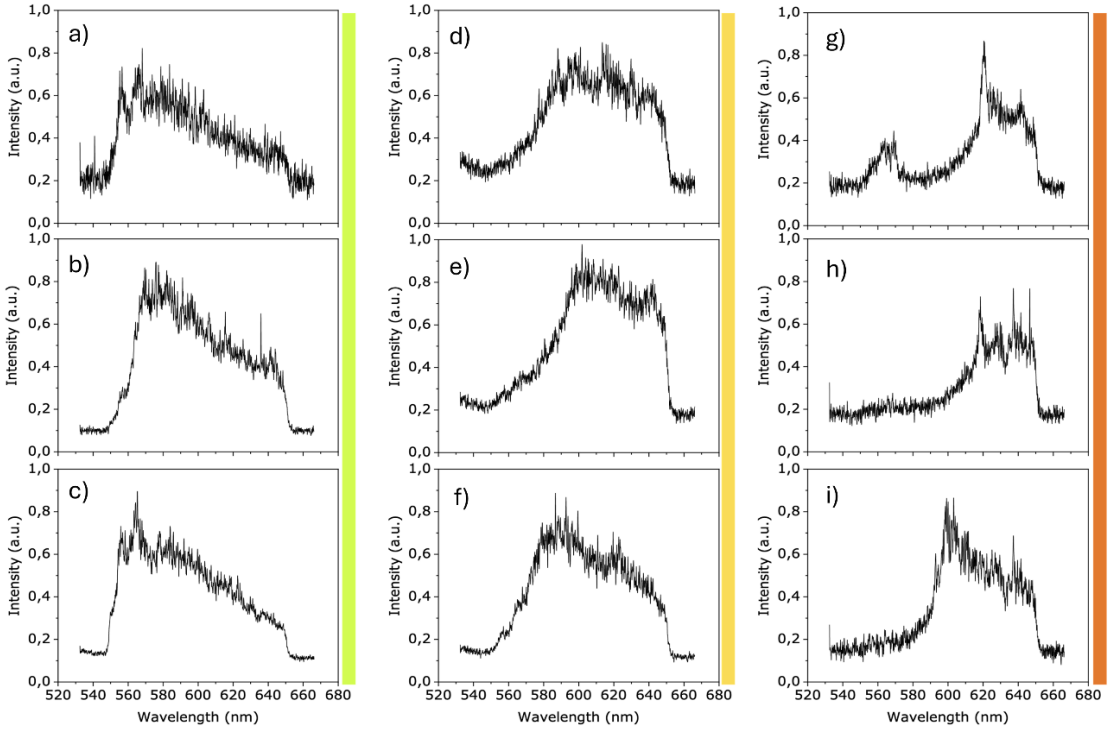

Figure 113 *Set of emission spectra from individual emitters acquired from the sample following different processing steps: a) unimplanted sample; b) 10^{12} cm^{-2} ion fluence, as implanted; c) 10^{13} cm^{-2} ion fluence, 600 °C annealing; d) unimplanted sample, 400 °C annealing; e)10^{12} cm^{-2} ion fluence, 400 °C annealing; f) 10^{13} cm^{-2} ion fluence, 600 °C annealing; g) unimplanted sample; h) 10^{13} cm^{-2} ion fluence, as implanted; i) 10^{12} cm^{-2} ion fluence, as implanted.*

Due to the wide variety of emission spectra that was observed during the study, a statistical analysis of the main spectral signatures was performed on a set of 58 emitters. In **Figure 114** a, the ZPL position of those emitters as a function of the annealing temperature is presented, independently of the region where they were acquired. As was highlighted in **Figure 113**, it is visible how two main ZPL ranges are present: around 560 nm and 600 nm. No difference is observed as a function of the annealing treatment, mainly the fact that the majority of the emitters have the ZPL at wavelengths below 600 nm.

In **Figure 114** b, the occurrence of the ZPL as a function of the implantation fluence independently of the annealing treatment is represented. In none of these cases, the PL spectra coming from the regions at $1x10^{13}$ and $1x10^{14}$ cm^{-2}, was considered as no individual emitters were studied.

From both these statistical analyses, the presence of the two groups of emission lines ~560 nm and ~600 nm becomes clearer. This trend may be indicative of the presence of two different classes of emitters or of the effect of the local lattice on the electronic states of the same point defect. This latter interpretation may be justified by the piezoelectric properties of AlN, which may induce local strains leading to changes in the electronic properties of the defects[123], [183], [191], [295].

Additionally, the spectrum acquired from the ensemble of $1x10^{14}$ cm^{-2} implanted region upon 400 ºC annealing, is reported in **Figure 114**. The broad PL emission in the 560-640 nm range is similar to the individual PL peaks seen at the single-photon emitter level. This suggests that the combined emission is a result of the multiple spectral components recorded in **Figure 113** and **Figure 114** a-b. This finding confirms that ion implantation plays a role in creating optically active intrinsic defects in AlN. The observation of increasing ensemble emission intensity at higher ion fluences supports this interpretation, indicating that overall PL emission increases with the density of ion-induced radiation damage in the crystal.

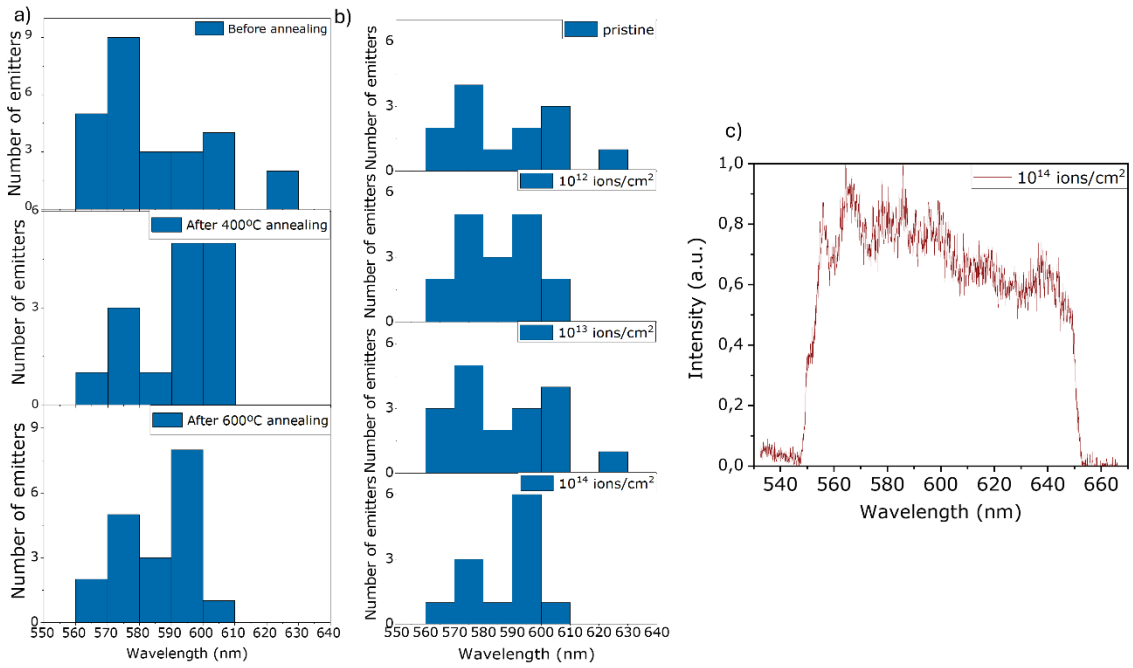

Figure 114 *Statistical analysis of the central wavelength of the main PL emission peaks from a set of individual emitters in AlN. a) distribution of the emitters at different annealing temperatures; b) distribution for different ion implantation fluences. c) PL spectra of the background acquired from the 10^{14} cm^{-2} region after 400 ºC annealing*

4.4.4 Single-photon analysis

As was anticipated before, after the spectral analysis, the antibunched emission from the individual spots was verified by HBT interferometry on a set of 10 emitters for each of the considered regions after each processing step. In this section, the characterization of two individual exemplary emitters, one with the ZPL around 560 nm and the other 600 nm, is presented as an example of the parameters found for each of these sources.

The first emitter reported is highlighted in **Figure 111**k as 'C1', and it is one with the ZPL ~560 nm. First, the second-order autocorrelation histograms were acquired using the HBT interferometer for this center at several excitation powers, as can be pointed out in **Figure 115**a. The non classical emission originating from the individual source was verified by the $g^{(2)}(t=0)<0.5$ criteria. These curves were fitted according to the three-level system that allows for the consideration of a metastable shelving state[47]:

$$g^{(2)}(t) = 1 - A_1 \cdot exp(-\lambda_1 \cdot |t|) + A_2 \cdot exp(-\lambda_2 \cdot |t|) \qquad \textit{Equation 59}$$

As can be pointed out in **Figure 115**a, under low optical excitation power, the decay rate through the shelving state of the three-level system is negligible with respect to that of the radiative transitions, as the bunching effect (shelving state effect) becomes much lower while the antibunching is always present (radiative decay effect).

Using **Equation 59**, as was explained in Section 4.1.3, it is possible to extract the excited state radiative lifetime of the center, as (3.4 ± 0.12) ns, as it is plotted in Figure 115b. The emission intensity and power at saturation were both calculated and plotted in Figure 115c, according to the saturation formula presented in the first section, showing a value of (119 ± 9) kcps for the intensity and (0.28 ± 0.09) mW for the power. The spectrum acquired in the studied range (550-650 nm) is presented in Figure 115d, showing a ZPL peak around 560 and a wide phonon sideband.

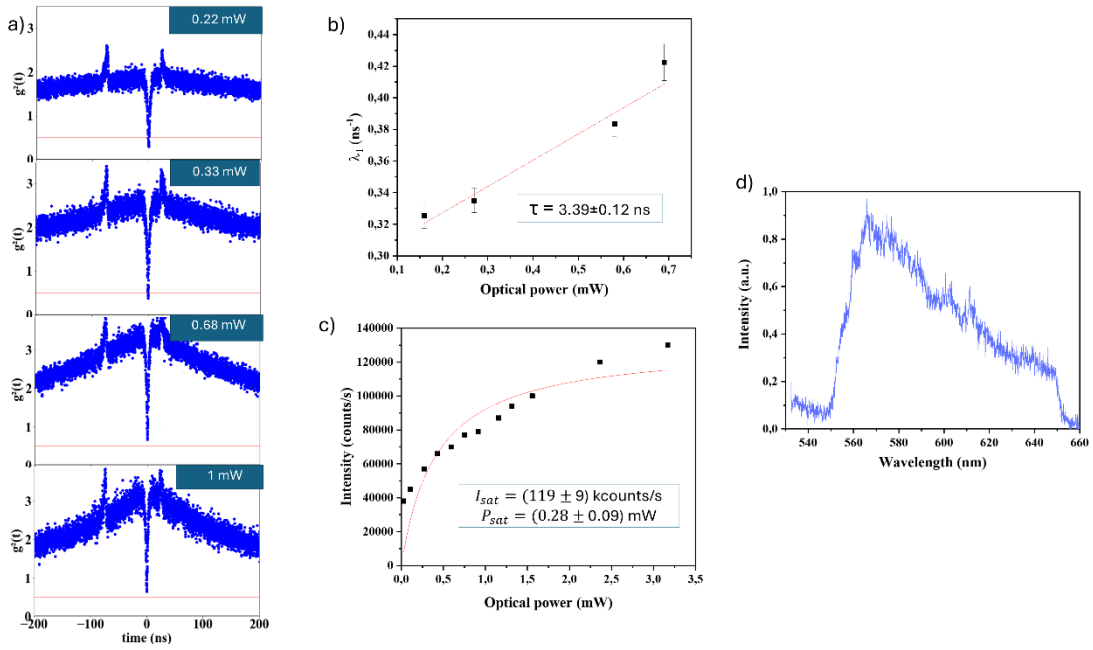

Figure 115 *Antibunched emission parameters from an individual center in the region implanted at 1x10^{13} cm^{-2} fluence after the 600°C thermal processing. The emitter is circled in white and labelled as "C1" in Fig. 111k:* ***a)*** *Second order correlation measurements and lifetime extracted from the power dependence of the λ_1 fitting parameter. The peaks at t ~ -2 ns and t~ +80 ns correspond to the backflash peaks of the detection system, originating from photon backflash from one single photon detector reaching the other detector through the reflection of photons at the terminations of the two branches of the fiber-coupled HBT interferometer.* ***b)*** *Linear regression of the λ_1 parameter as a function of the excitation power.* ***c)*** *Saturation curve of the emitter, after background subtraction.* ***d)*** *PL spectrum with spectral filtering to remove light outside the 550-650 nm range.*

The second emitter reported is highlighted in **Figure 111**i as 'C2', and it is one with the ZPL ~600 nm. First, the second-order autocorrelation histograms were acquired using the HBT interferometer for this center at several excitation power, as can be pointed out in Figure 116a. The non classical emission originating from the individual source was verified in the same as for the 'C1' center by the $g^{(2)}(t=0)<0.5$ criteria.

As can be pointed out in Figure 116a, under low optical excitation power, the decay rate through the shelving state of the three-level system is negligible with respect to that of the radiative transitions, as the bunching effect (shelving state effect) becomes much lower while the antibunching is always present (radiative decay effect).

Using **Equation 59** , as was explained in the first section of this Chapter, it is possible to extract the excited state radiative lifetime of the center, as (5.7 ± 0.5) ns, as it is plotted in Figure 116b. The emission intensity and power at saturation were both calculated and plotted in Figure 116c, according to the saturation formula presented in the first section, showing a value of (65 ± 8) kcps for the intensity and (0.16 ± 0.06) mW for the power. On what regards the spectrum of the studied emitter, in Figure 116d is shown how the other type of emitter with ZPL around 600 was studied.

For both the centers studied, it is worth mentioning that the emission intensity of the emitters refers only to the mentioned spectral range and in general the overall emission intensity of the emitters is higher.

Additionally, the differences we observed in the lifetime, emission intensity, and excitation power of the centers under saturation conditions could be explained by considering the different spectral signatures of the centers. These signatures indicate different defective complexes, which are consistent with what has been reported in the scientific literature for unimplanted AlN.

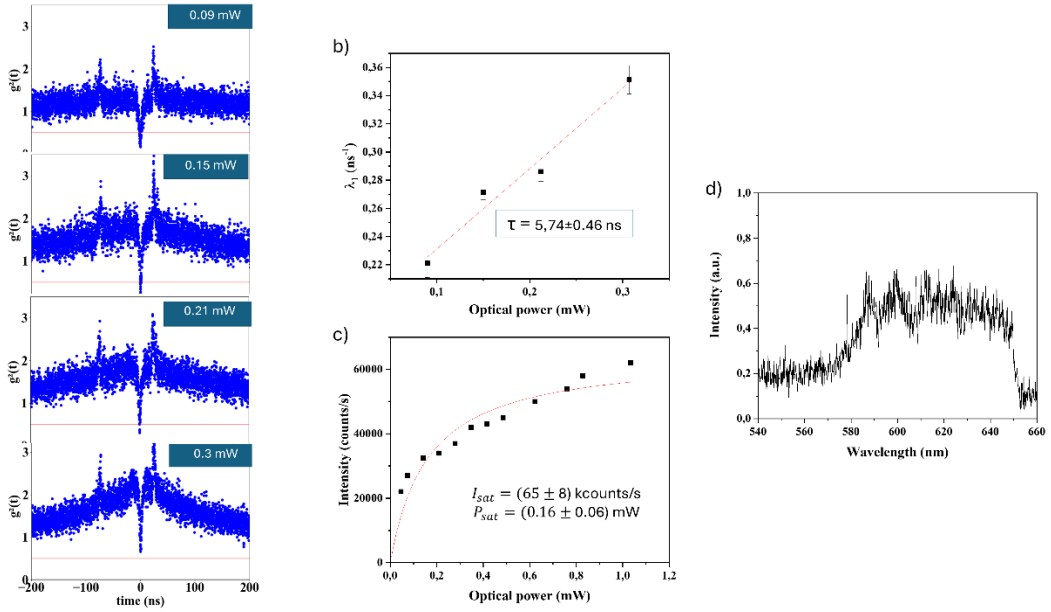

Figure 116 *Antibunched emission parameters from an individual center in the unimplanted region after the 400°C thermal processing. The emitter is circled in white and labelled as "C2" in Fig. 111i* ***a)*** *Second order correlation measurements and lifetime extracted from the power dependence of the λ_1 fitting parameter.* ***b)*** *Linear regression of the λ_1 parameter as a function of the excitation power.* ***c)*** *Saturation curve of the emitter, after background subtraction.* ***d)*** *PL spectrum with spectral filtering to remove light outside the 550-650 nm range.*

4.4.5 Stability of the centers

After conducting an analysis on the C2 emitter situated in the unimplanted region, plotted in Figure 111i, following each thermal treatment, the effect of the thermal annealing process on the properties of the emitters was studied. The emitter reported in Figure 30a, displayed a broad emission band centered at approximately 600 nm, Figure 117d, and this characteristic remained unchanged after each subsequent annealing step (Figure 117 b-c, e-f). This observation suggests that the isolated defect remained optically active even after annealing at temperatures of 600 °C and that its emission spectrum was not affected by the thermal process.

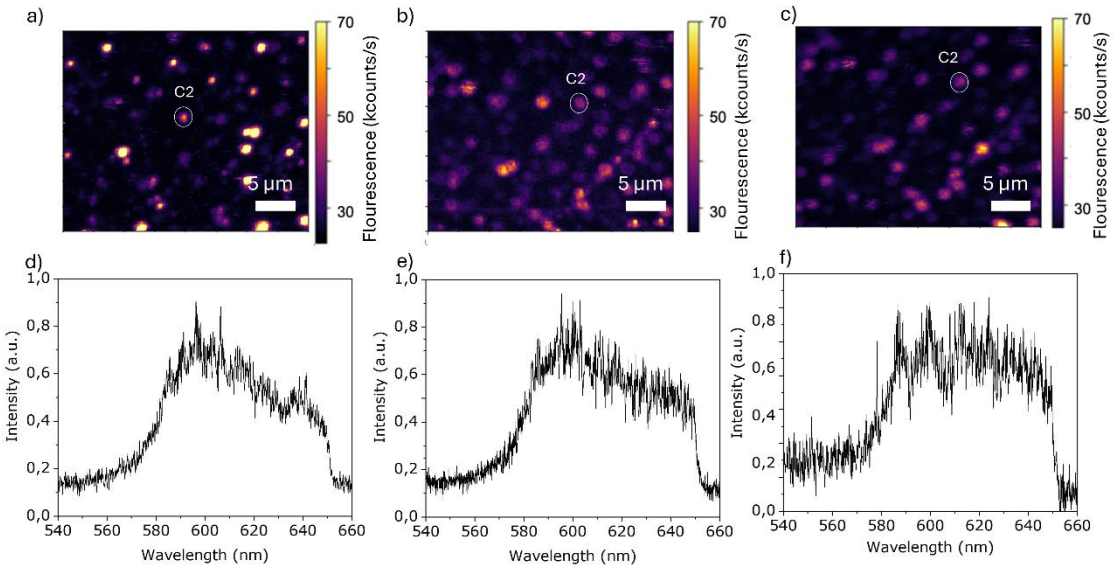

Figure 117 *Spectral comparison of the same single emitter (labelled as "C2" in the PL maps isolated in the unimplanted region after each post-implantation process): a) pristine material; b) following 400 °C thermal annealing; c) following 600 °C thermal annealing.*

Chapter 5

In this Chapter the main results explained in Chapter 4 will be summarized, giving an overview of the main advantages of the outcomes of each work and the future works the future works could be done for each of them. Additionally, a summary of the published works that my work during the three-year PhD contributed to, will be presented.

5.1 Conclusions and future perspectives

In my dissertation, I have discussed several fabrication techniques that have allowed me to fabricate several types of color centers, in diamond and AlN and study their optical properties, in order to understand the advantages of each of the proposed techniques, with respect to the state of the art.

Firstly, the commissioning of the 100 keV multi-elemental ion implanter presented in Section 3.1, constituted a key part of the PhD activities, as its use was of strategical importance for the fabrication of color centers not only in diamond and AlN, but also in silicon, silicon carbide and other wide bandgap semiconductors, whose results have not been reported in this thesis. Ion implantation offers a really versatile technique to repeatedly fabricate quantum sources and electronic structures (such as PN junctions) in semiconductors. During the PhD period, the machine was built up and made operational, allowing for the extraction of the first ions from the source, around the end of the first year of the PhD. The test and improvement of the different parts of the machine functioning, was carried out during the next two years of the PhD, allowing to conduct the studies reported in Section 4.1 and 4.2, among others that will be discussed in the collaborations section. The goal regarding the ion implanter now is to move towards a deterministic scheme of implantation via collimating masks of decreasing the dimensions with respect to the ones used in the results work (< 100 x 100 μm^2), combining this position sensitivity with some single ion counting technique, such as IBIC, to perform single-ion implantation experiments.

On what regards the results discussed in this dissertation, first a systematic investigation of the main emission parameters (namely, excited state radiative lifetime, saturation excitation power and emission intensity at saturation) for GeV centers created in diamond through different annealing conditions, was conducted. The results indicate that there is a trend towards lower optical excitation powers at higher annealing temperatures. This trend likely corresponds to an increase in emission intensity, although the data variability prevented us from identifying a clear trend in this parameter. The overall effectiveness of the excitation and emission processes is described by the ratio between emission intensity and optical excitation power at saturation, which showed an 8-fold improvement for the sample treated with high-pressure, high-temperature (HPHT) compared to conventional thermal annealing at 900-1000 °C in vacuum conditions.

This improvement in the emission properties of the center upon HPHT treatment is in line with the previous reported results on SnV and PbV centers, suggesting that the use of higher temperatures treatments is required to stabilize the large nuclei into the diamond lattice.

This significant increase in the single-photon source efficiency could potentially be applied to other types of quantum emitters in diamond and other host material platforms. This suggests an effective and highly controllable processing route towards creating ultra-bright GeV centers with optimal emission properties for single-photon generation and quantum technology applications. However, the actual implementation of these fabricated sources into quantum devices is still a challenge. Further study would be needed to understand the coherence times that the fabricated defects can reach, in order to use them as quantum nodes. Moreover, the HPHT parameters should still be improved to decrease the surface damage caused by the treatment into the diamond that may lead to changes in the polarization of the emitted photons.

Secondly, the optical activation process of Sn-related defects was reported upon keV ion implantation and CW laser irradiation. The results suggest the high structural formation efficiency of bond centered Sn related defects in diamond allows for the sole stable photoactivation of the defects, without the necessity

of an additional thermal process. In this dissertation was shown how the focusing of a continuous wave laser in the mW range (1-25 mW) for fixed periods of time (1-75 min) leads to an energy dependent activation of meanly the 595 nm peak related to the Sn ion implantation. A dependence on the processing laser wavelength was also observed, with a clear increase in formation efficiency with decreasing wavelength, being maximum upon 405 nm laser processing. Upon this irradiation wavelength the presence of the 620 nm ZPL of SnV^- center was also pointed out, suggesting that even upon no thermal treatment the Sn atom is present in split-vacancy configuration, and it is the electronic configuration that needs to be changed by means of photo-induced carriers.

Although the formation efficiency of the defects is quite low with respect to the ones reported in previous works on SnV centers, this work paves the way for the diffraction-limited optical activation of as-implanted defects in diamond. Additionally, the stability in time observed in the activated spots after months suggest, along with the simplicity of the technique, compared to other laser related activation techniques that relay on the thermal heating of the sample (fs laser irradiation), suggests the possibility of reproducibly fabricate bond-centered centers in diamond, even at single emitter level, by controlling the activation parameters and monitoring the PL of the irradiated spot.

Extensive research needs to be done on this fabrication technique, first on the properties of 595 nm peak for which single-photon emission was observed in this work at room temperature but no specific information on the energy levels of this defects is still available in literature. Additionally, further studies need to be performed on the fabrication of 620 nm using this technique, as the time limitation of the PhD thesis didn't allow to prove the physics behind the preferential formation of one of the peaks with respect to the other.

In the third study, it was shown that the graphitization threshold can be increased through MeV nitrogen implantation at high temperatures. By irradiating diamond samples at temperatures above 500°C, we were able to introduce vacancy densities of over 9×10^{23} cm^{-3} without irreversibly graphitizing the substrate. This suggests the potential for creating larger ensembles of color centers, which could enhance the sensitivity of the system.

A study on the formation efficiency of both the NV center and MgV center, was also conducted. The results showed that the photoluminescence increased in regions implanted at higher temperatures compared to those implanted at room temperature. Assuming a linear relationship between the PL intensity and the number of optically active centers, we estimated an increased formation efficiency of approximately 22% for the NV center and 20% for the MgV center when implanted at temperatures of 750°C and 700°C, respectively, compared to conventional room-temperature processes. These values are likely to depend on other processing parameters such as implantation fluence and ion beam current.

The same trend for both impurity-vacancy (NV center) and split-vacancy (MgV center) defect configurations was observed, suggesting that this behavior may be expected in general for the formation of extrinsic color centers in diamond. However, the formation enhancement associated with high-temperature ion implantation may vary depending on the specific ion species and defect structure. Further research will be needed to precisely assess the role of these parameters in the efficient manufacturing of diamond-based color centers, as this is beyond the scope of the present study. The findings of this study are crucial for creating large ensembles of color centers in diamond, which could significantly improve the field sensitivity for color center-based sensing protocols in future experiments without sacrificing spatial resolution by increasing the sensing volume.

In the last study, a systematic investigation on the impact of ion implantation on the creation of single-photon emitting intrinsic defects in AlN was carried out. Our research showed that implanting 60 keV Al-ions increased the density of individual color centers, and the background emission intensity was linked to the ion fluence. Although our study did not address whether the optically active quantum emitters were already present or implanted, it would require a specific investigation to analyze the properties of the implanted defects. We found that the highest formation yield occurred when irradiated at a fluence of $1x10^{13}$ cm^{-2} without subsequent thermal treatment of the sample. Higher ion fluences led to the formation of emitter

ensembles that had limited ability to isolate single color centers. Spectral analysis of the emitters revealed that all the point defects in the ion implantation region had similar characteristics to those found in pristine AlN, highlighting that Al- ion implantation results in the formation of intrinsic defects, indicating that the emitters are not related to foreign introduction into the AlN lattice. Furthermore, we demonstrated the structural and spectral stability of individual color centers following thermal processes up to 600 °C. These results indicate a promising pathway, based on industry-compatible ion implantation techniques, which could potentially be scaled to the single-ion delivery level for the fabrication of quantum emitters in chip-integrable AlN platforms. Future work is planned on the fabrication of single emitters in AlN upon Al ion implantation on lithographically marked samples, aiming to distinguish the differences between the ion implantation and annealing created emitters and the already pristine present ones. Additionally, both theoretical and experimental work needs still to be done to understand the structure of the defects formed.

5.2 Additional work and publications

During the PhD period several more activities were carried out centered in the optical characterization and ion implantation for the fabrication of single-photon sources in several wide bandgap semiconductors. Among the activities that were conducted, the most significant ones that lead to publications but were not explained in Sections 4.1, 4.2, 4.3 and 4.4, were the following:

- **Ion implantation** of carbon for the fabrication of G and W emitters upon ion implantation and nanosecond laser annealing in silicon, that led to the publication: G. Andrini *et al.*, "Activation of telecom emitters in silicon upon ion implantation and ns pulsed laser annealing," *Commun Mater*, vol. 5, no. 1, p. 47, Apr. 2024, doi: 10.1038/s43246-024-00486-4.
- **Optical characterization** of MgV color centers in keV ion implanted diamond to understand the optical features and single photon properties of the center. E. Corte *et al.*, "Magnesium-Vacancy Optical Centers in Diamond," *ACS Photonics*, vol. 10, no. 1, pp. 101–110, Jan. 2023, doi: 10.1021/acsphotonics.2c01130.
- **Photocurrent characterization** of a silicon photodiode probed by IBIC technique. G. Andrini *et al.*, "An ion beam spot size monitor based on a nano-machined Si photodiode probed by means of the ion beam induced charge technique," *Vacuum*, vol. 205, p. 111392, Nov. 2022, doi: 10.1016/j.vacuum.2022.111392.

Additionally, the knowledge acquired on fabrication of color centers and optical characterization allowed me to contribute to the writing on several reviews on integration of solid-state defects in semiconductors for photonic based quantum technologies:

- G. Andrini *et al.*, "Solid-State Color Centers for Single-Photon Generation," *Photonics*, vol. 11, no. 2, p. 188, Feb. 2024, doi: 10.3390/photonics1102.
- P. Piergentili *et al.*, "Quantum Information with Integrated Photonics," *Applied Sciences*, vol. 14, no. 1, p. 387, Dec. 2023, doi: 10.3390/app14010387
- D. Prete *et al.*, "Hybrid Integrated Silicon Photonics Based on Nanomaterials," *Photonics*, vol. 11, no. 5, p. 418, Apr. 2024, doi: 10.3390/photonics11050418.

The results presented in the in Sections 4.1, 4.3 and 4.4 were published in the following presented papers:

- E. N. Hernández *et al.*, "Efficiency Optimization of Ge-V Quantum Emitters in Single-Crystal Diamond upon Ion Implantation and HPHT Annealing," *Adv Quantum Technol*, vol. 6, no. 8, Feb. 2023, doi: 10.1002/qute.202300010.
- E. Nieto Hernandez *et al.*, "Efficient fabrication of high-density ensembles of color centers via ion implantation on a hot diamond substrate", paper accepted in Advanced Physics Research.

- E. Nieto Hernández *et al.*, “Fabrication of quantum emitters in aluminum nitride by Al-ion implantation and thermal annealing,” *Appl Phys Lett*, vol. 124, no. 12, Mar. 2024, doi: 10.1063/5.0185534.

In addition, the results presented in Section 4.2 belong to a paper under preparation.

Bibliography

[1] "https://www.azom.com/article.aspx?ArticleID=610."

[2] J. P. Dowling and G. J. Milburn, "Quantum technology: the second quantum revolution," *Philosophical Transactions of the Royal Society of London. Series A: Mathematical, Physical and Engineering Sciences*, vol. 361, no. 1809, pp. 1655–1674, Feb. 2003, doi: 10.1098/rsta.2003.1227.

[3] J. L. O'Brien, A. Furusawa, and J. Vučković, "Photonic quantum technologies," *Nat Photonics*, vol. 3, no. 12, pp. 687–695, Dec. 2009, doi: 10.1038/nphoton.2009.229.

[4] N. Gisin and R. Thew, "Quantum communication," *Nat Photonics*, vol. 1, no. 3, pp. 165–171, Mar. 2007, doi: 10.1038/nphoton.2007.22.

[5] A. F. J. L. O. J. Vuckovic, "Photonic quantum technologies," *Nat. Photon.*, vol. 3, pp. 687–695, 2009.

[6] T. D. Ladd, F. Jelezko, R. Laflamme, Y. Nakamura, C. Monroe, and J. L. O'Brien, "Quantum computers," *Nature*, vol. 464, no. 7285, pp. 45–53, Mar. 2010, doi: 10.1038/nature08812.

[7] C. L. Degen, F. Reinhard, and P. Cappellaro, "Quantum sensing," *Rev Mod Phys*, vol. 89, no. 3, p. 035002, Jul. 2017, doi: 10.1103/RevModPhys.89.035002.

[8] C. F. Roos, M. Chwalla, K. Kim, M. Riebe, and R. Blatt, "'Designer atoms' for quantum metrology," *Nature*, vol. 443, no. 7109, pp. 316–319, Feb. 2006, doi: 10.1038/nature05101.

[9] J. Poizat *et al.*, "Single Photon Quantum Cryptography," *Phys Rev Lett*, vol. 89, no. 18, Feb. 2002, doi: 10.1103/PhysRevLett.89.187901.

[10] B. Lounis and M. Orrit, "Single-photon sources," *Reports on Progress in Physics*, vol. 68, no. 5, pp. 1129–1179, May 2005, doi: 10.1088/0034-4885/68/5/R04.

[11] S. Scheel, "Single-photon sources–an introduction," *J Mod Opt*, vol. 56, no. 2–3, pp. 141–160, Jan. 2009, doi: 10.1080/09500340802331849.

[12] M. Oxborrow and A. G. Sinclair, "Single-photon sources," *Contemp Phys*, vol. 46, no. 3, pp. 173–206, May 2005, doi: 10.1080/00107510512331337936.

[13] S. Al-Kathiri, W. Al-Khateeb, M. Hafizulfika, M. R. Wahiddin, and S. Saharudin, "Characterization of mean photon number for key distribution system using faint laser," in *2008 International Conference on Computer and Communication Engineering*, IEEE, May 2008, pp. 1237–1242. doi: 10.1109/ICCCE.2008.4580803.

[14] F.-G. Deng and G. L. Long, "Bidirectional quantum key distribution protocol with practical faint laser pulses," *Phys Rev A (Coll Park)*, vol. 70, no. 1, p. 012311, Jul. 2004, doi: 10.1103/PhysRevA.70.012311.

[15] A. Christ, A. Fedrizzi, H. Hübel, T. Jennewein, and C. Silberhorn, "Parametric Down-Conversion," 2013, pp. 351–410. doi: 10.1016/B978-0-12-387695-9.00011-1.

[16] C. Caputo, M. Simoni, G. A. Cirillo, G. Turvani, and M. Zamboni, "A simulator of optical coherent-state evolution in quantum key distribution systems," *Opt Quantum Electron*, vol. 54, no. 11, p. 689, Nov. 2022, doi: 10.1007/s11082-022-04041-8.

[17] N. Akopian, G. Patriarche, L. Liu, J.-C. Harmand, and V. Zwiller, "Crystal Phase Quantum Dots," *Nano Lett*, vol. 10, no. 4, pp. 1198–1201, Apr. 2010, doi: 10.1021/nl903534n.

[18] P. Lodahl, S. Mahmoodian, and S. Stobbe, “Interfacing single photons and single quantum dots with photonic nanostructures,” *Rev Mod Phys*, vol. 87, no. 2, pp. 347–400, May 2015, doi: 10.1103/RevModPhys.87.347.

[19] “https://edwardflagg.faculty.wvu.edu/research/quantum-dots.”

[20] “https://vescent.com/it/company/technology-innovations/applications/cold-atom-science.html.”

[21] I. Aharonovich and E. Neu, “Diamond nanophotonics,” *Adv Opt Mater*, vol. 2, no. 10, pp. 911–928, Oct. 2014, doi: 10.1002/adom.201400189.

[22] G. Andrini *et al.*, “Solid-State Color Centers for Single-Photon Generation,” *Photonics*, vol. 11, no. 2, p. 188, Feb. 2024, doi: 10.3390/photonics11020188.

[23] A. Sipahigil *et al.*, “Indistinguishable Photons from Separated Silicon-Vacancy Centers in Diamond,” *Phys Rev Lett*, vol. 113, no. 11, p. 113602, Sep. 2014, doi: 10.1103/PhysRevLett.113.113602.

[24] J. Arjona Martínez *et al.*, “Photonic Indistinguishability of the Tin-Vacancy Center in Nanostructured Diamond,” *Phys Rev Lett*, vol. 129, no. 17, p. 173603, Oct. 2022, doi: 10.1103/PhysRevLett.129.173603.

[25] T. Iwasaki, “Color centers based on heavy group-IV elements,” 2020, pp. 237–256. doi: 10.1016/bs.semsem.2020.03.007.

[26] *Fox, Mark. Quantum Optics : An Introduction. Oxford University Press, 2006, https://public.ebookcentral.proquest.com/choice/publicfullrecord.aspx?p=430851.*

[27] I. Aharonovich, D. Englund, and M. Toth, “Solid-state single-photon emitters,” *Nat Photonics*, vol. 10, no. 10, pp. 631–641, Feb. 2016, doi: 10.1038/nphoton.2016.186.

[28] S. Hong *et al.*, “Nanoscale magnetometry with NV centers in diamond,” *MRS Bull*, vol. 38, no. 02, pp. 155–161, Feb. 2013, doi: 10.1557/mrs.2013.23.

[29] L. Childress and R. Hanson, “Diamond NV centers for quantum computing and quantum networks,” *MRS Bull*, vol. 38, no. 2, pp. 134–138, Feb. 2013, doi: 10.1557/mrs.2013.20.

[30] S. Guo, “An Overview of NV Centers,” *Journal of Applied Mathematics and Physics*, vol. 11, no. 11, pp. 3666–3675, 2023, doi: 10.4236/jamp.2023.1111231.

[31] N. Aslam *et al.*, “Quantum sensors for biomedical applications,” *Nature Reviews Physics*, vol. 5, no. 3, pp. 157–169, Feb. 2023, doi: 10.1038/s42254-023-00558-3.

[32] G. Petrini *et al.*, “Nanodiamond–Quantum Sensors Reveal Temperature Variation Associated to Hippocampal Neurons Firing,” *Advanced Science*, vol. 10, no. 11, Feb. 2023, doi: 10.1002/advs.202301101.

[33] M. Fujiwara *et al.*, “Real-time nanodiamond thermometry probing in vivo thermogenic responses,” *Sci Adv*, vol. 6, no. 37, pp. eaba9636–eaba9636, 2020, doi: 10.1126/sciadv.aba9636.

[34] S. Choe *et al.*, “Precise temperature sensing with nanoscale thermal sensors based on diamond NV centers,” *Current Applied Physics*, vol. 18, no. 9, pp. 1066–1070, Sep. 2018, doi: 10.1016/j.cap.2018.06.002.

[35] M. A. Bashar, M. A. Chowdhury, R. Islam, M. S. Rahman, and S. K. Das, “A Review and Prospects of Quantum Teleportation,” in *2009 International Conference on Computer and Automation Engineering*, IEEE, Mar. 2009, pp. 213–217. doi: 10.1109/ICCAE.2009.77.

[36] Y. H. Shih, “Quantum entanglement and quantum teleportation,” *Ann Phys*, vol. 513, no. 1–2, pp. 19–34, Feb. 2001, doi: 10.1002/andp.200151301-202.

[37] N. Gisin, G. Ribordy, W. Tittel, and H. Zbinden, “Quantum cryptography,” *Rev Mod Phys*, vol. 74, no. 1, pp. 145–195, Mar. 2002, doi: 10.1103/RevModPhys.74.145.

[38] C. Portmann and R. Renner, “Security in quantum cryptography,” *Rev Mod Phys*, vol. 94, no. 2, p. 025008, Jun. 2022, doi: 10.1103/RevModPhys.94.025008.

[39] M. Ruf, N. H. Wan, H. Choi, D. Englund, and R. Hanson, “Quantum networks based on color centers in diamond,” *J Appl Phys*, vol. 130, no. 7, Aug. 2021, doi: 10.1063/5.0056534.

[40] P. L. Stanwix *et al.*, “Coherence of nitrogen-vacancy electronic spin ensembles in diamond,” *Phys Rev B*, vol. 82, no. 20, p. 201201, Feb. 2010, doi: 10.1103/PhysRevB.82.201201.

[41] J. Görlitz *et al.*, “Coherence of a charge stabilised tin-vacancy spin in diamond,” *npj Quantum Inf*, vol. 8, no. 1, Dec. 2022, doi: 10.1038/s41534-022-00552-0.

[42] S. Pezzagna and J. Meijer, “Quantum computer based on color centers in diamond,” *Appl Phys Rev*, vol. 8, no. 1, Feb. 2021, doi: 10.1063/5.0007444.

[43] T. Lühmann, R. John, R. Wunderlich, J. Meijer, and S. Pezzagna, “Coulomb-driven single defect engineering for scalable qubits and spin sensors in diamond,” *Nat Commun*, vol. 10, no. 1, p. 4956, Feb. 2019, doi: 10.1038/s41467-019-12556-0.

[44] B. Naydenov *et al.*, “Engineering single photon emitters by ion implantation in diamond,” *Appl Phys Lett*, vol. 95, no. 18, p. 181109, Feb. 2009, doi: 10.1063/1.3257976.

[45] A. M. Zaitsev, “Vibronic spectra of impurity-related optical centers in diamond,” *Phys Rev B*, vol. 61, no. 19, pp. 12909–12922, Feb. 2000, doi: 10.1103/PhysRevB.61.12909.

[46] A. M. Zaitsev, “Optical Properties of Diamond,” 2001, doi: 10.1007/978-3-662-04548-0.

[47] E. Corte *et al.*, “Magnesium-Vacancy Optical Centers in Diamond,” *ACS Photonics*, vol. 10, no. 1, pp. 101–110, Jan. 2023, doi: 10.1021/acsphotonics.2c01130.

[48] S. Pezzagna, D. Rogalla, D. Wildanger, J. Meijer, and A. Zaitsev, “Creation and nature of optical centres in diamond for single-photon emission—overview and critical remarks,” *New J Phys*, vol. 13, no. 3, p. 035024, Mar. 2011, doi: 10.1088/1367-2630/13/3/035024.

[49] A. Haque and S. Sumaiya, “An Overview on the Formation and Processing of Nitrogen-Vacancy Photonic Centers in Diamond by Ion Implantation,” *Journal of Manufacturing and Materials Processing*, vol. 1, no. 1, p. 6, Aug. 2017, doi: 10.3390/jmmp1010006.

[50] M. W. Doherty, N. B. Manson, P. Delaney, F. Jelezko, J. Wrachtrup, and L. C. L. L. Hollenberg, “The nitrogen-vacancy colour centre in diamond,” *Phys Rep*, vol. 528, no. 1, pp. 1–45, 2013, doi: 10.1016/j.physrep.2013.02.001.

[51] L. Rondin, J.-P. Tetienne, T. Hingant, J.-F. Roch, P. Maletinsky, and V. Jacques, “Magnetometry with nitrogen-vacancy defects in diamond,” *Reports on Progress in Physics*, vol. 77, no. 5, p. 56503, Feb. 2014, doi: 10.1088/0034-4885/77/5/056503.

[52] S. Pezzagna, B. Naydenov, F. Jelezko, J. Wrachtrup, and J. Meijer, “Creation efficiency of nitrogen-vacancy centres in diamond,” *New J Phys*, vol. 12, no. 6, p. 65017, Feb. 2010, doi: 10.1088/1367-2630/12/6/065017.

[53] K. Nemoto *et al.*, “Photonic Quantum Networks formed from NV- centers,” *Sci Rep*, vol. 6, Feb. 2016, doi: 10.1038/srep26284.

[54] P. Wang, B. Liu, and W. Yang, “Strongly polarizing weakly coupled 13C nuclear spins with optically pumped nitrogen-vacancy center,” *Sci Rep*, vol. 5, no. 1, p. 15847, Nov. 2015, doi: 10.1038/srep15847.

[55] M. Haruyama *et al.*, “Triple nitrogen-vacancy centre fabrication by C5N4Hn ion implantation,” *Nat Commun*, vol. 10, no. 1, p. 2664, Jun. 2019, doi: 10.1038/s41467-019-10529-x.

[56] Y. Miura, S. Kashiwaya, and S. Nomura, “Frequency modulation technique for wide-field imaging of magnetic field with nitrogen-vacancy ensembles,” *Jpn J Appl Phys*, vol. 56, no. 4S, p. 04CK03, Feb. 2017, doi: 10.7567/JJAP.56.04CK03.

[57] H. J. Mamin *et al.*, “Nanoscale Nuclear Magnetic Resonance with a Nitrogen-Vacancy Spin Sensor,” *Science (1979)*, vol. 339, no. 6119, pp. 557–560, Feb. 2013, doi: 10.1126/science.1231540.

[58] C. Chen, D. Dong, R. Long, I. R. Petersen, and H. A. Rabitz, “Sampling-based learning control of inhomogeneous quantum ensembles,” *Phys Rev A*, vol. 89, no. 2, p. 23402, Feb. 2014, doi: 10.1103/PhysRevA.89.023402.

[59] E. H. Chen *et al.*, “High-sensitivity spin-based electrometry with an ensemble of nitrogen-vacancy centers in diamond,” *Phys Rev A (Coll Park)*, vol. 95, no. 5, p. 53417, Feb. 2017, doi: 10.1103/PhysRevA.95.053417.

[60] B. J. M. Hausmann *et al.*, “Single-color centers implanted in diamond nanostructures,” *New J Phys*, vol. 13, no. 4, p. 45004, Feb. 2011, doi: 10.1088/1367-2630/13/4/045004.

[61] K. Groot-Berning, G. Jacob, C. Osterkamp, F. Jelezko, and F. Schmidt-Kaler, “Fabrication of $^{15}NV^{-}$ centers in diamond using a deterministic single ion implanter,” *New J Phys*, vol. 23, no. 6, p. 63067, Feb. 2021, doi: 10.1088/1367-2630/ac0753.

[62] D. D. Awschalom, R. Hanson, J. Wrachtrup, and B. B. Zhou, “Quantum technologies with optically interfaced solid-state spins,” *Nat Photonics*, vol. 12, no. 9, pp. 516–527, Sep. 2018, doi: 10.1038/s41566-018-0232-2.

[63] C. Bradac, W. Gao, J. Forneris, M. E. Trusheim, and I. Aharonovich, “Quantum nanophotonics with group IV defects in diamond,” *Nat Commun*, vol. 10, no. 1, p. 5625, Feb. 2019, doi: 10.1038/s41467-019-13332-w.

[64] G. Thiering and A. Gali, “Ab Initio Magneto-Optical Spectrum of Group-IV Vacancy Color Centers in Diamond,” *Phys Rev X*, vol. 8, no. 2, p. 21063, Feb. 2018, doi: 10.1103/PhysRevX.8.021063.

[65] D. Chen, N. Zheludev, and W. Gao, “Building Blocks for Quantum Network Based on Group-IV Split-Vacancy Centers in Diamond,” *Adv Quantum Technol*, vol. 3, no. 2, Feb. 2020, doi: 10.1002/qute.201900069.

[66] T. Müller *et al.*, “Optical signatures of silicon-vacancy spins in diamond,” *Nat Commun*, vol. 5, no. 1, p. 3328, 2014, [Online]. Available: http://www.nature.com/articles/ncomms4328

[67] W. Liu *et al.*, “Silicon-Vacancy Nanodiamonds as High Performance Near-Infrared Emitters for Live-Cell Dual-Color Imaging and Thermometry,” *Nano Lett*, vol. 22, no. 7, pp. 2881–2888, Apr. 2022, doi: 10.1021/acs.nanolett.2c00040.

[68] A. I. Zeleneev *et al.*, “Nanodiamonds with SiV colour centres for quantum technologies,” *Quantum Elec (Woodbury)*, vol. 50, no. 3, pp. 299–304, Mar. 2020, doi: 10.1070/QEL17189.

[69] B. Pingault *et al.*, “Coherent control of the silicon-vacancy spin in diamond,” *Nat Commun*, vol. 8, no. 1, p. 15579, Feb. 2017, doi: 10.1038/ncomms15579.

[70] T. Iwasaki *et al.*, “Germanium-Vacancy Single Color Centers in Diamond,” *Sci Rep*, vol. 5, no. 1, p. 12882, Feb. 2015, doi: 10.1038/srep12882.

[71] M. K. Bhaskar *et al.*, “Quantum Nonlinear Optics with a Germanium-Vacancy Color Center in a Nanoscale Diamond Waveguide,” *Phys Rev Lett*, vol. 118, no. 22, p. 223603, Feb. 2017, doi: 10.1103/PhysRevLett.118.223603.

[72] K. Senkalla, G. Genov, M. H. Metsch, P. Siyushev, and F. Jelezko, “Germanium Vacancy in Diamond Quantum Memory Exceeding 20 ms,” *Phys Rev Lett*, vol. 132, no. 2, p. 026901, Jan. 2024, doi: 10.1103/PhysRevLett.132.026901.

[73] Y. Zhou *et al.*, “Direct writing of single germanium vacancy center arrays in diamond,” *New J. Phys.*, vol. 20, no. 12, p. 125004, Feb. 2018, doi: 10.1088/1367-2630/aaf2ac.

[74] E. N. Hernández *et al.*, “Efficiency Optimization of Ge-V Quantum Emitters in Single-Crystal Diamond upon Ion Implantation and HPHT Annealing,” *Adv Quantum Technol*, vol. 6, no. 8, Feb. 2023, doi: 10.1002/qute.202300010.

[75] T. Iwasaki *et al.*, “Tin-Vacancy Quantum Emitters in Diamond,” *Phys Rev Lett*, vol. 119, no. 25, p. 253601, Dec. 2017, doi: 10.1103/PhysRevLett.119.253601.

[76] J. Görlitz *et al.*, “Coherence of a charge stabilised tin-vacancy spin in diamond,” *npj Quantum Inf*, vol. 8, no. 1, p. 45, Feb. 2022, doi: 10.1038/s41534-022-00552-0.

[77] A. E. Rugar *et al.*, “Quantum Photonic Interface for Tin-Vacancy Centers in Diamond,” *Phys Rev X*, vol. 11, no. 3, p. 031021, Jul. 2021, doi: 10.1103/PhysRevX.11.031021.

[78] J. Görlitz *et al.*, “Spectroscopic investigations of negatively charged tin-vacancy centres in diamond,” *New J Phys*, vol. 22, no. 1, p. 13048, Feb. 2020, doi: 10.1088/1367-2630/ab6631.

[79] E. I. Rosenthal *et al.*, “Microwave Spin Control of a Tin-Vacancy Qubit in Diamond,” *Phys Rev X*, vol. 13, no. 3, p. 31022, Feb. 2023, doi: 10.1103/PhysRevX.13.031022.

[80] A. A. Razgulov, S. G. Lyapin, A. P. Novikov, and E. A. Ekimov, “Low-temperature photoluminescence study of SnV centers in HPHT diamond,” *Diam Relat Mater*, vol. 116, p. 108379, Feb. 2021, doi: 10.1016/j.diamond.2021.108379.

[81] S. D. Tchernij *et al.*, “Single-Photon Emitters in Lead-Implanted Single-Crystal Diamond,” *ACS Photonics*, vol. 5, no. 12, pp. 4864–4871, Feb. 2018, doi: 10.1021/acsphotonics.8b01013.

[82] M. E. Trusheim *et al.*, “Lead-related quantum emitters in diamond,” *Phys Rev B*, vol. 99, no. 7, p. 75430, Feb. 2019, doi: 10.1103/PHYSREVB.99.075430.

[83] P. Wang *et al.*, “Transform-Limited Photon Emission from a Lead-Vacancy Center in Diamond above 10 K,” *Phys Rev Lett*, vol. 132, no. 7, p. 073601, Feb. 2024, doi: 10.1103/PhysRevLett.132.073601.

[84] P. Wang, T. Taniguchi, Y. Miyamoto, M. Hatano, and T. Iwasaki, “Low-Temperature Spectroscopic Investigation of Lead-Vacancy Centers in Diamond Fabricated by High-Pressure and High-Temperature Treatment,” *ACS Photonics*, vol. 8, no. 10, pp. 2947–2954, Oct. 2021, doi: 10.1021/acsphotonics.1c00840.

[85] T. Lühmann, J. Meijer, and S. Pezzagna, “Charge-Assisted Engineering of Color Centers in Diamond,” *physica status solidi (a)*, vol. 218, no. 5, Feb. 2021, doi: 10.1002/pssa.202000614.

[86] I. Aharonovich, A. D. Greentree, and S. Prawer, “Diamond photonics,” *Nat. Photonics*, vol. 5, no. 7, pp. 397–405, Feb. 2011, doi: 10.1038/nphoton.2011.54.

[87] N. Li, C. P. Ho, S. Zhu, Y. H. Fu, Y. Zhu, and L. Y. T. Lee, "Aluminium nitride integrated photonics: a review," *Nanophotonics*, vol. 10, no. 9, pp. 2347–2387, Jul. 2021, doi: 10.1515/nanoph-2021-0130.

[88] M. Lipson, "Silicon photonics: An exercise in self control," Feb. 2007. doi: 10.1038/nphoton.2006.63.

[89] A. Lohrmann, B. C. Johnson, J. C. McCallum, and S. Castelletto, "A review on single photon sources in silicon carbide," *Reports on Progress in Physics*, vol. 80, no. 3, p. 34502, Feb. 2017, doi: 10.1088/1361-6633/aa5171.

[90] D. Riedel, "Resonant addressing and manipulation of silicon vacancy qubits in silicon carbide," *Phys. Rev. Lett.*, vol. 109, p. 226402, 2012.

[91] M. E. Bathen and L. Vines, "Manipulating Single-Photon Emission from Point Defects in Diamond and Silicon Carbide," *Adv Quantum Technol*, vol. 4, no. 7, Feb. 2021, doi: 10.1002/qute.202100003.

[92] D. M. Lukin *et al.*, "4H-silicon-carbide-on-insulator for integrated quantum and nonlinear photonics," *Nat Photonics*, vol. 14, no. 5, pp. 330–334, Feb. 2020, doi: 10.1038/s41566-019-0556-6.

[93] A. Lohrmann *et al.*, "Single-photon emitting diode in silicon carbide," *Nat. Commun.*, vol. 6, pp. 1–7, 2015, doi: 10.1038/ncomms8783.

[94] A. L. Falk *et al.*, "Polytype control of spin qubits in silicon carbide," *Nat Commun*, vol. 4, no. 1, p. 1819, Feb. 2013, doi: 10.1038/ncomms2854.

[95] W. F. Koehl, B. B. Buckley, F. J. Heremans, G. Calusine, and D. D. Awschalom, "Room temperature coherent control of defect spin qubits in silicon carbide," *Nature*, vol. 479, no. 7371, pp. 84–87, Nov. 2011, doi: 10.1038/nature10562.

[96] T. Umeda, "Identification of the carbon antisite–vacancy pair in 4H-SiC," *Phys. Rev. Lett.*, vol. 96, p. 145501, 2006.

[97] J.-F. Wang *et al.*, "Coherent Control of Nitrogen-Vacancy Center Spins in Silicon Carbide at Room Temperature," *Phys Rev Lett*, vol. 124, no. 22, p. 223601, Jun. 2020, doi: 10.1103/PhysRevLett.124.223601.

[98] P. Cilibrizzi *et al.*, "Ultra-narrow inhomogeneous spectral distribution of telecom-wavelength vanadium centres in isotopically-enriched silicon carbide," *Nat Commun*, vol. 14, no. 1, p. 8448, Dec. 2023, doi: 10.1038/s41467-023-43923-7.

[99] S. Castelletto *et al.*, "Silicon Carbide Photonics Bridging Quantum Technology," *ACS Photonics*, vol. 9, no. 5, pp. 1434–1457, May 2022, doi: 10.1021/acsphotonics.1c01775.

[100] J. Wang *et al.*, "Bright room temperature single photon source at telecom range in cubic silicon carbide," *Nat Commun*, vol. 9, no. 1, p. 4106, Oct. 2018, doi: 10.1038/s41467-018-06605-3.

[101] G. Vizkelethy *et al.*, "Anomalous charge collection from silicon-on-insulator structures," *Nucl Instrum Methods Phys Res B*, vol. 210, pp. 211–215, Feb. 2003, doi: 10.1016/S0168-583X(03)01072-3.

[102] M. Vinet *et al.*, "Towards scalable silicon quantum computing," in *Technical Digest - International Electron Devices Meeting, IEDM*, Institute of Electrical and Electronics Engineers Inc., Feb. 2019, pp. 6.5.1–6.5.4. doi: 10.1109/IEDM.2018.8614675.

[103] C. Beaufils *et al.*, "Optical properties of an ensemble of G-centers in silicon," *Phys Rev B*, vol. 97, no. 3, p. 35303, Feb. 2018, doi: 10.1103/PhysRevB.97.035303.

[104] H. Quard *et al.*, “Femtosecond-laser-induced creation of G and W color centers in silicon-on-insulator substrates,” *Phys Rev Appl*, vol. 21, no. 4, p. 044014, Apr. 2024, doi: 10.1103/PhysRevApplied.21.044014.

[105] B. Lefaucher and J.-B. Jager, “Purcell enhancement of silicon W centers in circular Bragg grating cavities”, doi: 10.48550/arXiv.2310.18121.

[106] G. Andrini *et al.*, “Activation of telecom emitters in silicon upon ion implantation and ns pulsed laser annealing,” *Commun Mater*, vol. 5, no. 1, p. 47, Apr. 2024, doi: 10.1038/s43246-024-00486-4.

[107] A. Simon and G. Kalinka, “Investigation of charge collection in a silicon PIN photodiode,” *Nucl Instrum Methods Phys Res B*, vol. 231, no. 1–4, pp. 507–512, Feb. 2005, doi: 10.1016/j.nimb.2005.01.108.

[108] M. Hollenbach *et al.*, “Wafer-scale nanofabrication of telecom single-photon emitters in silicon,” *Nat Commun*, vol. 13, no. 1, p. 7683, Dec. 2022, doi: 10.1038/s41467-022-35051-5.

[109] G. Zhang, Y. Cheng, J.-P. Chou, and A. Gali, “Material platforms for defect qubits and single-photon emitters,” *Appl Phys Rev*, vol. 7, no. 3, Sep. 2020, doi: 10.1063/5.0006075.

[110] S. Kako, C. Santori, K. Hoshino, S. Götzinger, Y. Yamamoto, and Y. Arakawa, “A gallium nitride single-photon source operating at 200 K,” *Nat Mater*, vol. 5, no. 11, pp. 887–892, Feb. 2006, doi: 10.1038/nmat1763.

[111] J. Adam, R. Duffy, F. Roccaforte, F. Giannazzo, and G. Greco, “Ion Implantation Doping in Silicon Carbide and Gallium Nitride Electronic Devices,” *Micro 2022, Vol. 2, Pages 23-53*, vol. 2, no. 1, pp. 23–53, Feb. 2022, doi: 10.3390/MICRO2010002.

[112] A. M. Berhane *et al.*, “Photophysics of GaN single-photon emitters in the visible spectral range,” *Phys Rev B*, vol. 97, no. 16, p. 165202, Apr. 2018, doi: 10.1103/PhysRevB.97.165202.

[113] Y. Geng *et al.*, “Dephasing by optical phonons in GaN defect single-photon emitters,” *Sci Rep*, vol. 13, no. 1, p. 8678, May 2023, doi: 10.1038/s41598-023-35003-z.

[114] M. A. Reshchikov, “Photoluminescence from Vacancy-Containing Defects in GaN,” *physica status solidi (a)*, vol. 220, no. 10, May 2023, doi: 10.1002/pssa.202200402.

[115] M. Meunier *et al.*, “Telecom single-photon emitters in GaN operating at room temperature: embedment into bullseye antennas,” *Nanophotonics*, vol. 12, no. 8, pp. 1405–1419, Apr. 2023, doi: 10.1515/nanoph-2022-0659.

[116] S. G. Bishop, J. P. Hadden, R. Hekmati, J. K. Cannon, W. W. Langbein, and A. J. Bennett, “Enhanced light collection from a gallium nitride color center using a near index-matched solid immersion lens,” *Appl Phys Lett*, vol. 120, no. 11, Mar. 2022, doi: 10.1063/5.0085257.

[117] E. Ruiz, S. Alvarez, and P. Alemany, “Electronic structure and properties of AlN,” *Phys Rev B*, vol. 49, no. 11, pp. 7115–7123, Mar. 1994, doi: 10.1103/PhysRevB.49.7115.

[118] T.-J. Lu *et al.*, “Bright High-Purity Quantum Emitters in Aluminum Nitride Integrated Photonics,” *ACS Photonics*, vol. 7, no. 10, pp. 2650–2657, Oct. 2020, doi: 10.1021/acsphotonics.0c01259.

[119] J. K. Cannon, S. G. Bishop, J. P. Hadden, H. B. Yağcı, and A. J. Bennett, “Polarization study of single color centers in aluminum nitride,” *Appl Phys Lett*, vol. 122, no. 17, Apr. 2023, doi: 10.1063/5.0145542.

[120] J. K. Cannon *et al.*, “Colour Centres in Aluminium Nitride are Bright, Room-Temperature Quantum Light Sources,” in *2023 23rd International Conference on Transparent Optical Networks (ICTON)*, IEEE, Jul. 2023, pp. 1–2. doi: 10.1109/ICTON59386.2023.10207363.

[121] N. Li, C. P. Ho, S. Zhu, Y. H. Fu, Y. Zhu, and L. Y. T. Lee, “Aluminium nitride integrated photonics: a review,” *Nanophotonics*, vol. 10, no. 9, pp. 2347–2387, Jul. 2021, doi: 10.1515/nanoph-2021-0130.

[122] E. Nieto Hernández *et al.*, “Fabrication of quantum emitters in aluminum nitride by Al-ion implantation and thermal annealing,” *Appl Phys Lett*, vol. 124, no. 12, Mar. 2024, doi: 10.1063/5.0185534.

[123] Y. Tu *et al.*, “A paramagnetic neutral VAlON center in wurtzite AlN for spin qubit application,” *Appl Phys Lett*, vol. 103, no. 7, Aug. 2013, doi: 10.1063/1.4818659.

[124] T.-J. Lu *et al.*, “Bright High-Purity Quantum Emitters in Aluminum Nitride Integrated Photonics,” *ACS Photonics*, vol. 7, no. 10, pp. 2650–2657, Oct. 2020, doi: 10.1021/acsphotonics.0c01259.

[125] X.-J. Wang *et al.*, “Quantum Emitters with Narrow Band and High Debye–Waller Factor in Aluminum Nitride Written by Femtosecond Laser,” *Nano Lett*, vol. 23, no. 7, pp. 2743–2749, Apr. 2023, doi: 10.1021/acs.nanolett.3c00019.

[126] A. Senichev *et al.*, “Quantum emitters in aluminum nitride induced by heavy ion irradiation,” *APL Quantum*, vol. 1, no. 3, Sep. 2024, doi: 10.1063/5.0199647.

[127] A. M. Zaitsev *et al.*, “Nitrogen-doped CVD diamond: Nitrogen concentration, color and internal stress,” *Diam Relat Mater*, vol. 105, p. 107794, Feb. 2020, doi: 10.1016/j.diamond.2020.107794.

[128] M. Wolfer, A. Kriele, O. A. Williams, H. Obloh, C.-C. Leancu, and C. E. Nebel, “Nickel doping of nitrogen enriched CVD-diamond for the production of single photon emitters,” *physica status solidi (a)*, vol. 2015, no. 9, pp. 2012–2015, Feb. 2015, doi: 10.1002/pssa.200982231.

[129] R. J. Nemanich, J. A. Carlisle, A. Hirata, and K. Haenen, “CVD diamond—Research, applications, and challenges,” *MRS Bull*, vol. 39, no. 6, pp. 490–494, Feb. 2014, doi: 10.1557/mrs.2014.97.

[130] I. Aharonovich, C. Zhou, A. Stacey, F. Treussart, J. Roch, and S. Prawer, “Formation of color centers in nanodiamonds by plasma assisted diffusion of impurities from the growth substrate,” *Appl Phys Lett*, vol. 93, no. 24, pp. 2008–2010, Feb. 2008, doi: 10.1063/1.3049606.

[131] K. Li, Y. Zhou, A. Rasmita, I. Aharonovich, and W. B. Gao, “Nonblinking Emitters with Nearly Lifetime-Limited Linewidths in CVD Nanodiamonds,” *Phys Rev Appl*, vol. 6, no. 2, p. 24010, Feb. 2016, doi: 10.1103/PhysRevApplied.6.024010.

[132] I. Aharonovich, S. Castelletto, D. A. Simpson, C.-H. Su, A. D. Greentree, and S. Prawer, “Diamond-based single-photon emitters,” *Reports on Progress in Physics*, vol. 74, no. 7, p. 076501, Jul. 2011, doi: 10.1088/0034-4885/74/7/076501.

[133] Y. C. Chen *et al.*, “Laser writing of coherent colour centres in diamond,” *Nat. Photonics*, vol. 11, no. 2, pp. 77–80, 2016, doi: 10.1038/nphoton.2016.234.

[134] Y.-C. Chen *et al.*, “Laser writing of individual nitrogen-vacancy defects in diamond with near-unity yield,” *Optica*, vol. 6, no. 5, pp. 662–667, May 2019, doi: 10.1364/OPTICA.6.000662.

[135] J. Engel *et al.*, “Combining femtosecond laser annealing and shallow ion implantation for local color center creation in diamond,” *Appl Phys Lett*, vol. 122, no. 23, Feb. 2023, doi: 10.1063/5.0143922.

[136] M. Capelli *et al.*, “Increased nitrogen-vacancy centre creation yield in diamond through electron beam irradiation at high temperature,” *Carbon N Y*, vol. 143, pp. 714–719, Mar. 2019, doi: 10.1016/j.carbon.2018.11.051.

[137] C. A. McLellan, B. A. Myers, S. Kraemer, K. Ohno, D. D. Awschalom, and A. C. B. Jayich, “Patterned Formation of Highly Coherent Nitrogen-Vacancy Centers Using a Focused Electron

Irradiation Technique," *Nano Lett*, vol. 16, no. 4, pp. 2450–2454, Feb. 2016, doi: 10.1021/acs.nanolett.5b05304.

[138] J. W. Mayer, L. Eriksson, and J. A. Davies, *Ion Implantation in Semiconductors*. Academic, 1970.

[139] J. F. Prins, "Ion-implanted, shallow-energy, donor centres in diamond: the effect of negative electron affinity," *Nucl Instrum Methods Phys Res A*, vol. 514, no. 1–3, pp. 69–78, Feb. 2003, doi: 10.1016/j.nima.2003.08.085.

[140] S. Pezzagna *et al.*, "Creation of colour centres in diamond by collimated ion-implantation through nano-channels in mica," Feb. 2011, *John Wiley & Sons, Ltd*. doi: 10.1002/pssa.201100455.

[141] S. K. Tripathi *et al.*, "Resolution, masking capability and throughput for direct-write, ion implant mask patterning of diamond surfaces using ion beam lithography," *Journal of Micromechanics and Microengineering*, vol. 22, no. 5, p. 55005, Feb. 2012, doi: 10.1088/0960-1317/22/5/055005.

[142] J. M. King, J. E. Shigley, T. H. Gelb, S. S. Guhin, M. Hall, and W. Wang, "Characterization and Grading of Natural-Color Yellow Diamonds," *Gems & Gemology*, vol. 41, no. 2, pp. 88–115, Feb. 2005, doi: 10.5741/GEMS.41.2.88.

[143] J. J. Shea, "Properties, Growth and Applications of Diamond [Book Review]," *IEEE Electrical Insulation Magazine*, vol. 18, no. 5, p. 47, 2005, doi: 10.1109/mei.2002.1044323.

[144] X. Wu, M. Sprinkle, X. Li, F. Ming, C. Berger, and W. A. de Heer, "Epitaxial-Graphene/Graphene-Oxide Junction: An Essential Step towards Epitaxial Graphene Electronics," *Phys Rev Lett*, vol. 101, no. 2, p. 26801, Feb. 2008, doi: 10.1103/PhysRevLett.101.026801.

[145] J. Tetienne, N. Dontschuk, D. A. Broadway, A. Stacey, D. A. Simpson, and L. C. L. Hollenberg, "Quantum imaging of current flow in graphene," *Sci Adv*, vol. 3, no. 4, Feb. 2017, doi: 10.1126/sciadv.1602429.

[146] F. P. Bundy, W. A. Bassett, M. S. Weathers, R. J. Hemley, H. U. Mao, and A. F. Goncharov, "The pressure-temperature phase and transformation diagram for carbon; updated through 1994," *Carbon N Y*, vol. 34, no. 2, pp. 141–153, 1996, doi: 10.1016/0008-6223(96)00170-4.

[147] C. Chen and Q. Chen, "Recent development in diamond synthesis ," *Int J Mod Phys B*, vol. 22, no. 04, pp. 309–326, Feb. 2008, doi: 10.1142/S0217979208038685.

[148] H. O. Pierson, "Graphite Structure and Properties," in *Handbook of Carbon, Graphite, Diamonds and Fullerenes*, Elsevier, 1993, pp. 43–69. doi: 10.1016/B978-0-8155-1339-1.50008-6.

[149] E. Kaxiras, *Atomic and Electronic Structure of Solids*. Cambridge University Press, 2003. doi: 10.1017/CBO9780511755545.

[150] P. Pavone *et al.*, "*Ab initio* lattice dynamics of diamond," *Phys Rev B*, vol. 48, no. 5, pp. 3156–3163, Aug. 1993, doi: 10.1103/PhysRevB.48.3156.

[151] L. Tang, C. Tsai, W. W. Gerberich, L. Kruckeberg, and D. R. Kania, "Biocompatibility of chemical-vapour-deposited diamond," *Biomaterials*, vol. 16, no. 6, pp. 483–488, Jan. 1995, doi: 10.1016/0142-9612(95)98822-V.

[152] J. Barjon, N. Habka, C. Mer, F. Jomard, J. Chevallier, and P. Bergonzo, "Resistivity of boron doped diamond," *physica status solidi (RRL) – Rapid Research Letters*, vol. 3, no. 6, pp. 202–204, Sep. 2009, doi: 10.1002/pssr.200903097.

[153] J. F. Prins, "Ion implantation of diamond for electronic applications," *Semicond Sci Technol*, vol. 18, no. 3, pp. S27–S33, Mar. 2003, doi: 10.1088/0268-1242/18/3/304.

[154] A. T. Collins, “Diamond Electronic Devices—The End of a Dream?,” *Isr J Chem*, vol. 38, no. 1–2, pp. 121–133, Jan. 1998, doi: 10.1002/ijch.199800013.

[155] F. Fizzotti, A. Lo Giudice, Ch. Manfredotti, C. Manfredotti, M. Castellino, and E. Vittone, “Diamond surface conductivity after exposure to molecular hydrogen,” *Diam Relat Mater*, vol. 16, no. 4–7, pp. 836–839, Apr. 2007, doi: 10.1016/j.diamond.2006.11.094.

[156] C. M. Breeding and J. E. Shigley, “The ‘type’ classification system of diamonds and its importance in gemology,” *Gems and Gemology*, 2009.

[157] F. P. Bundy, H. T. Hall, H. M. Strong, and R. H. Wentorfjun, “Man-Made Diamonds,” *Nature*, vol. 176, no. 4471, pp. 51–55, Jul. 1955, doi: 10.1038/176051a0.

[158] F. Silva *et al.*, “High quality, large surface area, homoepitaxial MPACVD diamond growth,” *Diam Relat Mater*, vol. 18, no. 5–8, pp. 683–697, May 2009, doi: 10.1016/j.diamond.2009.01.038.

[159] “Element Six | Synthetic Diamond and Tungsten Carbide Experts - Element Six.” [Online]. Available: https://www.e6.com/

[160] V. N. Mochalin, O. Shenderova, D. Ho, and Y. Gogotsi, “The properties and applications of nanodiamonds,” *Nat Nanotechnol*, vol. 7, no. 1, pp. 11–23, Jan. 2012, doi: 10.1038/nnano.2011.209.

[161] “https://www.power-and-beyond.com/aluminium-nitride-the-semiconductor-of-the-future-a-cbded96a594a13720644c5653a3050af/.”

[162] A. Kobayashi, O. F. Sankey, S. M. Volz, and J. D. Dow, “Semiempirical tight-binding band structures of wurtzite semiconductors: AlN, CdS, CdSe, ZnS, and ZnO,” *Phys Rev B*, vol. 28, no. 2, pp. 935–945, Jul. 1983, doi: 10.1103/PhysRevB.28.935.

[163] “https://heegermaterials.com/blog/54_Aluminum-Nitride-Ceramic-Substrates--Factors-.html”.

[164] E. Österlund, J. Kinnunen, V. Rontu, A. Torkkeli, and M. Paulasto-Kröckel, “Mechanical properties and reliability of aluminum nitride thin films,” *J Alloys Compd*, vol. 772, pp. 306–313, Jan. 2019, doi: 10.1016/j.jallcom.2018.09.062.

[165] “Goldberg Yu. in Properties of Advanced SemiconductorMaterials GaN, AlN, InN, BN, SiC, SiGe . Eds. Levinshtein M.E., Rumyantsev S.L., Shur M.S., John Wiley & Sons, Inc., New York, 2001, 31-47.”

[166] “https://matmatch.com/suppliers/inno-xiamen-innovacera-advanced-materials-co-ltd/examples/aluminium-nitride-properties-applications.”

[167] E. Thomas and R. Ranjith, “Effect of Doping in Aluminium Nitride (AlN) Nanomaterials: A Review,” *ECS Trans*, vol. 107, no. 1, pp. 15229–15237, Apr. 2022, doi: 10.1149/10701.15229ecst.

[168] R. Kirste and Z. Sitar, “The growth of bulk aluminum nitride,” in *III-Nitride Semiconductors and their Modern Devices*, Oxford University Press, 2013, pp. 121–146. doi: 10.1093/acprof:oso/9780199681723.003.0004.

[169] S. Hasan, M. U. Jewel, S. G. Karakalos, M. Gaevski, and I. Ahmad, “Comparative Spectroscopic Study of Aluminum Nitride Grown by MOCVD in H2 and N2 Reaction Environment,” *Coatings*, vol. 12, no. 7, p. 924, Jun. 2022, doi: 10.3390/coatings12070924.

[170] B. Gil, Ed., *III-Nitride Semiconductors and their Modern Devices*. Oxford University Press, 2013. doi: 10.1093/acprof:oso/9780199681723.001.0001.

[171] E. Wang, H. Zhang, X. Xie, L. Xie, L. Bian, and G. Chen, “AlN Thin Films Grown on Different Substrates by Metal Nitride Vapor Phase Epitaxy,” *Crystal Research and Technology*, vol. 58, no. 3, Mar. 2023, doi: 10.1002/crat.202200196.

[172] X. Lin, H. Zhang, C. Li, X. Xie, L. Bian, and G. Chen, “Three-step growth of AlN films on sapphire substrates by metal nitride vapor phase epitaxy,” *J Cryst Growth*, vol. 625, p. 127451, Jan. 2024, doi: 10.1016/j.jcrysgro.2023.127451.

[173] “https://www.sciencedirect.com/topics/chemistry/aluminum-nitride.”

[174] M. Nastasi, J. Mayer, and J. K. Hirvonen, *Ion-Solid Interactions*. Cambridge University Press, 1996. doi: 10.1017/CBO9780511565007.

[175] “https://www.iue.tuwien.ac.at/phd/wittmann/node8.html.”

[176] H. M. Qadr and A. M. Hamad, “Using of Stopping and Range of Ions in Matter Code to Study of Radiation Damage in Materials,” *Radioelectronics. Nanosystems. Information Technologies*, vol. 12, no. 4, pp. 451–456, Dec. 2020, doi: 10.17725/rensit.2020.12.451.

[177] B. Rauschenbach, “Ion Beam-Induced Damages,” 2022, pp. 71–122. doi: 10.1007/978-3-030-97277-6_4.

[178] J. F. Ziegler, M. D. Ziegler, and J. P. Biersack, “SRIM – The stopping and range of ions in matter (2010),” *Nucl Instrum Methods Phys Res B*, vol. 268, no. 11–12, pp. 1818–1823, Feb. 2010, doi: 10.1016/j.nimb.2010.02.091.

[179] C. Uzan-Saguy, C. Cytermann, R. Brener, V. Richter, M. Shaanan, and R. Kalish, “Damage threshold for ion-beam induced graphitization of diamond,” *Appl Phys Lett*, vol. 67, no. 9, pp. 1194–1196, Feb. 1995, doi: 10.1063/1.115004.

[180] R. Kalish, A. Reznik, K. W. Nugent, and S. Prawer, “The nature of damage in ion-implanted and annealed diamond,” *Nucl. Instruments Methods Phys. Res. Sect. B Beam Interact. with Mater. Atoms*, vol. 148, no. 1, pp. 626–633, Feb. 1999, doi: 10.1016/S0168-583X(98)00857-X.

[181] Q. Bai, Z. Wang, Y. Guo, J. Chen, and Y. Shang, “Graphitization Behavior of Single Crystal Diamond for the Application in Nano-Metric Cutting,” *Curr Nanosci*, vol. 14, no. 5, pp. 377–383, Jul. 2018, doi: 10.2174/1573413714666180517080721.

[182] J. Forneris *et al.*, “Electroluminescence from a diamond device with ion-beam-micromachined buried graphitic electrodes,” *Nucl. Instruments Methods Phys. Res. Sect. B Beam Interact. with Mater. Atoms*, vol. 348, 2015, doi: 10.1016/j.nimb.2014.12.036.

[183] S. O. Kucheyev *et al.*, “Ion-beam-produced damage and its stability in AlN films,” *J Appl Phys*, vol. 92, no. 7, pp. 3554–3558, Oct. 2002, doi: 10.1063/1.1501746.

[184] D. N. Jamieson *et al.*, “Deterministic doping,” *Mater. Sci. Semicond. Process.*, vol. 62, no. October, pp. 23–30, 2017, doi: 10.1016/j.mssp.2016.10.039.

[185] L. G. Wang and A. Zunger, “Phosphorus and sulphur doping of diamond,” *Phys Rev B Condens Matter Mater Phys*, vol. 66, no. 16, pp. 1–4, 2002, doi: 10.1103/PhysRevB.66.161202.

[186] J. Barjon, N. Habka, C. Mer, F. Jomard, J. Chevallier, and P. Bergonzo, “Resistivity of boron doped diamond,” *physica status solidi (RRL) – Rapid Research Letters*, vol. 3, no. 6, pp. 202–204, Feb. 2009, doi: 10.1002/pssr.200903097.

[187] J. P. Goss, P. R. Briddon, M. J. Rayson, S. J. Sque, and R. Jones, “Vacancy-impurity complexes and limitations for implantation doping of diamond,” *Phys Rev B Condens Matter Mater Phys*, vol. 72, no. 3, pp. 1–11, 2005, doi: 10.1103/PhysRevB.72.035214.

[188] Y. Katamune, A. Izumi, K. Ichikawa, and S. Koizumi, “Heavy phosphorus doping of diamond by hot-filament chemical vapor deposition,” *Diam Relat Mater*, vol. 134, p. 109789, Apr. 2023, doi: 10.1016/j.diamond.2023.109789.

[189] M. De Feudis *et al.*, “Characterization of surface graphitic electrodes made by excimer laser on CVD diamond,” *Diam Relat Mater*, vol. 65, pp. 137–143, Feb. 2016, doi: 10.1016/j.diamond.2016.03.003.

[190] F. Picollo *et al.*, “Fabrication and electrical characterization of three-dimensional graphitic microchannels in single crystal diamond,” *New J Phys*, vol. 14, no. 5, p. 53011, Feb. 2012, doi: 10.1088/1367-2630/14/5/053011.

[191] Y. Wu *et al.*, “Controlling Defect Formation of Nanoscale AlN: Toward Efficient Current Conduction of Ultrawide-Bandgap Semiconductors,” *Adv Electron Mater*, vol. 6, no. 9, Sep. 2020, doi: 10.1002/aelm.202000337.

[192] H. Fiedler *et al.*, “Giant Piezoelectricity of Deformed Aluminum Nitride Stabilized through Noble Gas Interstitials for Energy Efficient Resonators,” *Adv Electron Mater*, vol. 7, no. 8, Aug. 2021, doi: 10.1002/aelm.202100358.

[193] K. Larsson, “The Combined Influence of Dopant Species and Surface Termination on the Electronic Properties of Diamond Surfaces,” *C — Journal of Carbon Research*, vol. 6, no. 2, p. 22, Apr. 2020, doi: 10.3390/c6020022.

[194] S. Pezzagna and J. Meijer, “High-Resolution Ion Implantation from keV to MeV,” in *Ion Implantation*, InTech, 2012. doi: 10.5772/34601.

[195] T. Matsukawa, T. Fukai, S. Suzuki, K. Hara, M. Koh, and I. Ohdomari, “Development of single-ion implantation — controllability of implanted ion number,” *Appl Surf Sci*, vol. 117–118, pp. 677–683, Feb. 1997, doi: 10.1016/S0169-4332(97)80163-8.

[196] J. Meijer *et al.*, “Generation of single color centers by focused nitrogen implantation,” *Appl Phys Lett*, vol. 87, no. 26, pp. 2005–2007, Feb. 2005, doi: 10.1063/1.2103389.

[197] S. Lagomarsino *et al.*, “Optical properties of silicon-vacancy color centers in diamond created by ion implantation and post-annealing,” *Diam Relat Mater*, vol. 84, pp. 196–203, Feb. 2018, doi: 10.1016/j.diamond.2018.03.010.

[198] P. Spinicelli *et al.*, “Engineered arrays of nitrogen-vacancy color centers in diamond based on implantation of CN^- molecules through nanoapertures,” *New J Phys*, vol. 13, no. 2, p. 025014, Feb. 2011, doi: 10.1088/1367-2630/13/2/025014.

[199] V. M. Acosta *et al.*, “Diamonds with a high density of nitrogen-vacancy centers for magnetometry applications,” *Phys Rev B Condens Matter Mater Phys*, vol. 80, no. 11, pp. 1–15, Feb. 2009, doi: 10.1103/PhysRevB.80.115202.

[200] F. Forouzandeh, X. Li, and D. W. Banham, “The Effects of Hot Ion-Implantation on the Electrical Properties of Amorphous-Silicon Films Produced by Chemical-Vapor-Deposition Method You may also like Understanding the Corrosion Resistance of Meso-and Micro-Porous Carbons for Application in PEM Fuel Cells.”

[201] P. Olivero *et al.*, “Focused ion beam fabrication and IBIC characterization of a diamond detector with buried electrodes,” *Nucl. Instruments Methods Phys. Res. Sect. B Beam Interact. with Mater. Atoms*, vol. 269, no. 20, 2011, doi: 10.1016/j.nimb.2011.02.021.

[202] Z. Huang *et al.*, “Diamond nitrogen-vacancy centers created by scanning focused helium ion beam and annealing,” *Appl Phys Lett*, vol. 103, no. 8, p. 81906, Feb. 2013, doi: 10.1063/1.4819339.

[203] P. J. Sellin, A. Lohstroh, A. Simon, and M. B. H. Breese, “Digital IBIC—new spectroscopic modalities for ion-beam-induced charge imaging,” *Nucl Instrum Methods Phys Res A*, vol. 521, no. 2–3, pp. 600–607, Feb. 2004, doi: 10.1016/j.nima.2003.11.248.

[204] T. Osipowicz *et al.*, “IBIC analysis of high-power devices,” *Nucl Instrum Methods Phys Res B*, vol. 181, no. 1–4, pp. 311–314, Feb. 2001, doi: 10.1016/S0168-583X(01)00487-6.

[205] E. Vittone *et al.*, “Micro-IBICC and micro-IL analyses of CVD diamond microdosimeters,” *Nucl Instrum Methods Phys Res B*, vol. 181, no. 1–4, pp. 349–353, Feb. 2001, doi: 10.1016/S0168-583X(01)00527-4.

[206] S. Pezzagna and J. Meijer, “Single-Ion Implantation in Diamond with a High Lateral Resolution: A Key Technology for the Fabrication of Quantum Devices,” in *Comprehensive Hard Materials*, vol. 3, Elsevier Ltd., 2014, pp. 321–336. doi: 10.1016/B978-0-08-096527-7.00050-7.

[207] J. Cajzl *et al.*, “Erbium Luminescence centres in single- and nano-crystalline diamond-effects of ion implantation fluence and thermal annealing,” *Micromachines (Basel)*, vol. 9, no. 7, 2018, doi: 10.3390/mi9070316.

[208] N. Raatz, C. Scheuner, S. Pezzagna, and J. Meijer, “Investigation of Ion Channeling and Scattering for Single-Ion Implantation with High Spatial Resolution,” *physica status solidi (a)*, vol. 216, no. 21, Nov. 2019, doi: 10.1002/pssa.201900528.

[209] D. N. Jamieson *et al.*, “Controlled shallow single-ion implantation in silicon using an active substrate for sub-20-keV ions,” *Appl Phys Lett*, vol. 86, no. 20, p. 202101, Feb. 2005, doi: 10.1063/1.1925320.

[210] K. Groot-Berning *et al.*, “Deterministic Single-Ion Implantation of Rare-Earth Ions for Nanometer-Resolution Color-Center Generation,” *Phys Rev Lett*, vol. 123, no. 10, p. 106802, Feb. 2019, doi: 10.1103/PhysRevLett.123.106802.

[211] M. Current, L. Rubin, and F. Sinclair, “Commercial Ion Implantation Systems,” 2018.

[212] G. T. Caskey, R. A. Douglas, H. T. Richards, and H. V. Smith, “A simple negative-ion sputter source,” *Nuclear Instruments and Methods*, vol. 157, no. 1, pp. 1–7, Feb. 1978, doi: 10.1016/0029-554X(78)90581-5.

[213] R. Middleton, “A versatile high intensity negative ion source,” *Nuclear Instruments and Methods in Physics Research*, vol. 214, no. 2–3, pp. 139–150, Feb. 1983, doi: 10.1016/0167-5087(83)90580-X.

[214] “https://www.cmam.uam.es/facilities/accelerator/duoplasmatron-ion-source/.”

[215] S. Ahmad, M. S. Abbas, M. Yousuf, S. Javeed, S. Zeeshan, and K. Yaqub, “Space-filling, multifractal, localized thermal spikes in Si, Ge and ZnO,” *The European Physical Journal D*, vol. 72, no. 4, p. 70, Apr. 2018, doi: 10.1140/epjd/e2018-80149-5.

[216] J. D. Thomas, G. S. Hodges, D. G. Seely, N. A. Moroz, and T. J. Kvale, “Performance enhancement study of an electrostatic Faraday cup detector,” *Nucl Instrum Methods Phys Res A*, vol. 536, no. 1–2, pp. 11–21, Jan. 2005, doi: 10.1016/j.nima.2004.07.211.

[217] D. M. Montalvan Olivares *et al.*, “Monitoring of carbon ion therapeutic beams with thin silicon sensors,” *Nucl Instrum Methods Phys Res A*, vol. 1063, p. 169289, Jun. 2024, doi: 10.1016/j.nima.2024.169289.

[218] D. S. Levin *et al.*, “A prototype scintillator real-time beam monitor for ultra-high dose rate radiotherapy,” *Med Phys*, vol. 51, no. 4, pp. 2905–2923, Apr. 2024, doi: 10.1002/mp.17018.

[219] R. Hellborg, Ed., *Electrostatic Accelerators*. Springer Berlin Heidelberg, 2005. doi: 10.1007/b138596.

[220] B. Zhou, H. Zhang, P. Zhang, W. Li, and S. An, "Design and optimization study of a duoplasmatron ion source for high-intensity proton beam," *Nucl Instrum Methods Phys Res A*, vol. 1010, p. 165550, Feb. 2021, doi: 10.1016/j.nima.2021.165550.

[221] J. Küpper, J. Meijer, and P. D. Esquinazi, "Feasibility of room temperature detection of low energy single ions using nanometer-thick graphite," *Appl Phys Lett*, vol. 123, no. 17, Oct. 2023, doi: 10.1063/5.0165210.

[222] S. Tamura *et al.*, "Array of bright silicon-vacancy centers in diamond fabricated by low-energy focused ion beam implantation," *Applied Physics Express*, vol. 7, no. 11, p. 115201, Nov. 2014, doi: 10.7567/APEX.7.115201.

[223] Z. Tong, Z. Xu, W. Wu, and X. Luo, "Molecular dynamic simulation of low-energy FIB irradiation induced damage in diamond," *Nucl. Instruments Methods Phys. Res. Sect. B Beam Interact. with Mater. Atoms*, vol. 358, pp. 38–44, 2015, doi: 10.1016/j.nimb.2015.05.023.

[224] B. P. Ajith Kumar, J. Kannaiyan, P. Sugathan, and R. K. Bhowmik, "The NSC 16 MV tandem accelerator control system," *Nucl Instrum Methods Phys Res A*, vol. 343, no. 2–3, pp. 327–330, Apr. 1994, doi: 10.1016/0168-9002(94)90208-9.

[225] E. Losero *et al.*, "Creation of NV Centers in Diamond under 155 MeV Electron Irradiation," *Advanced Physics Research*, Feb. 2023, doi: 10.1002/apxr.202300071.

[226] S. M. Eaton *et al.*, "Quantum Micro–Nano Devices Fabricated in Diamond by Femtosecond Laser and Ion Irradiation," *Adv Quantum Technol*, vol. 2, no. 5–6, Feb. 2019, doi: 10.1002/qute.201900006.

[227] T. Lühmann *et al.*, "Screening and engineering of colour centres in diamond," *J Phys D Appl Phys*, vol. 51, no. 48, p. 483002, Feb. 2018, doi: 10.1088/1361-6463/aadfab.

[228] A. Senichev *et al.*, "Quantum Emitters in Aluminum Nitride Induced by Zirconium Ion Implantation," Jan. 2024.

[229] J. M. Smith, S. A. Meynell, A. C. Bleszynski Jayich, and J. Meijer, "Colour centre generation in diamond for quantum technologies," *Nanophotonics*, vol. 8, no. 11, pp. 1889–1906, Nov. 2019, doi: 10.1515/nanoph-2019-0196.

[230] S. J. Bauman, E. C. Novak, D. T. Debu, D. Natelson, and J. B. Herzog, "Fabrication of Sub-Lithography-Limited Structures via Nanomasking Technique for Plasmonic Enhancement Applications," *IEEE Trans Nanotechnol*, vol. 14, no. 5, pp. 790–793, Sep. 2015, doi: 10.1109/TNANO.2015.2457235.

[231] R. Fukuda *et al.*, "Lithographically engineered shallow nitrogen-vacancy centers in diamond for external nuclear spin sensing," *New J Phys*, vol. 20, no. 8, p. 083029, Aug. 2018, doi: 10.1088/1367-2630/aad997.

[232] A. Persaud *et al.*, "Single ion implantation with scanning probe alignment," *Journal of Vacuum Science & Technology B: Microelectronics and Nanometer Structures Processing, Measurement, and Phenomena*, vol. 22, no. 6, pp. 2992–2994, Nov. 2004, doi: 10.1116/1.1802891.

[233] R. Hellborg, H. J. Whitlow, and Y. Zhang, Eds., *Ion Beams in Nanoscience and Technology*. Berlin, Heidelberg: Springer Berlin Heidelberg, 2010. doi: 10.1007/978-3-642-00623-4.

[234] L. Bischoff, P. Mazarov, L. Bruchhaus, and J. Gierak, “Liquid metal alloy ion sources—An alternative for focussed ion beam technology,” *Appl Phys Rev*, vol. 3, no. 2, p. 21101, Feb. 2016, doi: 10.1063/1.4947095.

[235] M. Bawart, A. Jesacher, S. Bernet, and M. Ritsch-Marte, “Remote focusing in confocal microscopy by means of a modified Alvarez lens,” *J Microsc*, vol. 271, no. 3, pp. 337–344, Sep. 2018, doi: 10.1111/jmi.12724.

[236] J. Gierak, “Focused Ion Beam nano-patterning from traditional applications to single ion implantation perspectives,” *Nanofabrication*, vol. 1, no. 1, Jan. 2014, doi: 10.2478/nanofab-2014-0004.

[237] S. Friedensen, J. T. Mlack, and M. Drndić, “Materials analysis and focused ion beam nanofabrication of topological insulator Bi2Se3,” *Sci Rep*, vol. 7, no. 1, p. 13466, Oct. 2017, doi: 10.1038/s41598-017-13863-6.

[238] T. Schröder *et al.*, “Scalable focused ion beam creation of nearly lifetime-limited single quantum emitters in diamond nanostructures,” *Nat Commun*, vol. 8, no. 1, p. 15376, Feb. 2017, doi: 10.1038/ncomms15376.

[239] T. Calligaro *et al.*, “ERDA with an external helium ion micro-beam: Advantages and potential applications,” *Nucl Instrum Methods Phys Res B*, vol. 181, no. 1–4, pp. 180–185, Jul. 2001, doi: 10.1016/S0168-583X(01)00329-9.

[240] M. Jakšić, Z. Medunić, and N. Skukan, “On the use of pulsed microbeam in IBIC,” *Nucl Instrum Methods Phys Res B*, vol. 210, pp. 176–180, Sep. 2003, doi: 10.1016/S0168-583X(03)01051-6.

[241] C. Michelet and P. Moretto, “STIM tomography at the cell level,” *Nucl Instrum Methods Phys Res B*, vol. 158, no. 1–4, pp. 361–367, Sep. 1999, doi: 10.1016/S0168-583X(99)00348-1.

[242] “https://www.osti.gov/servlets/purl/937571.”

[243] E. Vittone *et al.*, “Charge collection efficiency degradation induced by MeV ions in semiconductor devices: Model and experiment,” *Nucl. Instruments Methods Phys. Res. Sect. B Beam Interact. with Mater. Atoms*, vol. 372, pp. 128–142, 2016, doi: 10.1016/j.nimb.2016.01.030.

[244] G. Vízkelethy, B. A. Brunett, D. S. Walsh, R. B. James, R. W. Olsen, and B. L. Doyle, “Ion microbeam studies of cadmium zinc telluride radiation detectors by IBICC,” *Nucl Instrum Methods Phys Res B*, vol. 158, no. 1–4, pp. 437–444, Feb. 1999, doi: 10.1016/S0168-583X(99)00381-X.

[245] E. Nieto Hernandez *et al.*, “Efficient fabrication of high-density ensembles of color centers via ion implantation on a hot diamond substrate.”

[246] S. Möller *et al.*, “A New High-Throughput Focused MeV Ion-Beam Analysis Setup,” *Instruments*, vol. 5, no. 1, p. 10, Feb. 2021, doi: 10.3390/instruments5010010.

[247] R. Reichle *et al.*, “Transport dynamics of single ions in segmented microstructured Paul trap arrays,” *Fortschritte der Physik*, vol. 54, no. 8–10, pp. 666–685, Feb. 2006, doi: 10.1002/prop.200610326.

[248] M. Mohr *et al.*, “Characterization of the recovery of mechanical properties of ion-implanted diamond after thermal annealing,” *Diam Relat Mater*, vol. 63, pp. 75–79, Feb. 2016, doi: 10.1016/j.diamond.2015.11.008.

[249] K. Wang, J. W. Steeds, Z. Li, and H. Wang, “Annealing and lateral migration of defects in IIa diamond created by near-threshold electron irradiation,” *Appl Phys Lett*, vol. 110, no. 15, Apr. 2017, doi: 10.1063/1.4980017.

[250] W. Zhao, Z. Xu, F. Ren, B. Dong, J. Zhao, and P. Wang, “Enhancing the fabrication yield of NV centers in diamond by pre-doping using molecular dynamics simulation,” *Diam Relat Mater*, vol. 132, p. 109683, Feb. 2023, doi: 10.1016/j.diamond.2023.109683.

[251] S. Pezzagna *et al.*, “Polymorphs of ^{17}O-Implanted ST1 Spin Centers in Diamond and Spectroscopy of Strongly Coupled ^{13}C Nuclear Spins,” *ACS Photonics*, vol. 11, no. 5, pp. 1969–1980, May 2024, doi: 10.1021/acsphotonics.4c00061.

[252] Xin Zhang, Tong-Yi Zhang, Man Wong, and Yitshak Zohar, “Rapid thermal annealing of polysilicon thin films,” *Journal of Microelectromechanical Systems*, vol. 7, no. 4, pp. 356–364, 1998, doi: 10.1109/84.735342.

[253] M. Nagamori *et al.*, “Optimum Rapid Thermal Activation of Mg-Doped p-Type GaN,” *Jpn J Appl Phys*, vol. 47, no. 4S, p. 2865, Apr. 2008, doi: 10.1143/JJAP.47.2865.

[254] I. D. Antoro, S. Itoh, S. Yamada, and T. Kawae, “Influence of rapid thermal annealing at varied temperatures on conductivity activation energy and structural properties of Si-doped β-Ga2O3 film grown by pulsed laser deposition,” *Ceram Int*, vol. 45, no. 1, pp. 747–751, Jan. 2019, doi: 10.1016/j.ceramint.2018.09.240.

[255] “https://photonexport.com/rapid-thermal-processing/.”

[256] H. Sumiya, K. Harano, and K. Tamasaku, “HPHT synthesis and crystalline quality of large high-quality (001) and (111) diamond crystals,” *Diam Relat Mater*, vol. 58, pp. 221–225, Feb. 2015, doi: 10.1016/j.diamond.2015.08.006.

[257] M. Lesik *et al.*, “Production of bulk NV centre arrays by shallow implantation and diamond CVD overgrowth,” *physica status solidi (a)*, vol. 213, no. 10, pp. 2594–2600, Oct. 2016, doi: 10.1002/pssa.201600219.

[258] “https://highpressure.ethz.ch/facilities/experimental/multianvil-presses.html.”

[259] M. W. Ngandeu Ngambou *et al.*, “Hot ion implantation to create dense NV center ensembles in diamond,” *Appl Phys Lett*, vol. 124, no. 13, Mar. 2024, doi: 10.1063/5.0196719.

[260] P. Baeri and E. Rimini, “Laser annealing of silicon,” *Mater Chem Phys*, vol. 46, no. 2–3, pp. 169–177, Feb. 1996, doi: 10.1016/S0254-0584(97)80010-7.

[261] A. L. Robinson, “Femtosecond Laser Annealing of Silicon,” *Science (1979)*, vol. 226, no. 4672, pp. 329–330, Feb. 1984, doi: 10.1126/science.226.4672.329.

[262] W. White, J. Narayan, and R. T. Young, “Laser Annealing of Ion-Implanted Semiconductors,” 1979. [Online]. Available: https://www.science.org

[263] J. Engel *et al.*, “Combining femtosecond laser annealing and shallow ion implantation for local color center creation in diamond,” *Appl Phys Lett*, vol. 122, no. 23, Jun. 2023, doi: 10.1063/5.0143922.

[264] R. Middleton, *A Negative-Ion Cookbook*. 1989.

[265] M. Wortmann, A. Ludwig, J. Meijer, D. Reuter, and A. D. Wieck, “High-resolution mass spectrometer for liquid metal ion sources,” *Review of Scientific Instruments*, vol. 84, no. 9, Feb. 2013, doi: 10.1063/1.4822275.

[266] “https://www.globalsino.com/EM/page4316.html.”

[267] A. C. Bovik, *Handbook of image and video processing*, 2nd ed. Amsterdam ; Boston, 2005. [Online]. Available: http://lib.ugent.be/catalog/ebk01:1000000000384560

[268] D. Soliman, “Augmented microscopy: Development and application of high-resolution optoacoustic and multimodal imaging techniques for label-free biological observation,” 2016. doi: 10.13140/RG.2.2.24410.03525.

[269] S. Buckley, K. Rivoire, and J. Vučković, “Engineered quantum dot single-photon sources,” *Reports on Progress in Physics*, vol. 75, no. 12, p. 126503, Feb. 2012, doi: 10.1088/0034-4885/75/12/126503.

[270] E. Corte *et al.*, “Spectral Emission Dependence of Tin-Vacancy Centers in Diamond from Thermal Processing and Chemical Functionalization,” *Adv. Photonics Res.*, vol. 3, no. 1, p. 2100148, Feb. 2022, doi: 10.1002/adpr.202100148.

[271] M. E. Trusheim *et al.*, “Lead-Related Quantum Emitters in Diamond,” in *Conference on Lasers and Electro-Optics*, OSA, 2018, p. FTu4H.2. doi: 10.1364/CLEO_QELS.2018.FTu4H.2.

[272] S. D. Tchernij *et al.*, “Spectral features of Pb-related color centers in diamond – a systematic photoluminescence characterization,” *New J Phys*, vol. 23, no. 6, p. 63032, Feb. 2021, doi: 10.1088/1367-2630/ac038a.

[273] S. D. D. Tchernij *et al.*, “Single-Photon-Emitting Optical Centers in Diamond Fabricated upon Sn Implantation,” *ACS Photonics*, vol. 4, no. 10, pp. 2580–2586, Feb. 2017, doi: 10.1021/acsphotonics.7b00904.

[274] U. Wahl *et al.*, “Structural formation yield of GeV centers from implanted Ge in diamond,” *Materials for Quantum Technology*, vol. 4, no. 2, p. 025101, Jun. 2024, doi: 10.1088/2633-4356/ad4b8d.

[275] E. Moreva *et al.*, “Practical Applications of Quantum Sensing: A Simple Method to Enhance the Sensitivity of Nitrogen-Vacancy-Based Temperature Sensors,” *Phys Rev Appl*, vol. 13, no. 5, p. 54057, Feb. 2020, doi: 10.1103/PhysRevApplied.13.054057.

[276] S. D. Tchernij *et al.*, “Single-Photon-Emitting Optical Centers in Diamond Fabricated upon Sn Implantation,” *ACS Photonics*, vol. 4, no. 10, pp. 2580–2586, Oct. 2017, doi: 10.1021/acsphotonics.7b00904.

[277] R. Brouri, A. Beveratos, J. Poizat, and P. Grangier, “Photon antibunching in the fluorescence of individual color centers in diamond,” *Opt Lett*, vol. 25, no. 17, p. 1294, Feb. 2000, doi: 10.1364/OL.25.001294.

[278] S. Blakley *et al.*, “Fiber-Optic Quantum Thermometry with Germanium-Vacancy Centers in Diamond,” *ACS Photonics*, vol. 6, no. 7, pp. 1690–1693, 2019, doi: 10.1021/acsphotonics.9b00206.

[279] V. G. Ralchenko *et al.*, “Observation of the Ge-vacancy color center in microcrystalline diamond films,” *Bulletin of the Lebedev Physics Institute*, vol. 42, no. 6, pp. 165–168, Feb. 2015, doi: 10.3103/S1068335615060020.

[280] S. Häußler *et al.*, “Photoluminescence excitation spectroscopy of SiV− and GeV− color center in diamond,” *New J Phys*, vol. 19, no. 6, p. 63036, Feb. 2017, doi: 10.1088/1367-2630/AA73E5.

[281] J. N. Becker *et al.*, “Ultrafast all-optical coherent control of single silicon vacancy colour centres in diamond,” *Nat. Commun.*, vol. 7, p. 13512, Feb. 2016, doi: 10.1038/ncomms13512.

[282] U. Wahl *et al.*, “Direct Structural Identification and Quantification of the Split-Vacancy Configuration for Implanted Sn in Diamond,” *Phys Rev Lett*, vol. 125, no. 4, p. 045301, Jul. 2020, doi: 10.1103/PhysRevLett.125.045301.

[283] D. Sovyk *et al.*, “Fabrication of diamond microstub photoemitters with strong photoluminescence of SiV color centers: bottom-up approach,” *Appl Phys A Mater Sci Process*, vol. 118, no. 1, pp. 17–21, Feb. 2015, doi: 10.1007/s00339-014-8877-2.

[284] T. Lühmann, J. Küpper, S. Dietel, R. Staacke, J. Meijer, and S. Pezzagna, “Charge-State Tuning of Single SnV Centers in Diamond,” *ACS Photonics*, vol. 7, no. 12, pp. 3376–3385, 2020, doi: 10.1021/acsphotonics.0c01123.

[285] S. Sciortino *et al.*, “Micro-beam and pulsed laser beam techniques for the micro-fabrication of diamond surface and bulk structures,” *Nucl Instrum Methods Phys Res B*, vol. 348, pp. 191–198, Apr. 2015, doi: 10.1016/j.nimb.2014.11.061.

[286] Y. Gao, J.-M. Lai, Z.-Y. Li, P.-H. Tan, C.-X. Shan, and J. Zhang, “Local laser heating effects in diamond probed by photoluminescence of SiV− centers at low temperatures,” *Appl Phys Lett*, vol. 124, no. 9, Feb. 2024, doi: 10.1063/5.0184331.

[287] N. Aslam, G. Waldherr, P. Neumann, F. Jelezko, and J. Wrachtrup, “Photo-induced ionization dynamics of the nitrogen vacancy defect in diamond investigated by single-shot charge state detection,” *New J Phys*, vol. 15, no. 1, p. 013064, Jan. 2013, doi: 10.1088/1367-2630/15/1/013064.

[288] S. Lagomarsino *et al.*, “Photoionization of monocrystalline CVD diamond irradiated with ultrashort intense laser pulse,” *Phys Rev B*, vol. 93, no. 8, Feb. 2016, doi: 10.1103/PhysRevB.93.085128.

[289] R. Kalish and S. Prawer, “Graphitization of diamond by ion impact: Fundamentals and applications,” *Nucl. Inst. Methods Phys. Res. B*, vol. 106, no. 1–4, pp. 492–499, Feb. 1995, doi: 10.1016/0168-583X(95)00758-X.

[290] S. A. Solin and A. K. Ramdas, “Raman Spectrum of Diamond,” *Phys Rev B*, vol. 1, no. 4, pp. 1687–1698, Feb. 1970, doi: 10.1103/PhysRevB.1.1687.

[291] D. G. Monticone *et al.*, “Systematic study of defect-related quenching of NV luminescence in diamond with time-correlated single-photon counting spectroscopy,” *Phys Rev B*, vol. 88, no. 15, p. 155201, Feb. 2013, doi: 10.1103/PhysRevB.88.155201.

[292] A. M. Edmonds *et al.*, “Production of oriented nitrogen-vacancy color centers in synthetic diamond,” *Phys Rev B*, vol. 86, no. 3, p. 035201, Jul. 2012, doi: 10.1103/PhysRevB.86.035201.

[293] G. Davies, S. C. Lawson, A. T. Collins, A. Mainwood, and S. J. Sharp, “Vacancy-related centers in diamond,” *Phys Rev B*, vol. 46, no. 20, pp. 13157–13170, Feb. 1992, doi: 10.1103/PhysRevB.46.13157.

[294] J. O. Orwa *et al.*, “Fabrication of single optical centres in diamonda review,” in *Journal of Luminescence*, Feb. 2010, pp. 1646–1654. doi: 10.1016/j.jlumin.2009.12.028.

[295] S. G. Bishop *et al.*, “Room-Temperature Quantum Emitter in Aluminum Nitride,” *ACS Photonics*, vol. 7, no. 7, pp. 1636–1641, Jul. 2020, doi: 10.1021/acsphotonics.0c00528.